UNIVERSITY OF CALIFORNIA SAN DIEGO

FeAl-based Metallic-Intermetallic Laminate (MIL) Composites

A dissertation submitted in partial satisfaction of the
requirements for the degree Doctor of Philosophy

in

NanoEngineering

by

Haoren Wang

Committee in charge:

Professor Kenneth S. Vecchio, Chair
Professor Farhat Beg
Professor Shadi A. Dayeh
Professor Jian Luo
Professor Kesong Yang

2021

The dissertation of Haoren Wang is approved, and it is acceptable in quality and form for publication on microfilm and electronically.

University of California San Diego

2021

TABLE OF CONTENTS

LIST OF ABBREVIATIONS

MIL Composites:	Metallic-Intermetallic Laminate Composites
SPS:	Spark Plasma Sintering
SEM:	Scanning Electron Microscope
EDS:	Energy-Dispersive X-ray Spectrometer
EBSD:	Electron BackScattered Diffraction
XRD:	X-Ray Diffractometer
GND:	Geometrically Necessary Dislocation
FEA:	Finite Element Analysis
HDI Stress:	Hetero-Deformation Induced Stress
430SS:	430 Stainless Steel
304SS：	304 Stainless Steel

LIST OF FIGURES

LIST OF TABLES

ACKNOWLEDGEMENTS

I would like to acknowledge Professor Kenneth Vecchio for his support as the chair of my committee. Through multiple drafts and many long nights, his guidance has proved to be invaluable.

I would also like to acknowledge Yu Wang, Tyler Harrington, Chaoyi Zhu, Rui Kou, Haozhe Yi, Samuel Figueroa, Xiao Liu, Chunhuan Guo, Stephen Horvath, Sabine Faulhaber, Wayne Neilson, Eduardo Marin, Grant Schrader, and all other members of Vecchio's group. Without them, my research would have no doubt taken five times as long. It is their support that helped me in an immeasurable way.

Chapter 2, in full, is a reprint of the material as it appears in Acta Materialia, 2019, Elsevier. Wang, Haoren; Harrington, Tyler; Zhu, Chaoyi; Vecchio, Kenneth S. The dissertation author was the primary investigator and author of this paper.

Chapter 3, in full, is a reprint of the material as it appears in Acta Materialia, 2020, Elsevier. Wang, Haoren; Zhu, Chaoyi; Vecchio, Kenneth S. The dissertation author was the primary investigator and author of this paper.

Chapter 4, in full, is a reprint of the material as it appears in Acta Materialia, 2021, Elsevier. Wang, Haoren; Kou, Rui; Yi, Haozhe; Figueroa, Samuel; Vecchio, Kenneth S. The dissertation author was the primary investigator and author of this paper.

Chapter 5, in full, is a reprint of the material as it appears in Materialia, 2020, Elsevier. Wang, Haoren; Kou, Rui; Vecchio, Kenneth S. The dissertation author was the primary investigator and author of this paper.

Chapter 6, in full, is a reprint of the material as it appears in Acta Materialia, 2020, Elsevier. Wang, Haoren; Kou, Rui; Harrington, Tyler; Vecchio, Kenneth S. The dissertation author was the primary investigator and author of this paper.

VITA

2013	Bachelor of Engineering, Shanghai Jiao Tong University
2015	Master of Science, University of Pennsylvania
2015-2021	Research Assistant, University of California San Diego
2016-2021	Teaching Assistant, University of California San Diego
2021	Doctor of Philosophy, University of California San Diego

PUBLICATIONS

Wang, H., Kou, R., Yi, H., Figueroa, S. and Vecchio, K. S. Mesoscale Hetero-Deformation Induced (HDI) Stress in FeAl-Based Metallic-Intermetallic Laminate (MIL) Composites. *Acta Materialia* (2021)

Wang, H., Kou, R. and Vecchio, K. S. Design, Fabrication and Optimization of FeAl-FeAl2 Eutectoid Metallic-Intermetallic Laminate (MIL) Composites. *Materialia* (2020).

Wang, H., Zhu, C. and Vecchio, K. S. Deformation and Fracture Evolution of FeAl-based Metallic-Intermetallic Laminate (MIL) Composites. *Acta Materialia* (2020).

Wang, H., Kou, R., Harrington, T. and Vecchio, K. S. Electromigration Effect in Fe-Al Diffusion Couples with Field Assisted Sintering. *Acta Materialia* (2020).

Wang, H., Harrington, T., Zhu, C. and Vecchio, K. S. Design, fabrication and characterization of FeAl-based metallic-intermetallic laminate (MIL) composites. *Acta Materialia* (2019).

Zhang, C., Wang, H., Zhu, C., Xu, M., Zhao, S., Kou, R., Wang, X., MacDonald, B., Ye, F., Vecchio, K.S., Rupert, T. and Lavernia, E. Strong and Ductile Refractory High-Entropy Alloys with Super Formability (under review at *Science*)

Zhu, C., Wang, H., Kaufmann, K. and Vecchio, K. S. A Computer vision approach to study surface deformation of materials. *Measurement Science and Technology* (2019).

Wang, Y., Wang, H., Liu, X. and Vecchio, K.S. Microstructure evolution in pure Ni and Invar-based Metallic-Intermetallic Laminate (MIL) composites. *Materials Science and Engineering: A* (2017).

Wang, Y., Wang, H., Liu, X. and Vecchio, K.S. Microstructure evolution in Ni and Ni-superalloy based metallic-intermetallic laminate (MIL) composites. *Intermetallics* (2017).

Dong, Y., Wang, H. and Chen, I.W. Electrical and hydrogen reduction enhances kinetics in doped zirconia and ceria: I. grain growth study. *Journal of the American Ceramic Society* (2017).

Qin, M. Yan, Q., Wang, H., Vecchio, K.S. and Luo J. High-Entropy Rare Earth Tetraborides. *Journal of the European Ceramic Society* (2021).

Qin, M., Yan, Q., Wang, H., Vecchio, K.S. and Luo J. High-Entropy Monoborides: Towards Superhard Materials. *Scripta Materialia* (2020).

Wang, Y., Liu X., Wang, H. and Vecchio K.S. The Effect of Oxides on Fe/Al Interfacial Reaction in Metallic-Intermetallic Laminate (MIL) Composites. *Journal of Alloys and Compounds* (2020).

Qin, M., Yan, Q., Liu, Y., Wang, H., Wang, C. Lei, T., Vecchio, K.S., Xin, H.L., Rupert, T. and Luo, J. Bulk High-Entropy Hexaborides. *Journal of the European Ceramic Society* (2021).

Zhang, C., MacDonald, B.E., Guo, F., Wang, H., Zhu, C., Liu, X., Kang, Y., Xie, X., Zhou, Y., Vecchio, K.S. and Lavernia, E.J. Cold-workable Refractory Complex Concentrated Alloys with Tunable Microstructure and Good Tensile Behavior. *Scripta Materialia* (2020).

Qin, M., Gild, J., Hu, C., Wang, H., Hoque, S.B., Braun, J.L., Harrington, T.J., Hopkins, P.E., Vecchio, K.S. and Luo, J. Dual-Phase High-Entropy Ultrahigh Temperature Ceramics. *Journal of the European Ceramic Society* (2020).

Qin, M., Gild, J., Wang, H., Harrington, T., Vecchio, K.S. and Luo J. Dissolving and Stabilizing Soft WB2 and MoB2 Phases into High-Entropy Borides via Boron-Metals Reactive Sintering to Attain Higher Hardness. *Journal of the European Ceramic Society* (2020).

Kaufmann, K., Zhu, C., Rosengarten, A.S., Maryanovsky, D., Wang, H. and Vecchio, K.S. Phase Mapping in EBSD Using Convolutional Neural Networks. *Microscopy and Microanalysis* (2020).

Zhang, Z., Hu, W., Deng, Y., Zhong, C., Wang, H., Wu, Y. and Liu, L. The effect of complexing agents on the oriented growth of electrodeposited microcrystalline cuprous oxide film. *Materials Research Bulletin* (2012).

FIELDS OF STUDY

Major Field: Engineering

Studies in NanoEngineering, Materials Science Focus

Professor Kenneth Vecchio

ABSTRACT OF THE DISSERTATION

FeAl-based Metallic-Intermetallic Laminate (MIL) Composites

by

Haoren Wang

Doctor of Philosophy in NanoEngineering

University of California San Diego, 2021

Professor Kenneth S. Vecchio, Chair

FeAl-based Metallic-Intermetallic Laminate (MIL) composites and FeAl/$FeAl_2$ eutectoid MIL composites of various iron alloys were fabricated with an innovative "multiple-thin-foil" configuration and "two-stage reaction" strategy. Alternating stacked metal foils were reactive sintered via spark plasma sintering (SPS) (a.k.a. field assisted sintering) to grow intermetallics. The "multiple-thin-foil" configuration reduces reaction time, enables local chemical composition control and allows metal/intermetallic combinations, which cannot be produced via the conventional methods. Fe-FeAl, 430SS-FeAl, and 304SS-FeAl MIL composites can be synthesized with desired metallic/intermetallic ratios, where FeAl is the single intermetallic phase present in the composites. The deformation and fracture evolution of the FeAl-based MIL

composites is investigated here via incremental compression testing. Geometrically necessary dislocation (GND) analysis indicates the FeAl regions deform in similar manners for the three MIL composites, and each fails in a similar mode. Single-phase intermetallic FeAl layered material is also synthesized using a similar approach to study the fracture mechanisms of FeAl-based MIL composites. Mesoscale hetero-deformation induced (HDI) stress, which is tensile on the FeAl layers of MIL composites, accelerates crack nucleation and crack propagation, eventually inducing failure. The HDI stress evaluated via finite element analysis (FEA) simulation explains the difference between 430SS-FeAl and 304SS-FeAl MIL composites, which possess similar microstructure and composition, but very different strengths. Meanwhile, the electromigration effect in SPS is quantitively analyzed in the Fe-Al diffusion couple system. In SPS, the samples are heated by the applied voltage and a high electric current, which can lead to an electromigration effect. FEA simulation is utilized to determine the voltage applied to the Fe-Al diffusion couple, which is found to be extremely small to induce any voltage effect. Additionally, the simulation suggests the temperature and current density distribution is uniform across the metallic diffusion couple, which makes quantitative measurement feasible. For the first time, a mathematic algorithm, which allows diffusivity and electromigration coefficients to be solved, is developed for the system with multiple reactive layers.

Chapter 1 Introduction

1.1 MIL Composites in Fe-Al System

Metal-intermetallic laminate (MIL) composites are produced via incorporating layers of ductile metals into strong, but brittle intermetallics for optimizing mechanical behaviors. Generally, aluminide-intermetallics possess ordered crystalline structures with high specific modulus and high specific compressive strength, but often very limited plasticity or toughness. Reinforcing these intermetallics with particles, fibers or layers of ductile metals can enhance the toughness [1], making the materials more efficient for structural applications.

MIL composites are typically synthesized via hot pressing alternating stacked metal foils so that intermetallic layers form as the result of interdiffusion and chemical reaction, while an appropriate pressure ensures intimate contact between the sheets of metal foils. The selection of the foil composition and thickness can determine the physical and mechanical properties of the MIL composites so that the specific performance requirements can be fulfilled. The ability to tailor composite microstructure, and the low cost of the initial metallic foils make MIL composites ideal as commercially scalable structural materials, suitable for aerospace applications that require lightweight materials with high specific properties. By tuning the geometry of the initial metal foils, MIL composites can be synthesized into complex shapes, such as rods, tubes or cones, for specific platforms. In addition, multi-functionality can be incorporated into MIL composites, i.e. having the initial foils pre-machined with cavities to provide pathways in the composites for sensors to be embedded for damage detection [2].

Predecessors of MIL composite materials were first synthesized via a solid-state combustion wave in 1989, but little control of microstructure was achievable due to the self-

sustaining reaction kinetics [3]. The concept of 'moderated-reactive sintering' leading to the formation of microstructure-controlled MIL composites was systemically introduced in 2001 by Harach and Vecchio for the Ti-Al system [4]. Since then, studies of MIL composites have primarily focused on the Ti-Al system to understand mechanical behaviors. Rohatgi *et al.* [5] investigated the fracture behavior, Adharapurapu *et al.* [6] investigated the fatigue crack resistance, Li *et al.* [7,8] investigated the damage evolution, Cao *et al.* [9] investigated the ballistic performance, and Jiang et al. [10] investigated the dynamic fracture behavior. The effect of metallic/intermetallic ratio was investigated for optimizing the properties [11,12], and other reinforcements, such as ceramic fibers [13], were also introduced to the Ti-Al system to enhance the properties of the MIL composites. However, Al_3Ti, which exhibits little plasticity, is the only intermetallic phase formed when reacting Al foils with Ti foils due to extremely slow growth kinetics for other intermetallics. Therefore, MIL composites in the Ti-Al system exhibit limited plasticity, while the lack of available intermetallics limits the ability to tune the properties of the materials. In order to lower the cost and optimize strength and ductility for MIL composites, Ni-Al [14–16] and Fe-Al [17–19] systems, which process ductile intermetallic phases, have begun to attract more attention in recent years.

In the Fe-Al system, the conventional fabrication process occurs between the eutectic temperature of Al-Fe (655^{o}C) and the melting point of Al (660^{o}C) to achieve the fastest reaction rate without macroscale melting. However, previous studies of microstructure evolution in MIL composites in the Fe-Al system [17,19], including pure iron, 430 stainless steel and 304 stainless steel, suggest that the conventional sintering temperature (655^{o}C to 660^{o}C) only generates brittle intermetallics, such as Fe_2Al_5, Fe_4Al_{13} and Cr_2Al_{13}. On the other hand, studies using Fe-Al diffusion couples [20] confirm the formation of FeAl at 1000^{o}C, which is reported to be a ductile

intermetallic phase [21–23]. Although subsequent annealing of pure Fe-Al MIL composites can transform some intermetallics to FeAl, when either 430 or 304 stainless steel is incorporated, other brittle phases, such as $FeAl_2$ and Cr_5Al_8, form [18]. In summary, synthesizing MIL composites with only ductile intermetallics, such as FeAl, remains a significant challenge for the field.

In the present study, an innovative fabrication process for MIL composites is proposed to solve the challenge of controlling selective phase formation. MIL composites, where FeAl is the single intermetallic phase, have been successfully synthesized with pure iron or stainless steels. Microstructure assessment of the composites was investigated to evaluate the fabrication process, and growth kinetics were analyzed to understand the design for sintering parameters. Local mechanical behaviors were estimated via nanoindentation and global mechanical properties were measured via compression testing.

The FeAl-based MIL composites have demonstrated the highest levels of both strength and ductility among all MIL composites to date [5,15,24–33]. We aim to understand the dramatic improvement in the mechanical behavior of FeAl-based MIL composites. Incremental compression testing is conducted to investigate the deformation and fracture evolution processes. The microstructures of the deformed specimens are characterized via electron backscatter diffraction (EBSD). From the orientation data obtained in EBSD, lattice curvature is derived to compute geometrically necessary dislocation (GND) density via the Nye-Kröner-Bilby relationship [34]. GND density is thought to accommodate plastic strain non-uniformity in polycrystalline materials [35], Therefore, GND density during plastic deformation is used to correlate the mechanical response of FeAl-based MIL composites with variation in composition and loading conditions.

Hetero-deformation induced (HDI) stress describes the internal stress in heterostructured materials during deformation [36]. The constituents in heterostructured materials possess dissimilar mechanical behaviors, which create the long-range internal stress, conventionally known as back stress and forward stress, that can potentially enhance mechanical properties. Recent studies by *Zhu* and *Wu* suggest "HDI stress" is a more accurate description of the interactions in the heterostructured materials during the plastic deformation [37]. Investigations of HDI stress mostly focus on the interface scale, where HDI stress is typically produced by geometrically necessary dislocations (GND) [36–39].

Single-phase layered FeAl material is synthesized following the same processing as FeAl-based MIL composites from our previous studies. The mechanical properties measured here for this unique microstructured single-phase FeAl are used in subsequent finite element analysis (FEA) modeling to assess the properties of the FeAl-based MIL composites fabricated with similar FeAl layers. Comparisons between these MIL composites and single-phase FeAl material indicate that the HDI stress occurs at the scale of the layers, which are on the order of 100s of microns. These HDI stresses resulting from these mesoscale microstructure features have not been previously reported. Estimation of HDI stress via simulation coincides with the experimental observations, which suggests the mesoscale HDI stress is crucial, but has a negative strength effect in these MIL composites. In addition, fracture toughness of both materials, single-phase FeAl and FeAl-based MIL composites is measured to evaluate the enhancement of MIL composites over the single-phase FeAl, in terms of toughness.

Except for FeAl-based MIL composites, another new type of MIL composite in the Fe-Al system is created by forming the eutectoid structure of FeAl and $FeAl_2$ as the intermetallic regions. The $FeAl_2$ phase, which possesses a triclinic structure, is hard, but extremely brittle. Meanwhile,

the lamellar nature of the eutectoid structure itself can be regarded as a natural form of composite, wherein the fine-scale lamellar $FeAl_2$ phase is toughened by the fine-scale, relatively ductile FeAl phase [40–42].

For these eutectoid-MIL composites, the metal layers and volume fraction of the eutectoid structure are varied for optimizing the performance. Heat treatment is utilized to fine-tune the microstructure, demonstrating another approach to adjust the properties rather than only the initial foil combination. Furthermore, a new hybrid MIL composite, which possesses both single-phase FeAl layers and FeAl-$FeAl_2$ eutectoid layers, is synthesized as a 'proof-of-concept' of tailoring structure to performance. Incremental compression testing was conducted to evaluate the mechanical properties and investigate the fracture evolution mechanisms.

1.2 Electromigration Effect in Field Assisted Sintering

During the processing for MIL composites via SPS, we noticed the asymmetric growth of intermetallics, which is induced by the electromigration effect. The electromigration phenomenon was first discovered by Gerardin in 1861 [43], which refers to the motion of atoms in metals under an applied voltage. Under the concept of electromigration, two opposite effects were proposed: the direct electrostatic force acting on the positive-charged metal ions, and the scattering of the current (electron flow) off the metal atoms [44]. The balance between the direct electrostatic force and the electron force is captured in a quantity called the effective charge Z^*, written as Equation (1.1):

$$\boldsymbol{F} = \boldsymbol{F}_{direct} + \boldsymbol{F}_{wind} = (Z_{direct} + Z_{wind})eE = Z^* eE \tag{1.1}$$

Evaluation of Equation (1) via quantum mechanics demonstrates that the electron flow force would typically dominate the system [45], moving atoms towards the anode direction. The

motion of atoms would accumulate voids in metals, causing failure in integrated circuits [46]. As a result, investigations on electromigration became intensive in the 1990s, while the early-stage studies primarily focused on pure metal like aluminum and copper [47–49]. The electromigration effect upon the interface of dissimilar metals was first reported in the Ni-Al binary system [50], as the microscopic motion of atoms induced by electromigration would alter the macroscopic diffusivity, and consequently the thickness of the intermetallic layers. Since then, the electromigration phenomenon has been found in other metallic diffusion couples, such as Al-Au [51], Ni-Ti [52] and Ag-Zn [53]. Furthermore, quantitative analysis of electromigration in diffusion couples, which were used to calculate the diffusivity and the electromigration coefficient, and provides the prediction of intermetallic layer thickness, was first demonstrated in the Sn-Ag system, which forms a single intermetallic phase of Ag_3Sn [54]. However, the quantitative analysis of the system where multiple intermetallic phases coexist, which is common for transition metals, is still lacking.

The pioneering works of sparking plasma sintering (SPS) were first developed in 1906 [55], and became an industrial processing technology since the 1990s [56]. SPS equipment generally involves vacuum, load, cooling, control and electrical power supply systems, along with a sample-die-plunger assembly [57]. The samples (typically powders) would be sintered with pressure and the applied voltage, which heats up the materials. The early-stage studies about SPS proposed two mechanisms that raise the temperature: Joule heating effect, and spark discharge that was believed to occur at the tiny gap between the powder particles[57], hence the name. Doubt about the existence of the spark discharge remains, and the SPS technology consequently derived other names, such as pulsed electric current sintering (PECS) [58,59], plasma activated sintering (PAS)[60], electric current activated/assisted sintering (ECAS) [61], and field assisted/activated

sintering (FAST) [62]. In this work, we will continue to use the most common term, SPS, although neither spark nor plasma is expected to exist in the situation we are studying.

As the SPS has been widely used in both academia and industry, the investigations about the electromigration phenomena in SPS were thereby conducted [63–66] to evaluate the SPS technology. Unlike the conventional electromigration studies, where the electric field and temperature can be independently controlled, the electric field and temperature are strongly coupled in SPS. Any attempt to increase the electric field would inevitably raise the temperature. Meanwhile, SPS requires considerably higher voltage and current across the sample compared to other sintering approaches, because the heat energy is entirely generated from the applied electric field. However, SPS related electromigration studies are typically qualitative, while the quantitative analysis for the diffusivity and electromigration coefficient is lacking. Furthermore, the in-situ sample conditions, which are complicated in the SPS, but essential for a systematic study, are seldom considered due to the challenges in measurements.

In the present study, the electromigration effect via SPS in the Fe-Al diffusion couple system, where Fe_2Al_5 phase dominates at low temperature, and $FeAl_2$, FeAl and α-Fe solid solution coexist at high temperature, is investigated. The Fe-Al diffusion couple sintered via SPS exhibits a significant difference in the intermetallic layer thickness between forward and reverse directions. The voltage directly applied to the diffusion couple, along with the temperature and current density distribution, are evaluated via finite element analysis simulation. A mathematic algorithm is developed for not only the Fe-Al diffusion couple system, but also other metallic diffusion couples where multiple intermetallic phases can coexist, allowing diffusivity and electromigration coefficient to be solved.

Acknowledgment

Chapter 1, in part, is the reprint of the published articles:

Acta Materialia, Elsevier: Wang, Haoren; Harrington, Tyler; Zhu, Chaoyi; Vecchio, Kenneth S. Design, fabrication and characterization of FeAl-based metallic-intermetallic laminate (MIL) composites. Acta Materialia (2019).

Wang, Haoren; Zhu, Chaoyi; Vecchio, Kenneth S. Deformation and Fracture Evolution of FeAl-based Metallic-Intermetallic Laminate (MIL) Composites. Acta Materialia (2020).

Wang, Haoren; Kou, Rui; Yi, Haozhe; Figueroa, Samuel; Vecchio, Kenneth S. Mesoscale Hetero-Deformation Induced (HDI) Stress in FeAl-Based Metallic-Intermetallic Laminate (MIL) Composites. Acta Materialia (2021).

Wang, Haoren; Kou, Rui; Vecchio, Kenneth S. Design, Fabrication and Optimization of FeAl-$FeAl_2$ Eutectoid Metallic-Intermetallic Laminate (MIL) Composites. Materialia (2020).

Wang, Haoren; Kou, Rui; Harrington, Tyler; Vecchio, Kenneth S. Electromigration Effect in Fe-Al Diffusion Couples with Field-Assisted Sintering. Acta Materialia (2020).

I would like to thank Tyler Harrington, Chaoyi Zhu, Rui Kou, Haozhe Yi, Samuel Figueroa, and my principal investigator Professor Kenneth Vecchio, for their contribution in these works.

Chapter 2 Design, Fabrication and Characterization of FeAl-based MIL Composites

Chapter 2, in full, is the reprint of the published article in Acta Materialia, Elsevier: Wang, Haoren; Harrington, Tyler; Zhu, Chaoyi; Vecchio, Kenneth S. Design, fabrication and characterization of FeAl-based metallic-intermetallic laminate (MIL) composites. Acta Materialia (2019).

Abstract

FeAl-based MIL composites of various iron alloys were fabricated with an innovative "multiple-thin-foil" configuration and "two-stage reaction" strategy. Alternating stacked metal foils were reactive sintered via SPS at 600^{o}C and 1000^{o}C to grow intermetallics. The "multiple-thin-foil" configuration reduces reaction time, enables local chemical composition control and allows metal/intermetallic combinations, which cannot be produced via the conventional methods. Fe-FeAl, 430SS-FeAl, and 304SS-FeAl MIL composites can be synthesized with desired metallic/intermetallic ratios, where FeAl is the single intermetallic phase present in the composites. Microstructure analysis via SEM, EDS, and EBSD confirms phase identification and reveals the formation of transition layers. The transition layer, which incorporates the composition gradient between the metal (Fe, 430SS or 304SS) and the FeAl intermetallic phase, provides a gradual change in mechanical properties from the metal to intermetallic layers, and further functions as a chemical barrier into which other undesired intermetallics dissolve. Driven by diffusion-controlled growth, grains in the transition layers and FeAl regions exhibit ordered arrangement and sintering textures. Hardness profiles from the metal layer to FeAl region reveal the correlation

between local mechanical properties and local chemical compositions. In compression testing, the compressive strength can reach 2.3 GPa with considerable plasticity, establishing the best mechanical properties of any MIL composites synthesized to date.

2.1 Introduction

Metal-intermetallic laminate (MIL) composites are produced via incorporating layers of ductile metals into strong, but brittle intermetallics for optimizing mechanical behaviors. Generally, aluminide-intermetallics possess ordered crystalline structures with high specific modulus and high specific compressive strength, but often very limited plasticity or toughness. Reinforcing these intermetallics with particles, fibers or layers of ductile metals can enhance the toughness [1], making the materials more efficient for structural applications.

MIL composites are typically synthesized via hot pressing alternating stacked metal foils so that intermetallic layers form as the result of interdiffusion and chemical reaction, while an appropriate pressure ensures intimate contact between the sheets of metal foils. The selection of the foil composition and thickness can determine the physical and mechanical properties of the MIL composites so that the specific performance requirements can be fulfilled. The ability to tailor composite microstructure, and the low cost of the initial metallic foils make MIL composites ideal as commercially scalable structural materials, suitable for aerospace applications that require lightweight materials with high specific properties. By tuning the geometry of the initial metal foils, MIL composites can be synthesized into complex shapes, such as rods, tubes or cones, for specific platforms. In addition, multi-functionality can be incorporated into MIL composites, i.e. having the initial foils pre-machined with cavities to provide pathways in the composites for sensors to be embedded for damage detection [2].

Predecessors of MIL composite materials were first synthesized via a solid-state combustion wave in 1989, but little control of microstructure was achievable due to the self-sustaining reaction kinetics [3]. The concept of 'moderated-reactive sintering' leading to the formation of microstructure-controlled MIL composites was systemically introduced in 2001 by Harach and Vecchio for the Ti-Al system [4]. Since then, studies of MIL composites have primarily focused on the Ti-Al system to understand mechanical behaviors. Rohatgi *et al.* [5] investigated the fracture behavior, Adharapurapu *et al.* [6] investigated the fatigue crack resistance, Li *et al.* [7,8] investigated the damage evolution, Cao *et al.* [9] investigated the ballistic performance, and Jiang et al. [10] investigated the dynamic fracture behavior. The effect of metallic/intermetallic ratio was investigated for optimizing the properties [11,12], and other reinforcements, such as ceramic fibers [13], were also introduced to the Ti-Al system to enhance the properties of the MIL composites. However, Al_3Ti, which exhibits little plasticity, is the only intermetallic phase formed when reacting Al foils with Ti foils due to extremely slow growth kinetics for other intermetallics. Therefore, MIL composites in the Ti-Al system exhibit limited plasticity, while the lack of available intermetallics limits the ability to tune the properties of the materials. In order to lower the cost and optimize strength and ductility for MIL composites, Ni-Al [14–16] and Fe-Al [17–19] systems, which process ductile intermetallic phases, have begun to attract more attention in recent years.

In the Fe-Al system, the conventional fabrication process occurs between the eutectic temperature of Al-Fe (655^{o}C) and the melting point of Al (660^{o}C) to achieve the fastest reaction rate without macroscale melting. However, previous studies of microstructure evolution in MIL composites in the Fe-Al system [17,19], including pure iron, 430 stainless steel and 304 stainless steel, suggest that the conventional sintering temperature (655^{o}C to 660^{o}C) only generates brittle

intermetallics, such as Fe_2Al_5, Fe_4Al_{13} and Cr_2Al_{13}. On the other hand, studies using Fe-Al diffusion couples [20] confirm the formation of FeAl at 1000°C, which is reported to be a ductile intermetallic phase [21–23]. Although subsequent annealing of pure Fe-Al MIL composites can transform some intermetallics to FeAl, when either 430 or 304 stainless steel is incorporated, other brittle phases, such as $FeAl_2$ and Cr_5Al_8, form [18]. In summary, synthesizing MIL composites with only ductile intermetallics, such as FeAl, remains a significant challenge for the field.

In the present study, an innovative fabrication process for MIL composites is proposed to solve the challenge of controlling selective phase formation. MIL composites, where FeAl is the single intermetallic phase, have been successfully synthesized with pure iron or stainless steels. Microstructure assessment of the composites was investigated to evaluate the fabrication process, and growth kinetics were analyzed to understand the design for sintering parameters. Local mechanical behaviors were estimated via nanoindentation and global mechanical properties were measured via compression testing.

2.2 Experimental

2.2.1 Material Processing

Foils of commercial pure 1100 aluminum, pure iron (99.5%), 430 stainless steel (430SS, 18 wt% Cr) and 304 stainless steel (304SS, 18 wt% Cr and 8 wt% Ni) were feedstocks to produce MIL composites. The metal foils were first abraded with steel wool pads to remove surface oxides and contaminants, rinsed in acetone with ultrasound cleaning, and then stacked in the configuration shown schematically in Figure 2.1(a2). The full layering involves thick Fe/SS foils that are partially retained as remnant metal layers, and ensembles of alternatingly stacked Al-Fe-Al-Fe-Al thin foils, which are intended to transform into the FeAl phase, in between pairs of the thicker

Fe/SS foils. For convenience and distinguishing from the conventional 'thick-foil' stacking demonstrated in Figure 2.1(a1), this configuration is hereafter termed the "multiple-thin-foil" configuration. As illustrated in Figure 2.1(a3), fabrication of the Fe-FeAl MIL composites involved seven layers of 100 μm Al and six layers of 75 μm Fe foils in each "multiple-thin-foil" ensemble, and a total of four such ensembles were incorporated in the sample. These four ensembles were placed between the 500 μm Fe foils, resulting in a total of five layers of the 500 μm Fe foils in the sample. Fabrication of the corresponding 430SS-FeAl or 304SS-FeAl MIL composites, as shown in Figure 2.1(a4), replaced the 500 μm Fe foils by a sandwich structure consisting of 100 μm Fe, 300 μm stainless steel and 100 μm Fe (totaling 500 μm in thick metal layers).

The stacked foils, which were cut into 20mm diameter disks, were placed in a Thermal Technologies Sparking Plasma Sintering (SPS) Model GTAT 10-3 system for reactive sintering. As shown in Figure 2.1(b), the SPS assembly consists of a graphite die, with an inner diameter of 20mm, two cylindrical graphite plungers for loading and electric conductivity, and a thermal insulation blanket using graphite filter. Furthermore, samples were covered by molybdenum foils (99.95%, 0.025-mm-thick) to protect the sample from carbon contamination, and graphite film (0.12-mm-thick) to protect the SPS tooling. The plunger-die assembly is loaded into the vacuum chamber of the SPS machine, loaded axially, and current is passed through the sample via the graphite plungers so that Joule heating brings the sample up in temperature to activate reactive sintering [57]. Figure 2.1(c) shows a typical sintering curve for the materials. In stage 1, the temperature is quickly ramped to 500^{o}C, and then slowly ramped to 600^{o}C to prevent over-shooting this target temperature to avoid melting the Al. After holding at 600^{o}C for 20 minutes, the thin Al foils are completely consumed, transforming into Fe_2Al_5 phase with the adjacent thin

Fe foils. Once all Al is converted to this Fe_2Al_5 intermetallic, the temperature can be increased to 1000°C, and held for 1.5 hr as the second stage reaction to form the FeAl phase.

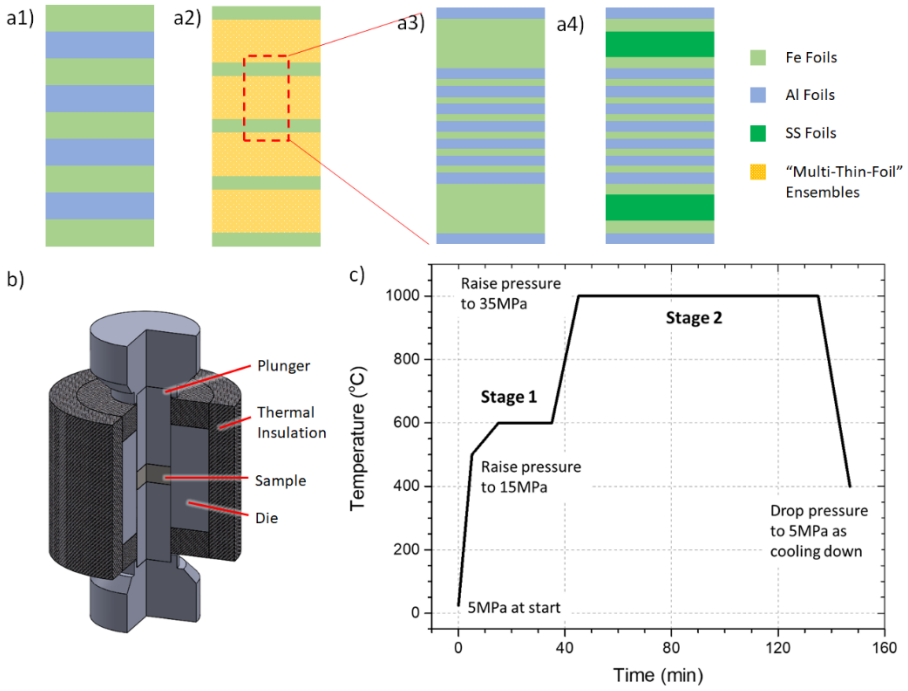

Figure 2.1: (a) Schematic diagrams illustrate the metal foils stacks for synthesizing MIL compositions: (a1) Conventional "thick-foil" configuration, (a2) "multiple-thin-foil" configuration invented in this work, (a3) and (a4) details about "multiple-thin-foil" ensembles for pure iron and stainless steel, respectively. (b) An illustration of SPS setup. (c) Sintering parameters.

2.2.2 Characterization

Fe-FeAl, 430SS-FeAl, and 304SS-FeAl MIL composites samples were mounted with layers perpendicular to the surface, and then polished following standard metallographic preparation procedures. The microstructure was investigated using a Thermo-Fisher (formerly FEI) Apreo scanning electron microscope (SEM) equipped with an Oxford Instrument's Energy-Dispersive X-ray Spectrometer (EDS) and an Oxford Instrument's Symmetry electron backscattered diffraction (EBSD) system. SEM images helped to identify metal/intermetallic layers for further EDS and EBSD analysis. EDS line scans were used to measure chemical

composition profiles from the metal to intermetallic layers, while EBSD mapping collected crystallographic information for identifying phases and grain orientations (textures). After microstructure characterization, the samples were placed into a KLA (formerly KEYSIGHT) G200 Nanoindenter for measuring hardness profiles across the layers. The tests were performed with the Berkovich tip under a load of 500 mN for 5s and repeated 40 times for each area of interest to ensure statistically representative results.

The sintered MIL composite disks were cut into 6 mm cubes for compression testing following standard ASTM E-9. The cubic geometry allows a straightforward comparison of the mechanical behaviors of the anisotropic composites in different directions. The cube dimension of the specimen was determined based on the samples' thickness, which was nominally 6 mm after sintering. The cubes were ground and polished to remove the damage region introduced during cutting and the molybdenum foil that was partially sintered to the top and bottom of the samples. A strain gauge was attached to the specimen, aligned with respect to the loading direction for accurate small-strain measurements; large strain measurements were recorded using crosshead displacement and then corrected with the specimen deformation. Quasi-static compression tests were performed using a standard screw-driven load frame at room temperature with a strain rate of 10^{-3}/s, and grease was applied to the sample ends to minimize friction. During the test, failure of the specimen was defined as the moment when the load undergoes a significant drop.

2.3 Results and Discussion

2.3.1 Microstructure

Figure 2.2 shows SEM images of the three MIL composite materials (Fe-FeAl, 430SS-FeAl, and 304SS-FeAl), where the metallic/intermetallic ratio is around 30/70. The intermetallic

FeAl phase formed as the result of interdiffusion between alternating stacked thin Fe and Al foils in the "multiple-thin-foil" ensembles, while the remnant metal layers remained from the initial thick metal foils. In contrast to most MIL composites, which exhibit sharp boundaries between metals and intermetallics, in these FeAl-based MIL composites, there exist chemical gradient regions, termed a "transition layer" between the FeAl phase and the pure iron or SS layers, which consists of an α-Fe solid solution layer and a FeAl solid solution layer.

2.3.1.1 Fe-FeAl MIL Composites

Figure 2.3(a) shows low magnification SEM micrographs of the microstructures of pure Fe-FeAl MIL composites. The FeAl region is located at the center of the image, while the pure iron layers are on the left and right sides. Considering the translational symmetry of the layering in the MIL composites, examining one region spanning from one remnant metal layer to another can be regarded as representative of the entire sample.

According to the Fe-Al phase diagram [67], the phase transformation of body-centered cubic (BCC) α-Fe (also known as ferrite) to face-centered cubic (FCC) austenite occurs at 914^{o}C for pure iron. Under the sintering condition of 1000^{o}C, aluminum can dissolve into α-Fe phase with a solubility up to 29 at%, while a second-order phase transformation (disordered α-Fe solid solution to ordered FeAl [B2]) occurs at above 29 at% without a step change in composition. The exact composition threshold for the phase transformation varies slightly with temperature along the α-Fe/FeAl solvus. Theoretically, when the temperature drops below 650^{o}C, there exists a compositional step between the α-Fe phase and the FeAl phase. Furthermore, when the temperature drops below 545^{o}C, the Fe_3Al phase would form prior to the ordered FeAl solid solution. While the formation of FeAl phase is proved by XRD analysis in Appendix 2.A, neither

the formation of Fe_3Al nor the compositional step between α-Fe and FeAl is observed in these FeAl-based MIL composites, which indicates that during the cooling stage, the microstructure evolution that formed at 1000°C remains when cooled to room temperature.

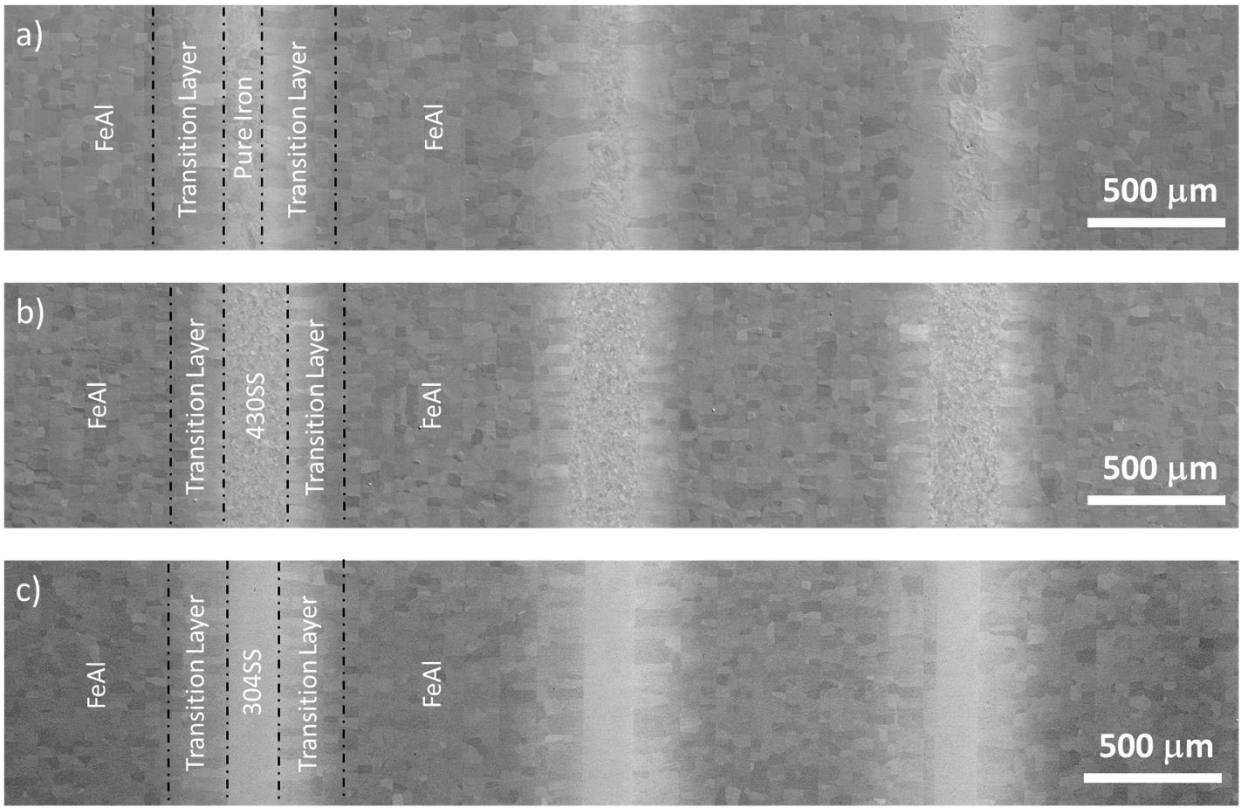

Figure 2.2: SEM micrographs showing the structure of (a) Fe-FeAl, (b) 430SS-FeAl and (c) 304SS-FeAl metallic-intermetallic laminate (MIL) composites. The sintering load direction would be in the horizontal direction perpendicular to the layers.

The thickness of each pure iron layer, measured from Figure 2.3(b) and 2.3(d), which had gone through the ferrite-austenite-ferrite phase transformation, is ~130 μm. Adjacent to the pure iron layer, an Al-enriched α-Fe solid solution layer exists. Based on the composition profile in Figure 2.3(b), the thickness for the α-Fe solid solution layer is around 140 μm. In this work, pure iron layers and α-Fe solid solution layers are regarded as the metal portion of the composites. As revealed in Figure 2.3(c), the α-Fe solid solution layer is composed of a single layer of columnar

grains. The grain structure indicates that the formation of the α-Fe solid solution layer is driven by aluminum diffusion, and the layer grows epitaxially towards the pure iron as the pure iron layer decreases in thickness.

Adjacent to the α-Fe solid solution layer is a 110-μm-thick FeAl solid solution layer. As demonstrated in Appendix 2.C, the α-Fe and FeAl phases possess similar crystal structure and lattice constants (bcc and ordered bcc [B2]). Hence, they can exhibit phase boundaries with a gradual change in microstructure. As discussed in Appendix 2.D, around 70% (length fraction) α-Fe/FeAl phase boundaries are low angle boundaries. Furthermore, as shown in the red circled region in Figure 2.3(c), both α-Fe and FeAl phases can coexist in the same grain, suggesting extra small misorientation across the phase boundary. The low angel grain boundaries allow dislocations to move more easily across the phase boundary, providing extra ductility and fracture toughness. Typically, the coherent interfaces possess relatively small interfacial energy, but generate strain energy due to lattice mismatch [68]. The lattice mismatch at the α-Fe/FeAl interface is relived as the chemical composition variation across the interface is neglectable, creating similar lattice parameters. The transition layer, referring to the combined α-Fe solid solution layer and the FeAl solid solution layer, can bond the pure iron and FeAl layers together, so that all the layers in the composites can respond to the applied stress in a more gradual manner across the layers.

The thickness of the FeAl layer, which contains 48 at% Al, measured from Figure 2.3(b) and 3(d), is ~660 μm. The chemical composition of FeAl is slightly off-stoichiometry, partially due to the Fe/Al foils not being the exact thickness ratio to produce stoichiometric FeAl. The non-stoichiometric FeAl phase can exhibit dramatically improved plasticity compared to the

stoichiometric FeAl [22]. According to the EBSD band contrast map in Figure 2.3(c), all of the FeAl grains assemble along the apparent vertical straight lines, which are identified as "centerline" according to previous MIL studies [4]. In the first stage of reactive sintering, as the intermetallics phase grows, contaminants on the original Fe/Al interface are pushed towards the Al foil side, at the transformation interface due to the faster diffusivity of Al. When aluminum is completely reacted, the oxides and impurities pushed from both sides would accumulate at the former aluminum center. Compared to the "thick-foil" configuration, "multi-thin-foil" configuration reduces the amount of impurities at each centerline, as each centerline concentrates impurities from significantly thinner aluminum foil, reducing the impact on mechanical behavior. Centerlines guide the grain alignment as the impurities hinder diffusion and grain growth. Grains grown from the two sides meet at the centerline with minimal curvature, diminishing the driven force for grain growth. Therefore, "centerlines" form within the FeAl grain regions at the middle of the thickness of the thin Al foils of each 'multiple-thin-foil' ensemble.

The grain orientation map and corresponding inverse pole figures shown in Figure 2.3(e) and 3(f) reveal the medium texture of the material along the primary diffusion direction, while inverse pole figures shown in Appendix 2.B suggest randomly and evenly distributed grain orientations in other directions. Formation and growth for both FeAl and α-Fe solid solution are driven by one-directional diffusion during the reaction, inducing the sintering texture for both phases. The texture aligns towards the <111> direction, rather than <100>, the conventional preferred growth direction, or <110>, the normal direction of close-packed planes for BCC materials. The formation and growth of intermetallics would not only consider the energetically favorable planes, but also be influenced by the orientation of parent grains and the diffusion rate

in various directions. The pure iron region would also retain some texture from the Fe foils that were rolled to the desired thickness.

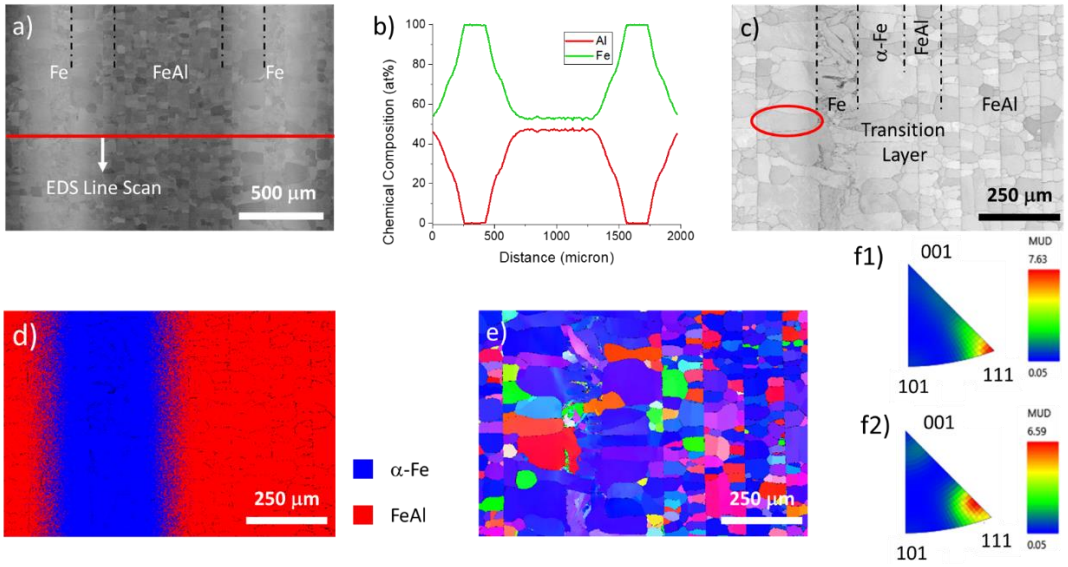

Figure 2.3: Microstructure characterization for Fe-FeAl MIL composite. (a) Low magnified SEM image investigates a "repeat unit" of the material. (b) EDS line scan along the red line notated in (a). (c) Band contrast map collected via EBSD reveals the grain structure. Circled in red is a grain where FeAl and α-Fe coexist. (d) EBSD phase map for the area in (c) supports phase identification. (e) Grain orientation map along the sintering direction (horizontal) for the region (c) indicates a sintering texture. (f1) and (f2) Inverse pole figures for FeAl and α-Fe phase (transition layer), respectively.

2.3.1.2 430SS-FeAl MIL Composites

Figure 2.4(a) shows low magnification SEM micrographs of the microstructures of 430SS-FeAl MIL composites. The FeAl region is located at the center of the image, while the 430SS layers are on the left and right sides.

The thickness of each 430SS layer, measured from Figure 2.4(b) and 2.4(d), is ~220µm. As illustrated in the experimental section, a pure Fe foil was inserted between the Al and SS foils as a 'buffer' layer to avoid the formation of Cr-Al compounds. 430SS is a ferritic stainless steel,

possessing the same α-Fe crystal structure as pure iron with a slightly different lattice constant. The addition of Cr stabilizes the 430SS's α-Fe structure during the sintering. Cr from the 430SS layer diffuses into the pure iron region to reduce the chemical gradient, while Fe also counter-diffuses into the 430SS. The diffusion process reduces the 430SS layer thickness and generates the shoulders of the Fe composition curve in Figure 2.4(b) marked by black arrows.

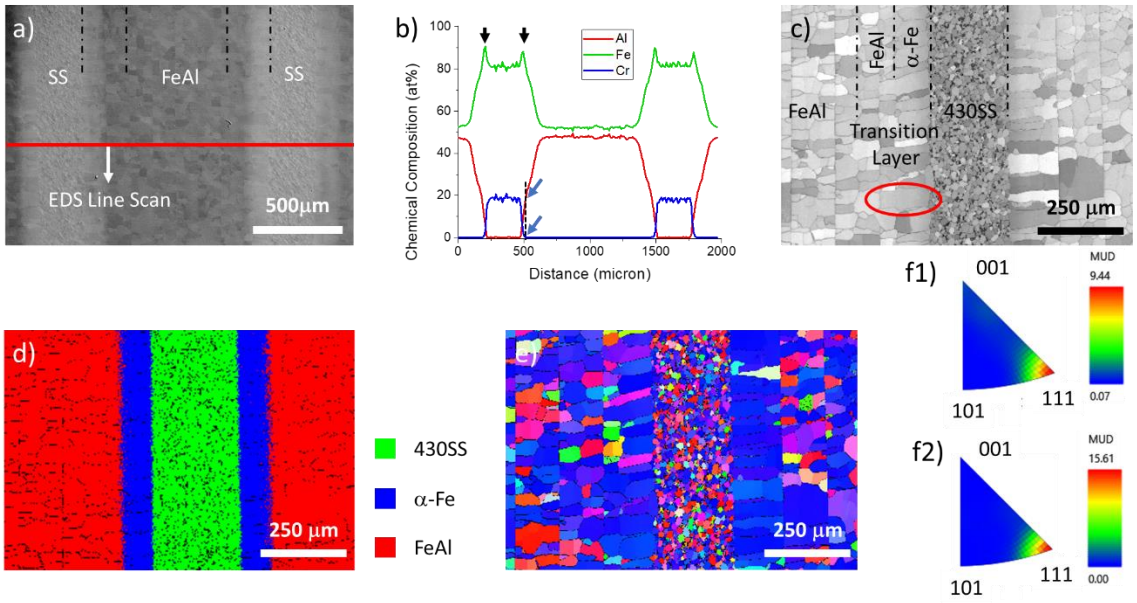

Figure 2.4: Microstructure characterization for 430SS-FeAl MIL composite. (a) Low magnified SEM image investigates a "repeat unit" of the material. (b) EDS line scan along the red line notated in (a). (c) Band contrast map collected via EBSD reveals the grain structure. Circled in red is a grain where FeAl and α-Fe coexist. (d) EBSD phase map for the area in (c) supports phase identification. (e) Grain orientation map along the sintering direction (horizontal) for the region (c) indicates a sintering texture. (f1) and (f2) Inverse pole figures for FeAl and α-Fe phase (transition layer), respectively.

As shown in Figure 2.4(c) and 2.4(f2), the α-Fe solid solution layer adjacent to the 430SS layer is ~100 μm thick, with a similar microstructure and texture as the α-Fe solid solution layer in Fe-FeAl. The penetration of Cr into the α-Fe solid solution terminates within 40 μm into the layer, where the Al concentration is lower than 20 at% (marked by blue arrows). In the α-Fe solid solution region, the Fe concentration is sufficiently high to dissolve all the aluminum and

chromium, preventing any Cr-Al intermetallic precipitation. According to previous work [18], without the extra Fe foil between 430SS and Al, the brittle Cr_5Al_8 phase would form, which can degrade the ductility and fracture resistance of the material.

The other portions of the material, including the 100-μm-thick FeAl solid solution layer and 670-μm-thick FeAl layer, which are free from Cr, are expected to be identical to the corresponding layers in Fe-FeAl. As revealed in Figure 2.4(e) and 2.4(f1), FeAl grains align by the centerlines with texture along the <111> direction.

2.3.1.3 304SS-FeAl MIL Composites

Figure 2.5(a) shows low magnification SEM micrographs of the microstructures of 304SS-FeAl MIL composites. The FeAl region is located at the center of the image, while the 304SS layers are on the left and right sides.

The thickness of each 304SS layer, measured from Figure 2.5(b) and 5(d), is ~200 μm. The 304SS, with an equal amount of Cr as 430SS, is stabilized to the FCC austenite structure at room temperature via the addition of Ni. The loss of Cr and Ni due to diffusion would reduce the 304SS layer thickness, and the region with insufficient Ni would transform into the BCC α-Fe structure.

As shown in Figure 2.5(c) and 2.5(f2), the α-Fe solid solution layer adjacent to the 304SS layer is ~120 μm, with a similar microstructure and texture as the α-Fe solid solution layer in Fe-FeAl and 430SS-FeAl. Cr and Ni have diffused through the entire α-Fe solid solution layer, while the penetration terminated just before entering the FeAl solid solution layer. At the current stage,

due to the lack of diffusion data, it is still unclear whether such a phenomenon is just coincident, or the diffusivity of Cr and Ni abruptly drops from α-Fe to FeAl. In either case, the α-Fe solid solution layer retains a sufficiently high Fe concentration to dissolve all the aluminum, chromium and nickel in solution, preventing the formation of other brittle intermetallics.

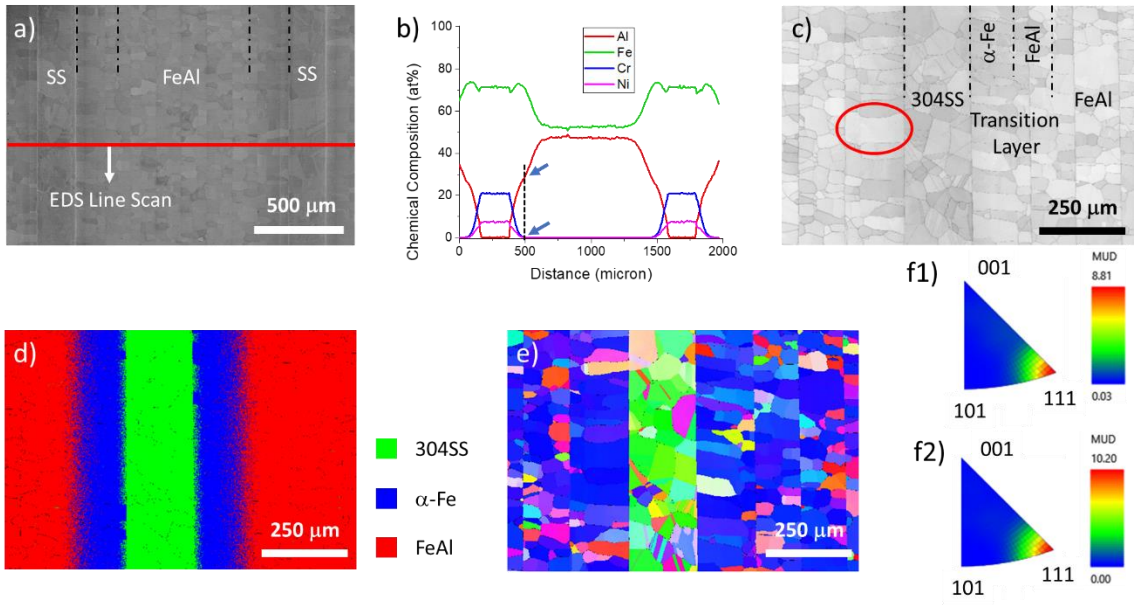

Figure 2.5: Microstructure characterization for 304SS-FeAl MIL composite. (a) Low magnified SEM image investigates a "repeat unit" of the material. (b) EDS line scan along the red line notated in (a). (c) Band contrast map collected via EBSD reveals the grain structure. Circled in red is a grain where FeAl and α-Fe coexist. (d) EBSD phase map for the area in (c) supports phase identification. (e) Grain orientation map along the sintering direction (horizontal) for the region (c) indicates a sintering texture. (f1) and (f2) Inverse Pole figures for FeAl and α-Fe phase (transition layer), respectively.

As revealed in Figure 2.5(e) and 2.5(f1), the remaining portions of the material, including the 120-μm-thick FeAl solid solution layer and 670-μm-thick FeAl layer, which are free from Cr and Ni, are identical to the corresponding layers in Fe-FeAl and 430SS-FeAl. The microstructure of the metal and intermetallic layers dissociate from each other, as the metal layers are governed by the initial thick metal foils and the intermetallic layers are governed by the "multiple-thin-foil" ensembles.

2.3.2 Growth Kinetics and Design of Fabrication Process

In a Fe-Al diffusion couple, Fe_2Al_5 would be the first-formed and dominant intermetallic phase at 600°C due to its fast growth kinetics [69]. A very thin layer of $FeAl_3$ may also appear at the aluminum interface [17]. Other Fe-Al intermetallics, including $FeAl_2$, FeAl and Fe_3Al, would remain neglectable at 600°C due to extremely slow growth kinetics [69]. Therefore, this study utilizes a "two-stage reaction" strategy to fabricate the FeAl-based MIL composites. The entire purpose for the first stage is to completely consume Al by transforming it to Fe_2Al_5, so that the samples can subsequently be heated above aluminum's melting temperature enabling more rapid growth kinetics for the FeAl phase.

As the temperature is ramped up in the second stage, diffusion of aluminum would transform Fe_2Al_5 into $FeAl_2$, and then FeAl. Higher temperatures can accelerate the growth of each phase, saving processing time, but the melting point of Fe_2Al_5 (1170°C) limits the reaction window. Additionally, since the aluminum diffusivity in α-Fe and FeAl are of similar rates, the formation of FeAl is always accompanied by the α-Fe solid solution.

All the phase transformations discussed above (formation of Fe_2Al_5, $FeAl_2$, FeAl and α-Fe solid solution) are diffusion controlled. Reactive diffusion in a binary system can be described by Fick's First Law:

$$J = -D\left(\frac{\partial c}{\partial x}\right) \tag{2.1}$$

and Fick's Second Law:

$$\frac{\partial c}{\partial t} = D\left(\frac{\partial^2 c}{\partial x^2}\right) \tag{2.2}$$

In the first stage of the reaction, Al to Fe_2Al_5, the system can be treated as a semi-infinite diffusion couple and solved analytically [70]:

$$l^2 = Kt, \tag{2.3}$$

where l is the intermetallic thickness, t is the time, and the coefficient K is a function of diffusion coefficients and phase boundary compositions. For the subsequent reactions at a higher temperature, the system becomes a finite diffusion couple, so Eq. (2.3) can no longer predict the thickness of the intermetallics. On the other hand, the system can still be numerically simulated via finite difference analysis [18] by rewriting Eq. (2.2) in a discrete form:

$$\frac{c_i^{n+1}-c_i^n}{\Delta t} = \frac{D^n_{i+\frac{1}{2}}\left(c^n_{i+1}-c^n_i\right)-D^n_{i-\frac{1}{2}}\left(c^n_i-c^n_{i-1}\right)}{\Delta x^2}, \tag{2.4}$$

allowing the required sintering time to be estimated. Meanwhile, both finite and semi-infinite diffusion couples possess self-similarity: if the length scale x is enlarged by n, as $X = nx$, extending the reaction time t by n^2, as $T = n^2 t$, would generate the same composition profile. The easiest way to understand such self-similarity is to multiple $1/n^2$ to both sides of Eq. (2.2):

$$\frac{\partial c}{n^2 \partial t} = \frac{\partial c}{\partial (n^2 t)} = \frac{\partial c}{\partial T} = D\left(\frac{\partial^2 c}{n^2 \partial x^2}\right) = D\left(\frac{\partial^2 c}{\partial (nx)^2}\right) = D\left(\frac{\partial^2 c}{\partial X^2}\right). \tag{2.5}$$

For example, doubling the initial foil thickness would extend the required reaction time fourfold, while reducing the initial foil thickness by 50% reduces processing time by 75%. Therefore, using thinner metal foils as feedstocks could dramatically decrease sintering time and consequently reduce the fabrication cost. Figure 2.6 presents the material sintered from conventional alternating stacked 'thick' foils as a comparison group, which utilized multiple 1000μm Fe and 600μm Al foils. In the "multiple-thin-foil" setup, each repeat unit, which refers

to one thick metal layer plus one "multiple-thin-foil" ensemble, contains 950μm (500μm+[6*75μm]) Fe and 700μm (7*100μm) Al.

Figure 2.6(a) shows the low magnification SEM micrographs of the microstructures for a 'thick-foil' Fe-Al MIL composite fabricated from alternating layers of 1000μm Fe and 600μm Al foils sintered at 600°C for 20 min. Measured from the composition profile in Figure 2.6(d), the composite consists of 330μm unreacted Al layers, 160μm finger-like Fe_2Al_5 layers adjacent to Al and residual pure Fe layers. Predicted from our previous diffusion analysis[17], the additional sintering time t_a required to complete the reaction can be estimated from the equation:

$$\frac{l_0 - l}{l_0} = \sqrt{\frac{t}{t + t_a}} \tag{2.6}$$

where l_0 is the initial Al thickness, and l is the residual Al layer thickness at time t. As $l_0 = 600\ \mu m$, $l = 340\ \mu m$ and $t = 20\ \min$, Eq. (2.6) predicts $t_a = 90\ \min$. In practice, due to variations in pre-existing surface oxides and uncertainty of exact sample sintering temperature, excess sintering time is often employed to guarantee the completion of the reaction.

Figure 2.6(b) shows low magnification SEM micrographs of the microstructure of the 'thick-foil' Fe-Al MIL composite sintered at 1000°C for 1.5 hr, subsequent to the complete consumption of Al that took 12 hr at 600°C. The required low temperature step (600°C) sintering time, which is calculated based on Eq. (2.3) with kinetic data from literatures [17], is significantly longer than the prediction above ($20 + 90 = 110$ min). It is reasonable to believe that inaccuracy in kinetic data and/or temperature measurement result in the different predictions, as Eq. (2.6) is directly derived from Eq. (2.3). Theoretically, 110 min should be more accurate as the sintering approach is consistent, while 12 hr would not introduce extra phase transformation as Fe_2Al_5 dominates at 600°C. Measured from the composition profile in Figure 2.6(e), this composite

consists of 280μm $FeAl_2$ layers, 350μm residual pure Fe layers and 320μm transition layers of α-Fe/FeAl solid solution. Extending the annealing time is necessary to transform the brittle $FeAl_2$ into the ductile FeAl phase of interest. For the 'thick-foil' Fe-Al MIL composite sintered from 1000 μm Fe and 600 μm Al foils, at the FeAl formation stage, $l_0 = 680$ μm, $l = 290$ μm and $t = 90$ min, then Eq. (2.6) predicts $t_a = 180$ min. However, in contrast to the 'multiple-thin-foil' Fe-Al MIL composites, where excess sintering brings no additional microstructure changes, in the 'thick-foil' MIL composite the transformation stage from $FeAl_2$ to Fe requires precisely reaction time control to obtain the desired FeAl composition.

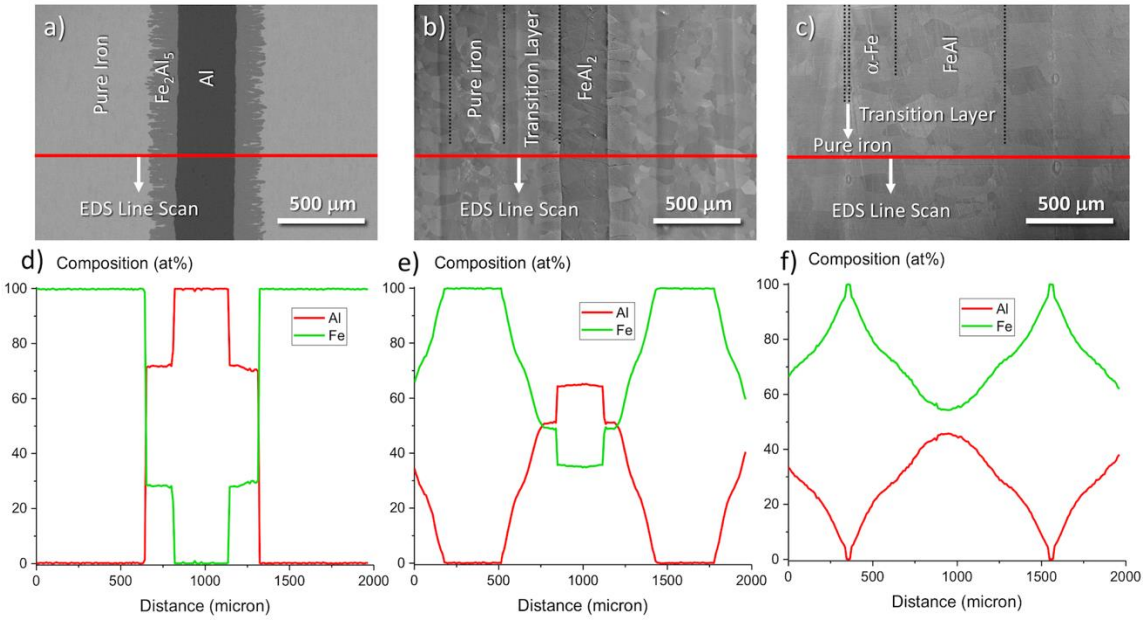

Figure 2.6: Microstructure of MIL composites synthesized via conventional alternating stacked 1000μm Fe and 600μm Al foils. SEM micrographs were collected at the same magnification as Figure 2.3(a), 2.5(a) and 2.6(a) for straightforward comparison. (a) Sintered at 600°C for 20 min; (b) Sintered at 600°C for 12 hr, then 1000°C for 1.5 hr; (c) Sintered at 600°C for 12 hr, then 1000°C for 5 hr. (d), (e) and (f) are corresponding composition profiles from EDS line scans.

Figure 2.6(c) shows low magnification SEM micrographs of the microstructure of the 'thick-foil' Fe-Al MIL composite sintered at 1000°C for 5 hr. This sample processing condition

represents the critical status of the ‘thick-foil’ Fe-FeAl MIL composites that can be synthesized with the conventional fabrication process. If the reaction time is reduced, the reaction will not go to completion, and there will exist a retained brittle $FeAl_2$ layer. In contrast, increasing reaction time will cause the FeAl phase to dissolve into the α-Fe solid solution phase, losing both strength and ductility. If thicker iron foils were initially used, the volume ratio of FeAl in the final product would correspondingly decrease, sacrificing strength. Meanwhile, since there is already relatively little pure iron remaining with the current Fe/Al ratio, starting with thicker Al foils would end up with the complete consumption of the pure iron layer. Therefore, the 1000 μm/600 μm foil thickness ratio may represent the only foil combination of the ‘thick-foil’ configuration that will result in the desired FeAl MIL composite. Since the initial foil thickness ratio is predetermined by the desired microstructure and diffusion kinetics, the metallic/intermetallic ratio in the fully reacted Fe-FeAl ‘thick-foil’ MIL composite is fixed to 50:50. In this case, the major portion of the material is either the α-Fe solid solution phase or the FeAl solid solution phase, as demonstrated by the composition curve in Figure 2.6(f).

As shown above, the ‘thick-foil’ configuration is significantly limited due to diffusion kinetics, which restricts both phase type and phase fraction, and the ‘multiple-thin-foil’ method can overcome these limitations. The ratio of the thin Fe/Al foils independently determines the chemical composition of the intermetallic phase, which in this study is selected to be close to 50:50 (at.%) to form FeAl. Meanwhile, since the thick metal foils utilized in these ‘multiple-thin-foil’ FeAl MIL composites are retained as the remnant metal layers in the material, their chemical composition, phases, and phase fractions are relatively unchanged during the intermetallic phase formation. As such, almost any metal/intermetallic combination can be achieved with the “multiple-thin-foil” configuration. The thickness of the thin foils determines the required sintering

time, and any additional processing time only influences the thickness of transition layers and grain sizes following a parabolic relationship. The number of thin foils in each "multiple-thin-layer" ensemble governs the thickness of the intermetallic layer. By adjusting the number of thin foils and/or selecting the thickness of the thick metal foils, tuning the metallic/intermetallic ratio becomes feasible and convenient. In summary, the "multiple-thin-foil" method has modularized the design for MIL composites, as the intermetallic phase, metal type, grain size and metallic/intermetallic ratio can be independently adjusted to fulfill the specific performance requirements, while both efficiency and robustness for the fabrication process are promoted.

2.3.3 Mechanical Properties

2.3.3.1 NanoIndentation Measurements

Figure 2.7(a) compares the hardness distribution from metal to intermetallic layers in the Fe-FeAl, 403SS-FeAl and 304SS-FeAl MIL composites, with an example SEM image for the indents on a 304SS-FeAl sample. The reference hardness values for metals were collected from corresponding materials that went through the same heat treatment as MIL composites.

In the hardness profile for the Fe-FeAl MIL composite, the hardness increases with increasing in Al concentration due to enhanced solution strengthening. Based on the theory of solid solution strengthening, the difference in atomic size creates a local stress field, impeding dislocation motion and consequently increasing the hardness. The magnitude of the strengthening effect in a binary system can be estimated based on the equation [23,71–73]:

$$\Delta\sigma = \eta M \mu \varepsilon^{1.5} C^{0.5} \tag{2.7}$$

where η is an empirical number sensitive to the material [73], M is the Taylor factor which is a constant, μ is shear modulus, C is the solute concentration and ε is the misfit parameter, which

relates to modulus and atomic size difference. The strengthening effect in intermetallics is more complicated as short-range order, vacancies and other factors need to be taken into consideration [23]. The values collected from the pure iron region of the Fe-FeAl MIL composite are slightly higher than the reference pure Fe foils, but the values for the stainless steel layers in the 304SS-FeAl and 430SS-FeAl MIL composites are quite similar to their respective reference foils.

In the hardness profile for 430SS-FeAl, the hardness gradually rises from the 430SS layer to the FeAl layer. The overall solid solution strengthening effect increases, as the decrease in Cr concentration is overwhelmed by the increase in Al. Studies about Fe-Al-Cr ternary alloys [74] suggest that the addition of Cr to the Fe-Al binary system can increase the dislocation line energy via the strengthening of interatomic bonds, and consequently enhances the energy required for dislocation nucleation. Lower dislocation density can enhance the strength at low strain conditions, but is reversed at high strain conditions [75].

In the hardness profile for the 304SS-FeAl MIL composite, the hardness abruptly increases from the 304SS layer to the adjacent transition layer, then gradually drops, before rising again to the FeAl layer hardness. In the 304SS-FeAl MIL composite, Ni diffusion into the Fe transition layer leads to a gradient in hardening from a high value at the 304SS/Fe interface decreasing toward the center of the Fe transition layer, then rises toward the FeAl interface due to the Al gradient hardening the transition layer up to the FeAl hardness.

2.3.3.2 Compression Tests

The quasi-static stress-strain curves for MIL composites with the layers perpendicular to the load are shown in Figure 2.7(c). The compressive strength for Fe-FeAl, 430SS-FeAl and 304SS-FeAl MIL composites are 1250 MPa, 1390 MPa, and 2300 MPa, respectively. The

corresponding maximum plastic strain for the three composites are ~0.17, ~0.11 and ~0.17, respectively. During the test for the 304SS-FeAl MIL composite, the experiment was stopped, not due to the sample's failure, but the load limit of the load frame, indicating the actual compressive strength and ductility for 304SS-FeAl would be even higher.

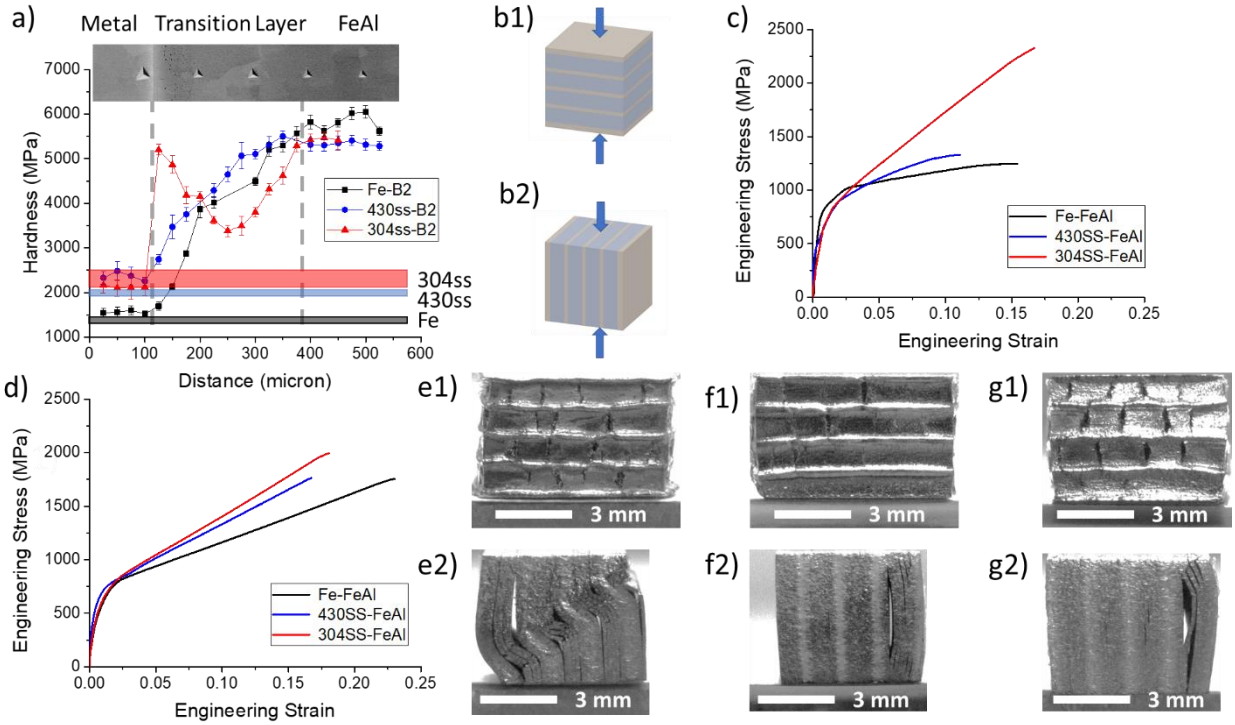

Figure 2.7: (a) Hardness curves measured from nanoindentation. The SEM image in the upper part demonstrates typical indent size and distribution. Shaded grey, blue and red bars represent the reference hardness values for the corresponding metals that experienced the same heat treatment. (b1) and (b2) are the definition for perpendicular and parallel testing directions, respectively. (c) and (d) Engineering strain-stress cures of the materials compressed in perpendicular and parallel directions, respectively. (e1) and (e2) Photos of Fe-FeAl specimens after compression testing in perpendicular and parallel directions, respectively. (f1) and (f2) Photos of 430SS-FeAl specimens after compression testing in perpendicular and parallel directions, respectively. (g1) and (g2) Photos of 304SS-FeAl specimens after compression testing in perpendicular and parallel directions, respectively.

The quasi-static stress-strain curves for these MIL composites with the layers parallel to the load are shown in Figure 2.7(d). The compressive strength for Fe-FeAl, 430SS-FeAl and 304SS-FeAl MIL composites are 1750 MPa, 1760 MPa, and 2000 MPa, respectively. The

corresponding maximum plastic strain for the three composites are ~0.23, ~0.17 and ~0.19, respectively. As demonstrated in Figure 2.7(b2), when the composites are tested with the layers parallel to the load, both metal and intermetallic layers would experience the same amount of stain along the loading direction.

The quasi-static flow curves in Figure 2.7(c) and 2.7(d) for the MIL composites show that the yield strength of the MIL composites is ~700MPa, almost irrespective to the type of metal layer. When loaded perpendicular to the layers, the metal layers will yield first, followed by the gradually yielding of the gradient transition regions. Subsequent to the yield of metal and transition layers, yielding of FeAl determines the apparent yield point for the entire composites, which included work hardening in the metallic layers. When loaded parallel to the layers, since iron and stainless steel possess higher Young's modulus [23] and much lower yield strength than FeAl, the metal layers will also yield first. Subsequently, the local stress applied to the FeAl layers is higher than the global stress readings, and the local stress applied to the metals layers is lower. The strain at the apparent yield point is determined by the FeAl phase, while the stress at the apparent yield point is affected by the metallic/intermetallic ratio and work hardening of metallic layers.

The quasi-static flow curves also show that both the compressive strength and ductility of the MIL composites depend on the metal layers. Compared to the Fe-FeAl MIL composite, the 430SS-FeAl MIL composite possesses slightly higher strength, but considerably lower plasticity. 430SS is inherently stronger than pure iron, while the addition of Cr also strengthens the transition layers, but at reduced ductility. Although 304SS itself possesses similar mechanical properties with 430SS, the 304SS-FeAl MIL composite exhibits significant improvement in compressive

strength and plasticity. The enhancement of the transition layer due to the addition of Ni dramatically enhances the global strain-stress response of the composites.

When MIL composites are loaded parallel to the layers, as shown in Figs. 7(e2), 7(f2) and 7(g2), the layers undergo uniform strains, but significant interfacial stresses evolve as plastic deformation proceeds leading to delamination, after which the separated layers bend and buckle. Rather than the sharp phase boundaries between metals and intermetallics in conventional 'thick-foil' MIL composites, the transition layers formed in the 'multiple-thin-foil' MIL composites enhance bonding between the metal and intermetallic layers, with coherent grain boundaries, and enables an extended strain gradient to develop between the metal layers and intermetallic layers through the transition layers. This effect acts to delay the delamination to much higher strains. When conventional 'thick-foil' MIL composites are loaded perpendicular to the layers, in-plane tensile stresses will induce "axial splitting" failure of the intermetallics, which is a common phenomenon in the compression of brittle ceramics. The metal layers adjacent to the fractured intermetallics then become unsupported and fail by shear. Typically, the combination of the two mechanisms generates a macrocrack that propagates along the sample diagonal through the entire thickness [5]. In contrast, when FeAl based MIL composites are loaded perpendicular to the layers, as shown in Figs. 7(e1), 7(f1) and 7(g1), macrocracks only exist in the FeAl region, and never penetrate through the metal layers. Cracks induced by "axial splitting" of the FeAl layer terminate in the transition layers, so shear displacement rarely occurs to the metal layers. Further, ambient condition fracture in FeAl typically occurs by transgranular cleavage [22]. As most FeAl grains form columnar grains growing perpendicular to the layering, these FeAl layers possess a high degree of grain shape and crystallographic anisotropy. When loaded parallel to the layers (i.e. perpendicular to the long axes of the columnar grains), the FeAl layers likely exhibit a slightly

higher fracture toughness, delaying axial splitting. When loaded perpendicular to the layers (i.e. parallel to the long axes of the columnar grains), this effect appears to be negligible due to the high degree of plasticity in this orientation.

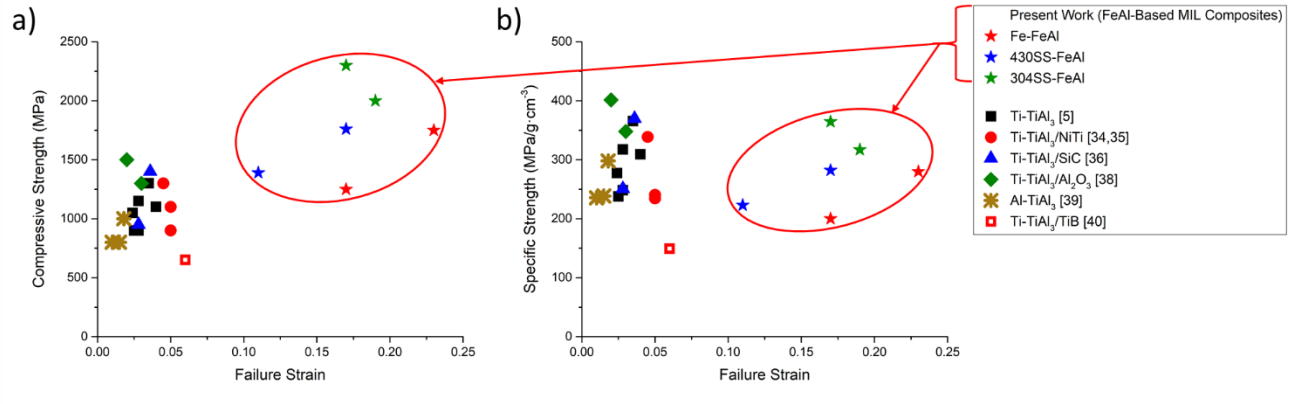

Figure 2.8: Comparison of mechanical properties of MIL composites (a) Compressive strength versus strain to failure, (b) Specific strength versus strain to failure. (Ti-$TiAl_3$ [5], Ti-$TiAl_3$/NiTi [24,25], Ti-$TiAl_3$/SiC [26], Ti-$TiAl_3$/Al_2O_3 [28], Al-$TiAl_3$ [29], Ti-$TiAl_3$/TiB [30]). [For (b), if the density is not provided, the volume fraction of metallic/intermetallic layers or the starting metal foils were used to estimate the density of the final MIL composites].

Figure 2.8(a) compares the ductility and compressive strength of the MIL composites, where the data is collected from the strain-stress profiles provided in the corresponding literature [5,24–26,28–30]. Figure 2.8(b) replots this same data using specific compressive strength in order to compare the results taking density into consideration. By tuning the metallic/intermetallic ratio and intermetallics, MIL composites typically possess either high strength with limited ductility, or relatively high ductility but sacrificing strength. On the other hand, when all these deformation features of the FeAl-based MIL composites are considered together: the enhanced plasticity of the FeAl phase over other aluminide phases, the lack of an obvious and continuous intermetallic centerline, and the presence of a metal to intermetallic transition layer, it is not surprising these FeAl-based MIL composites can exhibit record-high ductility and compressive strength, in both perpendicular and parallel directions, among the known MIL composite family of materials.

2.4 Conclusion

The present work discussed the material design, fabrication and characterization process to develop a new class of MIL composites. This new class of MIL composites is based on Fe and Al, the two least expensive metals, allowing the potential commercialization of a low-cost series of MIL composites that exhibit excellent mechanical properties. The main conclusions are:

1. Synthesis of MIL composites, where the relatively ductile FeAl is the single intermetallic phase formed, is feasible.

2. The fabrication process for MIL composites is reformed to improve the efficiency and flexibility for material synthesis. The "multiple-thin-foil" configuration saves reaction time, enables local chemical composition control and allows metal/intermetallic combinations, which cannot be produced via the conventional 'thick-foil' methods.

3. Microstructures of Fe-FeAl, 430SS-FeAl and 304SS-FeAl MIL composites were analyzed to evaluate the fabrication process and understand the materials' properties. The transition layer formed between the metal and FeAl regions allows for strain gradients between the metal and intermetallic layers, and additionally functions as a chemical barrier or dissolution layer that limits the formation of other intermetallics.

4. Nanoindentation measurements and compression tests were conducted to estimate both local and global mechanical behaviors. The FeAl-based MIL composites, especially the 304SS-FeAl MIL composite, achieved a new strength and ductility record for the MIL composites family. The mechanisms for the extraordinary mechanical properties are briefly discussed.

Appendix 2.A X-Ray Diffraction (XRD) Analysis of Fe-FeAl MIL Composites

XRD pattern for Fe-FeAl MIL composites confirms the formation of FeAl order phase. FeAl phase, which belongs to the primitive cubic space group, has no forbidden reflection. In contrast, α-Fe phase, which belongs body-centered cubic (BCC) space group, generates XRD peaks when the corresponding Miller indices:

$$h + k + l = even \tag{A1}$$

Meanwhile, the texture may alter the relative intensity of each peak.

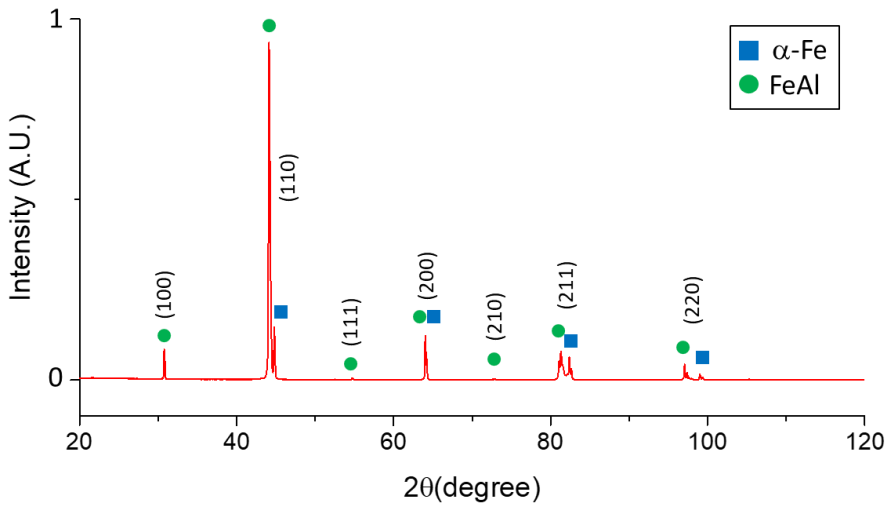

Figure 2.A1: XRD pattern for Fe-FeAl MIL.

Appendix 2.B Inverse Pole Figure for FeAl-based MIL Composites

Inverse pole figures reveal medium texture aligning towards the <111> direction in X (horizontal) direction along which the sintering load was applied and diffusion occurred. Plus, the directional preference in Y(vertical) and Z(in-plane) directions is extremely weak, suggesting randomly and evenly distributed grain orientations.

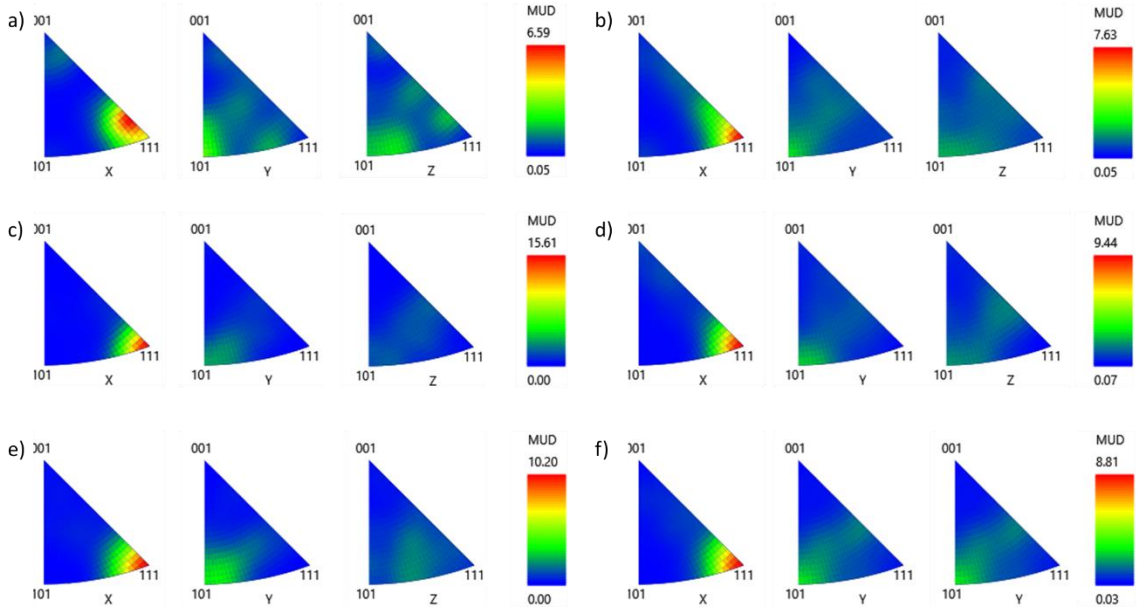

Figure 2.B1: Inverse Pole Figure for (a) α-Fe phase in Fe-FeAl, (b) FeAl phase in Fe-FeAl, (c) α-Fe phase in 430SS-FeAl, (d) FeAl phase in 430SS-FeAl, (e) α-Fe phase in 304SS-FeAl, (F) FeAl phase in 304SS-FeAl.

Appendix 2.C Crystal Structure of α-Fe and FeAl phase

FeAl and α–Fe phases belong to different space groups (primitive cubic for FeAl, BCC for Fe). On the other hand, α-Fe and FeAl phases possess similar crystal structure, as Al atom replaces the Fe atom at the body-center.

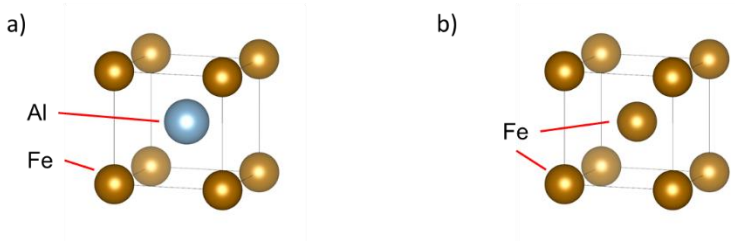

Figure 2.C1: Crystal structure of (a) FeAl phase and (b) α-Fe phase plotted via VESTA[76].

Appendix 2.D Grain Structure around the α-Fe/FeAl Phase Boundary

Measured from the grain maps collected around the phase boundary region via EBSD, around 40% (length fraction) α-Fe/FeAl phase boundaries are low angle boundaries with the misorientation less than 1°, 30% are low angle boundaries with 1° to 15° misorientation, and 30% are high angle boundaries.

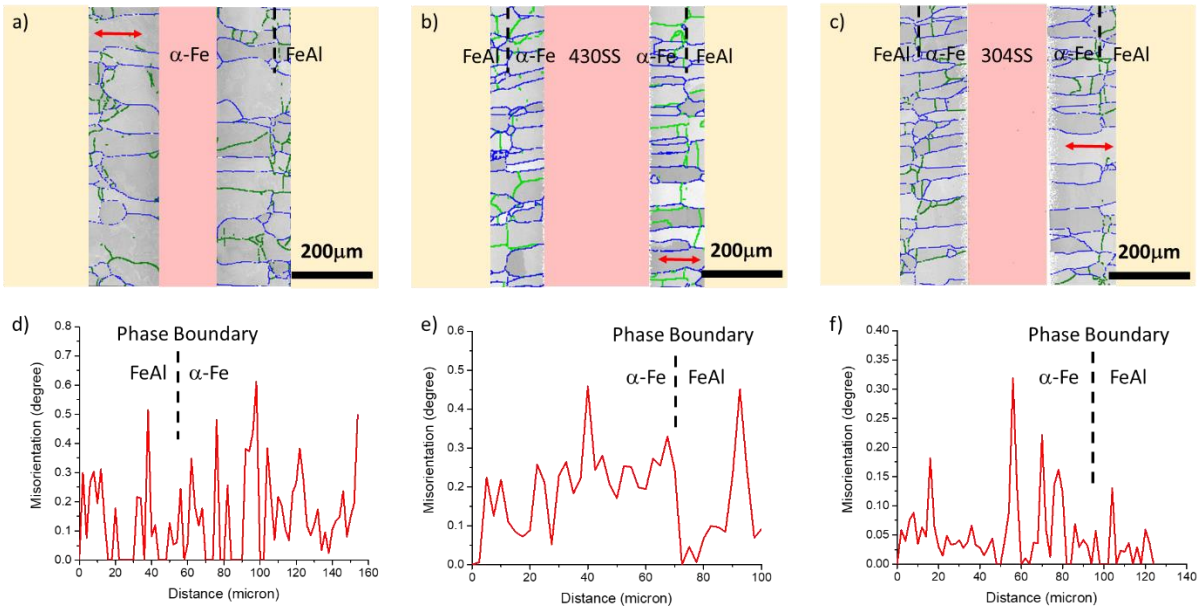

Figure 2.D1: Grain structure around the α-Fe/FeAl phase boundary region in (a)Fe-FeAl, (b)430SS-FeAl and (c) 304SS-FeAl. Non-phase-boundary regions are color shadowed for convenience, and the black dash lines indicate the α-Fe/FeAl phase boundaries. Low angle boundaries (1°-15°) are green and high angle boundaries are blue, while 1° is selected as the cut-off misorientation angle for identifying grain boundaries. Misorientation profile across the α-Fe/FeAl phase boundary along the annotated red lines are plot in (d)Fe-FeAl, (e)430SS-FeAl and (f) 304SS-FeAl.

Acknowledgment

Chapter 2, in full, is the reprint of the published article in Acta Materialia, Elsevier: Wang, Haoren; Harrington, Tyler; Zhu, Chaoyi; Vecchio, Kenneth S. Design, fabrication and characterization of FeAl-based metallic-intermetallic laminate (MIL) composites. Acta Materialia (2019).

I would like to thank Tyler Harrington, Chaoyi Zhu, and my principal investigator Professor Kenneth Vecchio, for their contribution in this work.

Chapter 3 Deformation and Fracture Evolution of FeAl-based MIL Composites

Chapter 3, in full, is the reprint of the published article in Acta Materialia, Elsevier: Wang, Haoren; Zhu, Chaoyi; Vecchio, Kenneth S. Deformation and Fracture Evolution of FeAl-based Metallic-Intermetallic Laminate (MIL) Composites. Acta Materialia (2020).

Abstract

FeAl-based Metallic-Intermetallic Laminate (MIL) composites exhibit enhanced strength and ductility compared to previously studied MIL composites. The deformation and fracture evolution of the FeAl-based MIL composites is investigated here via incremental compression testing. Microstructure assessment via electron backscatter diffraction EBSD suggests that deformation proceeds in a fairly homogeneous manner across gradients in the microstructure. Eventual failure is mainly induced by normal stresses, whereas other MIL composites typically fail by shear induced localizations. Geometrically necessary dislocation GND analysis indicates the FeAl regions deform in similar manners for the three MIL composites (Fe-FeAl-MIL, 430SS-FeAl-MIL, and 304SS-FeAl-MIL), and each fails in a similar mode. While the FeAl phase is the majority constituent of the composites, the mechanical properties are significantly influenced by the softer metal layers. The transition layer formed between the Fe-based metal layers and FeAl regions is the most critical constituent of the composites. Although the volume fraction of the transition layer is only ~15%, a stronger transition layer can improve the work hardening behavior of the FeAl phase, increasing MIL composite strength by as much as 1GPa. The findings can guide the design of the MIL composites to achieve even better mechanical properties.

3.1 Introduction

Metal-intermetallic laminate (MIL) composites are produced by reinforcing the strong, but brittle intermetallics with layers of ductile metals for optimizing mechanical performance. Aluminide-intermetallics typically possess ordered crystalline structures with low symmetry, while the lack of slip system induces high strength, but limits the plasticity and toughness. Reinforcing the aluminide with particles, fibers or layers of ductile metals can promote the toughness [1], enabling certain unique structural applications.

MIL composites are commonly fabricated by reactive sintering alternating stacked dissimilar metal foils to create an intermetallic phase via interdiffusion and chemical reactions. An appropriate pressure is applied perpendicular to the foils to ensure intimate contact. The various performance requirements can be fulfilled by adjusting the initial foils and thereby controlling phase type, phase fractions, and hence the properties of the MIL composites. Due to the ability to tailor the properties, and the economy of the low-cost metallic foils, MIL composites would be ideal for structural applications, such as the aerospace industry, which requires lightweight, high stiffness materials without compromising the performance. Additionally, via managing the shape of the initial metallic foils, MIL composites can be synthesized with complex geometry for specific platforms and multi-functionality [2]. For example, by pre-machining the initial foils with cavities, pathways can be created in the composites, where sensors can be embedded for monitoring the deformation or damage of the material [2].

The predecessors of MIL composites were synthesized in 1989 using solid-state combustion wave [3]. However, the self-sustaining reaction kinetics limit the ability to control the microstructure of the composites. The reactive sintering for the MIL composites, which controls the formation of the intermetallics, was first achieved in the Ti-Al system by Harach and Vecchio

in 2001 [4]. Subsequently, the mechanical properties of Ti-$TiAl_3$ MIL composites have been systematically investigated. Rohatgi *et al.* [5] studied the fracture behavior, Adharapurapu *et al.* [6] studied the resistance to fatigue crack growth, Li *et al.* [7,8] studied the crack evolution, Cao *et al.* [9] studied the performance in the ballistic test, and Jiang *et al*. [10] studied fracture under dynamic loading. Meanwhile, the optimization of the metallic/intermetallic ratio was pursued [11,12], and extra reinforcements, such as Al_2O_3 fibers [13], were embedded into the Ti-$TiAl_3$ to enhance the performance.

In the Ti-Al system, the ability to tailor the performance is limited, as Al_3Ti is the only intermetallic phase formed during the reactive sintering, which is extremely brittle. The effort to promote the ductility and lower the cost draws attention to the Ni-Al system [14–16] and Fe-Al system [17–19], where relatively ductile intermetallic phases, such as FeAl [21–23], could exist. Although the MIL composites containing FeAl phase have been successfully synthesized, the formation of FeAl is generally accompanied by other brittle intermetallics [18].

In our previous work, by introducing an innovative fabrication process, MIL composites containing the intermetallic region of single phase FeAl have been synthesized [77]. It was further demonstrated that the metal layer of pure iron can be replaced by 430 stainless steel (430SS) or 304 stainless steel (304SS) without altering the intermetallic region of the composites. The FeAl-based MIL composites have demonstrated the highest levels of both strength and ductility among all MIL composites to date [5,15,24–33].

In the present study, we aim to understand the dramatic improvement in the mechanical behavior of FeAl-based MIL composites. Incremental compression testing is conducted to investigate the deformation and fracture evolution processes. The microstructures of the deformed specimens are characterized via electron backscatter diffraction (EBSD). From the orientation

data obtained in EBSD, lattice curvature is derived to compute geometrically necessary dislocation (GND) density via the Nye-Kröner-Bilby relationship [34]. GND density is thought to accommodate plastic strain non-uniformity in polycrystalline materials [35], Therefore, GND density during plastic deformation is used to correlate the mechanical response of thee FeAl based MIL composites with variation in composition and loading conditions.

3.2 Experimental

3.2.1 Sample preparation

Foils of commercially pure aluminum, pure iron (99.5%), 430SS (18wt% Cr) and 304SS (18 wt% Cr and 8 wt% Ni) were taken as the feedstocks to produce the FeAl-based MIL composites. The foils were scrubbed using steel wool pads, then rinsed in acetone for ultrasonic cleaning. Subsequently, the foils were cut into 20-mm-diameter disks, alternating stacked in the "multiple-thin-foil" configuration shown in Figure 3.1(a), wrapped with molybdenum foil (99.95%, 0.025-mm-thick) and graphite foil, and loaded into the sintering assembly shown in Figure 3.1(b). The sintering assembly was placed in Thermal Technology Spark Plasma Sintering (SPS, a.k.a. field-assisted sintering) machine, Model GTAT 10-3, for reactive sintering, and the corresponding parameters are plotted in Figure 3.1(c). The details about the sample fabrication, as well as the effect of the applied electric field, have been presented in our previous studies [77,78].

The fully synthesized MIL composite disks, each approximately 20mm diameter and 6mm thick, hereafter referred to as: Fe-FeAl-MIL, 430SS-FeAl-MIL, and 304SS-FeAl-MIL, were cut into 6 mm cubes using alumina saw, then ground and polished using 320 grit, 600 grit and 1200 grit SiC sandpaper, then 1 mm diamond suspension, to remove the attached molybdenum foil and the damage zone introduced during cutting. Following standard ATSM E9, quasi-static

compression tests were performed using a standard screw-driven load frame, with a strain rate of 10^{-3}/s and grease applied to the sample ends for minimizing friction. At the present stage, an in-situ compression test is infeasible for us, because it requires very high load to deformed the specimen (at the level of serval tens kilonewton), and EBSD characterization requires extremely high sample surface quality. Instead, the incremental-load approach was utilized, loading to 500MPa for one cube, and loading to 1GPa to another cube, for comparison. When the external load on the specimen reached the desired value, the load frame crosshead stopped and retreated, we thereby obtained one specimen for each stress level. In other words, the stress level is the input parameter, whereas the strain is the result for the incremental compression test. Furthermore, as demonstrated in Figure 3.1(d) and 3.1(e), the compression tests were executed in both perpendicular and parallel directions relative to the MIL composites layers. The stress levels for the incremental compression test are listed in Table 1, while the last cell of each row, marked by *, refers to the ultimate strength measured. To ensure statistically representative results, each material was tested at least three times for the ultimate strength. The failure of the specimen is defined as the moment when the load undergoes a significant drop (<70% of P_{max}), when P_{max} corresponds to the ultimate strength for all the FeAl-based MIL composites.

3.2.2 Characterization

The loaded samples, along with unloaded ones as a reference state, were mounted perpendicular to the layers for cross-sections, and ground and polished following standard metallographic preparation procedures. The microstructure was characterized using Thermo-Fisher (formerly FEI) Apreo scanning electron microscope (SEM) equipped with Oxford Instrument's Symmetry EBSD system.

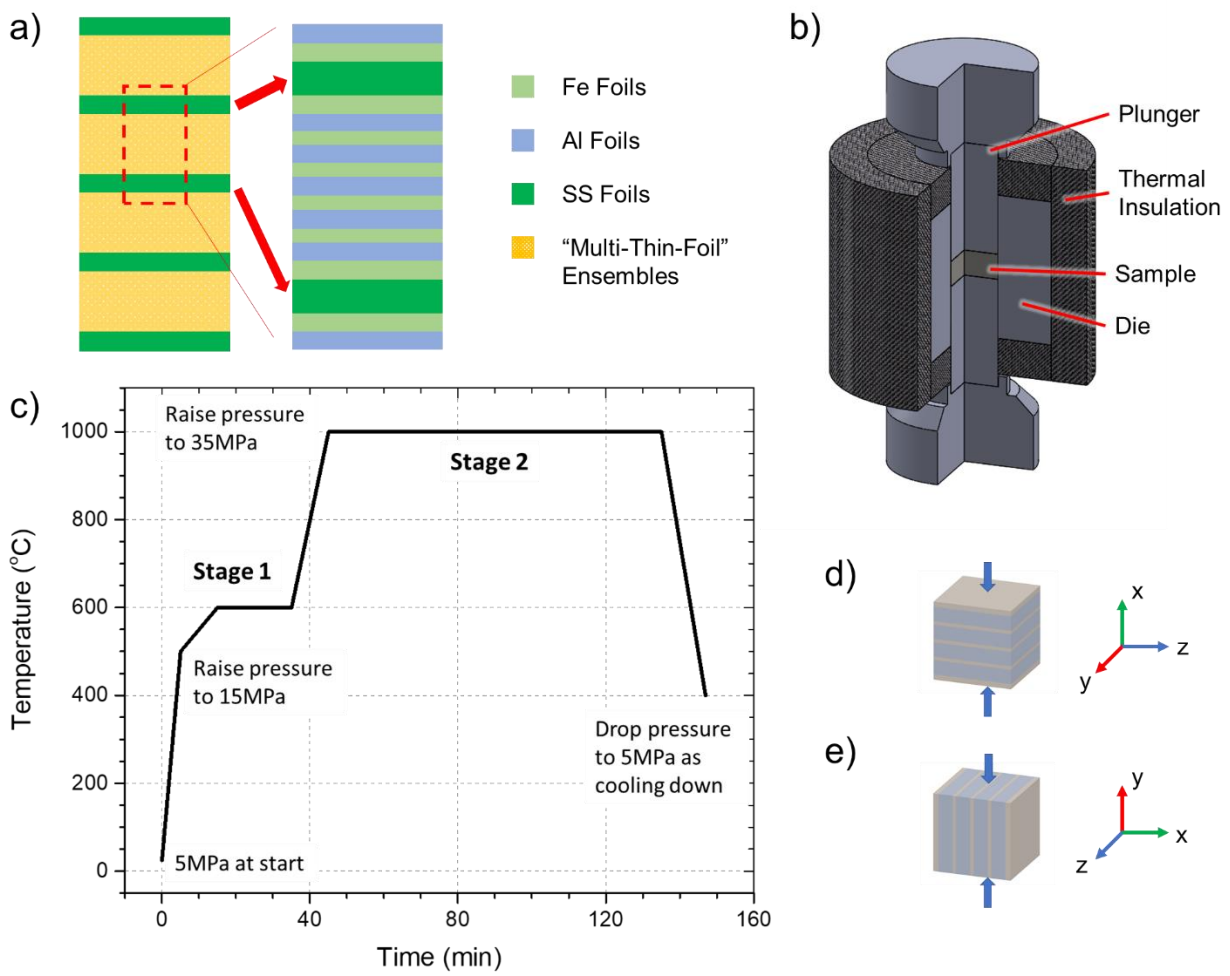

Figure 3.1: (a) the configuration of metal foils stacks for synthesizing MIL compositions [77]. (b) Schematic diagram of SPS setup [77,78]. (c) Sintering parameters [77]. (d) and (e) the definition of perpendicular and parallel directions for the compression test, respectively. XYZ coordinate axis system is denoted for stress-strain analysis, while the x-axis is perpendicular to the layers.

As introduced, the MIL composites consist of both metal and intermetallic layers, which possess different stress-strain responses. Global measurements, such as the total strain or total stress, are insufficient for describing the mechanical behavior of each constituent of the composites. Instead, local GND density evolution can be used to decouple this complexity during the incremental compression test. The GND density is calculated with an in-house code developed and described previously [34,79,80]. Due to the nature of GND measurements, its resolution, absolute value and noise floor depend on the step size of the corresponding EBSD scan [81]. In

the present work, we used 2 μm steps for large field assessments, and 0.5 μm steps for analyzing the details of the deformation of individual constituents. The GND density maps are plotted in log_{10} scale with the units m^{-2}.

3.3 Results

3.3.1 Microstructure

The microstructures of the undeformed Fe-FeAl-MIL, 430SS-FeAl-MIL and 304SS-FeAl-MIL are presented in Figure 3.2(a) to 3.2(c), respectively. As indicated by the dash lines, the relatively bright regions are the remnant metal layers. Adjacent to the metal layer are transition layers, which are the chemical gradient regions, consisting of α-Fe and FeAl solid solutions. The major portion of the materials is the pure FeAl phase, and the total intermetallic volume fraction is around 70% according to our previous measurement [77]. Considering the symmetry of the layering in the MIL composites, the region spanning from one metal layer to another can be regarded as the symmetric repeat structure of the entire sample. Shown in Figure 3.2(d) to 3.2(f) are the microstructure assessments at higher magnification via EBSD band contrast map. The apparent vertical straight lines in the FeAl region are identified as the "centerline", which are the impurities on the original Fe-Al foil interface being pushed towards the former aluminum center during reactive sintering [77].

According to our previous study, the FeAl regions (including the FeAl solid solution) of the three MIL composites (Fe-FeAl-MIL, 430SS-FeAl-MIL and 304SS-FeAl-MIL) are very similar in composition. Furthermore, as demonstrated in Appendix 3.A, the texture, grain size, and grain morphology of the FeAl phase of the three MIL composites is very similar.

Consequently, the FeAl regions, which are the majority constituent of the composites, are expected to behave similarly.

The metal layers of the three MIL composites are inherently different, depending on which metal foils were utilized in fabrication. 430ss and 304ss are known to possess similar mechanical properties (~200MPa yield strength and ~500MPa ultimate strength), while pure iron possesses significantly lower strength. Except for the metal layers themselves, the α-Fe solid solution regions formed adjacent to the metal layers would exhibit different properties due to the solution strengthening effect of Cr and Ni. As an example, the hardness distribution from metal to intermetallic layers in the three MIL composites, which was measured via nanoindentation [77], are plotted in Figure 3.2(g). In the Fe-FeAl-MIL system, the hardness increases with increasing Al concentration, which results from enhanced solution strengthening. In 430SS-FeAl-MIL, the hardness gradually rises from 430SS to the FeAl layer, as the decrease in Cr would be overwhelmed by the increase in Al, enhancing the overall solution strengthening effect. In 304SS-FeAl-MIL, the hardness abruptly increases in the transition region adjacent to the 304SS layer, gradually drops, then raises again to the value of the FeAl phase. This abnormal hardness profile is believed to relate to the composition evolution and the corresponding solution strengthening effect, which would be complicated [23] as the number of elements increases.

In general, 430SS-FeAl-MIL can be regarded as the enhanced Fe-FeAl-MIL, as the addition of Cr in the metal and α-Fe solid solution improves the strength, but may sacrifice a small level of ductility. The 304SS, which is stabilized to the austenite structure via the addition of Ni, was expected to perform similarly to 430SS as both metal layers possess similar strength. Meanwhile, the FeAl regions in both MIL composites are identical, and the stronger α-Fe solid solution regions of 304SS-FeAl-MIL (compared to that of 430SS-FeAl-MIL) only exhibits a small

volume fraction (around 15%) of the entire material. Therefore, the improvement in the mechanical properties of 304SS-FeAl-MIL was expected to be very limited; however, this is contrary to what was observed.

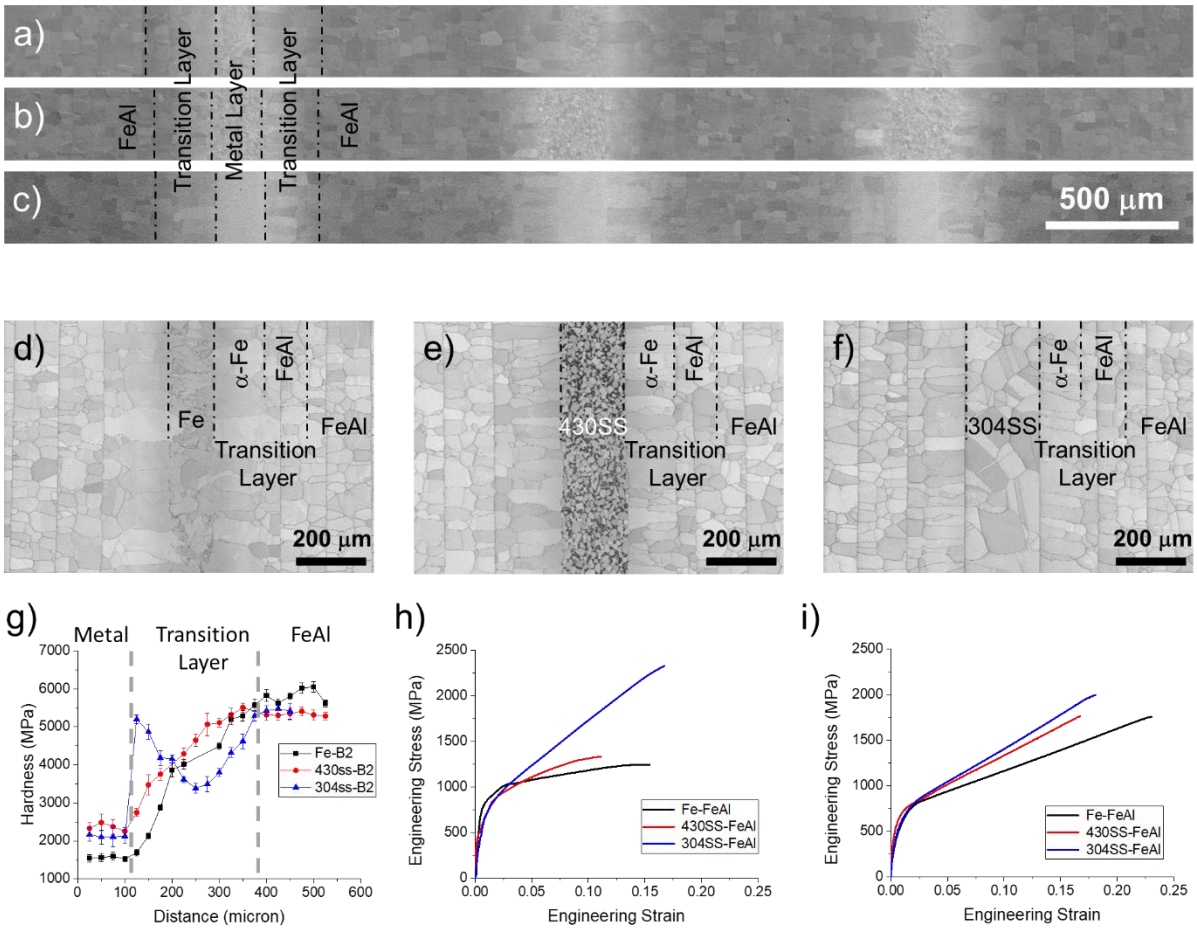

Figure 3.2: SEM images of (a) Fe-FeAl-MIL, (b) 430SS-FeAl-MIL and (c) 304SS-FeAl-MIL MIL composites [77]. (d), (e) and (f) are the microstructure characterized via the EBSD band contrast map. The dashed lines indicate the phase boundaries [77]. (g) Hardness profile measured from metal to FeAl region via nanoindentation [77]. (h) and (i) are engineering stress-strain curves for FeAl-based MIL composites compressed in perpendicular and parallel directions, respectively [77].

3.3.2 Compression Test

The results of the incremental compression tests are listed in Table 3.1. The strain was measured as the specimen's height change before and after the test, which is accurate for the plastic deformation, but ignores the small elastic deformation. When loaded perpendicular to the layers,

the specimen is in uniaxial stress, and the stress-strain curves are plotted in Figure 3.2(h). In general, the metal layers would yield first at low load, when the intermetallics are still in the elastic stage. For the FeAl-based MIL composites, as the load further increases, there would be an apparent yield point, which is primarily determined by the yielding of the FeAl phase [77]. When loaded parallel to the layers, the specimen is in uniaxial strain, as the deformation of each layer would be similar.

Table 3.1: The stress levels and the corresponding strain during the incremental compression test for FeAl-based MIL composites.

Fe-FeAl-MIL Perpendicular	Stress	0.5GPa	1GPa	1.25GPa*		
	Strain	<0.01	0.1	0.17*		
Fe-FeAl-MIL Parallel	Stress	0.5GPa	1GPa	1.4GPa	1.75GPa*	
	Strain	<0.01	0.05	0.11	0.23*	
430SS-FeAl-MIL Perpendicular	Stress	0.5GPa	1GPa	1.39GPa*		
	Strain	<0.01	0.02	0.11*		
430SS-FeAl-MIL Parallel	Stress	0.5GPa	1GPa	1.4GPa	1.76GPa*	
	Strain	<0.01	0.03	0.09	0.17*	
304SS-FeAl-MIL Perpendicular	Stress	0.5GPa	1GPa	1.4GPa	1.8GPa	2.30GPa*
	Strain	<0.01	0.02	0.06	0.11	0.17*
304SS-FeAl-MIL Parallel	Stress	0.5GPa	1GPa	1.4GPa	2.00GPa*	
	Strain	<0.01	0.03	0.08	0.19*	

*Ultimate strength and the corresponding strain.

As shown in Figure 3.2(i), the 304SS-FeAl-MIL and 430SS-FeAl-MIL exhibit similar stress-strain responses in the parallel direction. In contrast, the dramatic improvement in both strength and ductility in the perpendicular direction suggests that the interactions between the layers, especially the interaction between the transition and FeAl layers, should be investigated.

3.4 Discussion

Photos of the specimens at failure are presented in Figure 3.3(a) to 3.3(f). Generally, when loaded in the perpendicular direction, the specimen failed after large plastic strain by axial cracks

in the FeAl region. In contrast, when loaded in the parallel direction, the specimen failed after large plastic strain by delamination along the FeAl centerlines and subsequent buckling. Shown in Figure 3.3(g), 3.3(i) and 3.3(k) are the microstructure of the undeformed samples, while the corresponding GND density maps are plotted in Figure 3.3(h), 3.3(j) and 3.3(l) as a reference state.

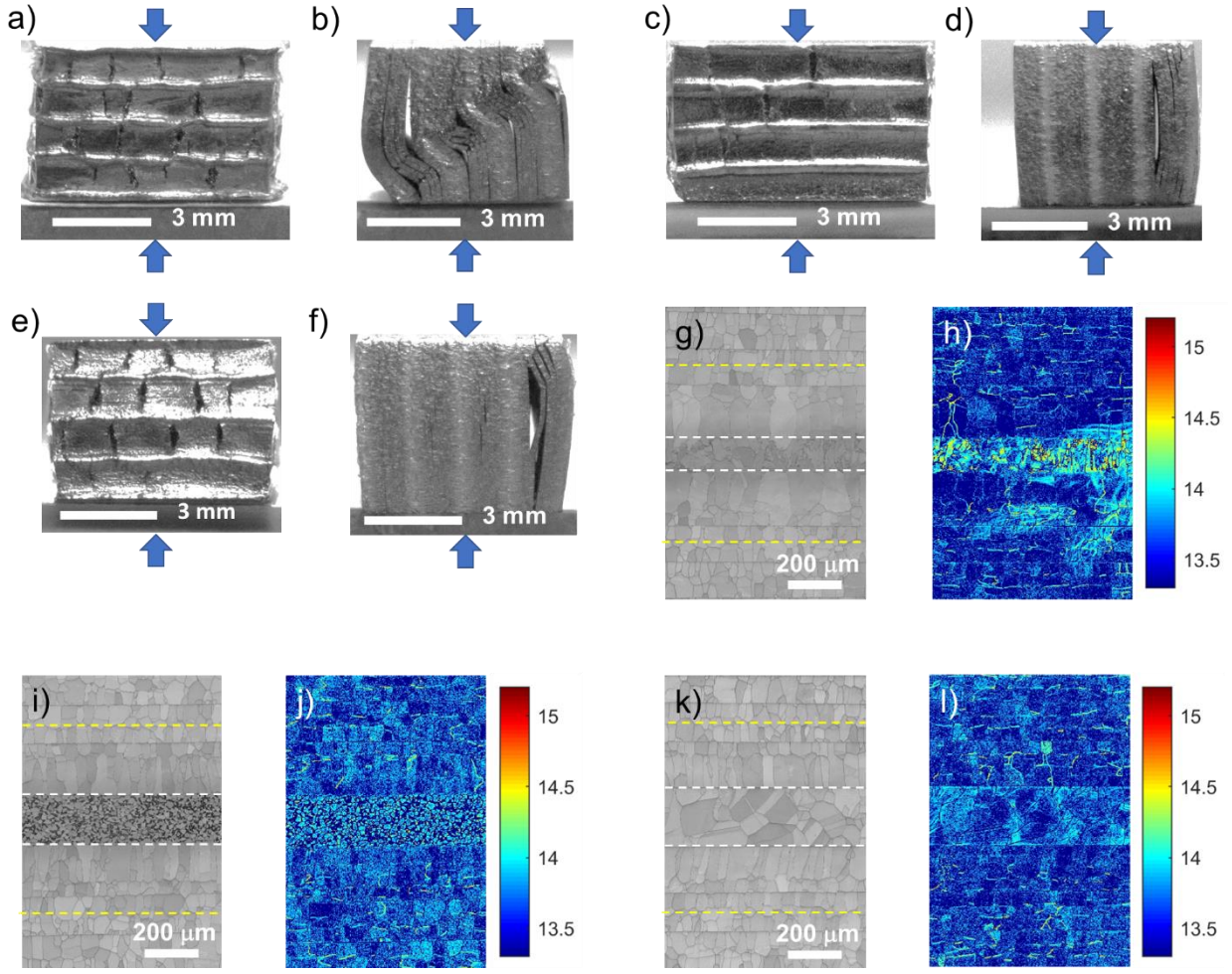

Figure 3.3: Photos of the specimen after the compression test in perpendicular loading: (a) Fe-FeAl-MIL, (b) 430SS-FeAl-MIL and (c) 304SS-FeAl-MIL, respectively. Photos of the specimen after the compression test in parallel loading: (d) Fe-FeAl-MIL, (e) 430SS-FeAl-MIL and (f) 304SS-FeAl-MIL, respectively. EBSD band contrast maps of the undeformed (g) Fe-FeAl-MIL, (i) 430SS-FeAl-MIL and (k) 304SS-FeAl-MIL. The white dashed lines indicate the boundary between metal and transition layers, the yellow dashed lines indicate the boundary between transition and FeAl layers. (h), (j) and (l) are the corresponding GND density maps using the same color scale.

3.4.1 Deformation of FeAl-based MIL Composites

3.4.1.1 Incremental Compression Testing of 500 MPa

Figure 3.4(a), 3.4(c) and 3.4(e) present the microstructure of the Fe-FeAl-MIL, 430SS-FeAl-MIL and 304SS-FeAl-MIL, respectively, at 500MPa perpendicular loading, and Figure 3.4(g), 3.4(i) and 3.4(k) present the microstructure of the Fe-FeAl-MIL, 430SS-FeAl-MIL and 304SS-FeAl-MIL, respectively, at 500MPa parallel loading. Compared to the undeformed samples in Figure 3.3(g), 3.3(i) and 3.3(k), the microstructures of the specimens loaded at 500MPa do not exhibit any noticeable difference. In addition, the loading directions, which would induce different stress-strain states, have not created any noticeable differences in deformed microstructures. Furthermore, the GND density maps of the undeformed materials shown in Figure 3.3(h), 3.3(j) and 3(l) are similar to those for the 500MPa samples shown in Figure 3.4. As discussed in Section 3.3.2, at 500MPa, although the metal layers have already yielded, the FeAl layers are still largely within the elastic region. In addition, due to the limitation on the accuracy of the GND calculation, which is demonstrated in Appendix 3.B, the small difference could be attributed to inherent noise in the GND measurement.

3.4.1.2 Incremental Compression Testing of 1 GPa

As shown in Figure 3.5(a), the Fe-FeAl-MIL specimen subjected to 1GPa loading perpendicular to the layers, the GND densities concentrate in the metal layers, and cracks appear as “axial splitting” of the FeAl grains. During the compression test, the stress tensor of the external load can be written as:

$$\sigma = \begin{bmatrix} C & 0 & 0 \\ 0 & 0 & 0 \\ 0 & 0 & 0 \end{bmatrix} \tag{3.1}$$

where C is the compression stress. In this situation, the material is in compression in the loading direction [x axis, defined in Figure 3.1(d)], which induces tension in the other two orthogonal, in-plane axes. Under this condition, the maximum shear stress, $\tau = \frac{C}{2}$, would occur at 45° to the loading direction. In other MIL composite systems, such as Ti-$TiAl_3$ [4,5,7], failure typically occurs by shearing through the thickness of the sample. In the FeAl-based MIL composites, however, all the major cracks are along the "axial-splitting" direction. Consequently, the cracks are caused by normal stresses induced in the plane perpendicular to the imposed compression.

The 430SS-FeAl-MIL and 304SS-FeAl-MIL specimens at 1GPa perpendicular loading are shown in Figure 3.5(c) and 3.5(e), respectively. The 430SS-FeAl-MIL only shows a few cracks, whereas 304SS-FeAl-MIL is free of cracks. Furthermore, GND densities evolve uniformly across the metal, transition and FeAl layers.

Figure 3.5(g), 3.5(i) and 3.5(k) present the microstructure of Fe-FeAl-MIL, 430SS-FeAl-MIL and 304SS-FeAl-MIL, respectively, subjected to 1GPa loading parallel to the layers. The parallel loading at this level would not induce any delamination or cracking, while GND densities evolve very uniformly across the metal, transition and FeAl layers. In addition, the Fe-FeAl-MIL exhibits slightly higher GND densities.

When loaded in the parallel direction, the specimen is in uniaxial strain:

$$\varepsilon_{yy,Metal} = \varepsilon_{yy,Transition} = \varepsilon_{yy,FeAl}, \tag{3.2}$$

and the stress tensor of the external load can be written as:

$$\sigma = \begin{bmatrix} 0 & 0 & 0 \\ 0 & C & 0 \\ 0 & 0 & 0 \end{bmatrix} \tag{3.3}$$

At the same strain level, the stress level for the metals would be lower than the intermetallics. In other words, the FeAl region would carry more load, leading to higher local stresses. Since 430SS and 304SS are inherently stronger than the pure iron, at the same global stress level, local stress on the FeAl region in the 430SS-FeAl-MIL or 304SS-FeAl-MIL would be lower than that of the Fe-FeAl-MIL; consequently, the global strain would be lower.

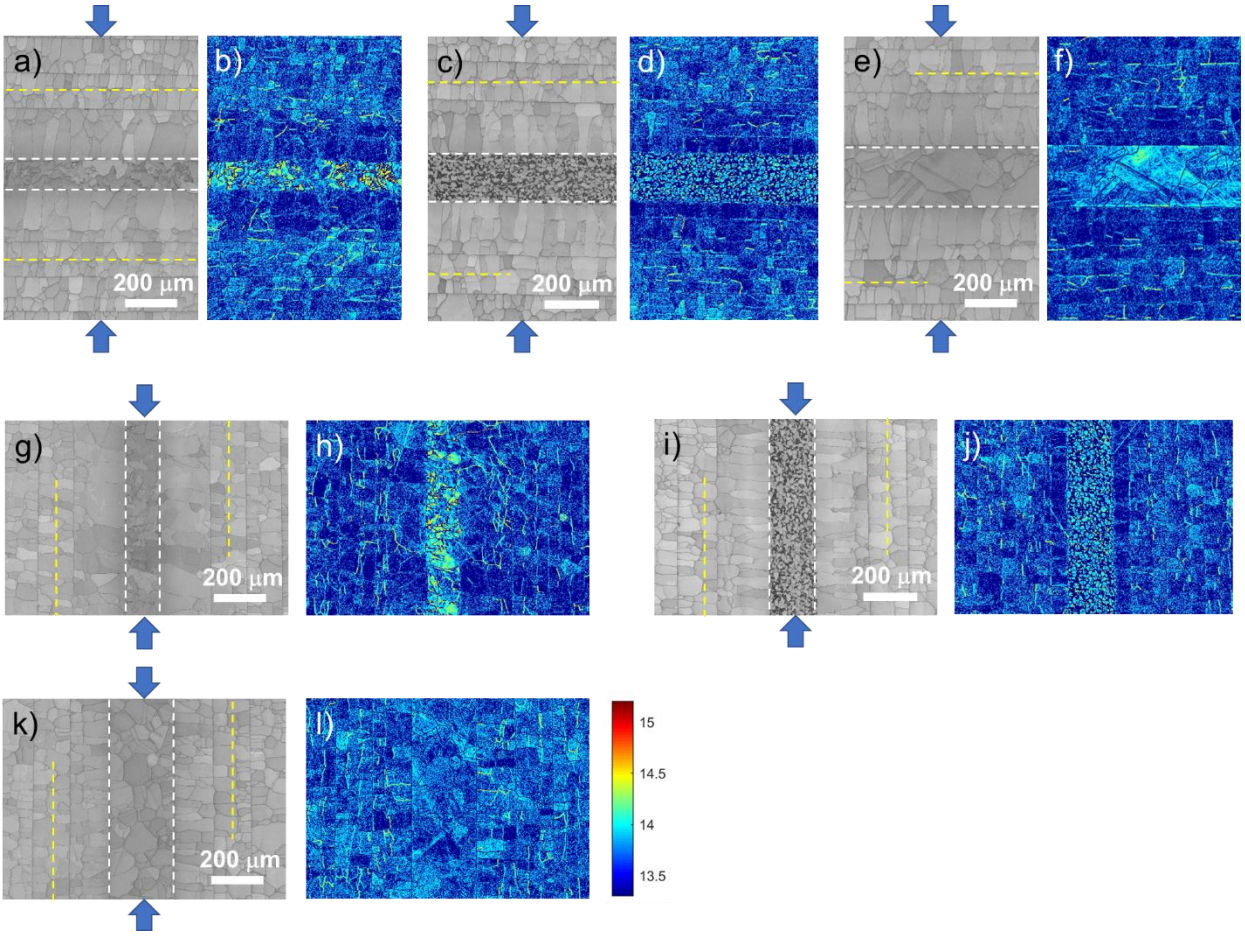

Figure 3.4: EBSD band contrast maps after compression testing conducted perpendicular to the layers at 500 MPa: (a) Fe-FeAl-MIL, (c) 430SS-FeAl-MIL, and (e) 304SS-FeAl-MIL. EBSD band contrast maps after compression testing conducted parallel to the layers at 500 MPa: (g) Fe-FeAl-MIL, (i) 430SS-FeAl-MIL, and (k) 304SS-FeAl-MIL. The white dashed lines indicate the boundaries between metals and transition layers, and the yellow dashed lines indicate the boundaries between transition and FeAl layers. (b), (d), (f), (h), (j) and (l) are the corresponding GND density maps using the same color scale.

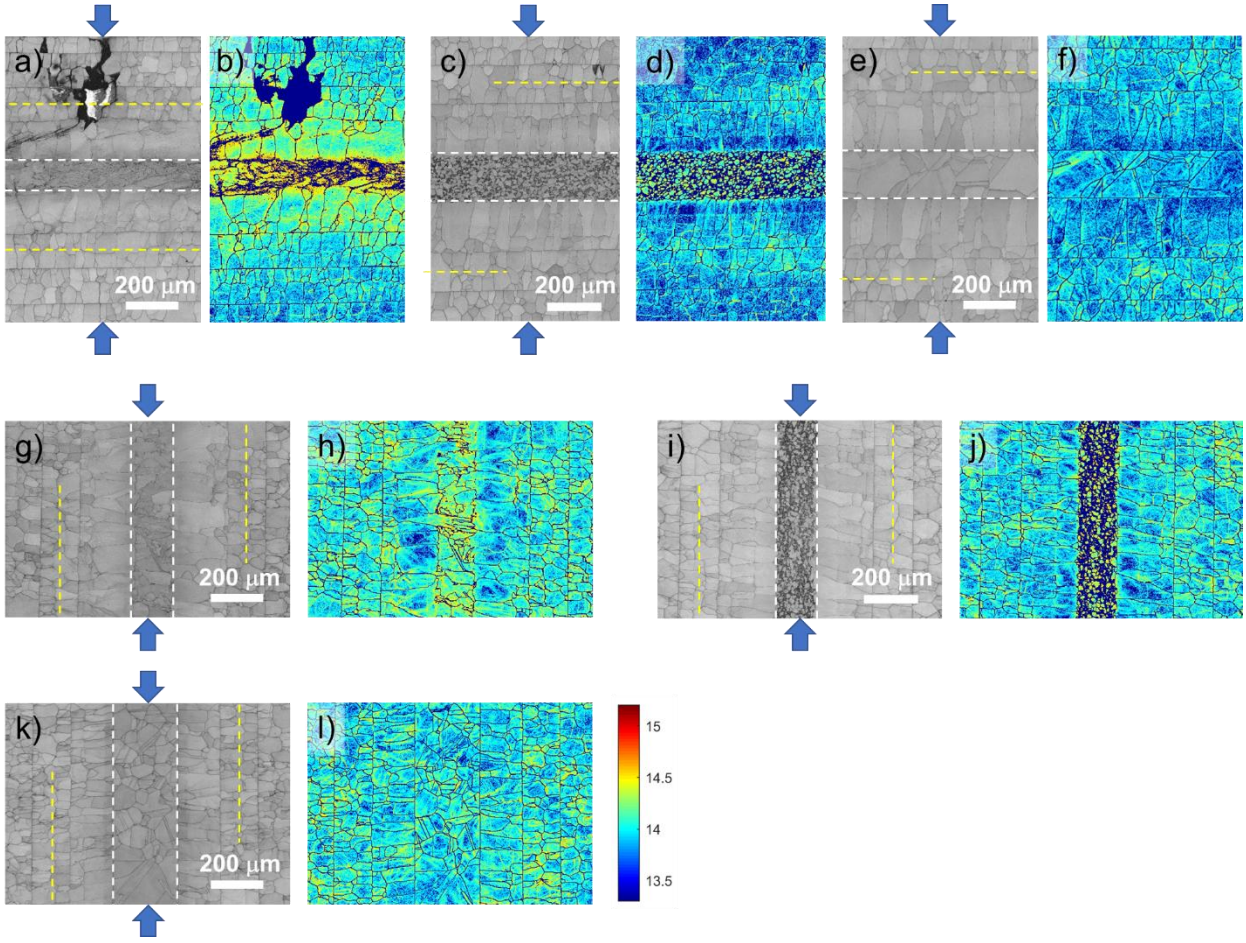

Figure 3.5: EBSD band contrast maps after compression testing conducted perpendicular to the layers at 1 GPa: (a) Fe-FeAl-MIL, (c) 430SS-FeAl-MIL, and (e) 304SS-FeAl-MIL. EBSD band contrast maps after compression testing conducted parallel to the layers at 1 GPa: (g) Fe-FeAl-MIL, (i) 430SS-FeAl-MIL, and (k) 304SS-FeAl-MIL. The white dashed lines indicate the boundaries between metals and transition layers, and the yellow dashed lines indicate the boundaries between transition and FeAl layers. (b), (d), (f), (h), (j) and (l) are the corresponding GND density maps using the same color scale.

3.4.1.3 Incremental Compression Testing of 1.4 GPa

As shown in Figure 3.6(a) [for perpendicular loading], the cracks continue to grow with increasing load until 1.25GPa, when the entire Fe-FeAl-MIL specimen fails by vertical linking of the FeAl cracks. The GND densities of the Fe and transition layers are similar to that at 1GPa, while the GND densities of the FeAl region increased slightly.

Recall that Figure 3.3(c) shows the 430SS-FeAl-MIL specimen after the compression test in the perpendicular direction. From a macroscopic view, the failure mode is quite similar to the Fe-FeAl-MIL: cracks grow in the FeAl region, but do not penetrate through the 430SS layer as indicated by the yellow arrows. The 430SS-FeAl-MIL failed at 1.4GPa in the perpendicular direction, 250MPa higher than the Fe-FeAl-MIL. In the 430SS-FeAl-MIL sample, GND densities also concentrate at the 430SS and transition layers, while the degree of GND density concentration is lower than in the Fe-FeAl-MIL. By contrast, the 304SS-FeAl-MIL is still crack-free under 1.4GPa perpendicular loading. Furthermore, as shown in Figure 3.6(f), there is no GND density concentration in the metallic regions of the 304SS-FeAl-MIL.

When compressed parallel to the layers with 1.4GPa load, all the three FeAl-based MIL composites exhibit similar deformed microstructures and GND distributions. Additionally, the GND densities are still uniform across the metal and intermetallic regions. At this stress level, perpendicular loaded specimens have already failed (except for 304SS-FeAl-MIL), and parallel loaded specimens are almost crack-free. The difference results from the stress-strain state of the layers under loading.

3.4.1.4 Incremental Compression Testing of 1.8 GPa and Above

Figure 3.7(a) presents the microstructure of the 304SS-FeAl-MIL at 1.8GPa perpendicular loading. The specimen only has a few micro-cracks, and GND densities are still uniform across the layers. As the loading further increased to 2.3GPa, the 304SS-FeAl-MIL eventually failed in a similar mode as the Fe-FeAl-MIL and 430SS-FeAl-MIL. Compared to Figure 3.7(b), the GND densities in Figure 3.7(d) concentrate somewhat around the metal layers.

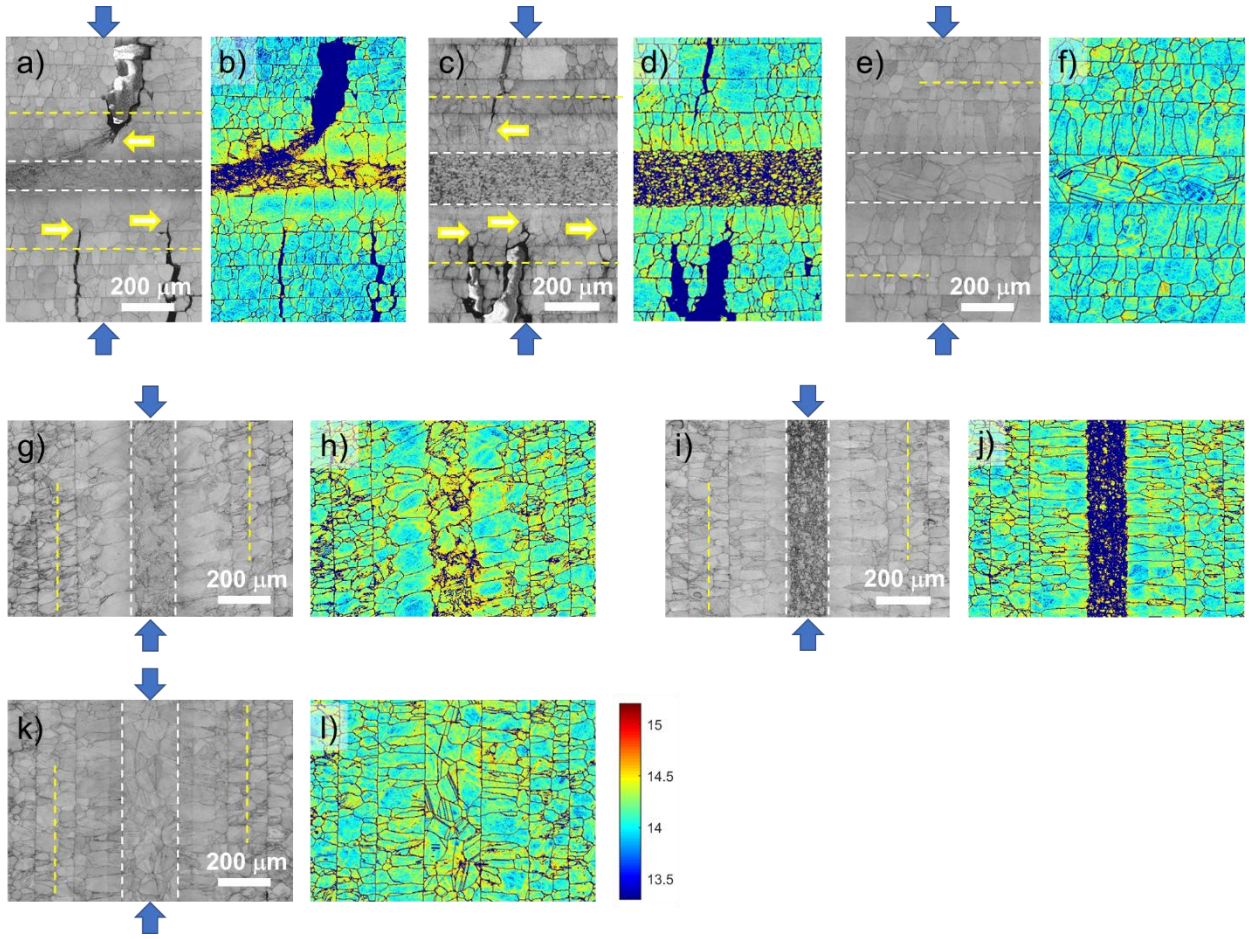

Figure 3.6: EBSD band contrast maps after compression testing conducted perpendicular to the layers: (a) Fe-FeAl-MIL failed at 1.25 GPa, (c) 430SS-FeAl-MIL failed at 1.39 GPa, and (e) 304SS-FeAl-MIL with 1.4GPa loading. EBSD band contrast maps after compression testing conducted parallel to the layers at 1.4 GPa: (g) Fe-FeAl-MIL, (i) 430SS-FeAl-MIL, and (k) 304SS-FeAl-MIL. The white dashed lines indicate the boundaries between metals and transition layers, and the yellow dashed lines indicate the boundaries between transition and FeAl layers. (b), (d), (f), (h), (j) and (l) are the corresponding GND density maps using the same color scale.

Figure 3.7(e), 3.7(g) and 3.7(i) present the microstructure of the Fe-FeAl-MIL and 430SS-FeAl-MIL under parallel loading, which both failed near 1.8GPa. The 304SS-FeAl-MIL is slightly stronger, failing at 2GPa when compressed in the parallel direction. With increasing load, the GND densities increase and cracks initiate in the centerlines. Due to the accumulation of impurities along centerlines, these "centerline" grain boundaries are more susceptible to stress concentration than normal FeAl grain boundaries. When loaded in the perpendicular direction, the

external force is perpendicular to the centerlines, hindering the growth of centerline cracks. In contrast, when loaded in the parallel direction, axial splitting is preferred at the centerlines. As the parallel loading further increases, delamination becomes more prevalent and separated layers begin to buckle, resulting in the failure of the entire specimen. Although the centerline cracks delaminate the FeAl layers, most FeAl layers are still partially attached to each other during the test. Furthermore, delaminated FeAl layers can still carry the load, contributing to mitigating catastrophic failure. Therefore, the FeAl-based MIL composites typically possess higher strength in the parallel direction compared to the perpendicular direction, although the 304SS-FeAl-MIL is an exception.

3.4.2 GND Density Evolution of FeAl-based MIL Composites

The initial 430SS foils used here possess a single-phase ferrite structure. However, as shown in Fig, 2(e), after MIL processing, the 430SS layers, as part of the MIL composites, exhibit a dual-phase structure of coarse ferrite and fine-grained martensite. Details about the 430SS microstructure are discussed in Appendix 3.C. The GND density calculations are very sensitive to the ratio between the EBSD scan step size and the microstructure feature size. Previous work on GND measurements demonstrate the correlation between GND density and slip distances [34]. As such, the fine grain structure of the martensite regions of the 430SS may lead to abnormal GND values.

When loaded perpendicular to the layers, as demonstrated in Figure 3.8(a), 3.8(b) and 3.8(c), the metal layers always exhibit higher GND densities compared to the transition layers, and transition layers always exhibit higher GND densities compared to FeAl layers. Since the metal

layers are softer, there would be more deformation in the metal layers. At the failure point, the GND densities of the metal layers are close among the three MIL composites, although their failure strain and ultimate strength are different.

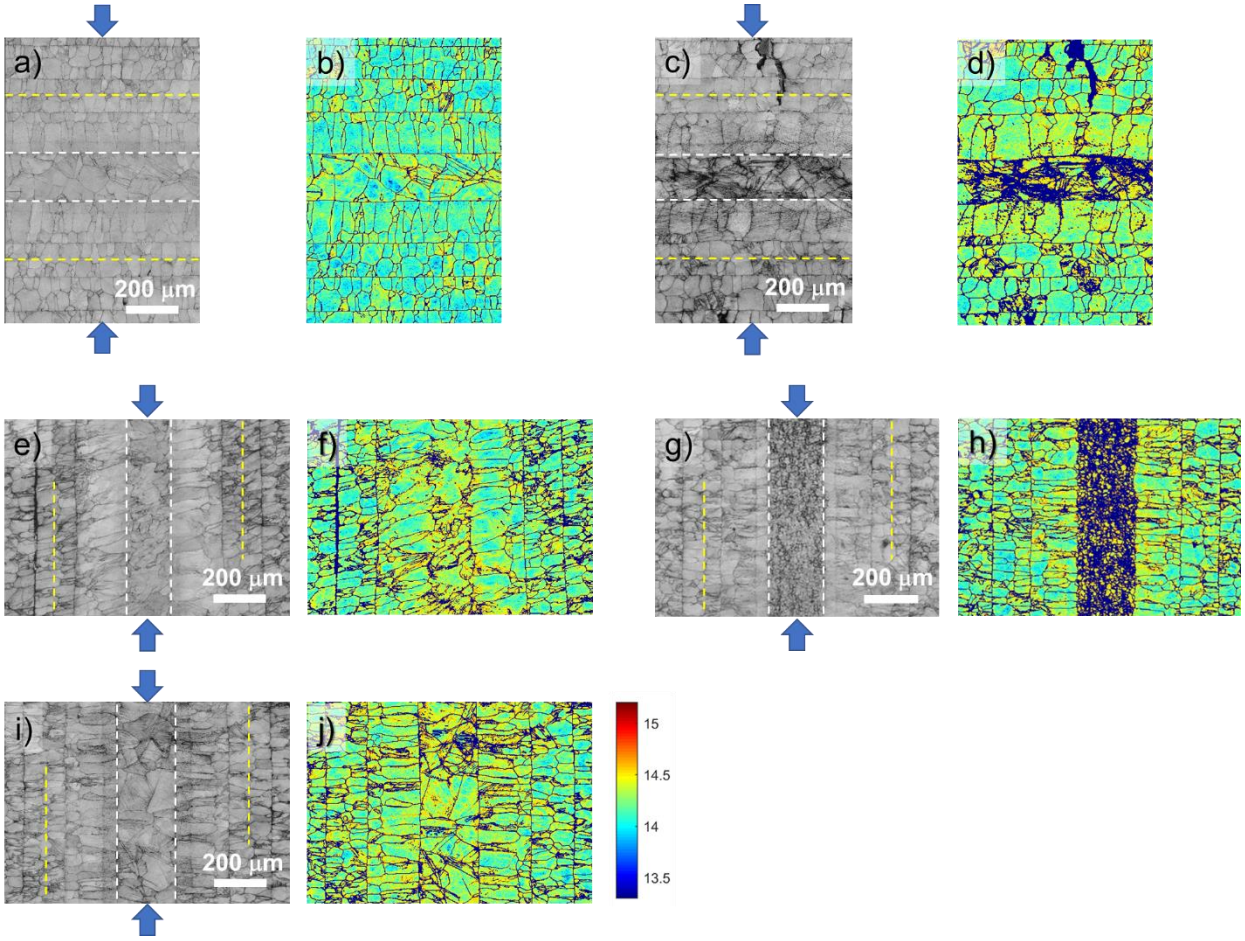

Figure 3.7: EBSD band contrast maps after compression testing conducted perpendicular to the layers: (a) 304SS-FeAl-MIL with 1.8 GPa loading, and (c) 304SS-FeAl-MIL failed at 2.3 GPa. EBSD band contrast maps after compression testing conducted parallel to the layers: (e) Fe-FeAl-MIL failed at 1.75 GPa, (g) 430SS-FeAl-MIL failed at 1.76 GPa, and (i) 304SS-FeAl-MIL failed at 2 GPa. The white dashed lines indicate the boundaries between metal and transition layers, and the yellow dashed lines indicate the boundaries between transition and FeAl layers. (b), (d), (f), (h) and (j) are the corresponding GND density maps using the same color scale.

At the same stress level, the FeAl layers of the 304-FeAl-MIL exhibit the lowest GND densities compared to the Fe-FeAl-MIL and 430SS-FeAl-MIL. Meanwhile, at the failure point, the FeAl layers of 304-FeAl-MIL exhibit the highest GND densities. This phenomenon indicates

the FeAl layers of 304-FeAl-MIL can accumulate more deformation, providing more work hardening, and consequently leading to a significantly higher ultimate strength.

When loaded parallel to the layers, as demonstrated in Figure 3.8(d), 3.8(e) and 3.8(f), the metal layers also show higher GND densities compared to the transition and FeAl layers. On the other hand, there does not exist any noticeable GND density concentration phenomenon as discusses in Section 3.4.1. The metal, transition and FeAl layers have undergone the same amount of deformation in the parallel-loaded compression testing. The GND density evolution is very similar in both the transition and FeAl layers, and very similar among the three FeAl-based MIL composites. The only exception is the transition layers of the 430SS-FeAl-MIL at the failure point, which is particularly higher, likely due to contributions in GND measurements associated with the martensite phase regions.

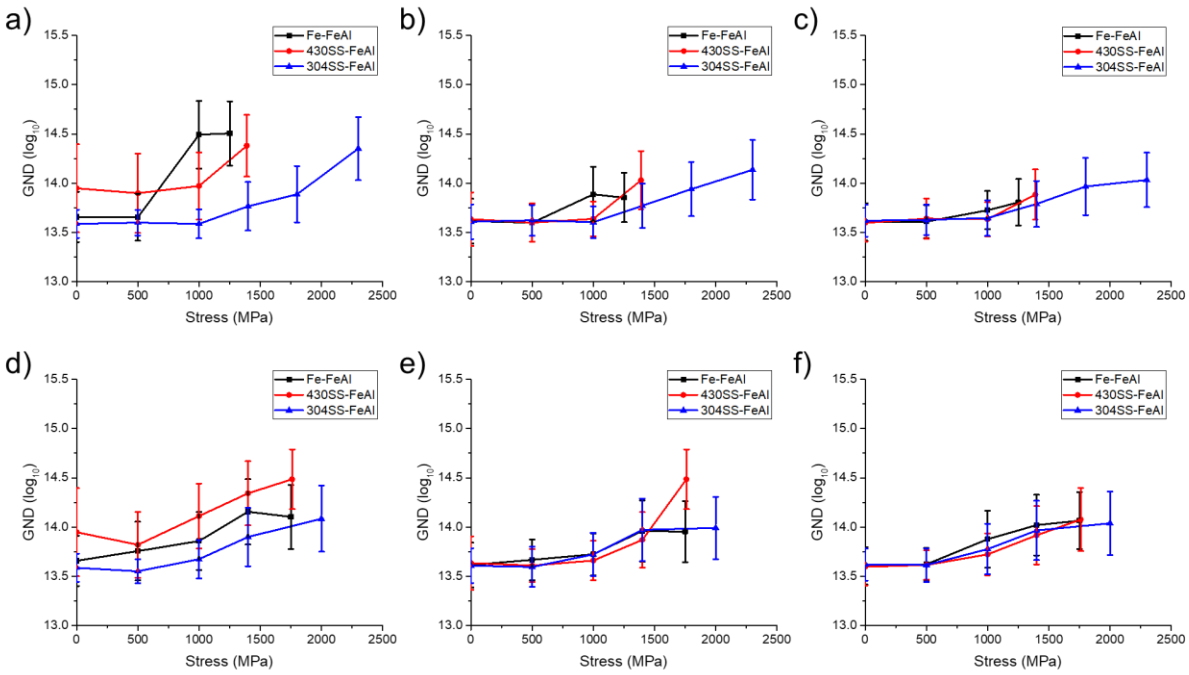

Figure: 3.8 GND density evolution of the FeAl-based MIL composites during the incremental compression testing: GND density of (a) metal layer, (b) transition layer and (c) FeAl layer loaded in perpendicular direction. GND density of (d) metal layer, (e) transition layer and (f) FeAl layer loaded in the parallel direction. The corresponding GND maps are listed in Appendix 3.D.

3.4.3 Fracture of FeAl-bases MIL Composites

3.4.3.1 Compression Perpendicular to the Layers

Figure 3.9(a) presents the microstructure of the Fe-FeAl-MIL at the failure point of perpendicular loading. As demonstrated in Figure 3.2(i), the FeAl-based MIL composites possess a strong work-hardening effect, as the ultimate strength is far above the yield point [77]. The cracks in the FeAl layers would lead to stress redistribution, unloading the ruptured FeAl intermetallics [7]. As a result, the uncracked regions need to carry more load, inducing more cracks and eventually failing the specimen. Meanwhile, as indicated by the yellow arrow in Figure 3.9(a), shear bands form, connecting the crack tip from one FeAl region to another across the Fe layer. Shear bands typically form during severe plastic deformation, suggesting that the cracks in the FeAl region localize deformation through the soft iron layers. For clarity, Figure 3.9(b) was scanned with a smaller step size, and its GND density is correspondingly higher than Figure 3.6(b), although they were collected from the same sample. The same conditions also apply to other GND density maps in Figure 3.9 and Figure 3.10.

As shown in Figure 3.9(c) and 3.9(e), shear bands do not exist in the 430SS-FeAl-MIL or 304SS-FeAl-MIL specimens. The absence of shear bands indicates that the metal layers have undergone less severe, localized deformation, which results from the higher strength of the 430SS and 304SS foils. Furthermore, the deformation of the metal layers is more uniform, as the absence of shear band leads to more homogeneous deformation throughout. In addition, the penetration of crack is stopped by the relatively ductile transition layer, as the deformation of the ductile material can relieve the stress concentration at the crack tip.

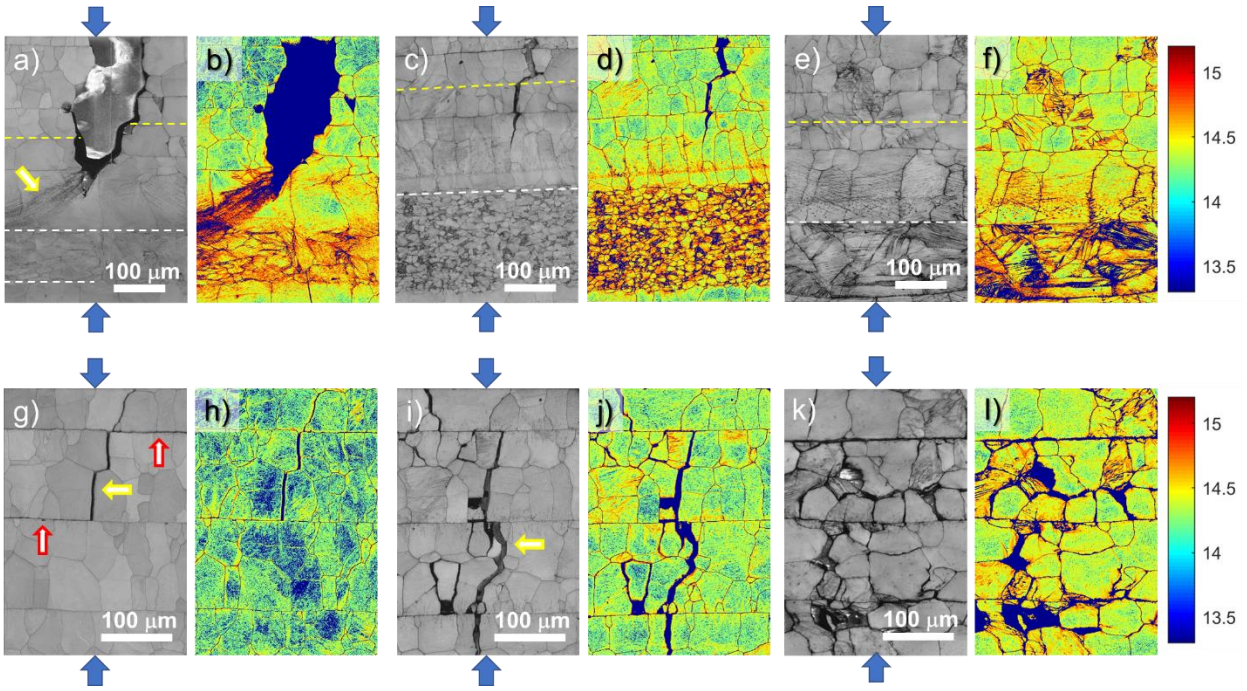

Figure 3.9: EBSD band contrast maps after compression testing conducted perpendicular to the layers: (a) metal and transition layer of Fe-FeAl-MIL, (c) metal and transition layer of 430SS-FeAl-MIL, (e) metal and transition layer of 304SS-FeAl-MIL, (g) FeAl layers of Fe-FeAl-MIL, (i) FeAl layers of 430SS-FeAl-MIL, and (k) FeAl layers of 304SS-FeAl-MIL. The white dashed lines indicate the boundaries between metal and transition layers, and the yellow dashed lines indicate the boundaries between transition and FeAl layers. (b), (d), (f), (h), (j) and (l) are the corresponding GND density maps using the same color scale.

The FeAl layers of the Fe-FeAl-MIL are presented in Figure 3.9(g), confirming that the fracture in the FeAl phase occurs by intergranular failure [22]. Furthermore, based on the width of the cracks, the primary cracks, which are along the vertical direction indicated by the yellow arrow, induce delamination between the FeAl layers indicated by the red arrows. On one hand, the delamination would toughen the composites via crack deflection, crack blunting and stress redistribution [5,82]. On the other hand, the delamination would be restrained by the external force, as the force is perpendicular to the layers.

As shown in Figure 3.9(k), after failure, the FeAl layers of the 304-FeAl-MIL have significantly more cracks compared to the Fe-FeAl-MIL and 430SS-FeAl-MIL. As discussed in Section 3.4.2, the higher GND densities indicate more deformation and consequently more work

hardening of the FeAl; as a result, there will be more cracks in the FeAl layers of the 304-FeAl-MIL.

As demonstrated in Appendix 3.A, the FeAl layers of the three MIL composites are very similar, and they failed in a similar mode. Therefore, the dramatic improvement of strength and ductile of 304SS-FeAl-MIL must result from its metallic constituents. Furthermore, 304SS and 430SS possess similar mechanical properties, which is demonstrated by the hardness measurement in Figure 3.2(g). Therefore, the transition layers must play a critical role when the composites are subjected to perpendicular loading.

When the FeAl-based MIL composites are loaded perpendicular to the layers, delamination never occurs at metal/transition layer interface or transition layer/FeAl interface. Consequently, their strain tensor ε_{Metal}, $\varepsilon_{Transition}$and ε_{FeAl} must be matched at the interface.

$$\varepsilon = \begin{bmatrix} \varepsilon_{xx} & 0 & 0 \\ 0 & \varepsilon_{yy} & 0 \\ 0 & 0 & \varepsilon_{zz} \end{bmatrix} \tag{3.4}$$

$$\varepsilon_{yy,Metal} = \varepsilon_{yy,Transition} = \varepsilon_{zz,Metal} = \varepsilon_{zz,Transition} \tag{3.5}$$

$$\varepsilon_{yy,FeAl} = \varepsilon_{yy,Transition} = \varepsilon_{zz,FeAl} = \varepsilon_{zz,Transition} \tag{3.6}$$

Note that Eq. (3.5) and Eq. (3.6) describe metal/transition layer interface and transition layer/FeAl interface, respectively. So $\varepsilon_{Transition}$ in Eq. (3.5) and Eq. (3.6) are different.

The metal, transition and FeAl layers possess dissimilar stress-strain responses. At the same stress level, the strain of the individual metals would be considerably larger than the individual FeAl phase. So, the constrain described by Eq. (3.5) and Eq. (3.6) would induce in-plane internal stress, limiting the expansion of the metal layers, but splitting the FeAl regions and

accelerating the crack growth. Furthermore, the transition layers, as a gradient material, needs to obey Eq. (3.5) and Eq. (3.6) not only at the interface, but also within the transition layer itself.

As all the cracks exist in the FeAl region, the focus shifts to the transition layer/FeAl interface for investigating the difference between the Fe-FeAl-MIL, 430SS-FeAl-MIL and 304SS-FeAl-MIL composites. In addition, as discussed in Section 3.4.1.1, all three MIL composites behave similarly before the yielding. The internal stress needs to be considered when all the layers are subjected to plastic deformation.

During the plastic deformation, the total strain can be split into the elastic part and the plastic part [83]: $\varepsilon = \varepsilon^E + \varepsilon^P$. The elastic strain follows Hooke's law as $\varepsilon^E = \frac{\sigma}{E}$, where σ is the total stress, and E is the Young's modulus, and the plastic strain can be described as the function of total stress: $\varepsilon^P = f(\sigma)$.

Let the internal stress σ_i acting on the transition layer take the same sign as the external load C, then the internal stress acting on the FeAl layer would be -σ_i as force pairs. Based on the definition of Poisson's ratio, the in-plane strain of the transition layer can be written as:

$$\varepsilon_{yy,\mathrm{T}} = \varepsilon_{zz,\mathrm{T}} = \frac{1}{E_T}[\sigma_i - \nu^E \cdot (C + \sigma_i)] + \{f_T(\sigma_i) - \nu^P \cdot [f_T(C) + f_T(\sigma_i)]\} \tag{3.7}$$

In Eq. (3.6), the first part is the contribution of elastic strain, and the second part is the contribution of plastic strain. E_T is Young's modulus for the transition layer, ν^E is the Poisson's ratio for elastic, which is typically 0.3 for metallic materials, and ν^P is the Poisson's ratio for plastic flow, which is 0.5 for incompressible materials [83].

Similarly, the in-plane strain of the FeAl layer can be written as:

$$\varepsilon_{yy,\mathrm{I}} = \varepsilon_{zz,\mathrm{I}} = \frac{1}{E_I}[-\sigma_i - \nu^E \cdot (C - \sigma_i)] + \{-f_I(\sigma_i) - \nu^P \cdot [f_I(C) - f_I(\sigma_i)]\} \tag{3.8}$$

The in-plane strain must be the same at the transition layer/FeAl interface: $\varepsilon_{yy,\mathrm{T}} = \varepsilon_{yy,\mathrm{I}}$. Additionally, Young's modulus of the transition layer (α-Fe solid solution) and FeAl is similar at the interface [23]: $E_T \approx E_I = E$. By linking Eq. (3.7) to Eq. (3.8), Equation (3.9) is obtained:

$$\frac{2}{E}(1-\nu^E)\cdot\sigma_i + (1-\nu^P)[f_T(\sigma_i) - f_I(\sigma_i)] = \nu^P[f_T(C) - f_I(C)] \tag{3.9}$$

If the internal stress σ_i is smaller than the yield point, Eq. (3.9) can be reduced to:

$$\frac{2}{E}(1-\nu^E)\cdot\sigma_i = \nu^P[f_T(C) - f_I(C)] \tag{3.10}$$

and further to:

$$\sigma_i = \frac{E\cdot\nu^P}{2(1-\nu^E)}[f_T(C) - f_I(C)] \tag{3.11}$$

The internal stress is proportional to the $[f_T(C) - f_I(C)]$ term, which represents the difference in stress-strain behavior between the transition layers and FeAl layers. The $[f_T(C) - f_I(C)]$ term represents the gap between the strain of individual transition layers and the strain of individual FeAl layers, when at the same stress level. Since delamination or slip does not occur at the interface, this gap must be compensated by the development of internal stress, which is a compression stress for the transition layers, and a tensile stress for FeAl layers. As demonstrated in Figure 3.11, a stronger transition layer would induce a smaller difference in strain, and thereby smaller internal stress.

When the internal stress σ_i exceeds the yield point, Eq. (3.9) is reorganized as:

$$\frac{2}{E}(1-\nu^E)\cdot\sigma_i = [\nu^P\cdot f_T(C) - (1-\nu^P)\cdot f_T(\sigma_i)] - [\nu^P\cdot f_I(C) - (1-\nu^P)\cdot f_I(\sigma_i)] \tag{3.12}$$

As $\nu^P = 0.5$ for incompressible materials,

$$\frac{2}{E}(1-\nu^E)\cdot\sigma_i = 0.5\{[f_T(C) - f_T(\sigma_i)] - [f_I(C) - f_I(\sigma_i)]\} \tag{3.13}$$

Eq. (3.13) also predicts that a stronger transition layer would induce smaller internal stress.

Indicated by the hardness profile in Fig.2(g), the transition layers of 304SS-FeAl-MIL are significantly stronger than those in the Fe-FeAl-MIL or 430SS-FeAl-MIL. Consequently, the internal stress, which splits FeAl grains and accelerates the crack growth, would be considerably smaller in the 304SS-FeAl-MIL, and the specimen can thereby exhibit dramatic improvement in strength.

3.4.3.2 Compression Parallel to the Layers

The metal and transition layers of the Fe-FeAl-MIL, 430SS-FeAl-MIL and 304SS-FeAl-MIL are shown in Figure 3.10(a), 3.10(c) and 3.10(e), respectively. The images are from the relatively uniformly deformed region, which is representative of the majority of the sample. The GND densities are uniform across the layers even at the failure point. Additionally, delamination never occurs at the metal and transition layers.

In contrast, as shown in Figure 3.12, the region of buckling undergoes significantly more severe deformation. The pure iron and attached transition layers are rotated by almost 90^{o} through a shearing mechanism. Subsequently, surrounding FeAl layers are all delaminated and cracked. Even in this situation, delamination between metal/transition layer or transition layer/FeAl has not occurred.

The FeAl layers of the three MIL composites are shown in Figure 3.10(g), 3.10(i) and 3.10(k). As indicated by the yellow arrows, the band contrast maps reveal that dislocations pile up around the centerlines, potentially increasing the stress concentration in these regions and making them prone to delamination. In addition to the delamination in the vertical direction, the

local stress field induces some horizontal cracks along grain boundaries. Since the external force would restrain the opening of horizontal cracks, their influence on the failure is limited.

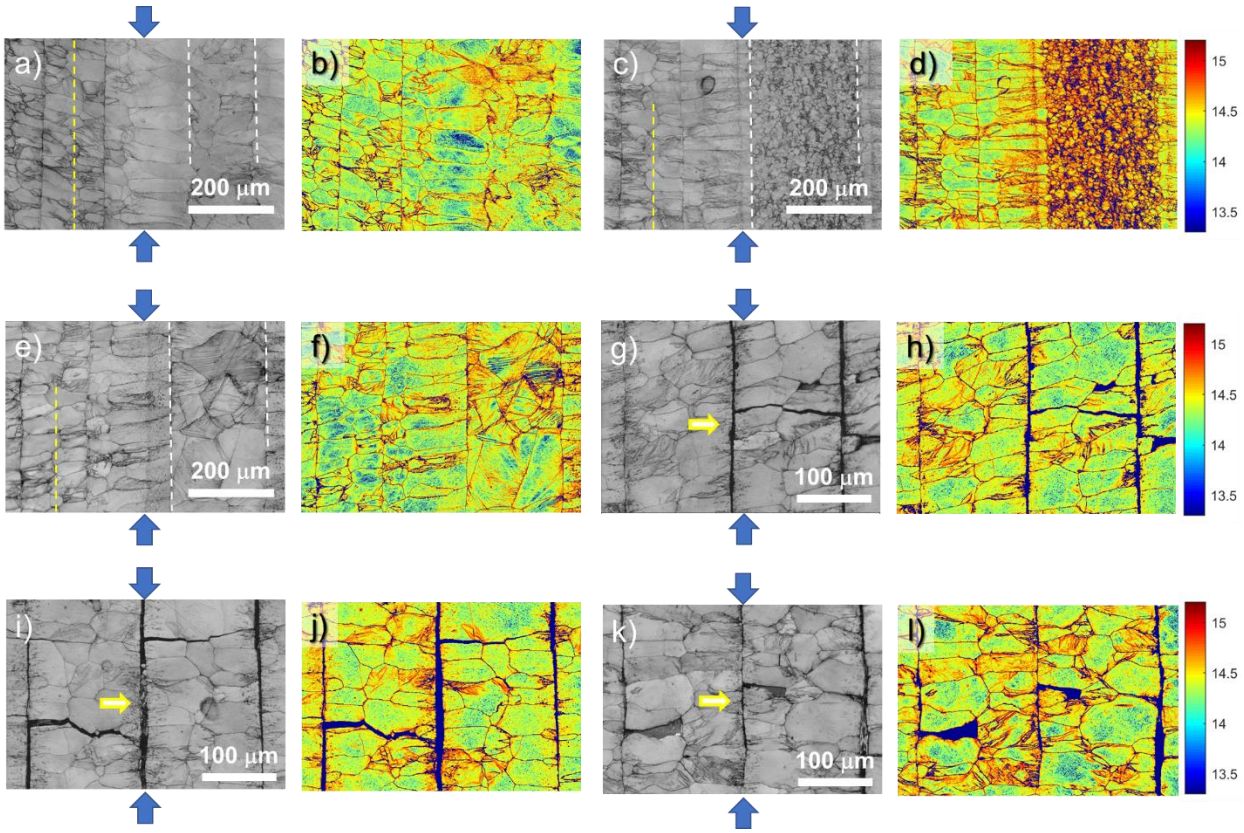

Figure 3.10: EBSD band contrast maps after compression testing conducted parallel to the layers: (a) metal and transition layer of Fe-FeAl-MIL, (c) metal and transition layer of 430SS-FeAl-MIL, (e) metal and transition layer of 304SS-FeAl-MIL, (g) FeAl layers of Fe-FeAl-MIL, (i) FeAl layers of 430SS-FeAl-MIL, and (k) FeAl layers of 304SS-FeAl-MIL. The white dashed lines indicate the boundaries between metal and transition layers, and the yellow dashed lines indicate the boundaries between transition and FeAl layers. (b), (d), (f), (h), (j) and (l) are the corresponding GND density maps using the same color scale.

Under the uniaxial strain condition, the strain along the loading direction is always the same among all the layers. If all the layers possess similar Poisson's ratios, the compression induced tension, $\varepsilon_{zz} = -\nu\varepsilon_{yy}$, will be very similar for all the layers. In other words, there would not be in-plane internal stress when these composites are subjected to parallel loading.

Consequently, the strong transition layers of the 304SS-FeAl-MIL do not dramatically improve the strength, and all three FeAl-based MIL composites exhibit similar stress-strain behavior.

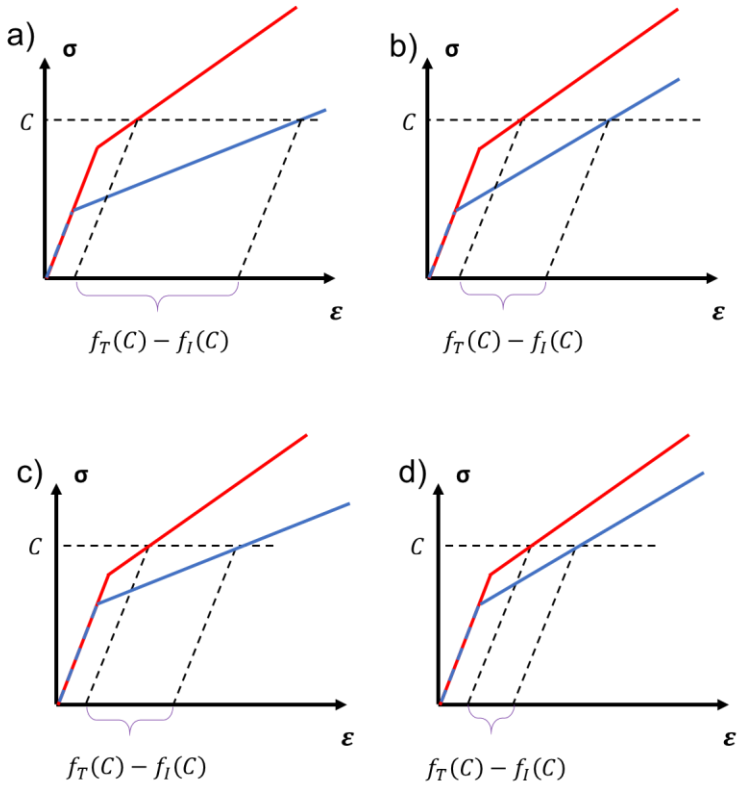

Figure 3.11: (a) Difference in strain when FeAl layers and transition layers are subjected to the same level of stress. The red curve represents individual FeAl layers, and the blue curve represents individual transition layers. When transition layers become stronger as (b) higher work hardening rate, (c) higher yield point, or (d) higher work hardening rate with higher yield point, the difference in strain decreases.

3.5 Conclusion

The present work investigates the microstructure evolution of FeAl-based MIL composites via the incremental compression test. The samples were characterized via EBSD and analyzed with GND distribution. The main conclusions are:

1. In the compression testing, the fracture of the FeAl-based MIL composites is induced by normal stress in the FeAl layers. Other MIL composites, such as Ti-Al_3Ti-MIL, which possess lower strength and ductility, typically failing by shear at small strains.

2. The FeAl regions of the three MIL composites (Fe-FeAl-MIL, 430SS-FeAl-MIL and 304SS-FeAl-MIL) are very similar. The failure mode, crack morphology and GND distribution in the FeAl region are very similar for the three MIL composites.

3. The transition layer formed between the metal and FeAl regions is crucial for FeAl-based MIL composites. Although the transition layers are not the strongest constituent, and the volume fraction of the transition layer is less than 15%, a stronger transition layer can improve the strength by as much as 1GPa, when loading perpendicular to the layers.

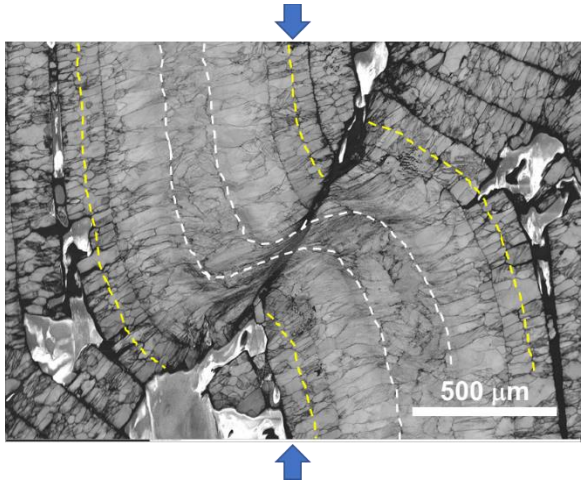

Figure 3.12: Microstructure of the buckling region of the failed specimen. The white dashed lines indicate the boundaries between Fe and transition layers, and the yellow dashed lines indicate the boundaries between transition and FeAl layers.

Appendix 3.A Texture of FeAl Phase in the FeAl-base MIL Composites

The EBSD scan of the FeAl phase in Fe-FeAl-MIL, 430SS-FeAl-MIL and 304SS-FeAl-MIL is presented in Figure 3.A1. Based on the inverse pole figure, the texture of the FeAl phase in the three MIL composites is identical. Consequently, FeAl regions are expected to exhibit similar mechanical behavior.

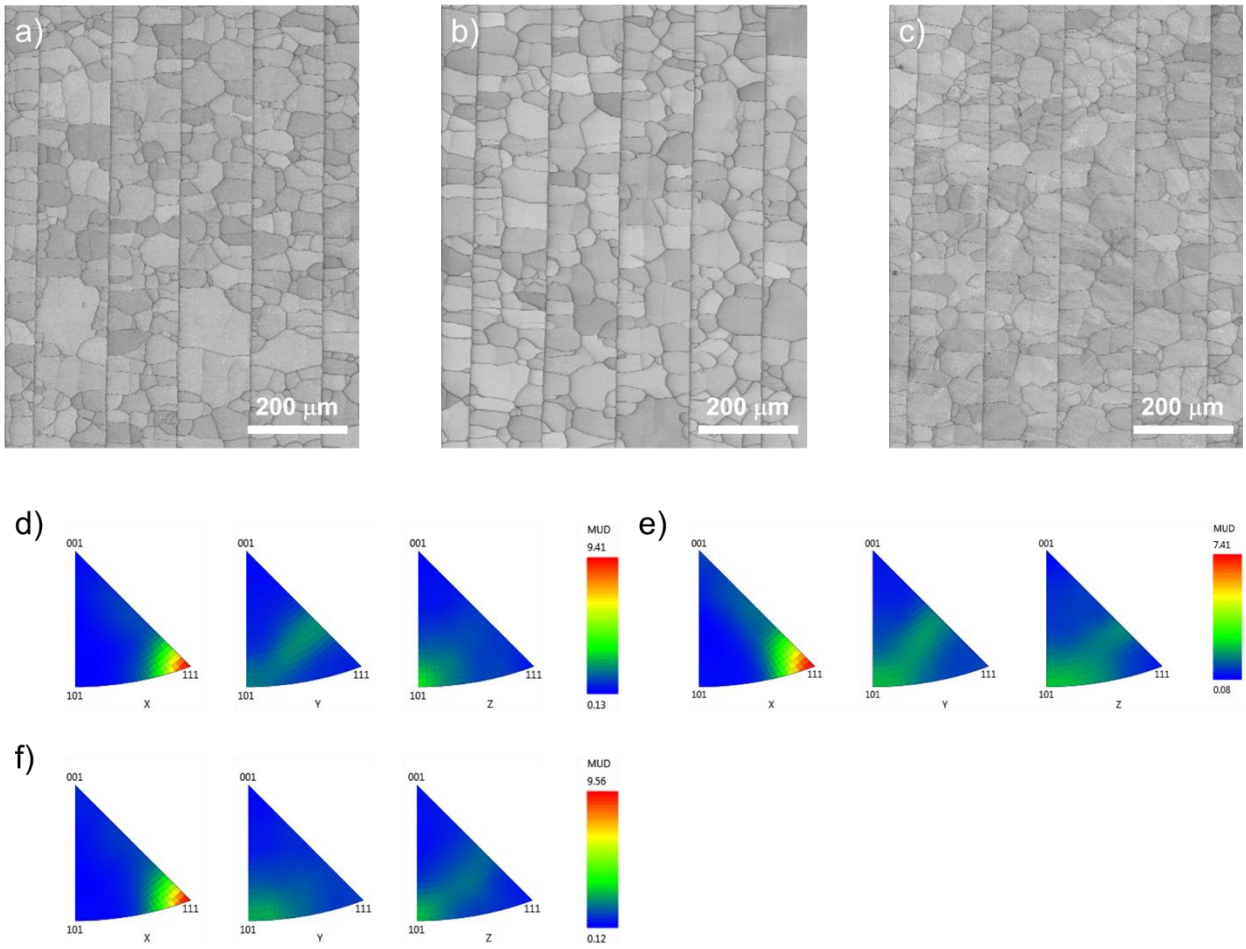

Figure 3.A1: Microstructure of FeAl phase in (a) Fe-FeAl-MIL, (b) 430SS-FeAl-MIL, and (c) 304SS-FeAl-MIL. The inverse pole figure is plotted in (d), (e) and (f), respectively.

Appendix 3.B Noise Floor of the GND Analysis

The accuracy of GND calculation is limited by the EBSD measurement, as the ideal geometrical relationship for the scan can not be strictly satisfied in reality [84]. The inaccuracy would induce noise to the GND density map, and anything below the noise floor would be overwhelmed. The noise floor of the GND analysis can be estimated using the angular resolution and step size of the EBSD scan [81]:

$$\rho_{GND}^{res} = \frac{Angular\ Resolution\ (rad)}{Step\ Size\ (m) \times\ Burger's\ Vector(m)} \tag{3.B1}$$

The angular resolution of modern SEM is typically $0.2^O \sim 0.4^O$ $(0.0035 \sim 0.0070\ rad)$ [34]. Meanwhile, Burger's vector can be calculated as:

$$Burger's\ Vector = \frac{\sqrt{2}}{2}a \quad for\ FCC \tag{3.B2}$$

$$Burger's\ Vector = \frac{\sqrt{3}}{2}a \quad for\ BCC \tag{3.B3}$$

where a is the lattice constant. In the present work, we use $a = 0.28\ nm$ for α-Fe and FeAl phase, and $a = 0.359\ nm$ for the austenite phase. Thereby, the estimated noise floor is $10^{12.8} \sim 10^{13.2}\ m^{-2}$ when the step size is 2 μm, and $10^{13.5} \sim 10^{13.8}\ m^{-2}$ when the step size is 0.5 μm. As the smaller step size yields a higher noise floor, the difference of GND density at low load would be further overwhelmed.

Appendix 3.C Structure of the 430SS

Figure 3.C1 (a) and (c) compare the microstructure of the 430SS in the MIL composites with the as-received 430SS foil. 430SS is known to possess a pure ferrite structure, which is confirmed in Figure 3.C1(c). However, after the annealing, the 430SS layer exhibits a dual-phase structure. The microstructure of the fine grain region is similar to the 420SS, which is known to possess a pure martensite structure. In addition, as compared in Table 3.C1, the hardness measurement via nanoindentation also indicates that the fine grain region is the martensite.

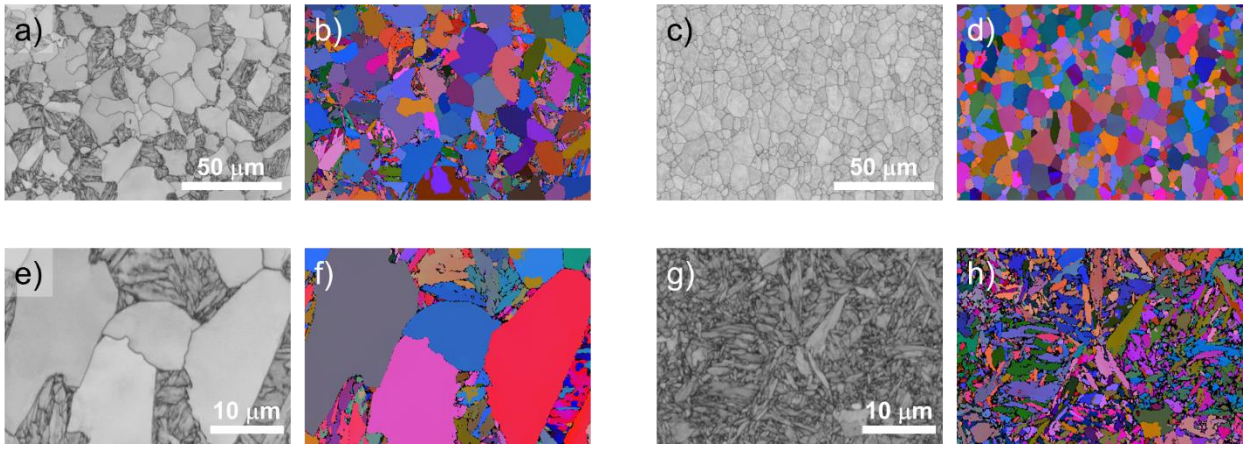

Figure 3.C1: Microstructure of (a) and (e) 430SS in MIL composites, (c) as-received 430SS foil, (g) 420SS. (b), (d), (f) and (h) is the corresponding Euler color map of grain orientation.

Table 3.C1: Hardness of 430SS and 420SS

	430SS		420SS
	Corse Grain Region	Fine Grain Region	
Hardness	2570 ± 600MPa	6300 ± 1200MPa	7500 ± 1100MPa

Furthermore, Table 3.C2 compares the composition of 430SS in the MIL composites. We believe the phase transformation of ferrite to martensite is induced by composition fluctuation

during the annealing, and the region with insufficient Cr could not be stabilized to ferrite during the heat treatment.

Table 3.C2: Composition of 430SS measured via Energy-Dispersive X-ray Spectrometer

	Coarse Grain Region	Fine Grain Region	Average
Cr (wt%)	18.4 ± 0.04	16.0 ± 0.06	17.2
Fe (wt%)	81.6 ± 0.04	84.0 ± 0.06	82.8

Appendix 3.D GND map of the FeAl-based MIL composites

The GND maps utilized for plotting Figure 3.8 are presented in Figure 3.D1 to Figure 3.D12. The data was collected with a small step size (0.5 μm) to reveal more details. Furthermore, the GND distribution curve is plotted in Figure 3.D13 and Figure 3.D14 to show the evolution.

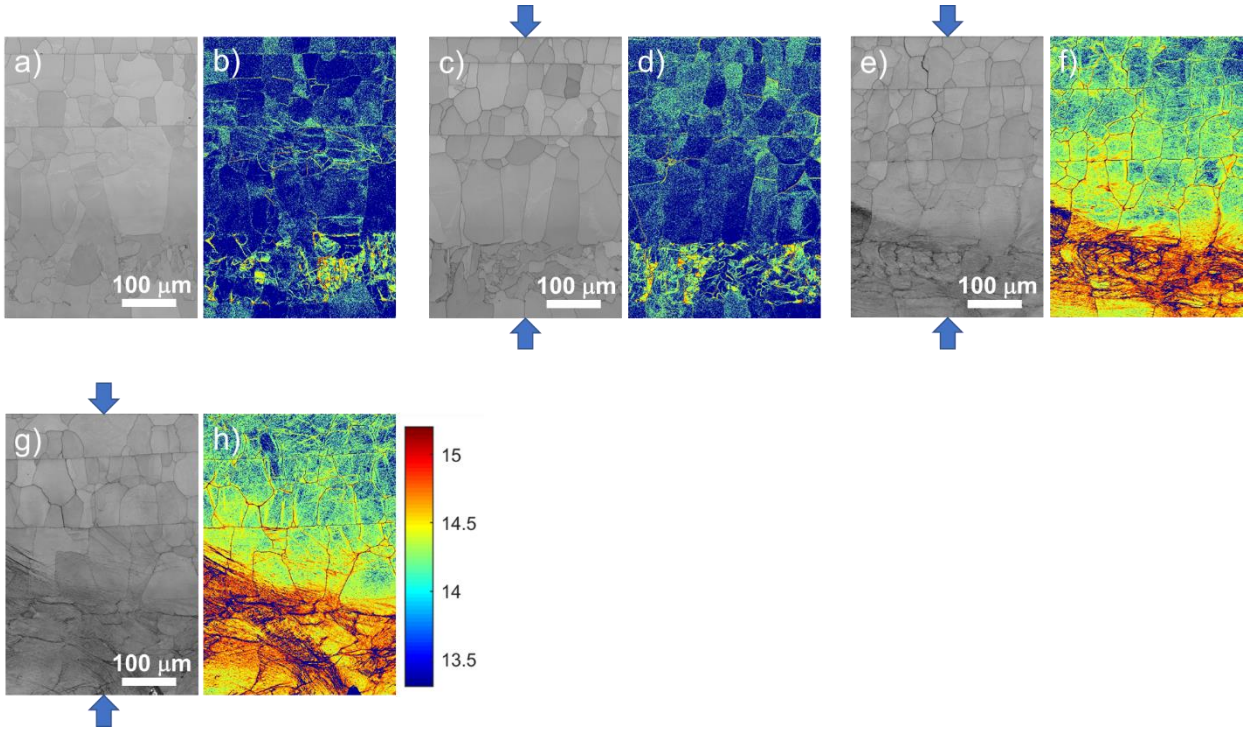

Figure 3.D1: Microstructure of metal and transition layers in the Fe-FeAl-MIL specimen compressed in the perpendicular direction with the incremental load: (a) 0, (c) 500MPa, (e) 1000MPa, and (g) 1250MPa (failure point). (b), (d), (f) and (h) are the corresponding GND density maps using the same color scale.

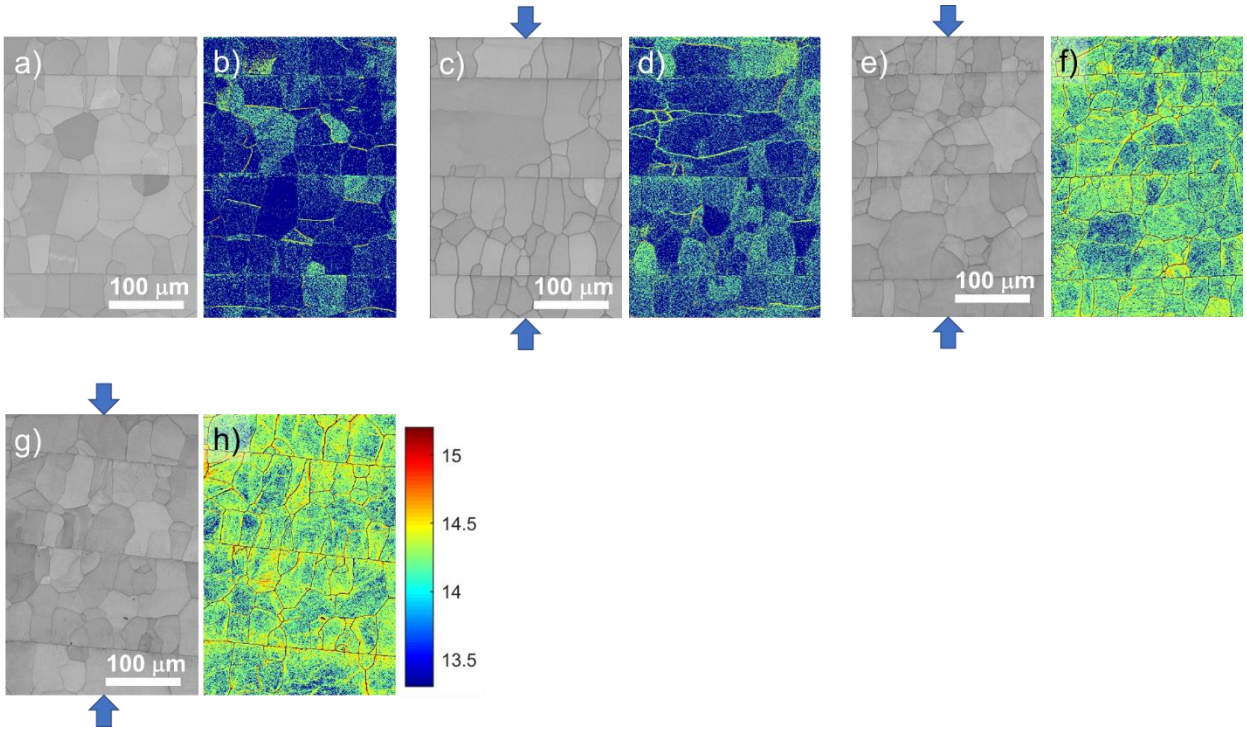

Figure 3.D2: Microstructure of FeAl layers in the Fe-FeAl-MIL specimen compressed in the perpendicular direction with the incremental load: (a) 0, (c) 500MPa, (e) 1000MPa, and (g) 1250MPa (failure point). (b), (d), (f) and (h) are the corresponding GND density maps using the same color scale.

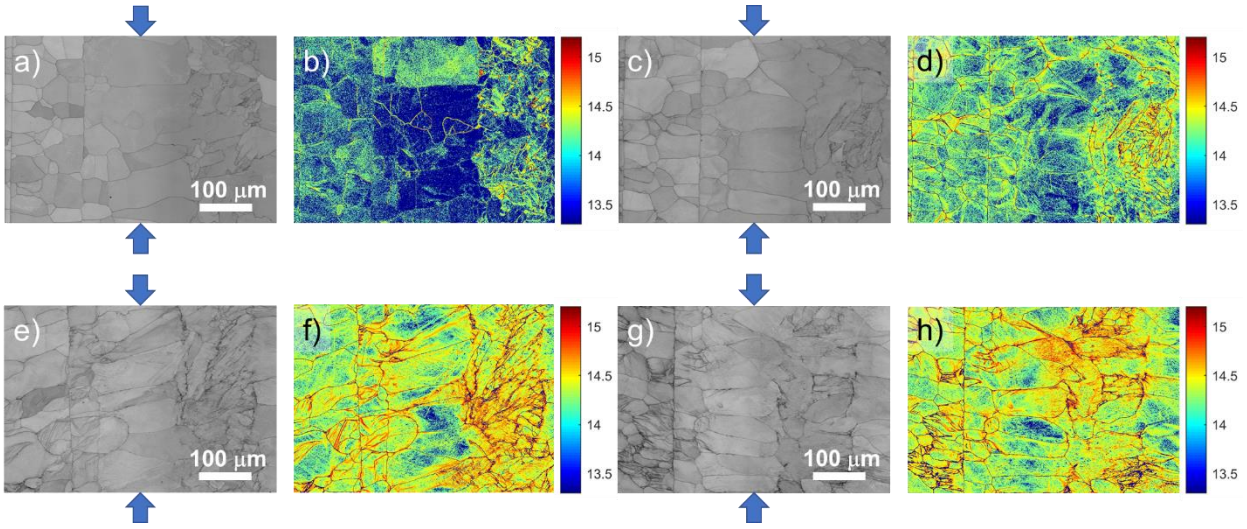

Figure 3.D3: Microstructure of metal and transition layers in the Fe-FeAl-MIL specimen compressed in the parallel direction with the incremental load: (a) 500MPa, (c) 1000MPa, (e) 1400MPa, and (g) 1750MPa (failure point). (b), (d), (f) and (h) are the corresponding GND density maps using the same color scale.

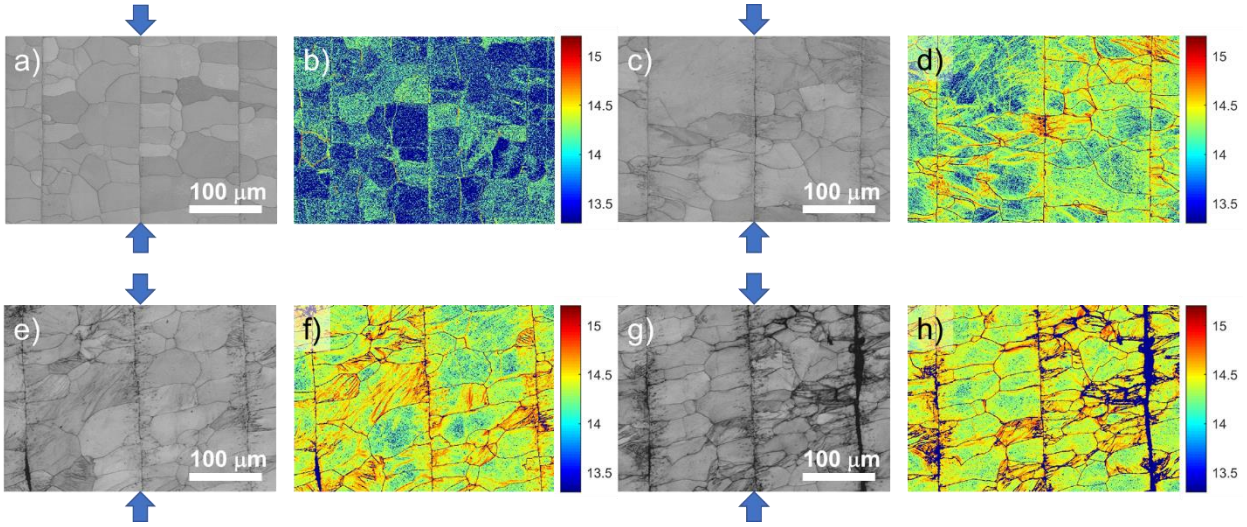

Figure 3.D4: Microstructure of FeAl layers in the Fe-FeAl-MIL specimen compressed in the parallel direction with the incremental load: (a) 500MPa, (c) 1000MPa, (e) 1400MPa, and (g) 1750MPa (failure point). (b), (d), (f) and (h) are the corresponding GND density maps using the same color scale.

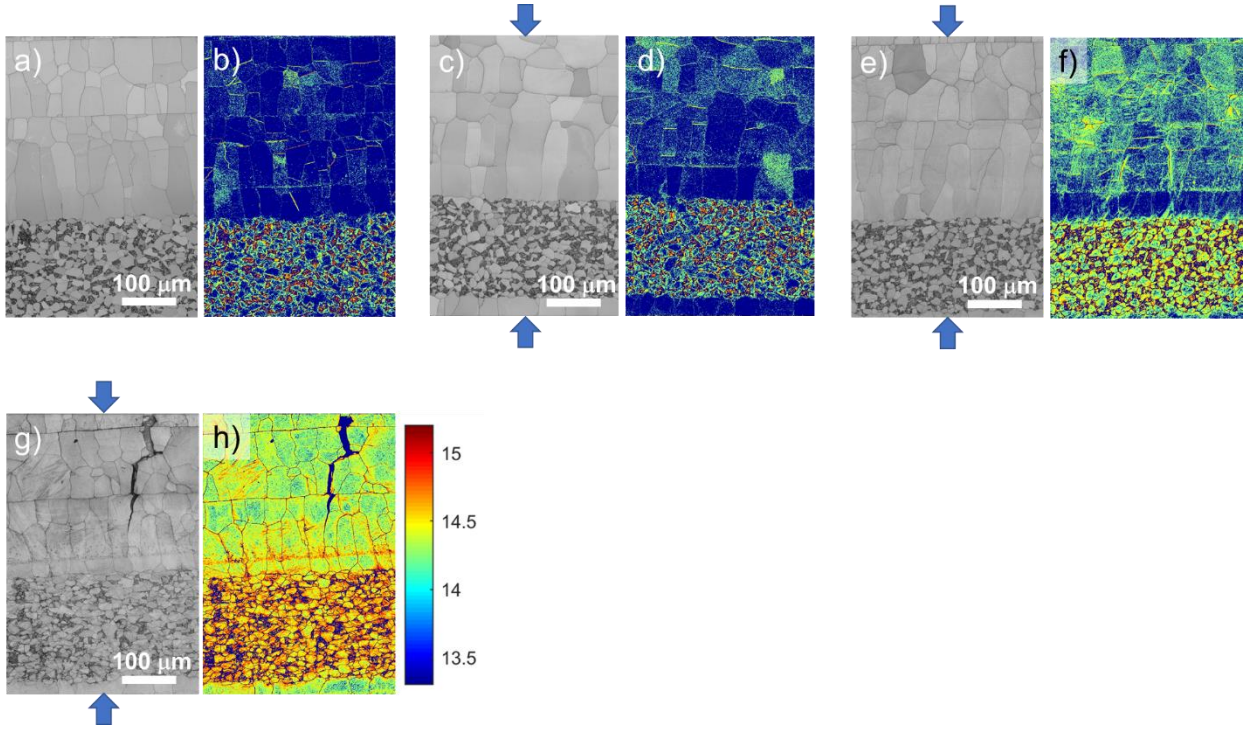

Figure 3.D5: Microstructure of metal and transition layers in the 430SS-FeAl-MIL specimen compressed in the perpendicular direction with the incremental load: (a) 0, (c) 500MPa, (e) 1000MPa, and (g) 1390MPa (failure point). (b), (d), (f) and (h) are the corresponding GND density maps using the same color scale.

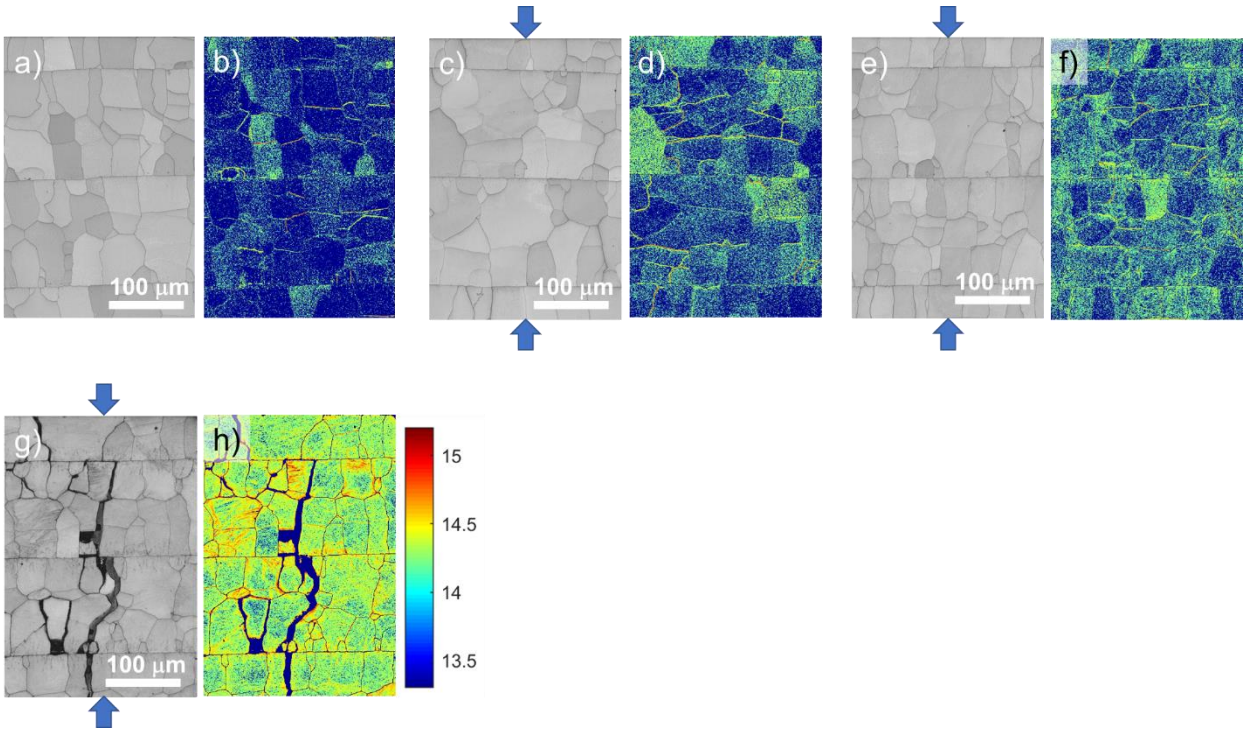

Figure 3.D6: Microstructure of FeAl layers in the 430SS-FeAl-MIL specimen compressed in the perpendicular direction with the incremental load: (a) 0, (c) 500MPa, (e) 1000MPa, and (g) 1390MPa (failure point). (b), (d), (f) and (h) are the corresponding GND density maps using the same color scale.

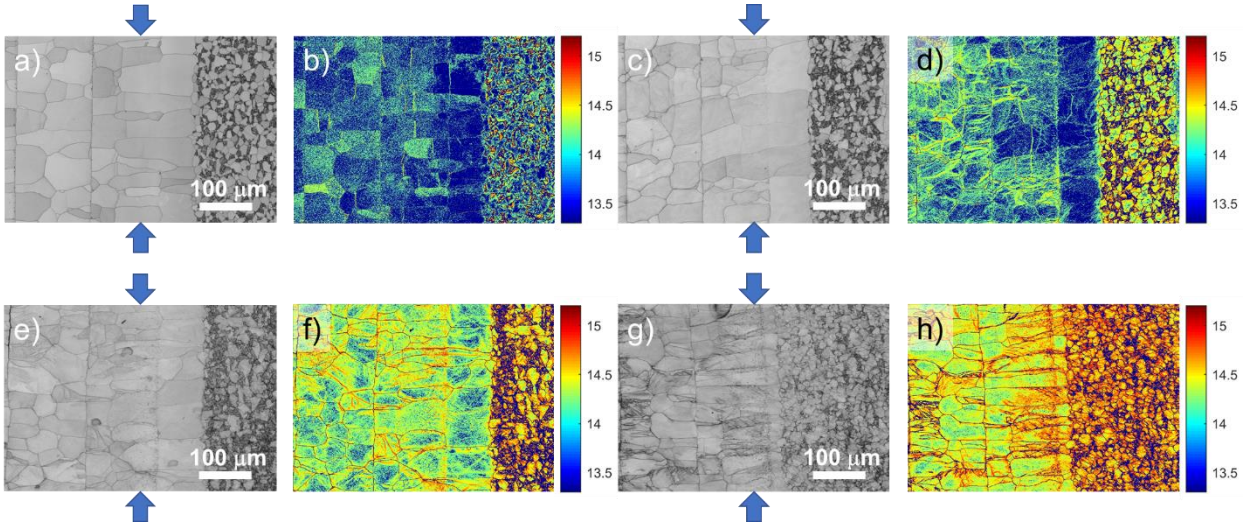

Figure 3.D7: Microstructure of metal and transition layers in the 430SS-FeAl-MIL specimen compressed in the parallel direction with the incremental load: (a) 500MPa, (c) 1000MPa, (e) 1400MPa, and (g) 1760MPa (failure point). (b), (d), (f) and (h) are the corresponding GND density maps using the same color scale.

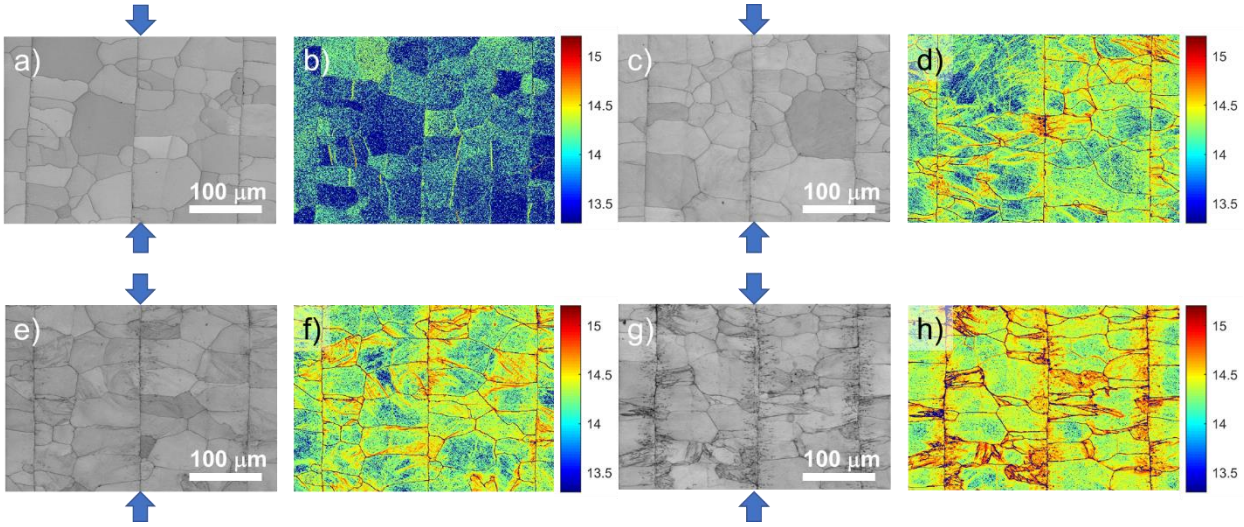

Figure 3.D8: Microstructure of FeAl layers in the 430SS-FeAl-MIL specimen compressed in the parallel direction with the incremental load: (a) 500MPa, (c) 1000MPa, (e) 1400MPa, and (g) 1760MPa (failure point). (b), (d), (f) and (h) are the corresponding GND density maps using the same color scale.

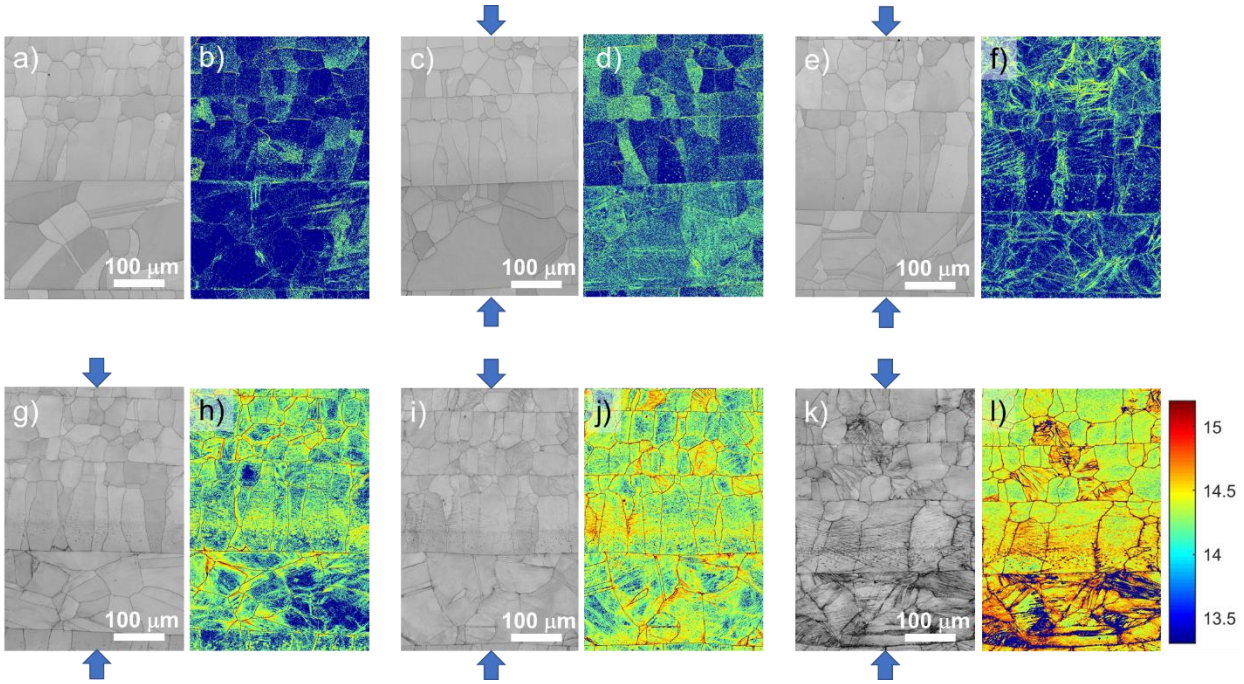

Figure 3.D9: Microstructure of metal and transition layers in the 304SS-FeAl-MIL specimen compressed in the perpendicular direction with the incremental load: (a) 0, (c) 500MPa, (e) 1000MPa, (g) 1400MPa, (i) 1800MPa, and (k) 2300MPa (failure point). (b), (d), (f), (h), (j) and (l) are the corresponding GND density maps using the same color scale.

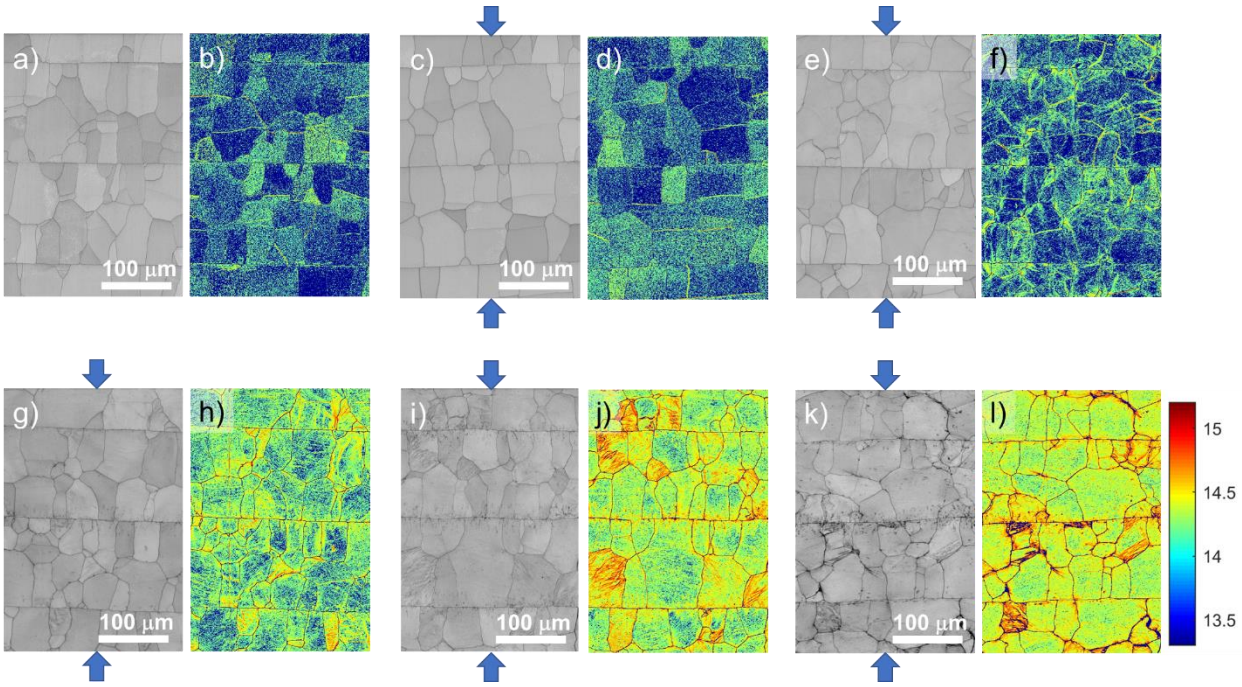

Figure 3.D10: Microstructure of FeAl layers in the 304SS-FeAl-MIL specimen compressed in the perpendicular direction with the incremental load: (a) 0, (c) 500MPa, (e) 1000MPa, (g) 1400MPa, (i) 1800MPa, and (k) 2300MPa (failure point). (b), (d), (f), (h), (j) and (l) are the corresponding GND density maps using the same color scale.

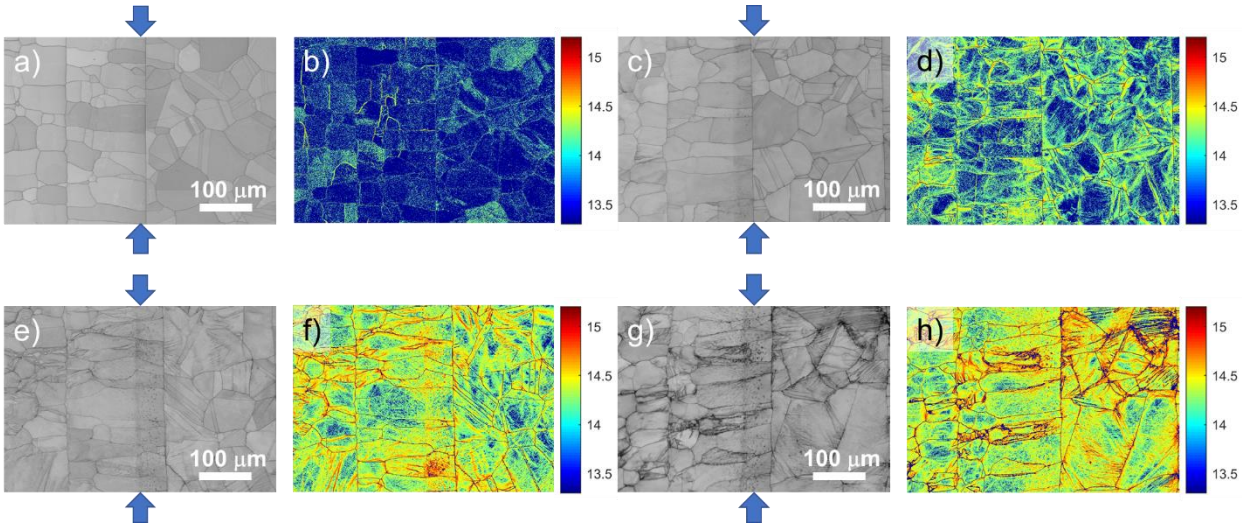

Figure 3.D11: Microstructure of metal and transition layers in the 304SS-FeAl-MIL specimen compressed in the parallel direction with the incremental load: (a) 500MPa, (c) 1000MPa, (e) 1400MPa, and (g) 2000MPa (failure point). (b), (d), (f) and (h) are the corresponding GND density maps using the same color scale.

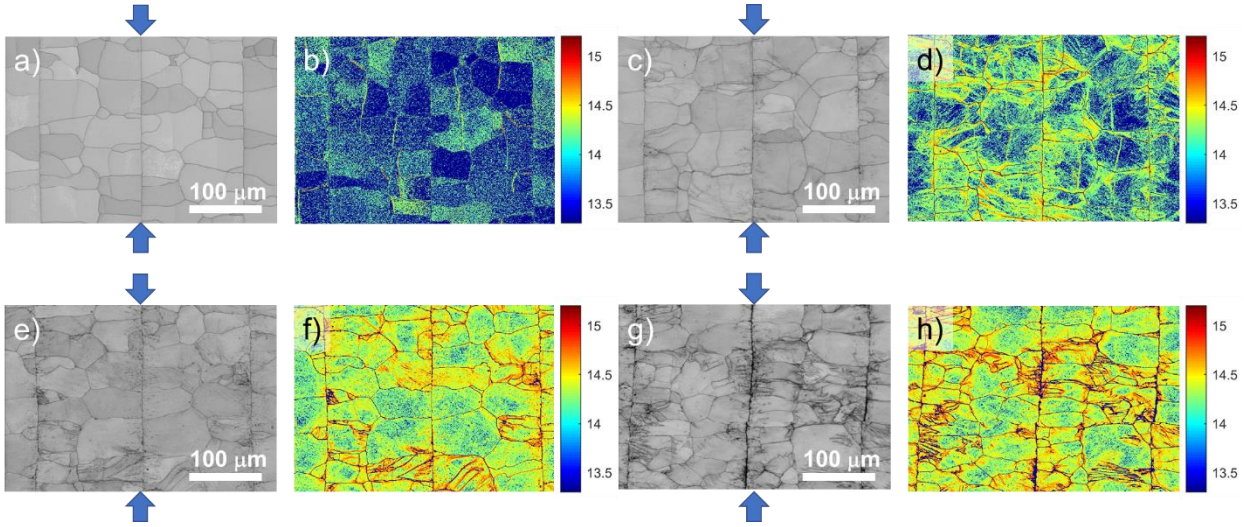

Figure 3.D12: Microstructure of FeAl layers in the 304SS-FeAl-MIL specimen compressed in the parallel direction with the incremental load: (a) 500MPa, (c) 1000MPa, (e) 1400MPa, and (g) 2000MPa (failure point). (b), (d), (f) and (h) are the corresponding GND density maps using the same color scale.

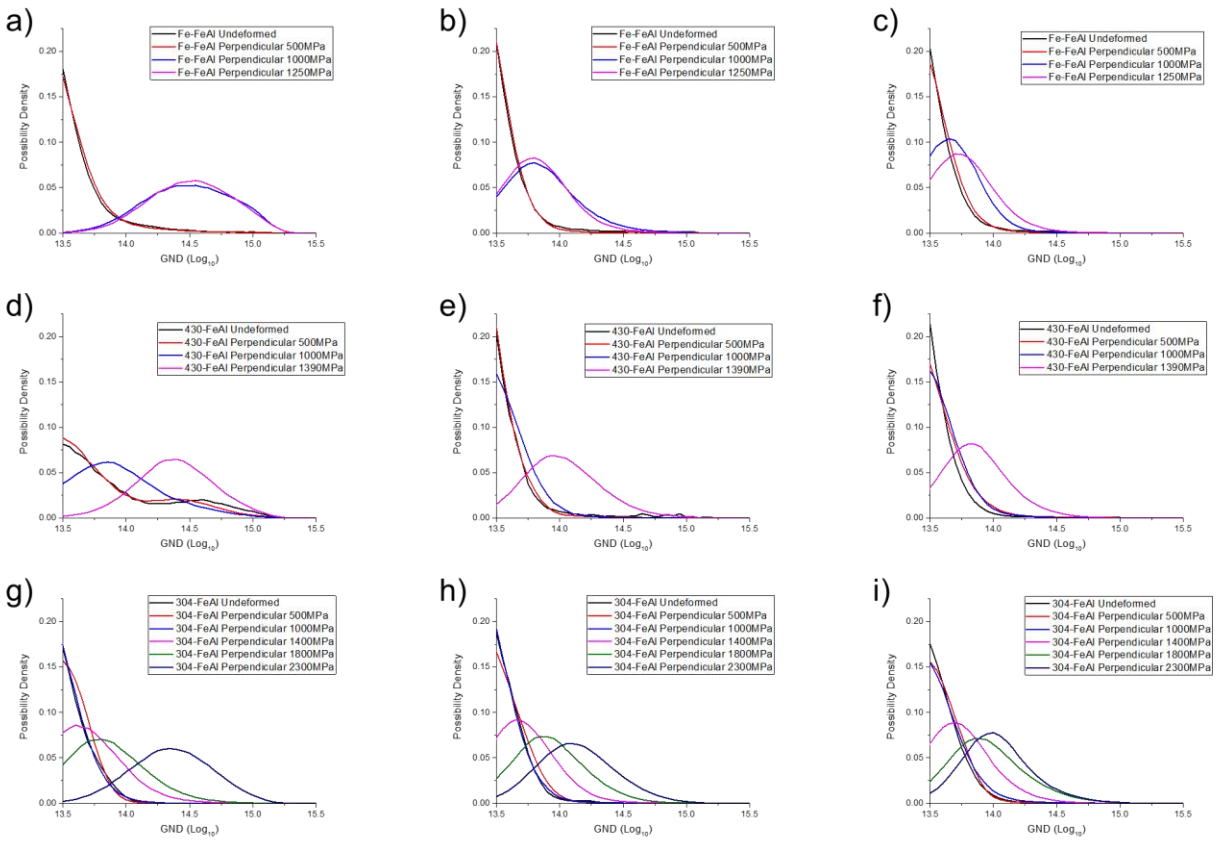

Figure 3.D13: GND distribution curve of MIL composites during the incremental compression test in perpendicular direction: (a) Metal layer in Fe-FeAl-MIL, (b) transition layer in Fe-FeAl-MIL, (c) FeAl layer in Fe-FeAl-MIL; (d) metal layer in 430SS-FeAl-MIL, (e) transition layer in 430SS-FeAl-MIL, (f) FeAl layer in 430SS-FeAl-MIL; (g) metal layer in 304SS-FeAl-MIL, (h) transition layer in 304SS-FeAl-MIL, (i) FeAl layer in 304SS-FeAl-MIL.

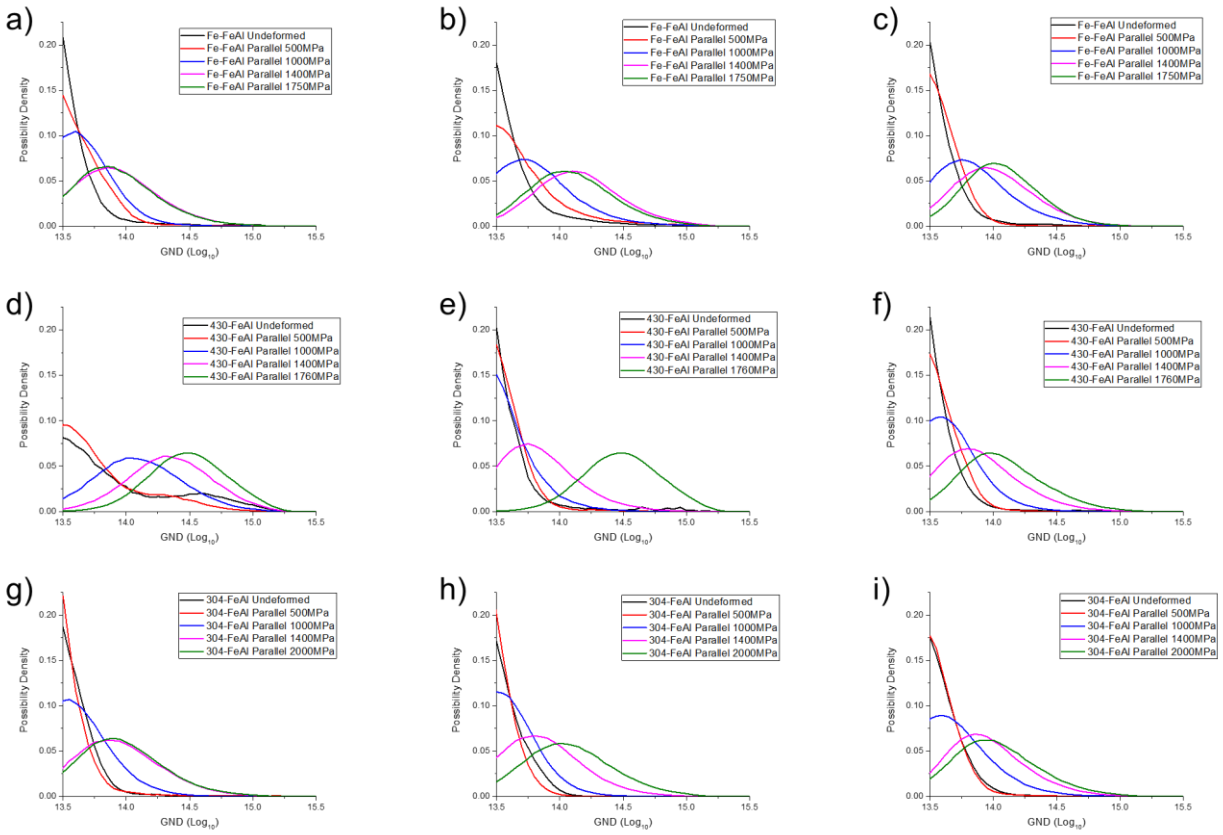

Figure 3.D14: GND distribution curve of MIL composites during the incremental compression test in parallel direction: (a) Metal layer in Fe-FeAl-MIL, (b) transition layer in Fe-FeAl-MIL, (c) FeAl layer in Fe-FeAl-MIL; (d) metal layer in 430SS-FeAl-MIL, (e) transition layer in 430SS-FeAl-MIL, (f) FeAl layer in 430SS-FeAl-MIL; (g) metal layer in 304SS-FeAl-MIL, (h) transition layer in 304SS-FeAl-MIL, (i) FeAl layer in 304SS-FeAl-MIL.

Acknowledgment

Chapter 3, in full, is the reprint of the published article in Acta Materialia, Elsevier: Wang, Haoren; Zhu, Chaoyi; Vecchio, Kenneth S. Deformation and Fracture Evolution of FeAl-based Metallic-Intermetallic Laminate (MIL) Composites. Acta Materialia (2020).

I would like to thank Chaoyi Zhu, and my principal investigator Professor Kenneth Vecchio, for their contribution in this work.

Chapter 4 Mesoscale HDI Stress in FeAl-Based MIL Composites

Chapter 4, in full, is the reprint of the published article in Acta Materialia, Elsevier: Wang, Haoren; Kou, Rui; Yi, Haozhe; Figueroa, Samuel; Vecchio, Kenneth S. Mesoscale Hetero-Deformation Induced (HDI) Stress in FeAl-Based Metallic-Intermetallic Laminate (MIL) Composites. Acta Materialia (2021).

Abstract

Single-phase intermetallic FeAl layered material is synthesized using a layered foil approach to study the fracture mechanisms of FeAl-based metallic-intermetallic laminate (MIL) composites containing a similarly fabricated structure. The mechanical properties and crack evolution of the single-phase FeAl are investigated via incremental compression testing. Microstructure and composition assessment confirm a similar intermetallic layer laminate microstructure of single-phase FeAl and FeAl-based MIL composites. When compressed perpendicular to the layers, both materials fail by the axial splitting of the FeAl phase along the loading direction. Mesoscale hetero-deformation induced (HDI) stress, which is tensile on the FeAl layers of MIL composites, accelerates crack nucleation and crack propagation, eventually inducing failure. The HDI stress evaluated via finite element analysis (FEA) simulation provides an explanation for the difference between 430SS-FeAl and 304SS-FeAl MIL composites, which possess similar microstructure and composition, but very different strengths. When compressed parallel to the layers, mesoscale HDI stress is expected to be negligible, whereas the geometrically necessary dislocation (GND) pile-up induced HDI stress can enhance the performance of the

composites. Fracture toughness is characterized via four-point bend testing, and the results demonstrate improvement of the FeAl-based MIL composites over the single-phase FeAl material.

4.1 Introduction

Metal-intermetallic laminate (MIL) composites are heterostructured materials that consist of alternating-layered, often brittle intermetallics and ductile metals for optimizing mechanical properties. Aluminide-intermetallics typically possess low-symmetric crystalline structures, which induce high strength, but limited plasticity and toughness. Toughness can be promoted by reinforcing the aluminides with particles, fibers or layers of ductile metals [1], so that the composites are more efficient for structural applications.

Predecessors of MIL composites were first produced in 1989 using solid-state combustion wave method [3], but the self-sustaining reaction kinetics limit the control of microstructure. In 2001, *Harach* and *Vecchio* firstly utilized the "moderated-reactive sintering" concept to synthesize MIL composites in the Ti-Al system [4]. During the reactive sintering, interdiffusion drives the formation of intermetallics between alternating stacked dissimilar metal foils. By adjusting the initial foils, the properties of MIL composites can be tailored to fulfill various performance requirements. Therefore, MIL composites are ideal for structural applications such as aerospace vehicles, which requires lightweight, high stiffness materials without compromising the performance. Furthermore, MIL composites with complex geometry, such as the pathways for sensors [2], can be synthesized by pre-machining the initial foils.

Previous studies on MIL composites mostly focus on the Ti-Al system for investigating the fracture mechanisms [5–10] and optimizing the performance [11–13]. However, restricted by

the growth kinetics, Al_3Ti is the only intermetallic phase formed, which possesses little ductility and limits the ability to tune the properties of the composites. The focus was then turned to the Ni-Al system [14–16] and Fe-Al system [17–19], seeking for ductile intermetallics like the FeAl phase [21–23].

In our previous work, FeAl-based MIL composites were synthesized, where the metal layers were switched among pure iron, 430 stainless steel (430SS) and 304 stainless steel (304SS) by adopting an innovative foil stack configuration [77]. Although all the FeAl-based MIL composites possess a very similar microstructure and fail under similar mechanisms, the difference in strength is far beyond any rule of mixture. By tracking the fracture evolution, the variation of thin transition layers between the metal and intermetallic layers appeared to alter the internal stress distribution, and affect the performance of the entire composite [85].

As the metallic layered materials are attracting increased attention for the high strength and other properties [86–88], the analysis for deformation mechanisms will help to understand their unique combinations. Hetero-deformation induced (HDI) stress describes the internal stress in heterostructured materials during deformation [36]. The constituents in heterostructured materials possess dissimilar mechanical behaviors, which create the long-range internal stress, conventionally known as back stress and forward stress, that can potentially enhance mechanical properties. Recent studies by *Zhu* and *Wu* suggest "HDI stress" is a more accurate description of the interactions in the heterostructured materials during the plastic deformation [37]. Investigations of HDI stress mostly focus on the interface scale, where HDI stress is typically produced by geometrically necessary dislocations (GND) [36–39].

In the present study, single-phase layered FeAl material is synthesized following the same processing as FeAl-based MIL composites from our previous studies [77,85,89]. The mechanical

properties measured here for this unique microstructured single-phase FeAl are used in subsequent finite element analysis (FEA) modeling to assess the properties of the FeAl-based MIL composites fabricated with similar FeAl layers. Comparisons between these MIL composites and single-phase FeAl material indicate that the HDI stress occurs at the scale of the layers, which are on the order of 100s of microns. These HDI stresses resulting from these mesoscale microstructure features have not been previously reported. Estimation of HDI stress via simulation coincides with the experimental observations, which suggests the mesoscale HDI stress is crucial, but has a negative strength effect in these MIL composites. In addition, fracture toughness of both materials, single-phase FeAl and FeAl-based MIL composites is measured to evaluate the enhancement of MIL composites over the single-phase FeAl, in terms of toughness.

4.2 Experimental

4.2.1 Material Processing

Foils of commercially pure aluminum (Goodfellow Cambridge Limited, 99.5%), pure iron (Goodfellow Cambridge Limited, 99.5%) and 304SS (Trinity Brand Industries, 18 wt% Cr and 8 wt% Ni) were the feedstocks for fabricating MIL composites and single-phase FeAl samples. In addition, 430SS (Trinity Brand Industries, 18 wt% Cr) foils were also taken in our previous work [77,85,89] for producing 430SS-FeAl MIL composites. More detailed composition analysis for the metal foils is listed in Appendix 4.K. The foils were cut into 40-mm-diameter disks, abraded with steel wool pads, and then rinsed in acetone for ultrasonic cleaning. As demonstrated in Figure 4.1(a), 75-mm-thick Fe foils and 100-mm-thick Al foils were alternating stacked to produce single-phase FeAl samples. At the top and bottom of the Fe-Al deck, a layer of 50-mm-thick 304SS foil was added as a diffusion barrier against Mo in the Spark Plasma Sintering (SPS) setup. Meanwhile, for FeAl-based MIL composites, the combination of 75-mm-Fe and 100-mm-Al was also adopted

to produce FeAl layers. The details about the foil stack configuration of MIL composites have been discussed in our previous works [77,85,89], and Appendix 4.A also provides an illustration.

The foil stack was wrapped using molybdenum foil (0.025-mm-thick) and graphite foil to protect the sample and graphite SPS tooling from contaminating each other. The sample-tooling assembly was loaded into a Thermal Technology GTAT 10-3 Spark Plasma Sintering unit, (a.k.a. field-assisted sintering) for reactive sintering, where the sample would be heated up by Joule heating effect [78]. Both MIL composite and single-phase FeAl samples were sintered following the profile plotted in Figure 4.1(b). At stage one, pure Al foils will completely transform into Fe_2Al_5 aluminide phase [77]. Subsequently, the temperature will be raised to 1050^{o}C to transform Fe_2Al_5 into single-phase FeAl. The annealing temperature used here is slightly higher than our previous studies for FeAl-based MIL composites (1000^{o}C) [77,85,89], due to the sample size being increased from 20-mm-diameter to 40-mm-diameter, which requires new SPS tooling and alters the temperature distribution. As the consequence, the target temperature has been tuned, so that the actual sample temperature, which strongly affects the samples' microstructure and composition distribution is preserved here to closely match our previous studies [77,85,89].

4.2.2 Characterization

The samples were mounted perpendicular to the layers for cross-section, then ground and polished following standard metallographic preparation procedures. After sintering, the top and bottom of the samples were ground to remove attached graphite and molybdenum foils. Samples of single-phase FeAl samples were further ground by at least 300mm to remove 304SS and the chemical gradient regions. The microstructure and composition were examined using Thermo-Fisher (formerly FEI) Apreo scanning electron microscope (SEM) equipped with an Oxford

Instrument's Symmetry Electron Backscatter Diffraction (EBSD) system and an Oxford Instrument's Energy-Dispersive X-ray Spectrometer (EDS)

Following the removal of unwanted surface layers described above, some samples were cut into 6 mm cubes for compression tests following standard ASTM E9. Meanwhile, other samples were cut into 6 mm x 3 mm x sample diameter strips, and notched for four-point bending test following standard ASTM E399.

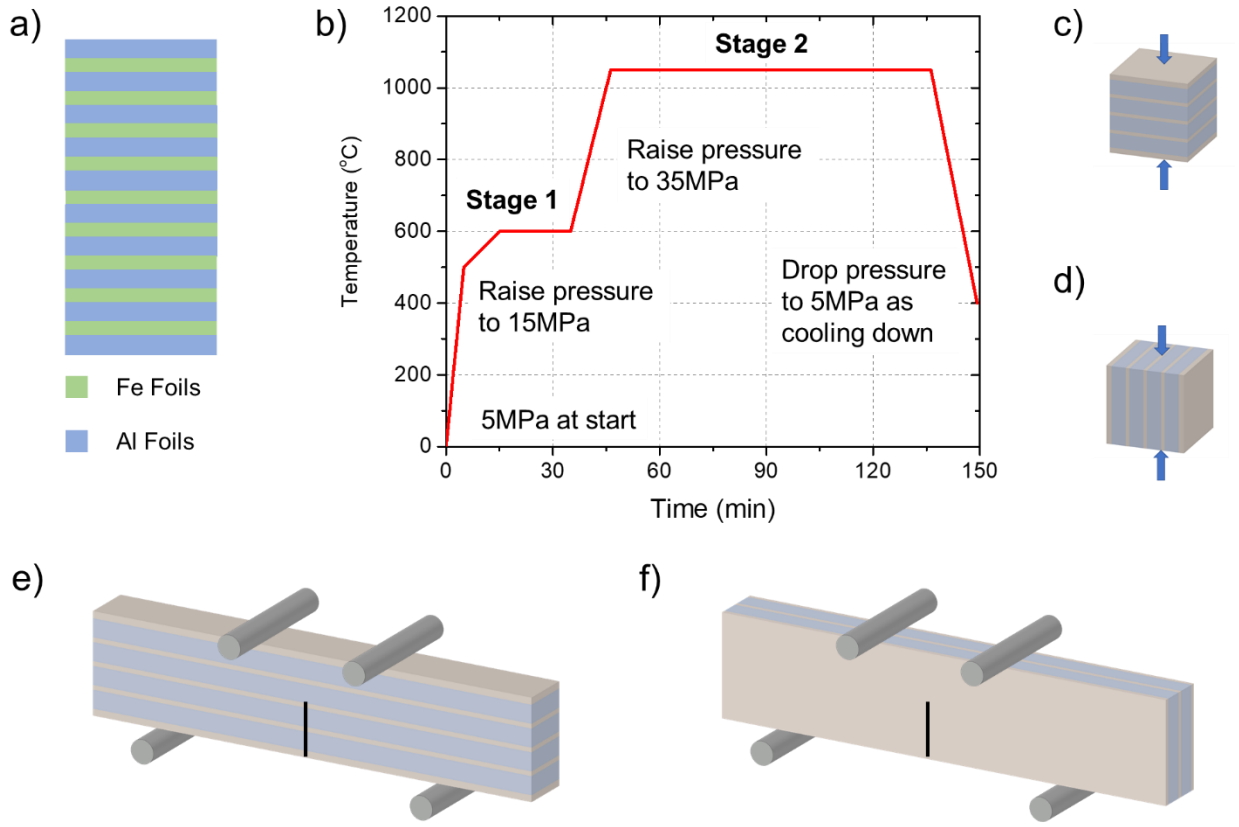

Fig 1: (a) The metal foil stack configuration and (b) SPS profile for synthesizing single-phase laminate FeAl material. (c) and (d) are the perpendicular and parallel loading directions for the compression test, respectively [77,85]. (e) and (f) are the perpendicular and parallel loading directions for the four-point bending test, respectively.

The quasi-static compression tests were conducted using conventional screw-driven or servo-hydraulic load frames at a strain rate of 10^{-3}/s. Strain gauges were applied to the specimens

to measure the elastic response and early yielding behavior, and specimens were lubricated using grease to minimize friction. Strain during the test is monitored using both strain gauge readings and displacement of the load frame crosshead, and corrected by measuring the deformation of the specimen after the test. Single-phase FeAl specimens failed at a single peak load condition, whereas the failure point of the MIL specimens was determined as the maximum load before undergoing a significant drop (>10%). In addition, as demonstrated in Figure 4.1(c) and 4.1(d), specimens were loaded either perpendicular or parallel to the layers, and hereafter referred as the 'perpendicular direction' and 'parallel direction'.

The four-point bending tests were also conducted using conventional screw-driven load frame. The support span was 16 mm, and the load span was 8 mm. The strain rate for loading was 10^{-3} /s, and the specimens were notched to between 0.45 and 0.55 of the sample height. Fracture toughness K_{1C} is calculated using [12,90]:

$$K_{1C} = \frac{3PL}{BW^2}\sqrt{\pi a}\cdot f\left(\frac{a}{w}\right) \quad (1)$$

$$f\left(\frac{a}{w}\right) = \left[1.122 - 1.121\left(\frac{a}{w}\right) + 3.74\left(\frac{a}{w}\right)^2 + 3.873\left(\frac{a}{w}\right)^3 - 19.05\left(\frac{a}{w}\right)^4 + 22.55\left(\frac{a}{w}\right)^5\right] \quad (2)$$

where P is the critical load, L is half of the difference between load span and support span, B is the thickness of the specimen, W is the height of specimen, a is the notch length. In addition, as demonstrated in Figure 4.1(e) and 4.1(f), specimens were loaded either perpendicular or parallel to the layers. Furthermore, to ensure that specimens for both directions possess similar dimensions, the thickness of the samples was adjusted by changing the number of initial foil layers. For example, 45 layers of 100-mm-thick Al foils and 44 layers of 75-mm-thick Fe foils will produce a 6-mm-thick FeAl sample, whereas 23 layers of 100- mm-thick Al foils and 22 layers of 75- mm-thick Fe foils will produce a 3-mm-thick FeAl sample

4.2.3 Simulation

FEA simulation using COMSOL software was carried out to quantitatively analyze the HDI stress in MIL composites, which is believed to induce very different failure strengths for Fe-FeAl, 430SS-FeAl and 304SS-FeAl composites [85]. The geometry and materials models for the simulation are explained in Appendix 4.F. For simplification, the FEA simulation is 2D, because the two orthogonal in-plane directions are symmetric for MIL composites. And linear elasticity and linear plasticity were assumed for all the materials. The yield point and the work hardening rate are listed in Table 4.1.

Table 4.1: Material properties for FEA simulation

	Metal Layer	Transition Layer	FeAl Layer
Young's Modulus	200 GPa	200 GPa	200 GPa
Yield Strength	200 MPa	300 - 900 MPa	1000 MPa
Work Hardening Rate	1 GPa	3 - 8 GPa	10 GPa

Values for the 304SS metal layers were taken from the literature [91]. Meanwhile, values for FeAl layers were measured by the compression test of single-phase FeAl specimens. The transition layer, which is the chemical gradient region from metal to FeAl, was assumed to be a uniform layer to reduce the complexity. Indicated by both nanoindentation and microhardness measurement discussed in Appendix 4.C, the strength of transition layers is between metal layers and FeAl layers [77]. Therefore, a parallel study was carried out, with the average yield strength of the transition layers varied from 300 MPa to 900 MPa, in 100 MPa steps, and the average work hardening rate was varied from 3 GPa to 8 GPa with 1 GPa intervals. Meanwhile, the properties of the metal and FeAl layers are the same among all the simulations, as the values are listed in

Table 4.1. The combination of low yield strength and low work hardening rate constitute a relatively soft transition layer, which represents the scenario of the 430SS-FeAl MIL composites. In contrast, the 304SS-FeAl MIL composites possess relatively strong transition layers, which is the major difference between 430SS-FeAl and 304SS-FeAl MIL composites, and this difference results in an increase in the compressive strength of 304SS-FeAl MIL composites by 1 GPa over the 430SS-FeAl MIL composites [85].

4.3 Results

Shown in Figure 4.2(a) is the microstructure of a FeAl sample, where the black regions on the left and right edges are the mounting material. In addition, the EDS line scan across the area is plotted in Figure 4.2(b), and the surface layers on the top and bottom, which were removed via grinding, are discussed in Appendix 4.G. The cross-section is 6~7 mm into the sample, which is sufficiently far from the edge region to represent the single-phase layered FeAl material. The sample process a relatively uniform microstructure and chemical composition across the thickness. EDS measurements confirm that the average composition is 47~48 at% Al, which is consistent with the ratio of the initial Fe/Al foils (~48 at% Al). Furthermore, as indicated by the arrow, the faint vertical lines in the image are identified as “centerlines”, similar to the microstructure formed in MIL composites [77], and their presence denotes the interface between intermetallic layers. During stage one of the reactive sintering, impurities in the metal foils are pushed towards the aluminum side. After all the aluminum is converted to intermetallic, the impurities accumulate at the former center of the aluminum foil, (i.e., the “centerline”).

Shown in Figure 4.2(c) is the EBSD band contrast map of a FeAl sample to reveal the grain morphology. FeAl grains form an ordered laminate structure, with very similar grain structure in each layer. The texture of the FeAl phase is plotted in Figure 4.2(d), whereas the corresponding

EBSD scan is presented in Appendix 4.G. According to the times random number color code, the samples exhibits medium-strong <111> texture along the diffusion/growth direction, which is perpendicular to the layers. Along the other two orthogonal directions, the texture is inherently symmetric and relatively week. Both microstructure and texture of the single-phase layered FeAl material are very similar to the FeAl layers in the FeAl-based MIL composites [77,85], as they were both synthesized from the same metal foils using the same sintering parameters.

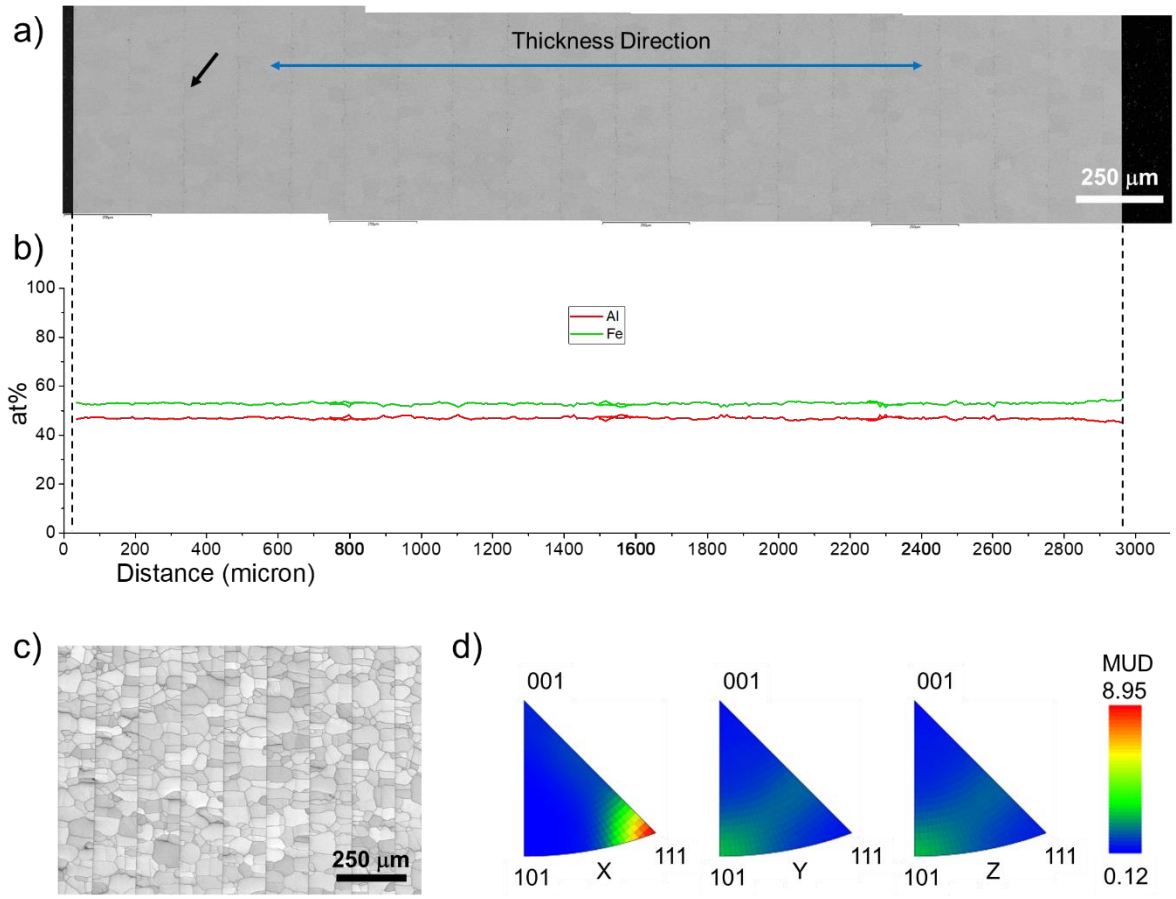

Figure 4.2: Characterization of single-phase laminate FeAl material: (a) SEM image and (b) EDS line scan across the thickness; (c) EBSD band contrast map presents the laminate microstructure; (d) inverse pole figures examine the texture. Black array in (a) indicates a "centerline".

The quasi-static stress-strain curves for the FeAl specimens, which were compressed perpendicular and parallel to the layers, are plotted in Figure 4.3(a) and 4.3(b), respectively; both specimens were loaded to 2.4 GPa to investigate fracture evolution. Figure 4.3(c) shows the

deformed structure of the specimen loaded to 2.4 GPa perpendicular to the layers, where few cracks formed on the surface. In contrast, as shown in Figure 4.3(g), the density of cracks is significantly higher when the specimen was loaded to 2.4 GPa parallel to the layers. Most cracks occurred as delaminations along the centerlines, an intuitive phenomenon since impurities accumulate at the centerlines. The images of the entire sample surface are presented in Appendix 4.B.

Figure 4.3(d) shows the microstructure of the undeformed FeAl specimen, and Figure 4.3(h) is the corresponding GND density map. Since GND density is calculated based on the change of grain orientation, the green lines in Figure 4.3(h) are induced by grain boundaries, rather than the actual GND. Note the grain boundaries identified by the green lines in Figure 4.3(h) correspond to dark boundaries in Figure 4.3(d) and appear dark due to surface relief (i.e. they are not cracks). Figure 4.3(e) and 4.3(f) are the microstructure of the specimens after loading to 2.4 GPa in perpendicular and parallel directions, respectively. By comparing the thickness of layers, the global plasticity shown in Figure 4.3(a) and Figure 4.3(b) is real plasticity, rather than simply the accumulation of cracks, which could generate some 'apparent' plasticity during the compression test for some brittle materials [89]. Furthermore, the GND density maps of Figure 4.3(i) and 4.3(j) also reveal the plasticity of the FeAl material.

Table 4.2 summarizes the mechanical properties of the single phase FeAl samples, which are measured from the stress-strain curves. When loaded parallel to the layers, the ultimate strength of the layered, single-phase FeAl can reach 2.7 GPa, even higher than a study on nanocrystalline FeAl [92]. Furthermore, when loaded perpendicular to the layers, the FeAl specimen exhibits an extraordinary ultimate strength of 3.5 GPa. In both loading cases, when the

FeAl samples fail, they shatter into small pieces. On the other hand, the FeAl-based MIL composites fail in a more gradual manner, and the specimens retain their structural integrity [77].

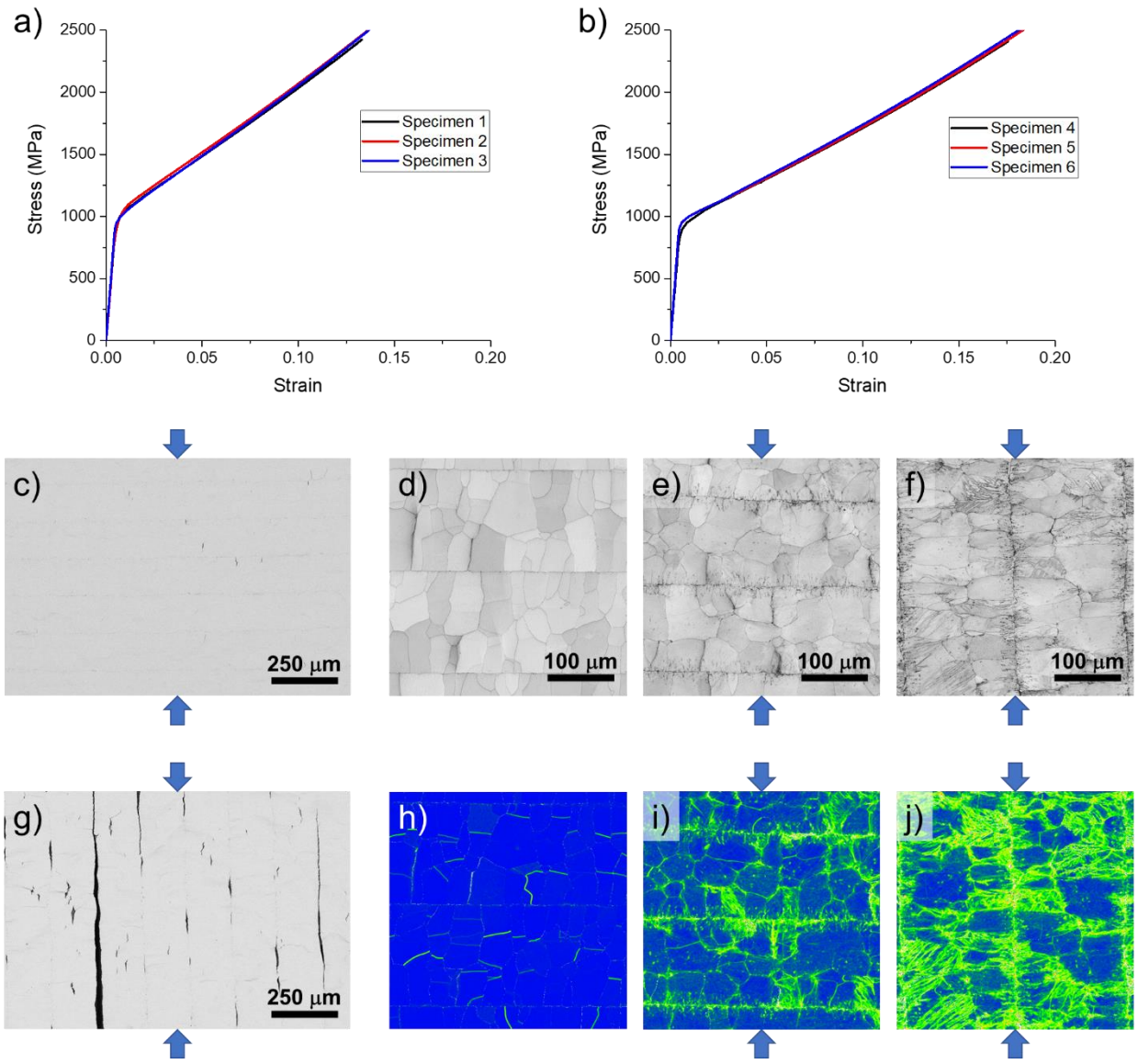

Figure 4.3: (a) and (b) are Strain-Stress curves of single-phase laminate FeAl material compressed to 2.4~2.5 GPa in perpendicular and parallel directions, respectively. (c) and (g) are surface morphology of the specimen in (a) and (b), respectively. EBSD band contrast maps of FeAl specimens after compression test: (d) undeformed, (e) compressed to 2.4 GPa in the perpendicular direction and (f) compressed to 2.4 GPa in the parallel direction; (h), (i) and (j) are corresponding GND density maps.

Appendix 4.B also presents a specimen loaded in the perpendicular direction at 3.3 GPa with 20% deformation. The major crack almost propagates through the entire thickness of the specimen, which must penetrate across each centerline. The centerlines can deflect crack growth and induce stress redistribution [5], so the layered FeAl material exhibits higher strength in the perpendicular loading direction over the parallel direction. The major crack occurs parallel to the loading direction, suggesting the axial splitting of FeAl grains, which is common for brittle materials due to local stress concentration induced tensile stresses [96–102]. Furthermore, although the single-phase FeAl exhibits considerable ductility, the fracture mostly occurs as intergranular cracks [77,85], another common phenomenon in brittle materials.

Table 4.2: Mechanical properties of layered single phase FeAl

	Layered Single Phase FeAl		Literature Values
	Perpendicular	Parallel	
Young's Modulus	200 ± 20 GPa	210 ± 10 GPa	180 [23,93] ~260 [94] GPa
Yield Strength	980 ± 10 MPa	950 ± 30 MPa	750~1250 MPa [22,95]
Ultimate Strength	3.5 ± 0.1 GPa	2.6 ± 0.1 GPa	2.4 GPa [92]
Work Hardening Rate	10 ± 0.4 GPa	7 ± 0.1 GPa	6~12 GPa [22,95]

4.4 Discussion

The results on the single-phase FeAl material were presented for two reasons. First, this is the first time, to the authors' knowledge, FeAl has been produced via this foil reactive sintering method, and this form of FeAl exhibits truly unique mechanical properties, significantly higher than any previously published data on FeAl. Second, the property data measured from the single-phase FeAl material is used for the mechanical properties of the FeAl layers in the FeAl-based

MIL composites, which are the subject of the FEA study to be presented next. The goal of the FEA study is to explain the rather different mechanical properties exhibited by FeAl-based MIL composites previously published [77,85], which were fabricated using pure Fe, 430SS, or 304SS, separately as the metal constituent of the MIL composites. Figure 4.4 presents the microstructure and chemical composition analysis for Fe-FeAl, 430SS-FeAl and 304SS-FeAl MIL composites. The SEM images and EDS line scans examine the region spanning from one remnant metal layer to another, which can represent the entire sample. The details have been discussed in our previous work [77]. The microstructure of these three different MIL composites appear very similar in terms of phase fractions, composition and structure of the FeAl layers. The only difference is the properties of the remnant Fe-based metal layers (which are actually quite similar), as well as the composition and mechanical properties of the rather narrow transition layers that form by diffusion between the metal layers and the near equiatomic FeAl layers. Evaluating the influence of these transition layers, via FEA modeling, on the mechanical response of the FeAl-based MIL composites, is the focus of the remaining section.

Intuitively, when the specimens are compressed perpendicular to the layers, all the layers in MIL composites are under the same level of external stress (the normal stress along the loading direction). In addition, the path of fracture evolution suggests that the failure of the FeAl-based MIL composites is induced by the cracks formed and propagated in FeAl layers [85]. Therefore, all the FeAl-based MIL composites are expected to fail at a similar stress level as the single-phase laminate FeAl material. Furthermore, in our study of FeAl-$FeAl_2$ eutectoid MIL composites, specimens indeed fail at a similar stress level, regardless of metal layer material or the metal to intermetallic ratio [89].

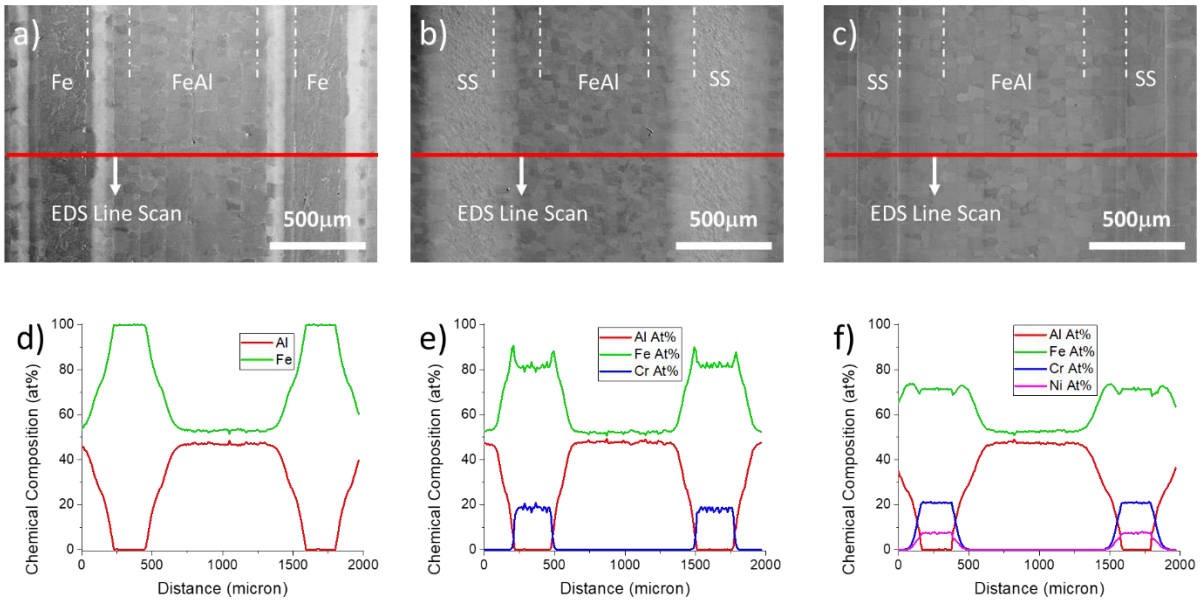

Figure 4.4: SEM images for (a) Fe-FeAl, (b) 430SS-FeAl, and (c) 304SS-FeAl. (d), (e) and (f) are EDS line scans along the red line notated in (a), (b) and (c), respectively. [77]

However, among the various FeAl-based MIL composites, 304SS-FeAl can reach an ultimate strength of 2.3 GPa, whereas 430SS-FeAl fails at 1.4 GPa, and none of the FeAl-based MIL composites can achieve the stress level of the single-phase layered FeAl. Furthermore, as presented in Appendix 4.C, multiple macro-cracks formed at each FeAl layer in the MIL composites, whereas the single-phase FeAl material only has one macro-crack. The dissimilar stress-strain response of metal layers, transition layers and FeAl layers would induce internal stresses [85], now classified as an HDI stress. For FeAl-based MIL composites, the HDI stresses are primarily the normal stresses along the in-plane directions. The mesoscale HDI stress, formed and evolving in the MIL composites is tensile within the FeAl layers, and has a negative limiting effect on the strength of the MIL composites.

Except for the HDI stress, other factors, including anisotropy, residual thermal stress and difference in Poisson's ratios, may also contribute to the fracture evolution in the FeAl-based MIL composites. On the other hand, although the inverse pole figures suggest medium to strong texture

of FeAl layers, the compression tests for single phase FeAl samples exhibit little difference between perpendicular and parallel orientations below 2 GPa, which indicates relatively weak anisotropy effects. Meanwhile, Appendix 4.H contains an investigation of the residual thermal stress in FeAl-based MIL composites, which would be overwhelmed by the HDI stress at high loading level. Furthermore, measured via the ultrasonic wave velocity method using Panametrics 5072 PR and 5077 PR transducers, the Poisson's ratio of the layered FeAl is around 0.33 in both perpendicular and parallel orientation, very close to metals (typically 0.3 to 0.33).

4.4.1 Compression Perpendicular to the Layers

When the FeAl-based MIL composites are compressed perpendicular to the layers, the path of fracture evolution reveals that cracks only occur in the FeAl region after the apparent yield point, and delamination never happens at the metal layer / transition layer interface or transition layer/FeAl layer interface [85]. Consequently, the in-plane strain on both sides of the interface should be equal.

Meanwhile, the constitutes of the MIL composites possess dissimilar stress-strain responses. When loaded perpendicular to the layers, all the layers are under the same external stress level (the normal stress along the loading direction). At the same stress level, especially after the yield point, the deformation of the individual metals would be considerably larger than the individual FeAl layers. However, the in-plane deformation of both sides of the interface should be equal to avoid delamination. This constrain leads to mesoscale in-plane internal stress (normal stress orthogonal to the loading direction), which is a compressive stress to limit the compression-induced orthogonal expansion of the metal layers, and in turn a tensile stress to the FeAl layers.

Since this type of internal stress is induced by heterogeneous deformation of different layers in the laminate composites, it is classified as an HDI stress.

Appendix 4.D demonstrates the analytical derivation of the mesoscale HDI stress, and FEA simulations were carried out to numerically estimate the HDI stress in 304SS-FeAl and 430SS-FeAl MIL composites. 304SS and 430SS are known to possess similar strength (~200MPa yield strength and ~500MPa ultimate strength), and the nanoindentation measurements shown in Appendix 4.C confirm the similarity in their hardness [85]. Meanwhile, FeAl layers in 304SS-FeAl and 430SS-FeAl MIL composites are very similar in microstructure and composition [77,85], because they were sintered from the same metal foils using the same sintering parameters. The major difference between 304SS-FeAl and 430SS-FeAl Mil composites is the transition layers, the chemical gradient region from 304SS or 430SS to FeAl. As indicated by the nanoindentation measurements, the transition layers in 304SS-FeAl MIL composites are significantly stronger than in the 430SS-FeAl MIL composites. Although the volume fraction of the transition layer is less than 15% in these MIL composites, the stronger transition layers of 304SS-FeAl are linked to the improvement in the strength by as much as 1 GPa [85].

Figure 4.5(a) and 4.5(d) present the simulation of the stress in the loading direction, the external stress (σ_{YY}), for MIL composites with soft and hard transition layers to represent 430SS-FeAl and 304SS-FeAl MIL composites, respectively. The model specimen with soft transition layers (300 MPa yield strength, 3 GPa work hardening rate) is referred to as the "soft specimen" hereafter, and the one with hard transition layers (900 MPa yield strength, 8 GPa work hardening rate) is referred to as the "hard specimen". Both specimens exhibit similar external stress distribution, because they are both compressed to 1.4 GPa, when the 430SS-FeAl MIL composite fails, whereas the 304SS-FeAl MIL composite is still crack-free. By definition, negative stress

represents compression and positive stress represents tension. At the loading level of 1.4 GPa, the plastic strain of 430SS-FeAl is 0.11 with macroscale cracks, whereas the plastic strain of 304SS-FeAl is 0.06 and the specimen is crack-free [85]. As a validation, the simulated strain of the soft specimen is 0.085, whereas the strain of the hard specimen is 0.057, which are very close to the experimental values and support the accuracy of the simulation.

Figure 4.5(b) and 4.4(e) present the HDI stress (σ_{XX}) distribution of the soft and hard specimens, respectively. Except for the edge effect, HDI stress distributes uniformly among each layer, rather than concentrating near the interfaces. Consequently, the HDI stress in MIL composites would be a mesoscale internal stress. Meanwhile, Figure 4.5(c) and 4.5(f) present the shear stress (σ_{XY}) distribution, which is relatively small compared to the normal stresses (σ_{XX} and σ_{YY}). In addition, the edge effect, which is critical for metal-ceramic composites [103], is believed to be insignificant for MIL composites, because no difference was found between the bulk and the edge regions in the failed specimens [85,89].

Figure 4.5(g) and 4.5(h) examine the external, HDI and shear stresses across the thickness of the soft and hard specimens, respectively. The external stress is uniform across different layers, as the specimens are under uniaxial loading. The HDI stress on metal layers in both soft and hard specimens is at a similar level, whereas the HDI stress in the FeAl layers varies near 100%, from 480 MPa in the hard specimen to 910 MPa in the soft specimen. Furthermore, the HDI stress curves numerically explain the role of the transition layers: hard transition layers can relieve the HDI tensile stress on FeAl layers, whereas soft transition layers increase these stresses. In addition, as discussed in Appendix 4.J, a more time-consuming 3D FEA simulation predicts slightly lower (15% lower on average) HDI tensile stress on FeAl layers. On the other hand, the magnitude and the tendency stay the same, and would not affect the conclusions about the mesoscale HDI stress.

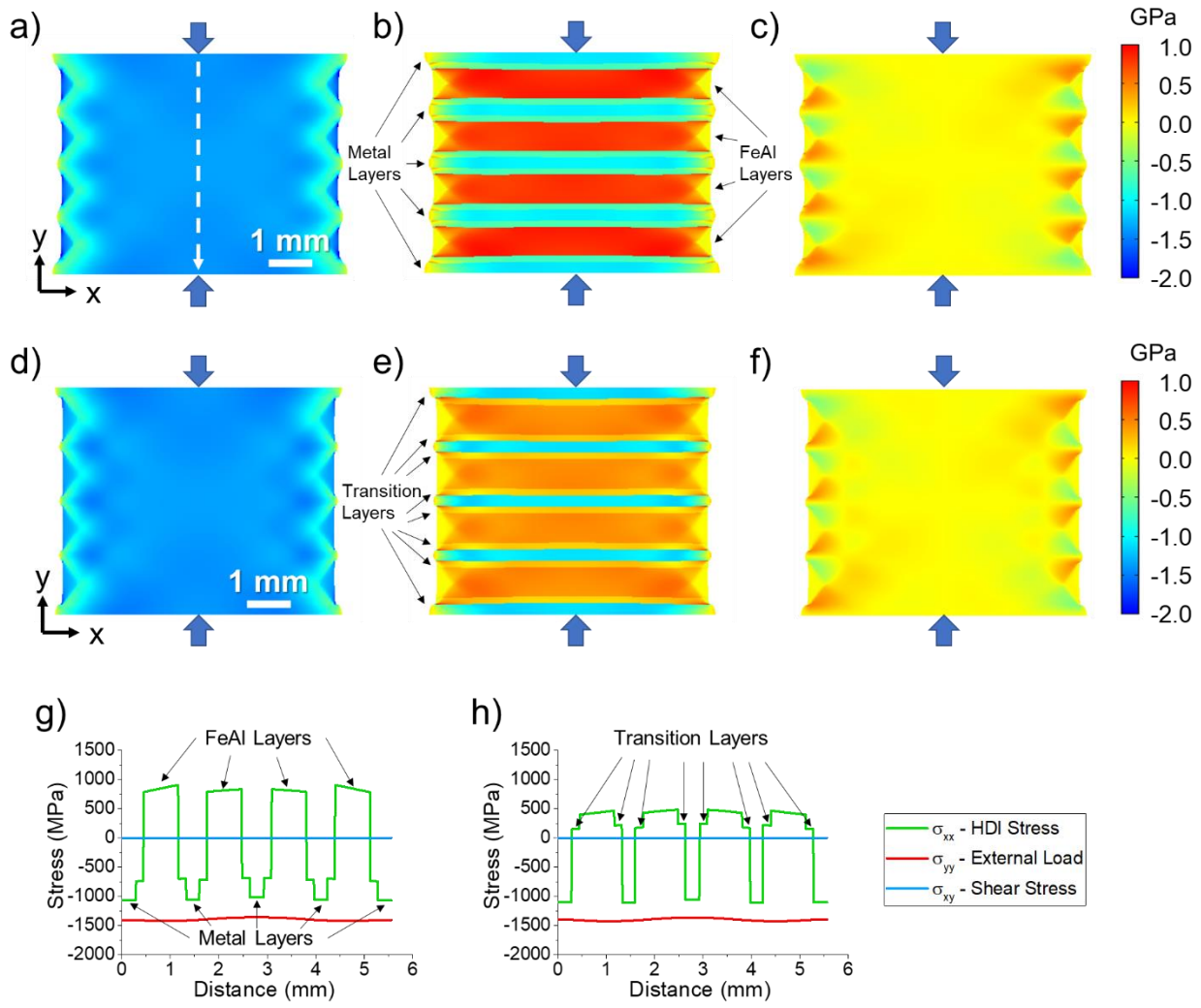

Figure 4.5: (a) External stress distribution (σ_{YY}), (b) HDI stress distribution (σ_{XX}), (c) shear stress distribution (σ_{XY}), and (g) stresses across the thickness of a MIL composite that possesses soft transition layers and is compressed to 1.4 GPa in the perpendicular direction. (d) External stress distribution (σ_{YY}), (e) HDI stress distribution (σ_{XX}), (f) shear stress distribution (σ_{XY}), and (h) stresses across the thickness of a MIL composite that possesses hard transition layers and is compressed to 1.4 GPa in the perpendicular direction.

Figure 4.6(a) shows the variation of HDI stress on FeAl layers by changing the properties of the transition layers. The innermost and outmost corners represent the soft and hard specimens, respectively. Increasing either yield strength or work hardening rate can relieve the HDI tensile stress acting on the FeAl layers, because the difference in stress-strain responses between transition layers and FeAl layers is reduced. For the soft transition layers, the HDI stress is compressive; for

the strong transition layers, the HDI stress is tensile. The amplitude of the change is large, but the value of the HDI stress in the transition layers is always between that of the metal layers and FeAl layers. Therefore, stronger transition layers can always benefit the intermetallic layers, which are typically the strongest and most brittle layers in MIL composites.

Similarly, Figure 4.6(b) shows the variation of HDI stress on FeAl layers by changing the properties of the metal layers. As a complementary study, the properties of the transition (900 MPa yield strength, 8 GPa work hardening rate) and FeAl (1000 MPa yield strength, 10 GPa work hardening rate) layers are the same among all the simulation. As the metal layers become stronger, the HDI stress on the FeAl layers decreases significantly. Since the mesoscale HDI stress arises from the difference in stress-strain responses of the different layers, stronger metal layers effectively reduce the difference, and consequently relieve the mesoscale HDI stress.

Figure 4.7(a), 7(b) and 4.7(c) plot the external, HDI and shear stresses distribution, when the soft specimen was compressed to 1 GPa. Similarly, Figure 4.7(d), 4.7(e) and 4.7(f) plot the external, HDI and shear stresses distribution, when the hard specimen was compressed to 1.8 GPa. When 430SS-FeAl was loaded to 1 GPa, or when 304SS-FeAl was loaded to 1.8 GPa, microcracks would appear in the samples [85]. Therefore, the corresponding loading levels could reflect the moment when cracks nucleate and begin to propagate in MIL composites.

External, HDI and shear stresses profiles across the thickness are plotted in Figure 4.7(g) for the soft specimen and Figure 4.7(h) for the hard specimen. Although the external load increases by 80%, the HDI stress on FeAl layers stays at a similar level, 620 MPa for the soft specimen and 650 MPa for the hard specimen. In addition, tensile tests suggest that FeAl materials can exhibit a little ductility in tension, and fail around 700 MPa [104]. Therefore, the development of cracks

in the FeAl regions, which occurs as axial splitting and eventually induces the failure of the entire specimen, is created by the HDI tensile stress acting on the FeAl layers.

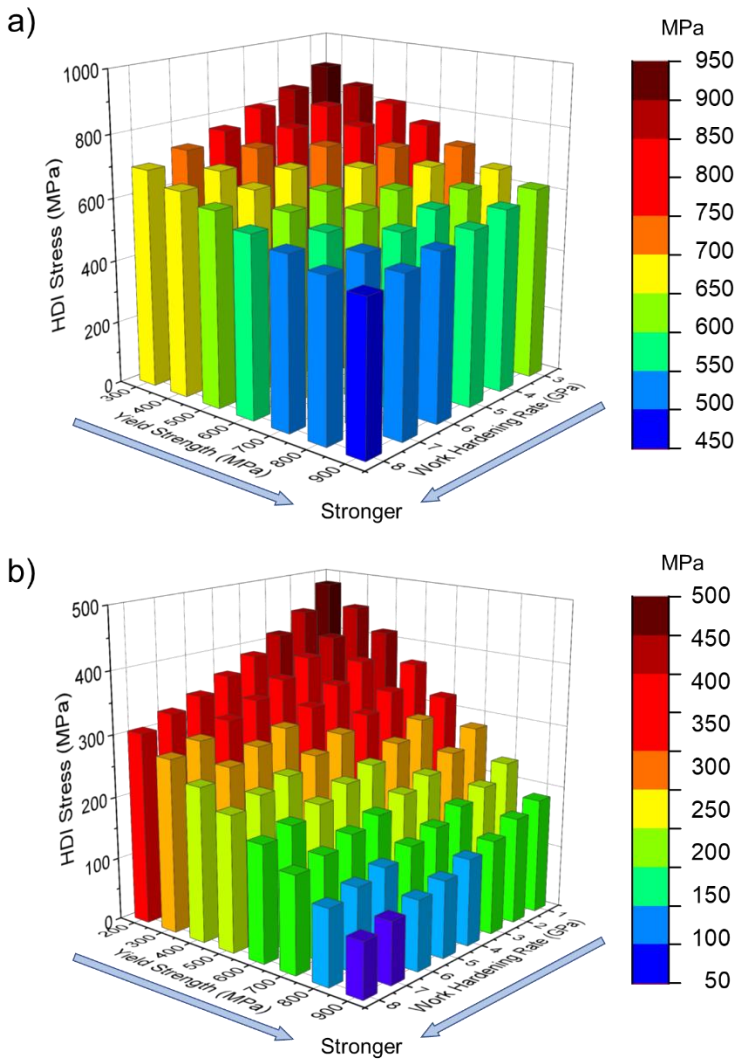

Figure 4.6: Variation of HDI stress on FeAl layers of MIL composites with (a) different transition layers and (b) different metal layers. All the samples are compressed to 1.4 GPa in the perpendicular direction.

4.4.2 Compression Parallel to the Layers

When the specimens were loaded parallel to the layers, Fe-FeAl, 430-FeAl and 304-FeAl exhibit similar compressive strength [85], which is 500 to 700 MPa lower than the single-phase

FeAl material. Meanwhile, by tracking crack evolution, the failure of both FeAl-based MIL composites and single-phase FeAl are induced by delamination that occurs along the centerlines and subsequent buckling.

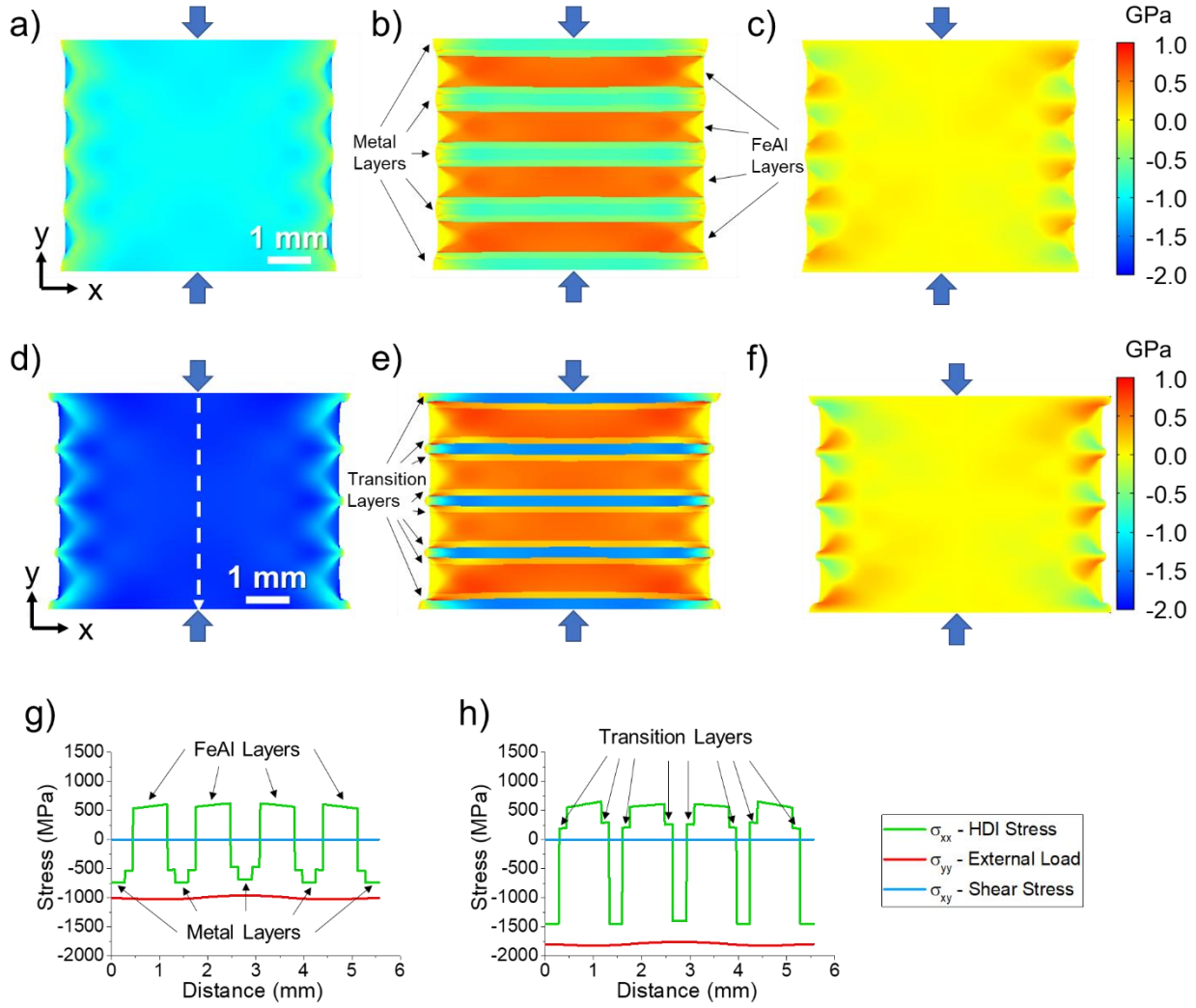

Figure 4.7: (a) External stress distribution (σ_{YY}), (b) HDI stress distribution (σ_{XX}), (c) shear stress distribution (σ_{XY}), and (g) stresses across the thickness of a MIL composite that possesses soft transition layers and is compressed to 1 GPa in the perpendicular direction. (d) External stress distribution (σ_{YY}), (e) HDI stress distribution (σ_{XX}), (f) shear stress distribution (σ_{XY}), and (h) stresses across the thickness of a MIL composite that possesses hard transition layers and is compressed to 1.8 GPa in the perpendicular direction.

Figure 4.8(a) and Figure 4.8(d) are the simulation of external stress distribution in the soft and hard specimens, respectively. Both specimens were compressed to 1.4 GPa as the average of

all the layers, the same stress level as the simulation in Figure 4.5. During the compression test, the external strain along the loading direction would always be the same among all the layers. So the external load would be shared among the layers, which possess dissimilar stress-strain responses. As a consequence, the local stress on the stronger layers is higher than the global average, whereas the local stress on the softer layers is lower.

The HDI stress, which occurs orthogonal to the loading, is plotted in Figure 4.8(b) for the soft specimen, and Figure 4.8(e) for the hard specimen. And the shear stress distribution is plotted in Figure 4.8(c) for the soft specimen, and in Figure 4.8(f) for the hard specimen. In addition, the external, HDI and shear stresses across the thickness are plotted in Figure 4.8(g) and Figure 4.8(h) for the corresponding specimens. The simulation indicates that the mesoscale HDI stress and the shear stress are negligible for the laminate composites when compressed parallel to the layers. Since the strain ε along the loading direction is always the same among all the layers under the uniaxial strain condition, the compression-induced extension, $\nu \cdot \varepsilon$, will be very similar for all the layers.

Furthermore, as analyzed in Appendix 4.J, the non-zero HDI stress could arise from the deformation stage between the yield of metal layers and the yield of FeAl layers. At this regime, the Poisson's ratio of the metal layers would be 0.5 as plastic deformation, and the Poisson's ratio of the FeAl layers would be 0.33 for elastic deformation. The difference in Poisson's ratio would induce different Poisson's expansion among the layers, and consequently induce mesoscale HDI stress. As the external load further increases, after the yield of the FeAl phase, the Poisson's ratio of all the layers would be the same again as 0.5, because all the layers deform plastically. The amount of deformation between the yield of metal layers and the yield of FeAl layers is relatively small compared to the total deformation, so the HDI stress induced by this mechanism is two

orders of magnitude smaller than the HDI stress in perpendicular loading conditions. The stress at a few MPa level is not expected to cause any significant effect.

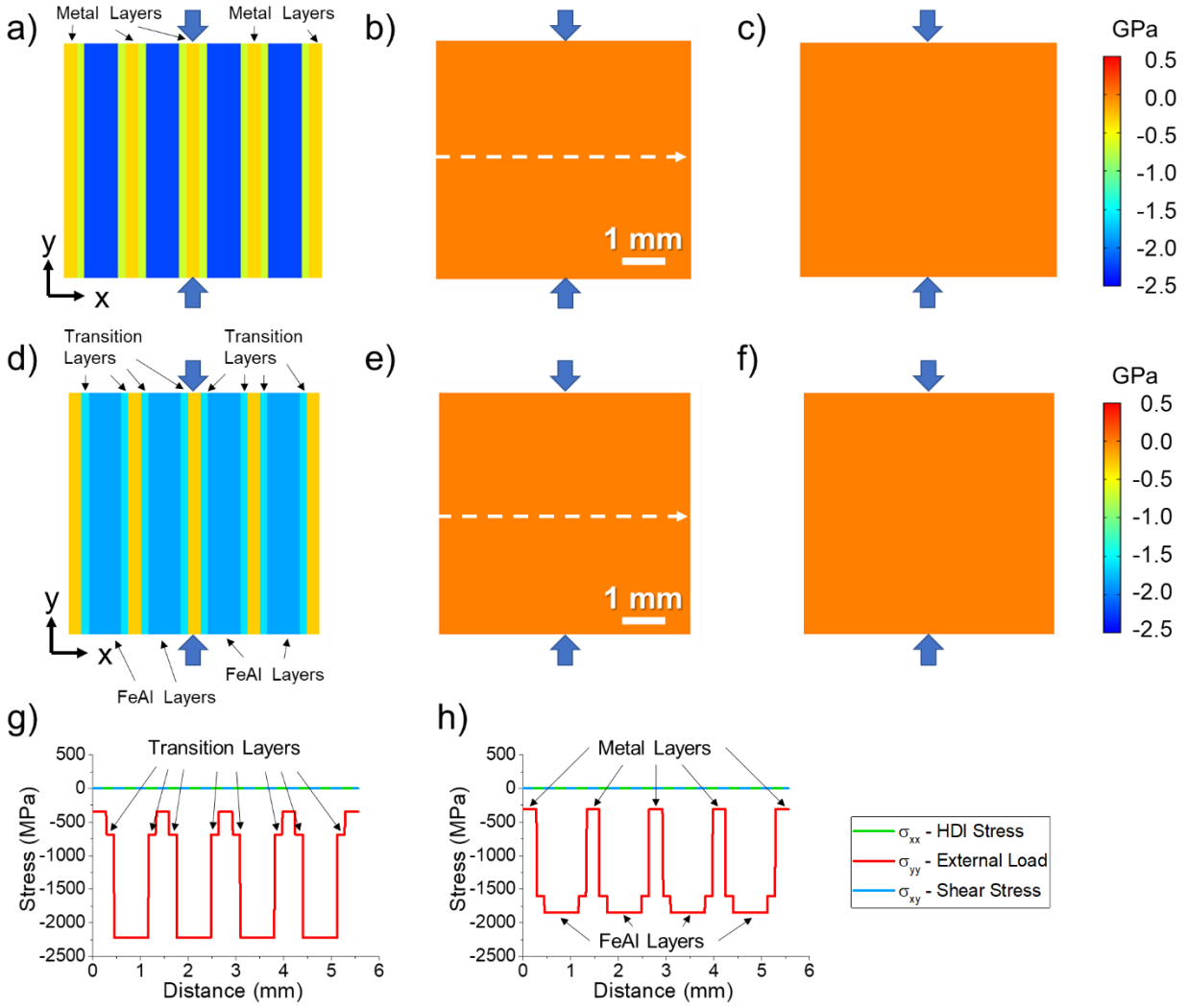

Figure 4.8: (a) External stress distribution (σ_{YY}), (b) HDI stress distribution (σ_{XX}), (c) shear stress distribution (σ_{XY}), and (g) stresses across the thickness of a MIL composite that possesses soft transition layers and is compressed to 1.4 GPa in the parallel direction. (d) External stress distribution (σ_{YY}), (e) HDI stress distribution (σ_{XX}), (f) shear stress distribution (σ_{XY}), and (h) stresses across the thickness of a MIL composite that possesses hard transition layers and is compressed to 1.4 GPa in the parallel direction.

Theoretically, the strength of FeAl-based MIL composites would follow a rule of mixture when compressed parallel to the layers. However, studies on other heterostructured materials suggest that the HDI stress would also be induced by GND pile-up at the interface of dissimilar

materials [36–39]. The HDI stress originating at the microscale tends to improve the strength of laminate composites beyond the rule of mixture [36]. This appears to explain the phenomenon that Fe-FeAl, 430-FeAl and 304-FeAl exhibit similar compressive strength (1.75, 1.76 and 2.0 GPa, respectively), although they possess dissimilar transition and/or metal layers. For metallic materials, the width of the interface-affected-zone would be a few micrometers [105], below the scale characterized here or simulated in the present work, which limits our ability to confirm GND-pile-up induced HDI stress in MIL composites.

4.4.3 Fracture Toughness

As discussed in Section 4.4.1, when compressed perpendicular to the layers, HDI stress accelerates crack nucleation and crack propagation in FeAl layers of MIL composites, inducing lower strength compared to the single-phase FeAl material. Meanwhile, as discussed in Section 4.4.2, when loaded parallel to the layers, MIL composites also fail at a lower stress level compared to single-phase FeAl material due to local stress distributions. MIL composites indeed sacrifice some strength in comparison to the single-phase FeAl. Although single-phase layered FeAl material exhibits 20% plasticity in compression, the failure still occurs catastrophically, as the specimens break into fragments. In contrast, FeAl-based MIL composites fail in a more gradual manner. As shown in Appendix 4.C, cracks are contained in the FeAl layers as the penetration of cracks is stopped by the transition layers [85]. The metal layers can bridge the fractured regions, so the specimen retains structural integrity. Furthermore, the strength of 304SS-FeAl, 2.3 GPa with 17% plasticity, is still a remarkable combination of properties for metallic material, especially considering that it only involves the use of inexpensive elements (Fe, Al, Cr and Ni) and metallic foils.

Summarized in Table 4.3 is the fracture toughness of 304SS-FeAl MIL composite and single-phase FeAl material, which were measured via four-point bending test. By reinforcing the FeAl with the layers of 304SS, the fracture toughness is improved by nearly 40% in both loading directions. In addition, Appendix 4.E presents the samples after the bending test. Similar to the compression tests, FeAl specimens failed catastrophically, whereas the failure of 304SS-FeAl occurred more incrementally.

Table 4.3: Fracture Toughness of 304SS-FeAl MIL Composite and Single-phase FeAl

	Fracture Toughness K_{1c} $(MPa\sqrt{m})$	
	Perpendicular	Parallel
304SS-FeAl MIL Composite	24.7 ± 3.9	25.0 ± 1.4
Single-phase Layered FeAl	18.8 ± 3.5	17.8 ± 1.3

When the parallel-loaded FeAl specimen failed, the load directly dropped to zero, and the sample broke into two pieces as the crack propagated from the notch through the entire sample. When the perpendicular-loaded FeAl specimen failed, the load also directly dropped to zero, and the sample broke into three pieces every time. Due to stress concentration associated with the notch, the region above the notch separates via the combination of cracks and delamination. In contrast, when the 304SS-FeAl MIL composite failed, the load gradually dropped, as the metal layers bridge the brittle layers of the composites.

4.5 Conclusions

The present work investigates the HDI stress in FeAl-based MIL composites. MIL composites and single-phase laminate FeAl are compared to study the fracture mechanisms. The main conclusions are:

1. Single-phase FeAl with laminate microstructure is synthesized. Due to the laminate structure, which hinders the crack propagation, the compressive strength can reach 3.5 GPa with 20% plasticity, a significant improvement compared to existing literature values.

2. HDI stress in MIL composites is evaluated via mechanical analysis and FEA simulation. Mesoscale HDI stress occurs when the laminate composites are loaded perpendicular to the layers. The HDI stress, as a tensile stress within the FeAl layers, accelerates crack nucleation and crack propagation.

3. Mesoscale HDI stress is expected to be negligible when the laminate composites are loaded parallel to the layers, while GND pile-up induced HDI stress can improve the performance of the composites beyond a rule of mixture.

4. Fracture toughness of single-phase FeAl and FeAl-based MIL composites is measured via four-point bending. By reinforcing the FeAl with metal layers, MIL composites can achieve 40% higher fracture toughness and avoid catastrophic failure.

Appendix 4.A Material Processing for MIL Composites

Figure 4.A1(a) demonstrates the foil stack configuration to produce MIL composites. "Multi-thin-foil" configuration is adopted to control the local composition. Details have been discussed in our previous work [77,78,85]. Figure 4.A1(b) demonstrates the sample-tooling assembly for SPS.

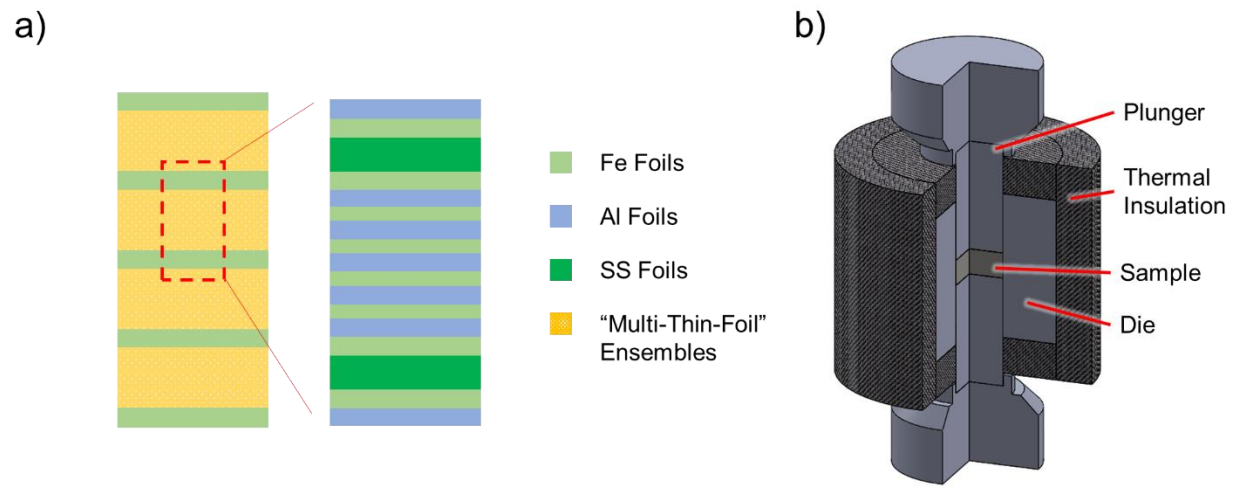

Figure 4.A1: (a) The metal foils stack configuration for synthesizing the FeAl-based MIL composites. (b) Schematic diagram of SPS setup [77,78,85,89]

Appendix 4.B FeAl Specimens After Compression Test

Figure 4.B1 presents the FeAl specimens after compression tests. All three tests were stopped before the samples' failure.

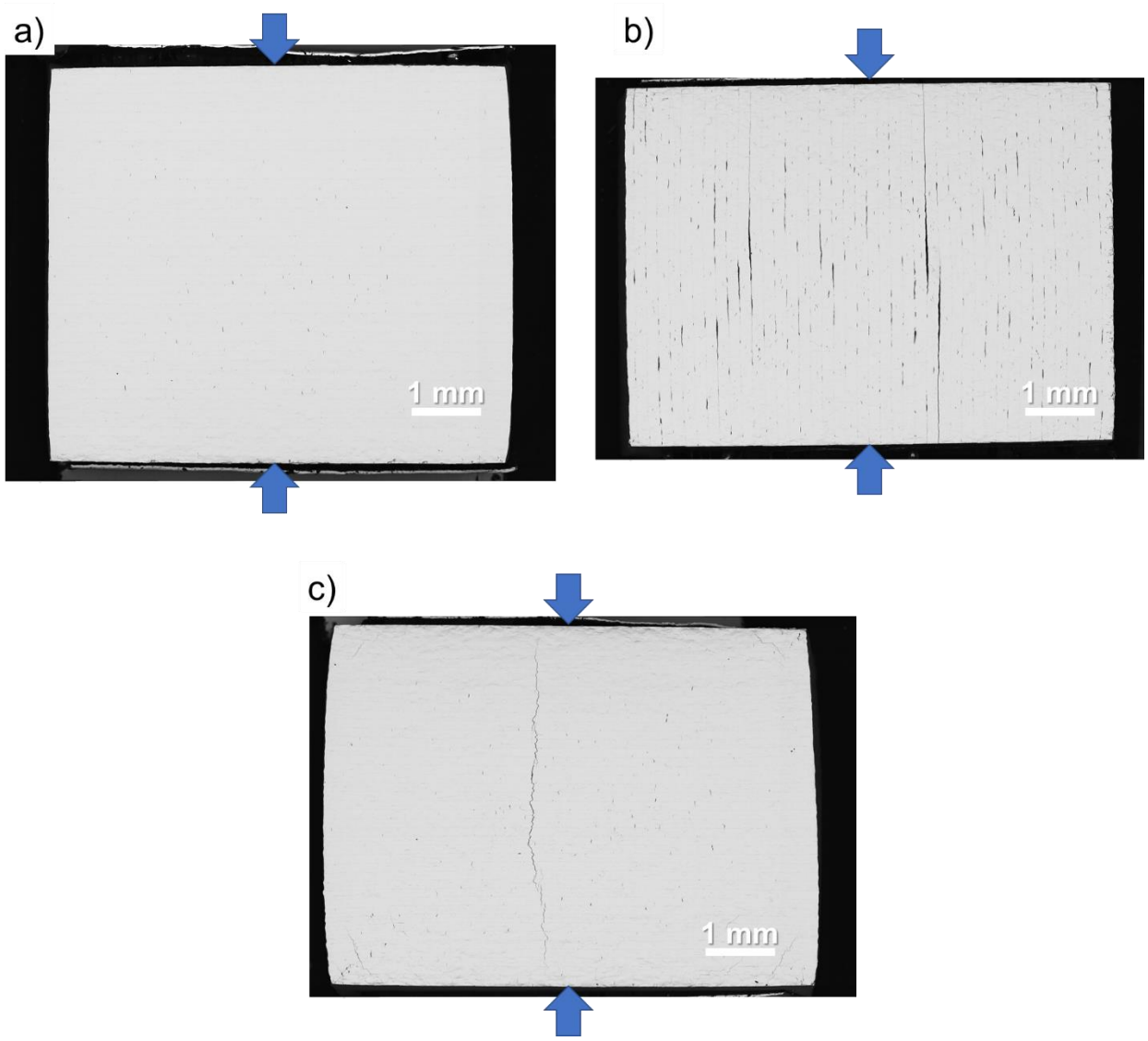

Figure 4.B1: Surface morphology of FeAl specimens after compression test: (a) 2.4 GPa loading in the perpendicular direction, (b) 2.4 GPa loading in the parallel direction, and (c) 3.3 GPa loading in the perpendicular direction.

Appendix 4.C Properties of FeAl-based MIL Composites

Figure 4.C1 are photos of FeAl-based MIL composites that failed in the compression test [77,85]. When loaded perpendicular to the layers, specimens failed due to axial splitting in FeAl layers. When loaded parallel to the layers, specimens failed due to delamination at centerlines and subsequently buckling.

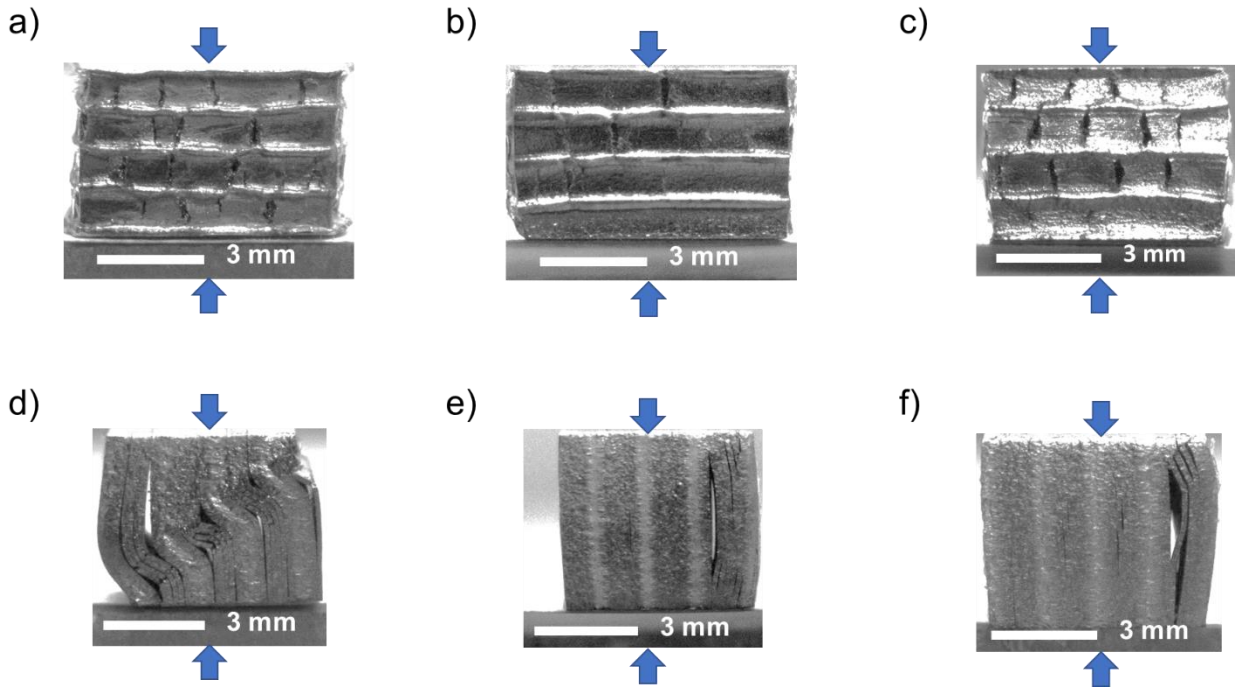

Figure 4.C1: Photos of the specimens failed at the compression tests conducted perpendicular to the layers: (a) Fe-FeAl, (b) 430SS-FeAl, and (c) 304SS-FeAl, respectively. Photos of the specimens failed at the compression tests conducted parallel to the layers: (a) Fe-FeAl, (b) 430SS-FeAl, and (c) 304SS-FeAl, respectively [77,85].

The microstructure of the three MIL composites is presented in Figure 4.C2(a), 4.C2(b) and 4.C2(c). The transition layers are the solid solution of α–Fe and FeAl phases, which take the chemical gradient from the metal layers to pure FeAl layers [77]. The thickness of the transition layers would be affected by the actual sample temperature during the reactive sintering. Figure 4.C2(d) plots the hardness profile from the metal to the FeAl layers, which suggests stronger

transition layers in 304SS-FeAl compared to 430SS-FeAl. The average hardness of the transition layer of 430SS-FeAl is 3.8 GPa, whereas the hardness of the transition layer of 304SS-FeAl is 4.3 GPa. Furthermore, we also measured microhardness of the transition layer via LECO M-400-H1 Hardness Testing Machine. Limited by the thickness of the layers, we are able to obtain two values, rather than the curve via nanoindentation. The α–Fe solid solution region of 430SS-FeAl is $220 \pm 7\ HV$, the FeAl solid solution region of 430SS-FeAl is $275 \pm 16\ HV$; the α–Fe solid solution region of 304SS-FeAl is $340 \pm 4\ HV$, and the FeAl solid solution region of 304SS-FeAl is $267 \pm 9\ HV$. As the comparison between Figure 4.C2(e) and 4.C2(f), although all three MIL composites exhibit similar mechanical performance in the parallel direction, 304SS-FeAl possesses significantly higher strength in the perpendicular direction.

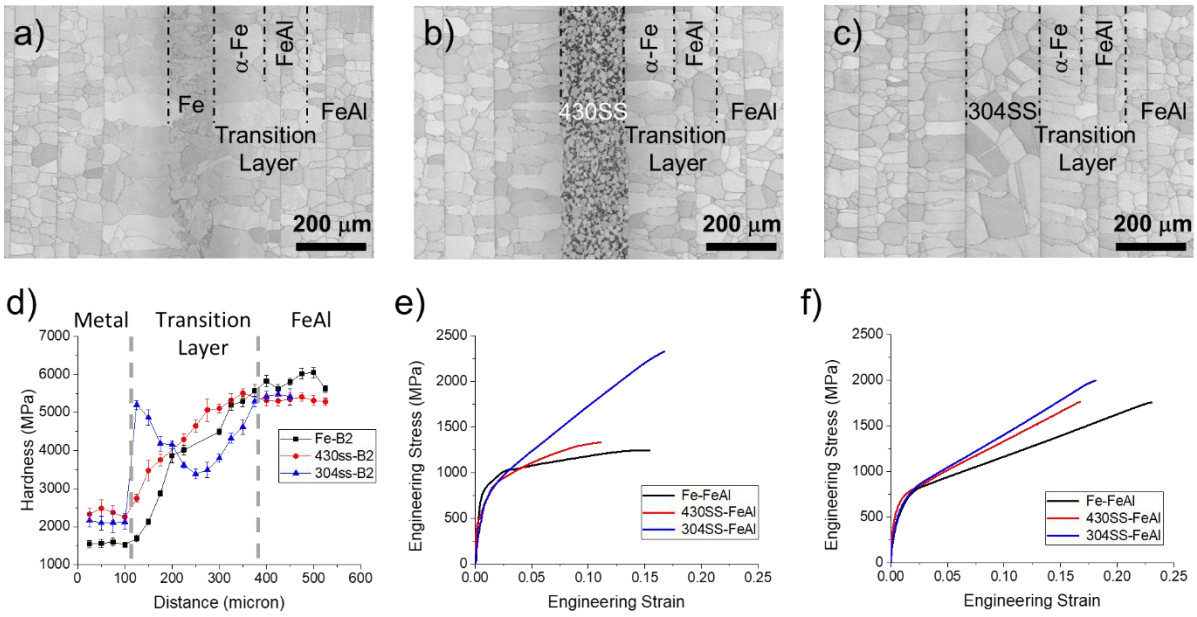

Figure 4.C2: Microstructure characterized via EBSD band contrast map for (a) Fe-FeAl, (b) 430SS-FeAl and (c) 304SS-FeAl, respectively. The dash lines indicate the phase boundaries. (d) Hardness profile of FeAl-based MIL composites. (e) and (f) are engineering strain-stress curves of MIL composites compressed in perpendicular and parallel directions, respectively [77,85].

Furthermore, the inverse pole figures for 430SS and 304SS layers are plotted in Figure 4.C3. Based on the corresponding times random numbers, the texture of 304SS layers in MIL

composites is very week, and the texture of 430SS layers is also not strong. Although the as-received SS foils could possess strong texture, the SS layers in FeAl-based MIL composites have been annealed at 1000°C for 90min. As the result, the anisotropy of the as-received foils would be relieved by grain growth.

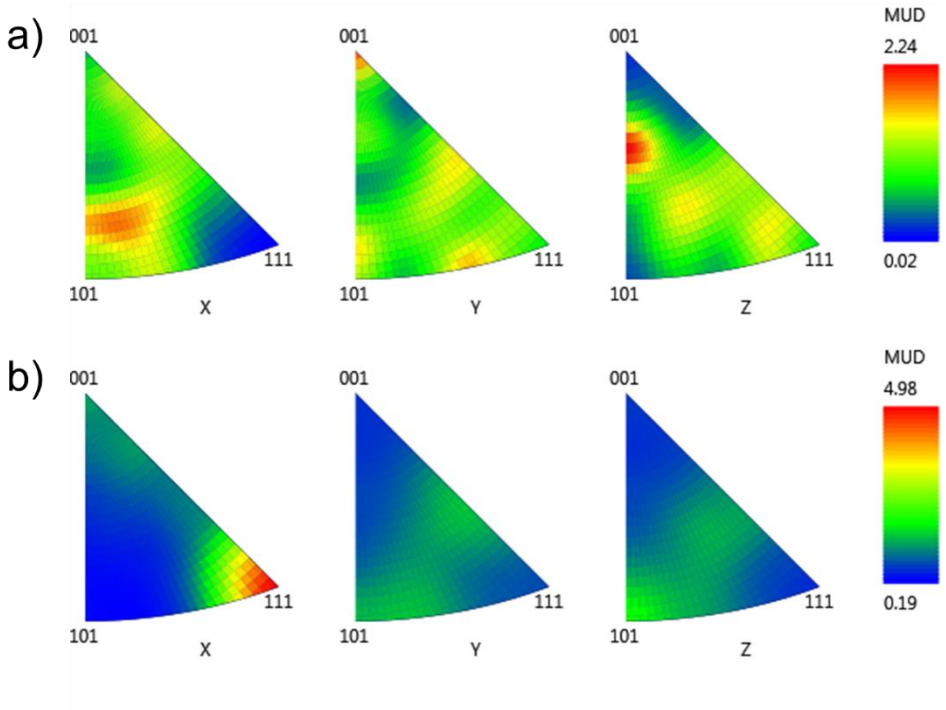

Figure 4.C3: Inverse pole figures of (a) 304SS and (b) 430SS layers in MIL composites.

Meanwhile, the microstructure and chemical composition analysis for Fe-FeAl, 430SS-FeAl and 304SS-FeAl MIL composites are presented in Figure 4.4, whereas the band contrast maps and phase maps are presented in Figure 4.C4. The content is cited from our previous work [77], as the similarity among the FeAl-based MIL composites are critical to the present study.

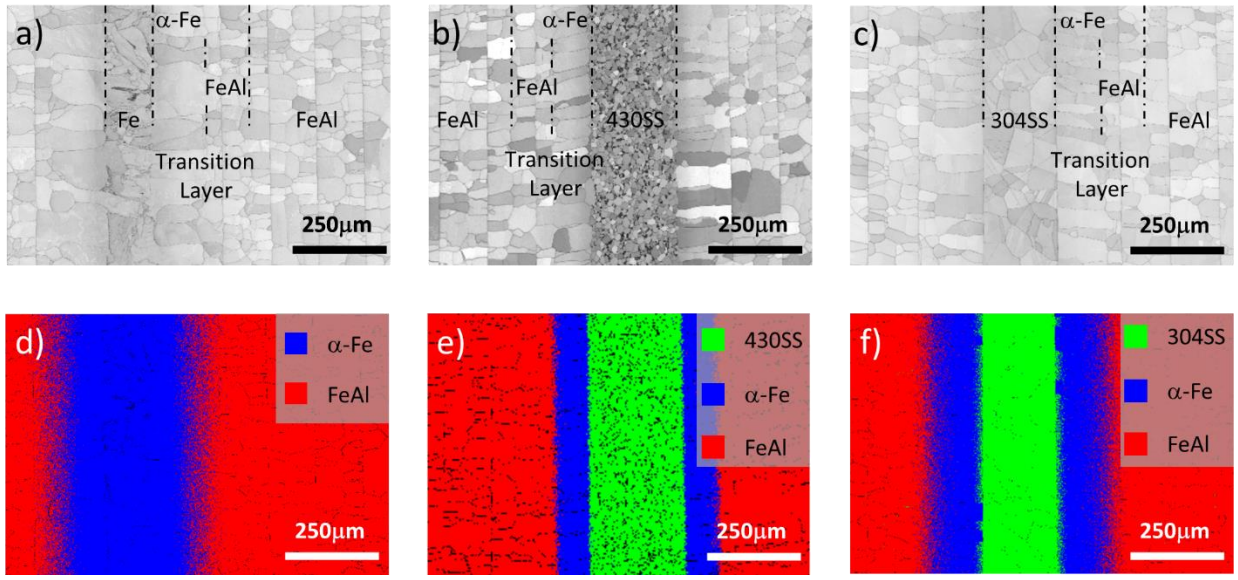

Figure 4.C4: EBSD band contrast maps for (a) Fe-FeAl, (b) 430SS-FeAl, and (c) 304SS-FeAl. (d), (e) and (f) are the phase maps for the area shown in (a), (b) and (c), respectively. [77]

Appendix 4.D An Algorithm for Solving for HDI Stress on MIL Composites

Assume the external stress loaded perpendicular to the layers is C, and the HDI stress on the metal, transition and FeAl layers in one in-plane direction are σ_M, σ_T and σ_I, respectively. Symmetrically, the HDI stress in the other in-plane orthogonal direction would also be σ_M, σ_T and σ_I, respectively. For the laminate composite that consists of an infinite number of infinitely large layers, σ_M, σ_T and σ_I would be the same on each corresponding layer. The assumption represents the MIL composites that consist of many layers. Since the HDI stress is an internal stress, the integration of HDI stress across the thickness t must be conserved:

$$\int \sigma_{\mathrm{M}}\,\mathrm{dt} + \int \sigma_{\mathrm{T}}\,\mathrm{dt} + \int \sigma_{\mathrm{I}}\,\mathrm{dt} = 0 \tag{4.D1}$$

Furthermore, as revealed by the FEA simulation, HDI stress would be uniform among each layer. In addition, the edge effect can be ignored under the assumption of infinitely large layers. One metal layer, one FeAl layer and two transition layers would represent a "repeating unit" for the composites. Therefore, Eq. (4.D1) can be rewritten as

$$\sigma_{\mathrm{M}} \cdot t_M + \sigma_I \cdot t_I + 2 \cdot \sigma_T \cdot t_T = 0 \tag{4.D2}$$

where t_M, t_T and t_I are the thickness of each metal, transition, and FeAl layers, respectively. Meanwhile, the strain can be divided into the elastic part and the plastic part [83]: $\varepsilon = \varepsilon^E + \varepsilon^P$. The elastic part ε^E follows Hooke's law: $\varepsilon^E = \frac{\sigma}{E}$, where σ is the total stress, and E is the Young's modulus. The plastic strain ε^P depends on the material's stress-strain curve and yield criterion, and can be described as a function of the stress σ: $\varepsilon^P = f(\sigma)$. The strain of the metal layer in one in-plane direction, which is the product of both external and HDI stresses, can be expressed based on the Poisson's ratio:

$$\varepsilon_M = \frac{1}{E_M}[\sigma_M - \nu^E(\mathrm{C} + \sigma_M)] + \{f_M(\sigma_M) - \nu^P[f_M(C) + f_M(\sigma_M)]\} \tag{4.D3}$$

where E_M is the Young's modulus of the metal layer, ν^E is the Poisson's ratio for elasticity, which is typically 0.3 for metallic materials, and ν^P is the Poisson's ratio for plastic flow, which is theoretically 0.5 for incompressible materials [83]. The first term represents the contribution of elastic strain ε^E, whereas the second term represents the contribution of plastic flow ε^P.

Similarly, the strain of the transition and FeAl layers can be written as:

$$\varepsilon_T = \frac{1}{E_T}[\sigma_T - \nu^E(\mathrm{C} + \sigma_T)] + \{f_T(\sigma_T) - \nu^P[f_T(C) + f_T(\sigma_T)]\} \tag{4.D4}$$

$$\varepsilon_I = \frac{1}{E_I}[\sigma_I - \nu^E(\mathrm{C} + \sigma_I)] + \{f_I(\sigma_I) - \nu^P[f_I(C) + f_I(\sigma_I)]\} \tag{4.D5}$$

Mathematically, there are three independent variables: σ_M, σ_T and σ_I. The constrain of non-delamination at the interface generates two independent equations:

$$\begin{cases} \varepsilon_{\mathrm{M}} = \varepsilon_{\mathrm{T}} \\ \varepsilon_{\mathrm{I}} = \varepsilon_{\mathrm{T}} \end{cases} \tag{4.D6}$$

Along with Eq. (4.D2), there are three independent equations, which are sufficient to analytically or numerically solve for the three independent variables.

Furthermore, for the laminate composite that consists of n dissimilar materials, there will be n independent variables as the HDI stress on each layer. Meanwhile, the constrain at the interface can provide $(n-1)$ independent equations, describing the match of the strain on both sides of the interface. Additionally, the conservation of the HDI stress can provide one more independent equation, describing that the summation of the HDI stress across the thickness always equals zero. So mathematically, the HDI stress would always be solvable for any given system.

For simplicity, let us consider a MIL composite that consists of only metal and intermetallic layers, such as the first MIL composite, Ti-$TiAl_3$. The conservation of HDI stress generates:

$$\sigma_{\mathrm{M}} \cdot t_M + \sigma_I \cdot t_I = 0 \tag{4.D7}$$

Assume both metal and intermetallic layers exhibit linear elasticity and linear plasticity, then the individual material under uniaxial loading follows:

$$\sigma = \begin{cases} E \cdot \varepsilon & , before\ yield\ point \\ \mathrm{H}\left(\varepsilon - \frac{\sigma_Y}{E}\right) + \sigma_Y & , after\ yield\ point \end{cases} \tag{4.D8}$$

where H is the work hardening rate, and σ_Y is the yield stress. Note that the positive value represents tension, whereas the negative value represents compression. Subsequently, the plastic strain ε^P at given a stress level can be calculated:

$$\varepsilon^P = \begin{cases} 0 & ,|\sigma| \le |\sigma_Y| \\ (\sigma - \sigma_Y)\left(\frac{1}{H} - \frac{1}{E}\right) & ,|\sigma| > |\sigma_Y| \end{cases} \tag{4.D9}$$

However, both metal and intermetallic are under triaxial loading, external stress in the plane-normal direction, HDI stresses in the other two in-plane orthogonal directions. Therefore, we need to consider the yield criterion.

To further simplify the situation, let us reduce it to the 2D situation. And assume that the material obeys von Mises yield criterion. As demonstrated in Figure 4.D1(a), the material is loaded in the x-direction, generating the external stress C. Meanwhile, the loading would induce an HDI stress σ_{HDI} in y-direction. As represented by the red arrow in Figure 4.D1(a), the vector sum of C and σ_{HDI} creates the net stress σ_{total}. If the external stress C has exceeded the yield point, the plastic strain in the σ_{total} direction is

$$\left(\sqrt{C^2 + {\sigma_{HDI}}^2} - \sigma_Y\right)\left(\frac{1}{H} - \frac{1}{E}\right) \tag{4.D10}$$

As demonstrated in Figure 4.D1(b) by the purple arrow, flowing Poisson's ratio, the deformation along σ_{total} direction would also induce a deformation in its orthogonal direction:

$$\nu^P\left(\sqrt{C^2 + {\sigma_{HDI}}^2} - \sigma_Y\right)\left(\frac{1}{H} - \frac{1}{E}\right) \tag{4.D11}$$

Subsequently, project both plastic flows back to the X and Y axes, we can obtain the plastic strain induced by the external and HDI stress:

$$\varepsilon_x^P = \frac{C}{\sqrt{\mathrm{C}^2+{\sigma_{\mathrm{HDI}}}^2}}\left(\sqrt{\mathrm{C}^2 + {\sigma_{\mathrm{HDI}}}^2} - \sigma_Y\right)\left(\frac{1}{\mathrm{H}} - \frac{1}{E}\right) + \frac{\nu^P \cdot \sigma_{\mathrm{HDI}}}{\sqrt{\mathrm{C}^2+{\sigma_{\mathrm{HDI}}}^2}}\left(\sqrt{\mathrm{C}^2 + {\sigma_{\mathrm{HDI}}}^2} - \sigma_Y\right)\left(\frac{1}{\mathrm{H}} - \frac{1}{E}\right) \tag{4.D12}$$

$$\varepsilon_y^P = \frac{\sigma_{\mathrm{HDI}}}{\sqrt{\mathrm{C}^2+{\sigma_{\mathrm{HDI}}}^2}}\left(\sqrt{\mathrm{C}^2 + {\sigma_{\mathrm{HDI}}}^2} - \sigma_Y\right)\left(\frac{1}{\mathrm{H}} - \frac{1}{E}\right) + \frac{\nu^P \cdot \mathrm{C}}{\sqrt{\mathrm{C}^2+{\sigma_{\mathrm{HDI}}}^2}}\left(\sqrt{\mathrm{C}^2 + {\sigma_{\mathrm{HDI}}}^2} - \sigma_Y\right)\left(\frac{1}{\mathrm{H}} - \frac{1}{E}\right) \tag{4.D13}$$

Then, the in-plane strain on the metal layers can be expressed as:

$$\varepsilon_M = \frac{1}{E_M}[\sigma_M - \nu^E C] + \left\{\left[\frac{\sigma_M}{\sqrt{C^2+\sigma_M{}^2}}\left(\sqrt{C^2+\sigma_M{}^2} - \sigma_{Y,M}\right)\left(\frac{1}{H_M} - \frac{1}{E_M}\right) + \frac{\nu^P \cdot C}{\sqrt{C^2+\sigma_M{}^2}}\left(\sqrt{C^2+\sigma_M{}^2} - \sigma_{Y,M}\right)\left(\frac{1}{H_M} - \frac{1}{E_M}\right)\right] - \nu^P\left[\frac{C}{\sqrt{C^2+\sigma_M{}^2}}\left(\sqrt{C^2+\sigma_M{}^2} - \sigma_{Y,M}\right)\left(\frac{1}{H_M} - \frac{1}{E_M}\right) + \frac{\nu^P \cdot \sigma_M}{\sqrt{C^2+\sigma_M{}^2}}\left(\sqrt{C^2+\sigma_M{}^2} - \sigma_{Y,M}\right)\left(\frac{1}{H_M} - \frac{1}{E_M}\right)\right]\right\}$$

$$= \frac{1}{E_M}[\sigma_M - \nu^E C] + \left(\sqrt{C^2+\sigma_M{}^2} - \sigma_{Y,M}\right)\left(\frac{1}{H_M} - \frac{1}{E_M}\right)\frac{\sigma_M}{\sqrt{C^2+\sigma_M{}^2}}\left(1+\nu^{P\,2}\right) \qquad (4.D14)$$

Similarly, the in-plane strain on the intermetallic layers can be expressed:

$$\varepsilon_I = \frac{1}{E_I}[\sigma_I - \nu^E C] + \left(\sqrt{C^2+\sigma_I{}^2} - \sigma_{Y,I}\right)\left(\frac{1}{H_I} - \frac{1}{E_I}\right)\frac{\sigma_I}{\sqrt{C^2+\sigma_I{}^2}}\left(1+\nu^{P\,2}\right) \qquad (4.D15)$$

Now, HDI stress can be calculated by solving Eq. (4.D7), (4.D14) and (4.D15). On the other hand, the equations have already become relatively complicated for the 2-layered composite in the 2D situation. Therefore, FEA simulation would be a more convenient method to evaluate the HDI stress in MIL composites.

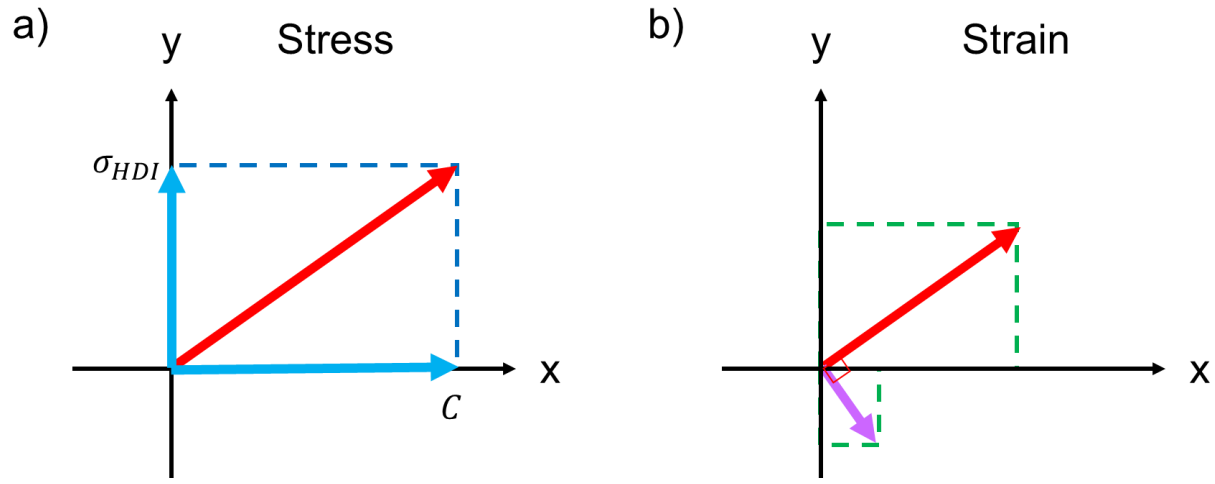

Figure 4.D1: Analysis for plastic strain induced by both external and HDI stresses.

Appendix 4.E Four-Point Bending Test

Figure 4.E1 presents the microstructure and chemical composition of 304SS-FeAl MIL composite and single-phase laminate FeAl material. The EDS profile of the 304SS-FeAl in the present study of fracture toughness is very similar to our previous work [77,85], although the size of the SPS tablet is enlarged to 40mm from 20mm.

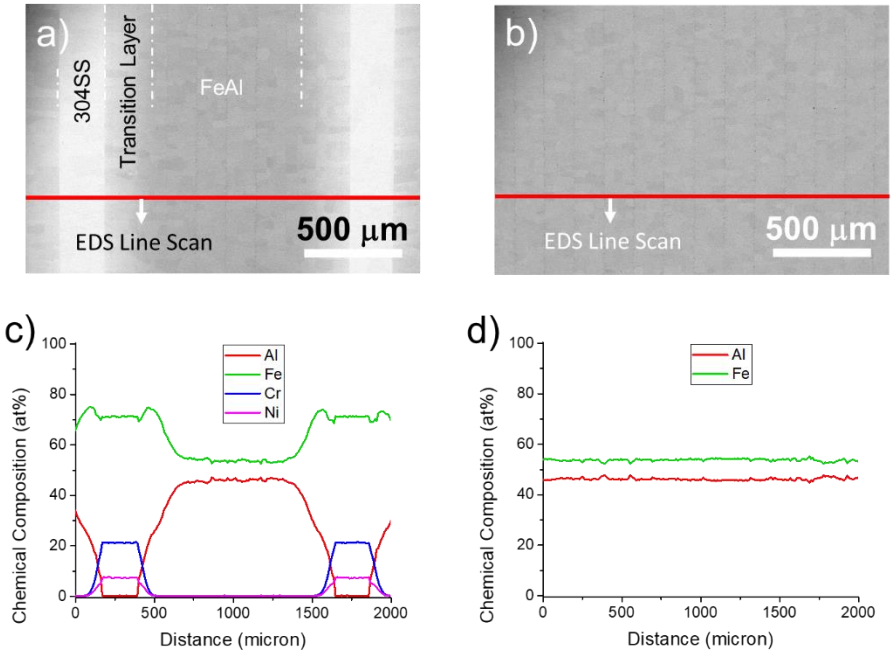

Figure 4.E1: SEM images of (a) 304SS-FeAl and (b) single phase laminate FeAl. (c) and (d) are EDS line scans along the red lines indicated in (a) and (b), respectively.

Four-point bending tests were conducted on both materials in both perpendicular and parallel directions for at least three times. Figure 4.E2 is the photos of the failed specimens. When failed, FeAl specimens broke into two or three pieces, whereas 304SS-FeAll all remained integrated. The typically loading curves are plotted in Figure 4.E3, as the fracture toughness K_{1C} is calculated using the maximum load. Displacement refers to the motion of the load frame crosshead. Trembles on the curve are induced by the formation of microcracks, which are hindered by the metal layers in the MIL composites.

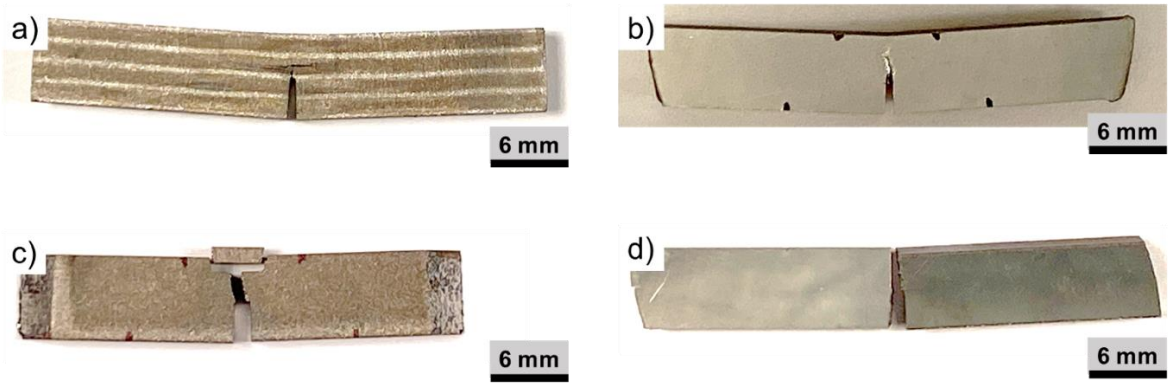

Figure 4.E2: Photos of specimens after failure in four-point bending test: (a) 304SS-FeAl loaded in the perpendicular direction, (b) 304SS-FeAl loaded in the parallel direction, (c) FeAl loaded in the perpendicular direction, and (d) FeAl loaded in the parallel direction.

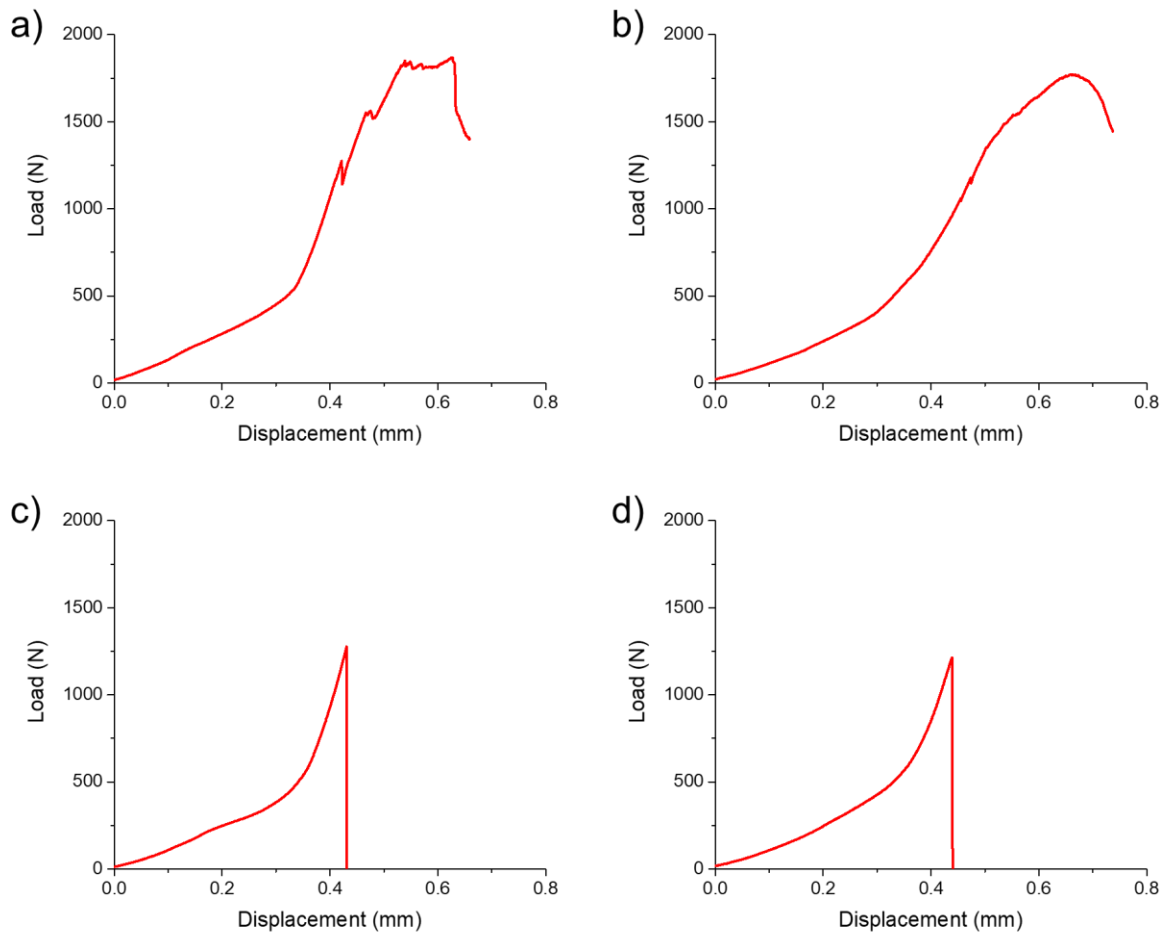

Figure 4.E3: Loading curves of four-point bending tests: (a) 304SS-FeAl bent in the perpendicular direction, (b) 304SS-FeAl bent in the parallel direction, (c) FeAl bent in the perpendicular direction, and (d) FeAl bent in the parallel direction.

Appendix 4.F 2D FEA Simulation Model for MIL Composites

Figure 4.F1(a) demonstrates the geometry model for the simulation, which reflects the actual size and layer thickness of the compression specimens. The FEA simulation is 2D, because the two orthogonal in-plane directions are symmetric for MIL composites. Therefore, we only need to consider the plan normal direction (Y axis) and one of the in-plan directions (X axis). Due to the symmetry, when the MIL composites are loaded perpendicular to the layers, the stress distribution in the other orthogonal in-plane direction (Z axis) would be the same as the X axis. For compression perpendicular to the layers, the bottom edge was fixed, as its displacement in the y-direction would always be zero but free to evolve in x-direction; the displacement of the top edge in the y-direction was manually tuned to reach the desired loading level. Similarly, for compression parallel to the layers, the right edge was fixed, and the displacement of the left edge in the x-direction was manually tuned to reach the desired loading level.

Shown in Figure 4.F1(b) are the material properties for the simulation. For simplification, linear elasticity and linear plasticity were assumed for all the materials.

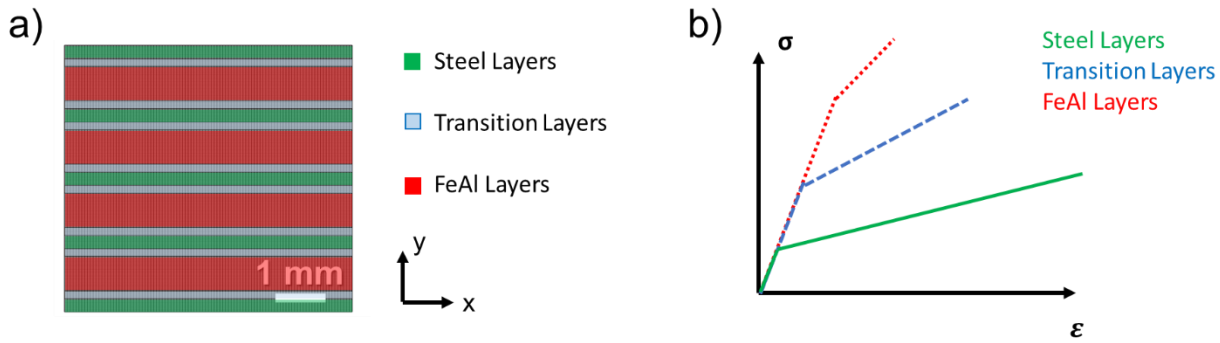

Figure 4.F1: (a) Geometry model and (b) material models for FEA simulation.

Appendix 4.G Surface Layers of the Single Phase FeAl Samples

Figure 4.G1(a) is the cross section of a single phase FeAl sample before grinding, and the corresponding EDS line scan is plotted in Figure 4.G1(b). The characterization investigates the surface layers on the top and bottom, which will be removed via grinding for the subsequent mechanical tests. The dark region on the left edge is the mounting material, and the adjacent bright region is the Mo layer. Adjacent to the Mo layer is the 304SS layer, and the transition layer forms between the 304SS layer and FeAl layer as the chemical gradient region.

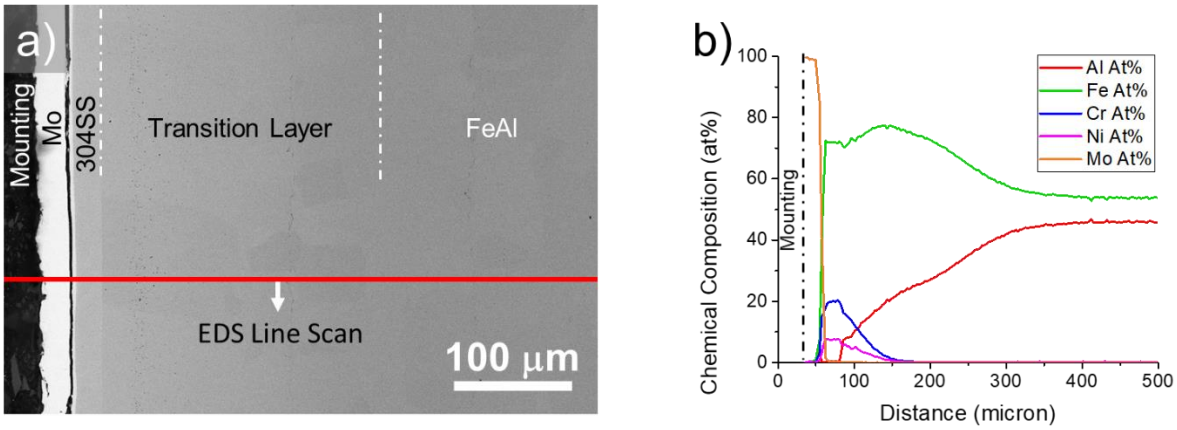

Figure 4.G1: (a) SEM image of single phase laminate FeAl sample before surface grinding. (b) is EDS line scan along the red line indicated in (a).

As a comparison, the microstructure and chemical composition of the single phase FeAl samples after surface layers removal are presented in Figure 4.2 and Figure 4.G2. The EDS line scans verify that the grinding work has removed all the non-FeAl layers.

Besides, Figure 4.G3 presents the band contrast map of an EBSD scan that measured the texture of the single phase FeAl sample.

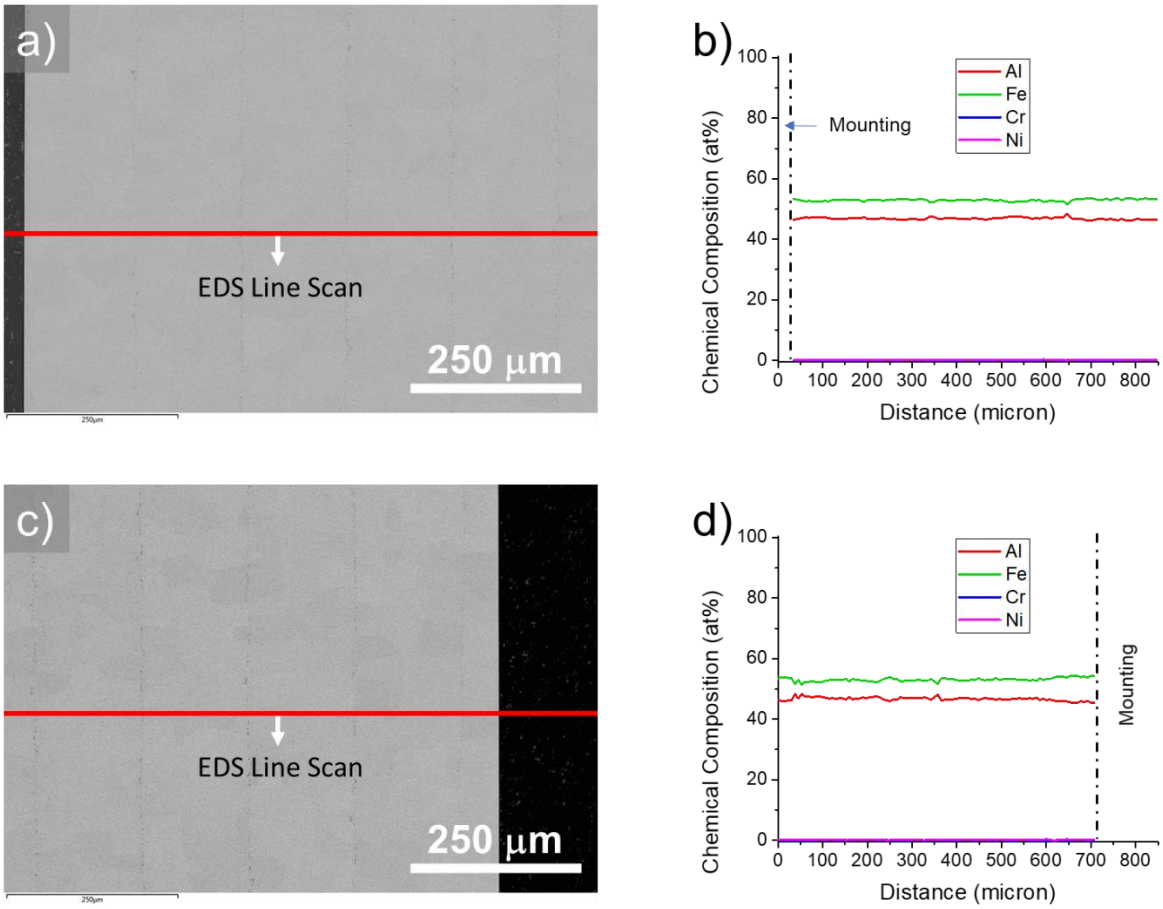

Figure 4.G2: SEM images of (a) top and (b) bottom of the single phase FeAl sample after grinding. (c) and (d) are EDS line scans along the red lines indicated in (a) and (b), respectively.

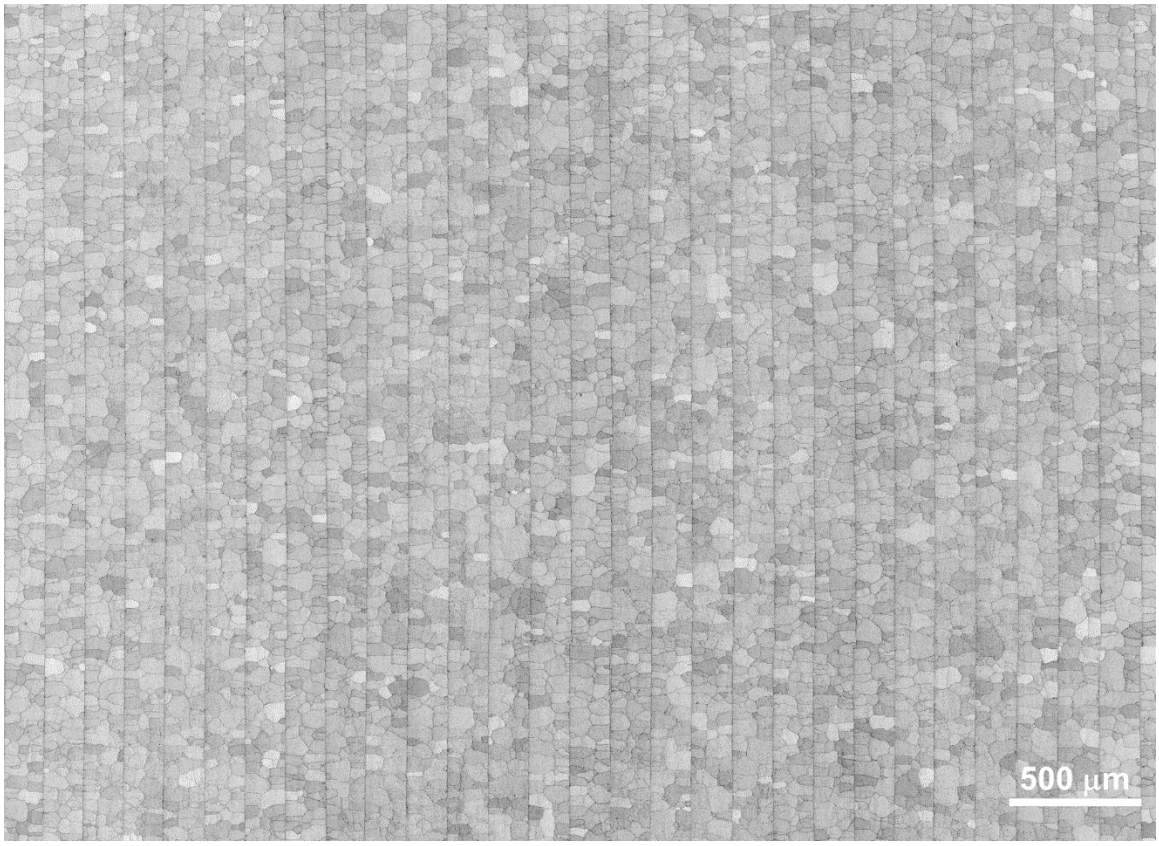

Figure 4.G3: Large area EBSD scan on the single phase FeAl sample to measure texture.

Appendix 4.H Thermal Stress in MIL Composites

After SPS sintering, samples cooled from the annealing temperature, around 1000°C, to the room temperature, inside the SPS chamber. Since metal and intermetallic layers might possess different thermal expansion coefficients, thermal stress would arise inside the MIL composites at the cooling stage. Table 4.H1 lists the thermal expansion coefficients of the constitutes of the FeAl-based MIL composites. The values were measured using Perkin Elmer DMA 7 dynamic mechanical Analyzer from the bulk materials that went through the very similar thermal treatments as the MIL composites.

Table 4.H1: Thermal expansion coefficients of layers in MIL composites

Material	Thermal Expansion Coefficient ($\mu m/m \cdot K$)
430SS	10.3
304SS	17.4
Layered FeAl (Perpendicular Orientation)	16.8
Layered FeAl (Parallel Orientation)	16.7

Cooling from 1000°C, and if only consider 430SS and FeAl layers, the difference would create 0.7% in-plane mismatch strain, which is shared between the layers:

$$\varepsilon_{430SS} + \varepsilon_{FeAl} = 0.7\% \tag{4.H1}$$

where ε_{430SS} and ε_{FeAl} is the strain of 430SS layers and FeAl layers, respectively. Meanwhile, as an internal stress, the integral of the in-plan thermal stress should equal zero. Assume the thermal stress is uniform at macroscale:

$$\sigma_{430SS} \cdot t_{430SS} = \sigma_{FeAl} \cdot t_{FeAl} \tag{4.H2}$$

where σ_{430} and σ_{FeAl} is the thermal stress of 430SS layers and FeAl layers, t_{430SS} and t_{FeAl} is the thickness of 430SS layers and FeAl layers. Considering the thermal expansion coefficients for 430SS and FeAl, σ_{430} would be compressive stress and σ_{FeAl} would be tensile stress. Take $t_{430SS} = 280\ \mu m$ and $t_{FeAl} = 720\ \mu m$ into Eq. (4.H2) and (4.H1), and assume that both 430SS layers and FeAl layers follow linear elasticity and linear plasticity demonstrated in Table 4.1. We will get $\sigma_{430SS} = 206\ MPa$ as compression and $\sigma_{FeAl} = 80\ MPa$ as tension, where as $\varepsilon_{430SS} = 0.0066$ and $\varepsilon_{FeAl} = 0.0004$. Because FeAl is much harder than 430SS, the thermal shrinkage induced strain would be mostly carried by the 430SS layers.

Figure 4.H1 demonstrates the 2D FEA simulation for the thermal stress distribution in a MIL composite material with soft transition layers (300 MPa yield strength, 3 GPa work hardening rate), when the specimen cools from 1000°C to room temperature. The thermal expansion coefficient of the transition layers is assumed to be 13.5 mm/m·K, the average of the 430SS and FeAl. The thermal stress on the FeAl layers is around 130 MPa, multiple times smaller than the HDI stress when the specimen is loaded to 1 GPa or higher.

The cooling rate for the SPS sintering was set to 50°C/min. And as shown in Figure 4.H2, the actual cooling rate would slow down due to limited heat conduction and thermal radiation. As the result, the residual thermal stress would partially relieve during the cooling stage. For example, 200~300 °C is the common stress reliving temperature for 430SS. To evaluate the residual thermal stress, Figure 4.H3 demonstrates the FEA simulation for the thermal stress when the specimen cools from 300°C to room temperature. Intuitively, the thermal stress from 300°C to room temperature should be less than one-third to the thermal stress from 1000°C to room temperature. However, the simulation predicts that the thermal stress on the FeAl layers is only reduced to 90

MPa. Since the in-plane mismatch strain has exceeded the yield point for 430SS, the thermal stress evolution would be nonlinear.

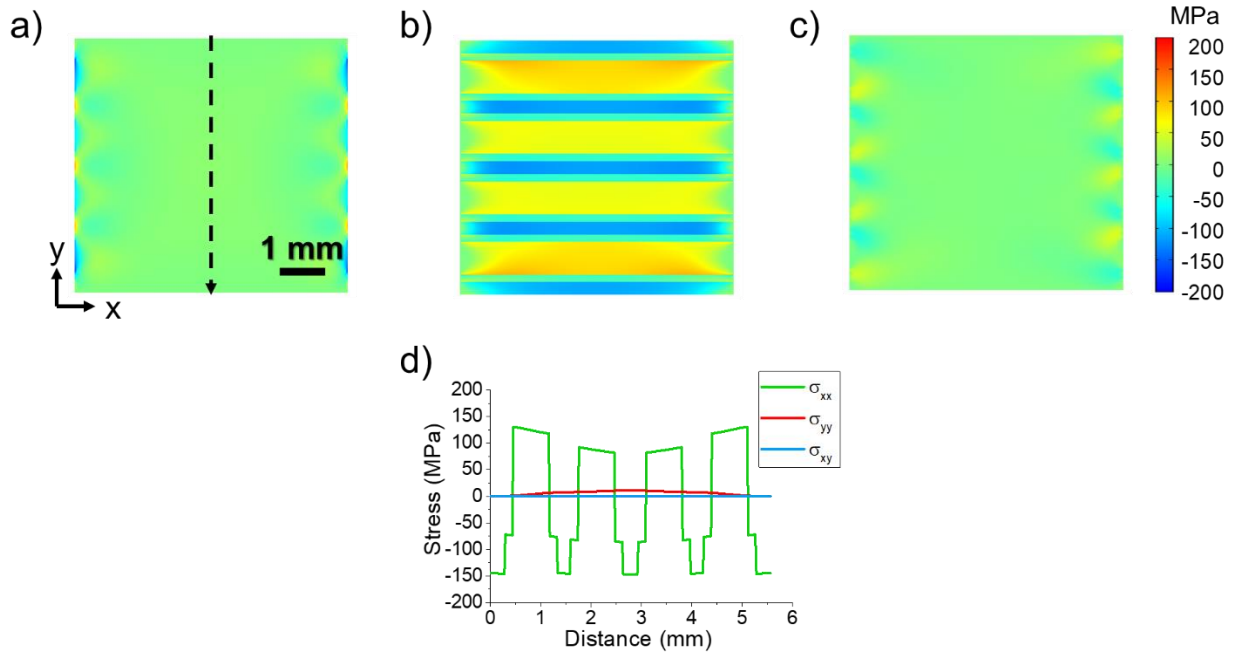

Figure 4.H1: Thermal stress distribution in MIL composites cooled from 1000°C to room temperature: (a) σ_{YY}, (b) σ_{XX}, and (c) σ_{YY}. (d) Stresses across the thickness.

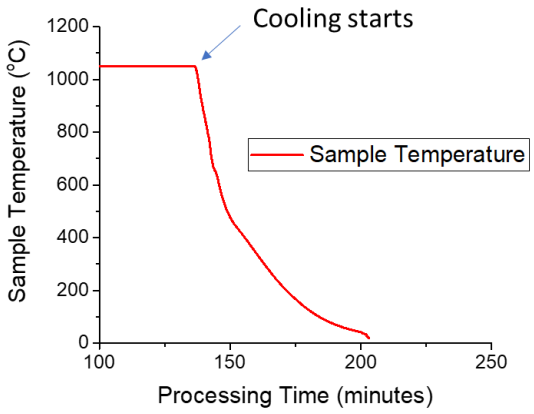

Figure 4.H2: Cooling curve for MIL composites in SPS sintering.

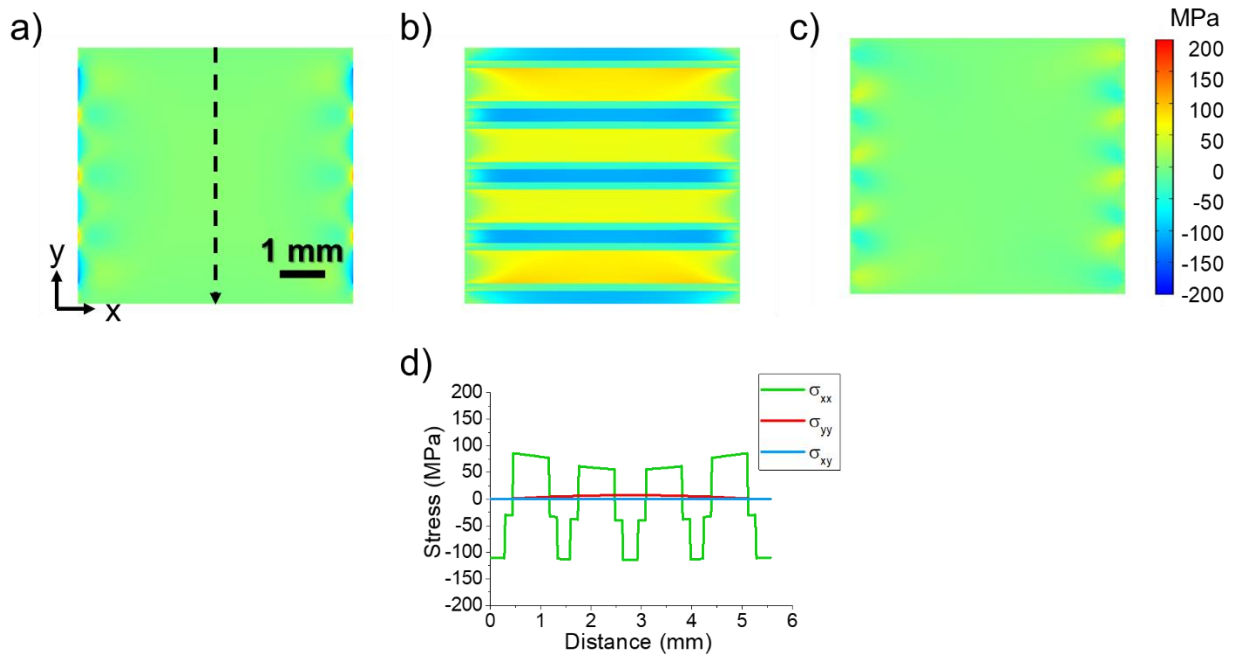

Figure 4.H3: Thermal stress distribution in MIL composites cooled from 300°C to room temperature: (a) σ_{YY}, (b) σ_{XX}, and (c) σ_{YY}. (d) Stresses across the thickness.

To evaluate the impact of residual thermal stress on HDI stress, Figure 4.H4 demonstrates the stress distribution in a MIL composite that undergoes both cooling and compression perpendicular to the layers. The cooling from both 1000°C and 300°C are simulated and the specimens are loaded to 1.4 GPa. Compared with the simulation shown in Figure 4.4(a) to 4.4(c), the stress distribution during compression is very similar with or without the residual thermal stress. The mesoscale HDI stress (σ_{XX}) on FeAl layers raises by 5 MPa (cooling from 300°C) or 15 MPa (cooling from 1000°C). The change is nonlinear considering the corresponding thermal stress itself is 80 to 130 MPa, because the layers are already under elastic-plastic deformation.

Similarly, Figure 4.H5 demonstrates the stress distribution in a MIL composite that undergoes both cooling and compression parallel to the layers. The cooling from both 1000°C and 300°C are simulated and the specimens are loaded to 1.4 GPa. Compared with the simulation shown in Figure 4.7(a) to 4. 7(c), the stress distribution during compression is also very similar

with or without the residual thermal stress. The external stress (σ_{YY}) on the FeAl layers would only increase by less than 20 MPa after introducing the residual thermal stress.

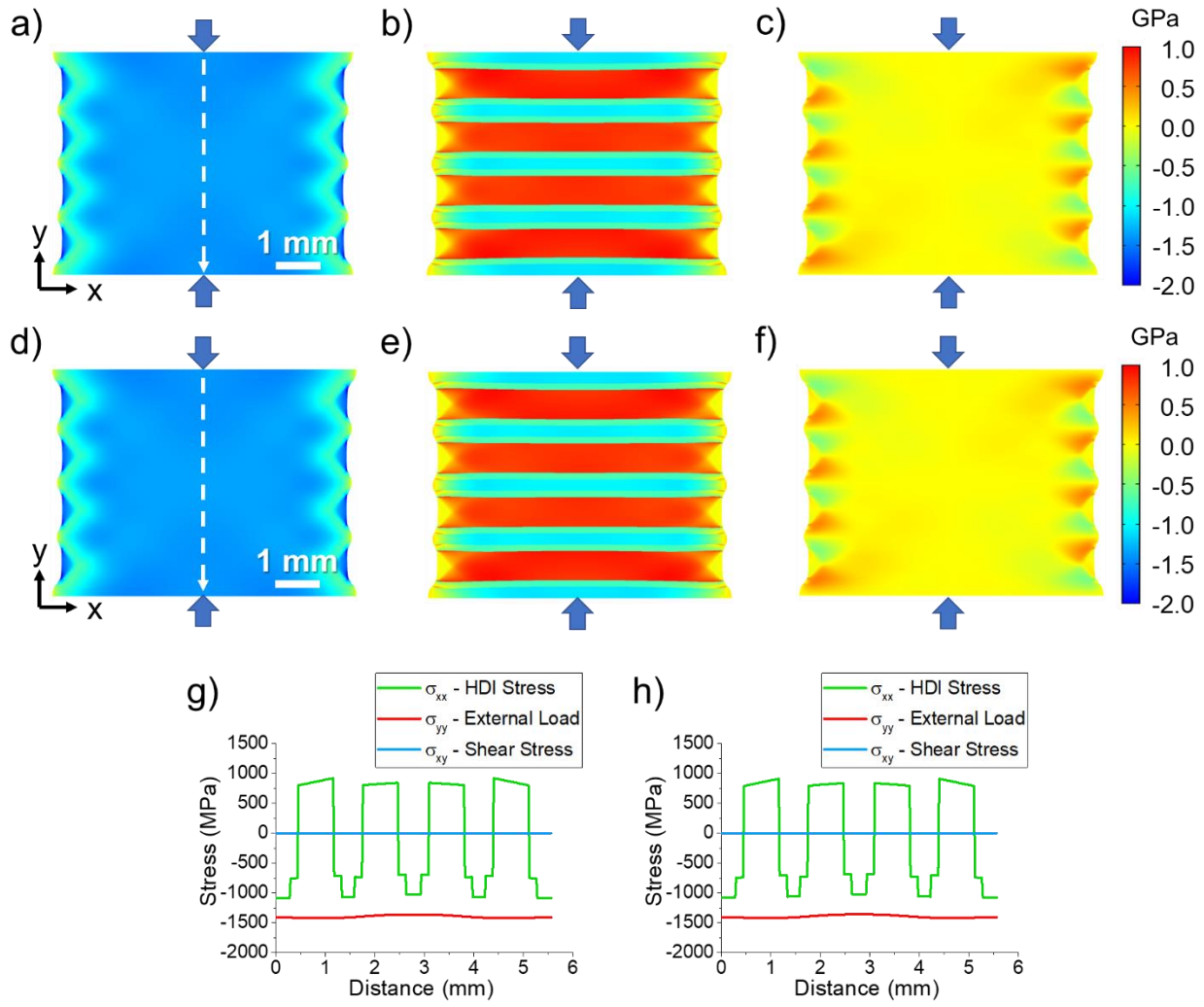

Figure 4.H4: (a) External stress distribution (σ_{YY}), (b) HDI stress distribution (σ_{XX}), (c) shear stress distribution (σ_{XY}), and (g) stresses across the thickness of a MIL composite that cooled from 1000°C to room temperature and is compressed to 1.4 GPa in the perpendicular direction. (d) External stress distribution (σ_{YY}), (e) HDI stress distribution (σ_{XX}), (f) shear stress distribution (σ_{XY}), and (h) stresses across the thickness of a MIL composite that cooled from 300°C to room temperature and is compressed to 1.4 GPa in the perpendicular direction.

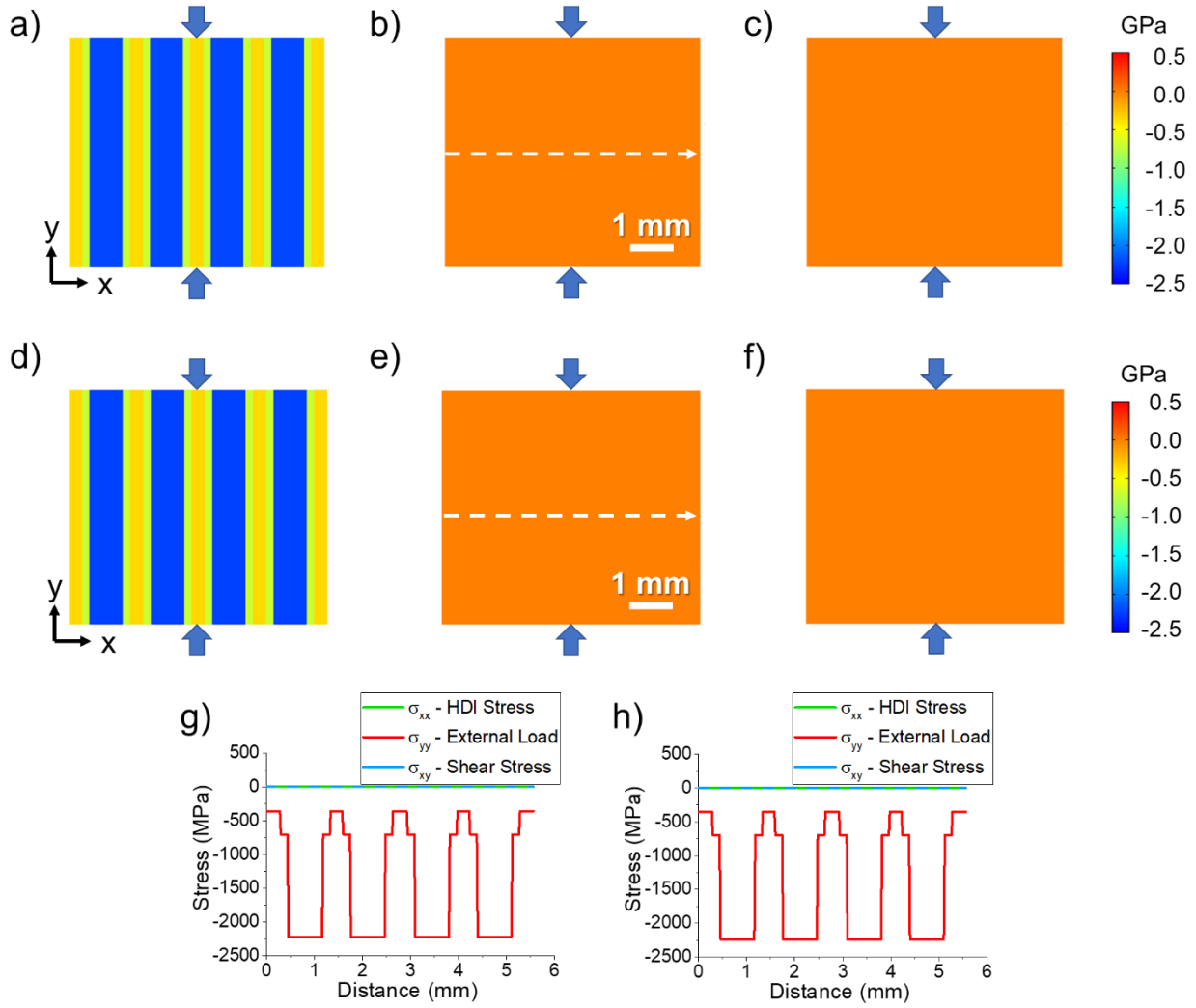

Figure 4.H5: (a) External stress distribution (σ_{YY}), (b) HDI stress distribution (σ_{XX}), (c) shear stress distribution (σ_{XY}), and (g) stresses across the thickness of a MIL composite that cooled from 1000°C to room temperature and is compressed to 1.4 GPa in the parallel direction. (d) External stress distribution (σ_{YY}), (e) HDI stress distribution (σ_{XX}), (f) shear stress distribution (σ_{XY}), and (h) stresses across the thickness of a MIL composite that cooled from 300°C to room temperature and is compressed to 1.4 GPa in the parallel direction.

In addition, our previous study about the GND density evolution of FeAl-based MIL composites [85] can also indicate that the effect of residual thermal stress is very limited to the compression. As shown in Figure 4.H6 and 4.H8, the GND densities of the undeformed samples and samples under 500 MPa loading are below the noise floor of the GND calculation. In contrast,

as shown in Figure 4.H7 and 4.H9, GND densities significantly rise with the increase of the compression pressure, which indicates that the microstructure evolution induced by the external loading overwhelms the effect of residual thermal stress, at least one order of magnitude stronger.

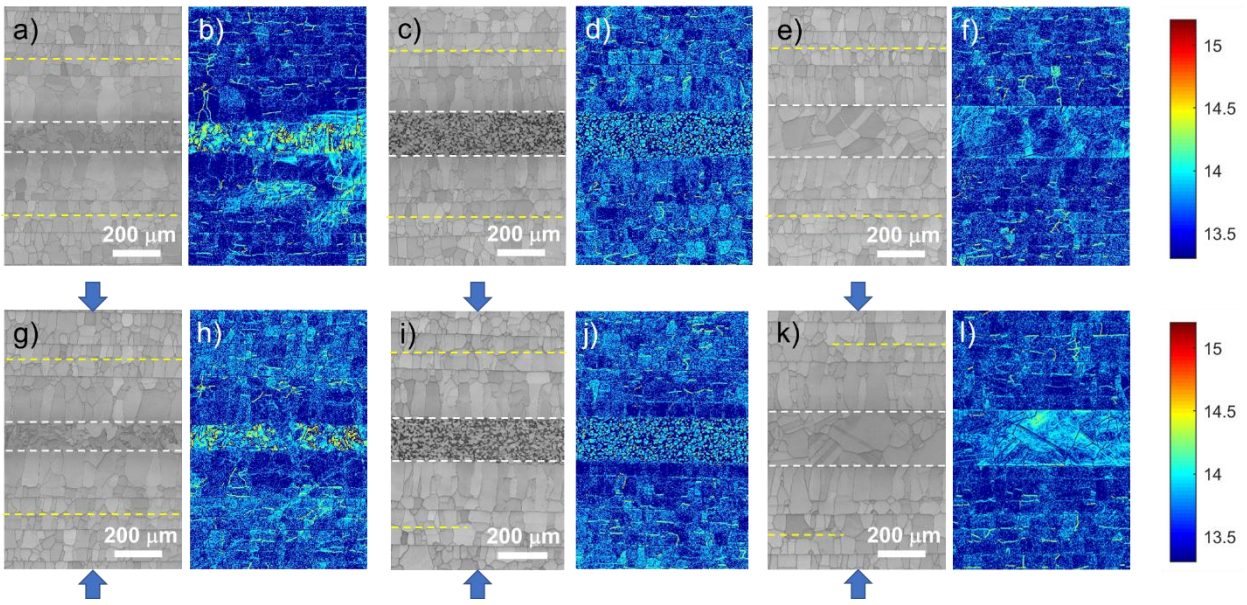

Figure 4.H6: EBSD band contrast maps of the undeformed (a) Fe-FeAl, (c) 430SS-FeAl and (e) 304SS-FeAl. EBSD band contrast maps after compression testing conducted perpendicular to the layers at 500 MPa: (g) Fe-FeAl, (i) 430SS-FeAl, and (k) 304SS-FeAl. The white dashed lines indicate the boundaries between metals and transition layers, and the yellow dashed lines indicate the boundaries between transition and FeAl layers. (b), (d), (f), (h), (j) and (l) are the corresponding GND density maps using the same color scale. [85]

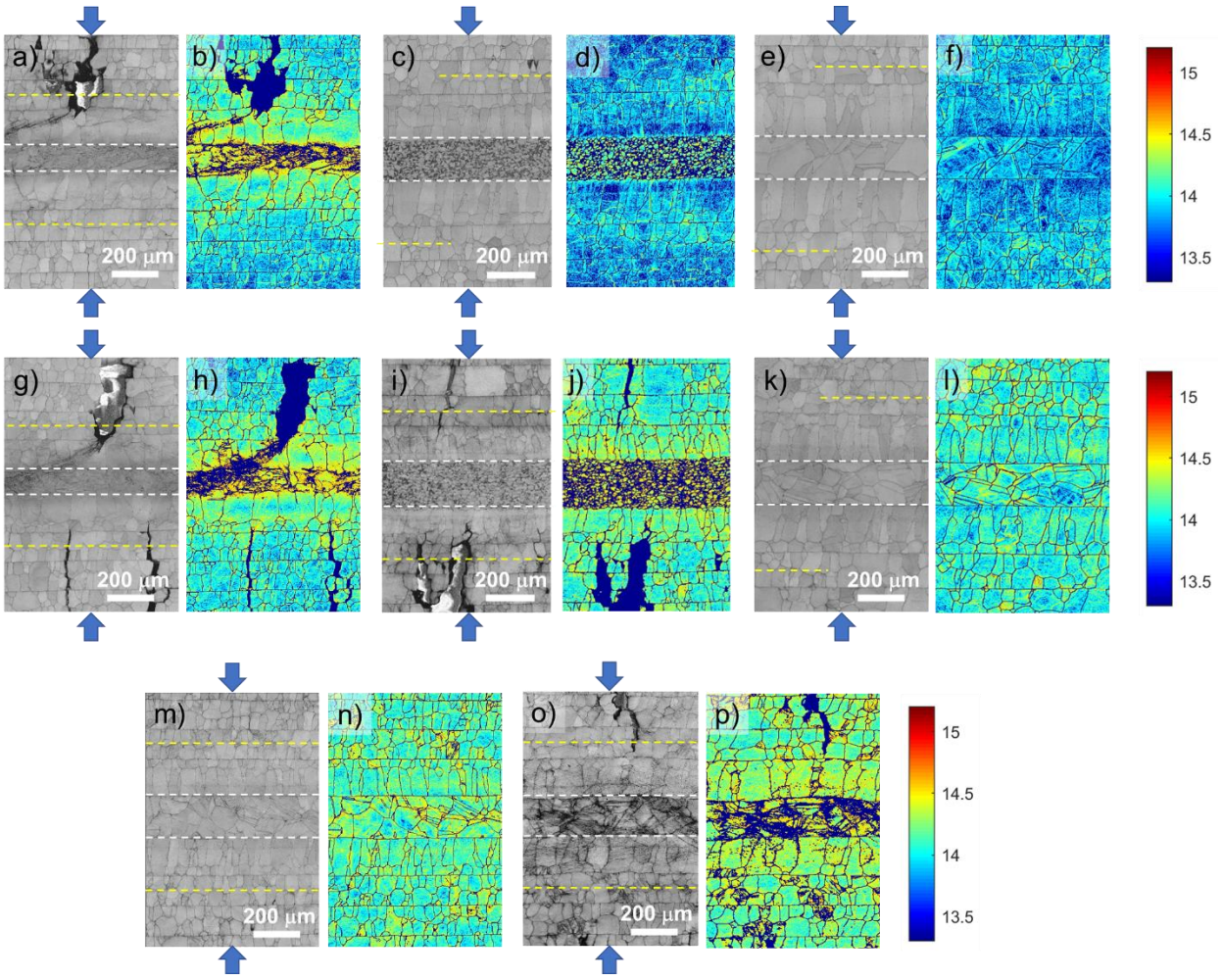

Figure 4.H7: EBSD band contrast maps after compression testing conducted perpendicular to the layers at 1 GPa: (a) Fe-FeAl, (c) 430SS-FeAl, and (e) 304SS-FeAl. EBSD band contrast maps after compression testing conducted perpendicular to the layers: (g) Fe-FeAl failed at 1.25 GPa, (i) 430SS-FeAl failed at 1.39 GPa, (k) 304SS-FeAl with 1.4GPa loading, (m) 304SS-FeAl with 1.8 GPa loading, and (o) 304SS-FeAl failed at 2.3 GPa. The white dashed lines indicate the boundaries between metals and transition layers, and the yellow dashed lines indicate the boundaries between transition and FeAl layers. (b), (d), (f), (h), (j), (l), (n) and (p) are the corresponding GND density maps using the same color scale. [85]

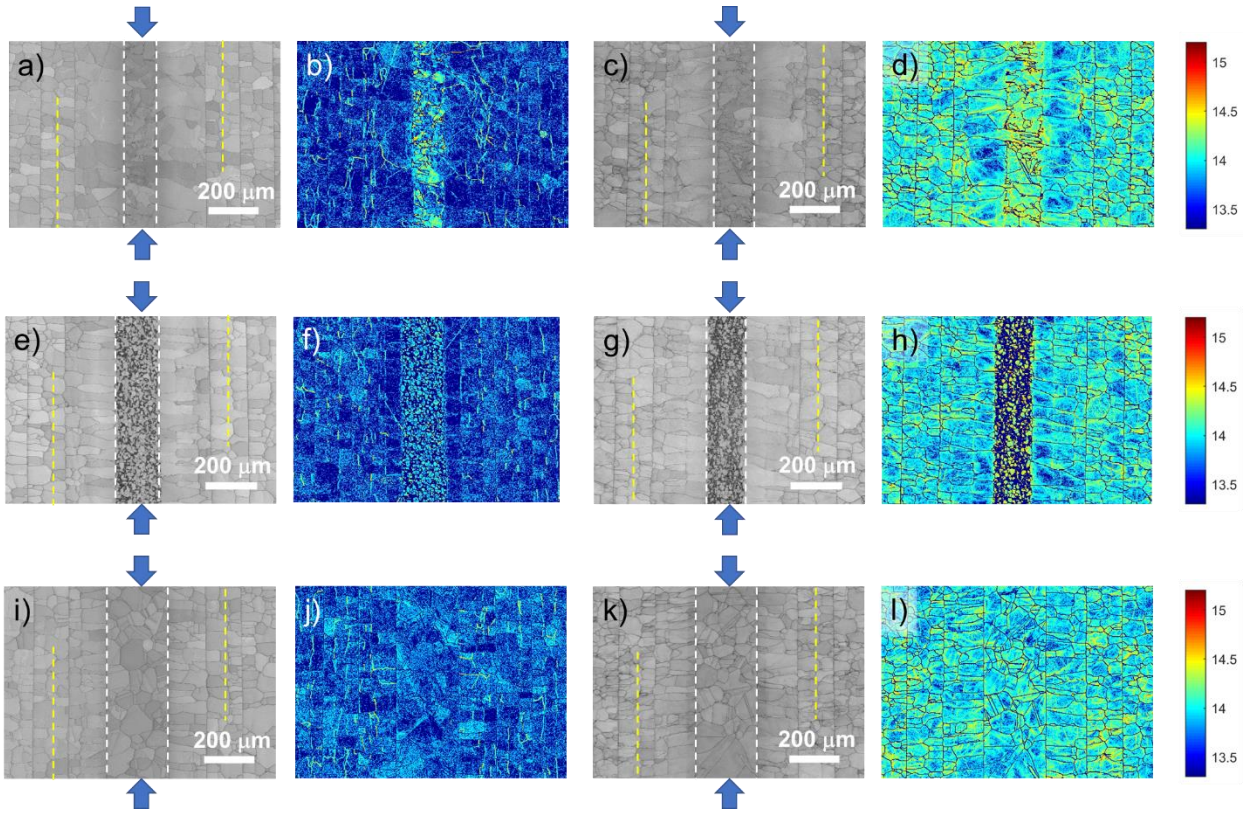

Figure 4.H8: EBSD band contrast maps after compression testing conducted parallel to the layers at 500 MPa: (a) Fe-FeAl, (e) 430SS-FeAl, and (i) 304SS-FeAl. EBSD band contrast maps after compression testing conducted parallel to the layers at 1 GPa: (c) Fe-FeAl, (g) 430SS-FeAl, and (k) 304SS-FeAl. The white dashed lines indicate the boundaries between metals and transition layers, and the yellow dashed lines indicate the boundaries between transition and FeAl layers. (b), (d), (f), (h), (j) and (l) are the corresponding GND density maps using the same color scale. [85]

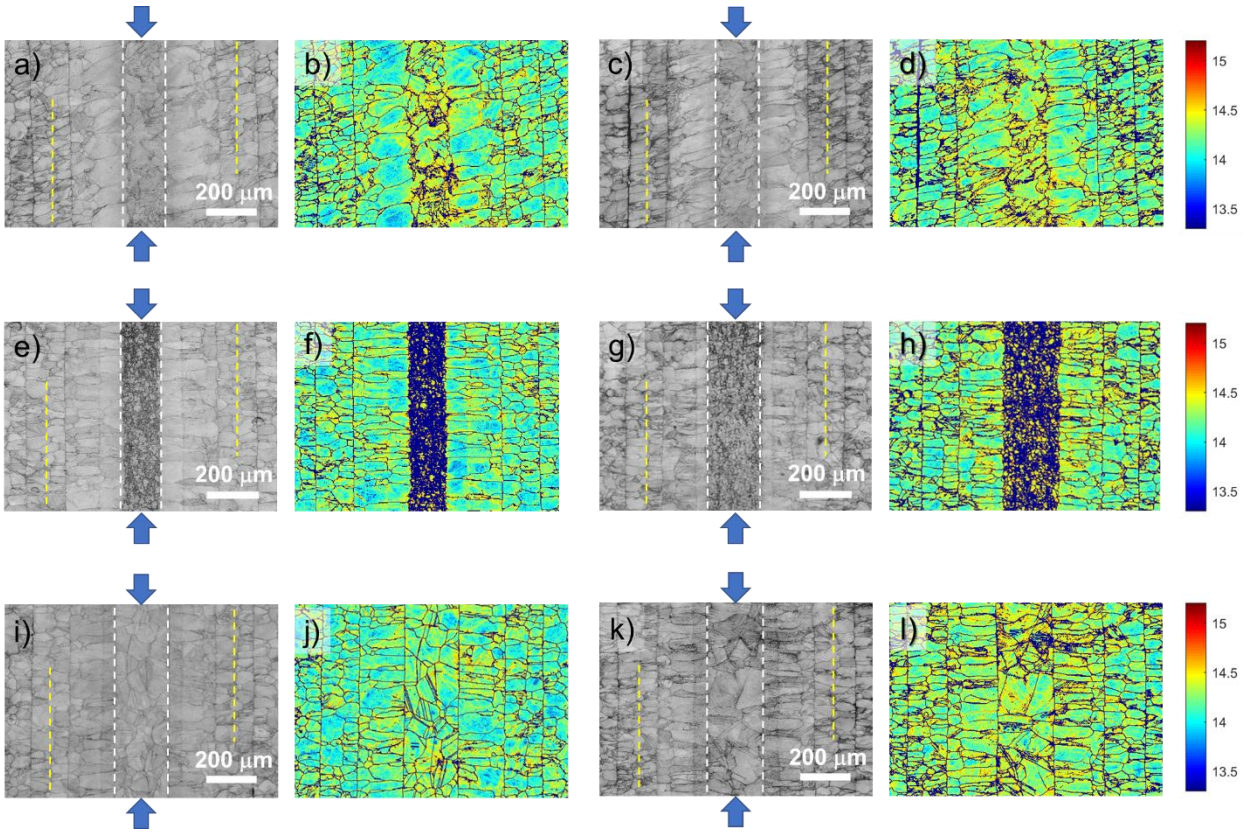

Figure 4.H9: EBSD band contrast maps after compression testing conducted parallel to the layers at 1.4 GPa: (a) Fe-FeAl, (e) 430SS-FeAl, and (i) 304SS-FeAl. EBSD band contrast maps after compression testing conducted parallel to the layers: (c) Fe-FeAl failed at 1.75 GPa, (g) 430SS-FeAl failed at 1.76 GPa, and (k) 304SS-FeAl failed at 2 GPa. The white dashed lines indicate the boundaries between metals and transition layers, and the yellow dashed lines indicate the boundaries between transition and FeAl layers. (b), (d), (f), (h), (j) and (l) are the corresponding GND density maps using the same color scale. [85]

Appendix 4.J 3D FEA Simulation for MIL Composites

As the symmetry of MIL composites provides us the convenience to utilize 2D FEA simulation to investigate the external and internal stress distribution under loading, we also set up a 3D FEA simulation to validate the conclusion. The 3D simulation dramatically increases the number of finite element meshes and consequently requires exponential more computation power and computation time.

In Figure 4.J1(a), for compression perpendicular to the layers, the bottom face was fixed, as its displacement in the y-direction would always be zero but free to evolve in x and z directions; the displacement of the top face in the y-direction was manually tuned to reach the desired loading level, and it is free to evolve in x and z directions. Similarly, In Figure 4.J1(b), for compression parallel to the layers, the bottom face was fixed, as its displacement in the y-direction would always be zero but free to evolve in x and z directions; the displacement of the top face in the y-direction was manually tuned to reach the desired loading level, and it is free to evolve in x and z directions.

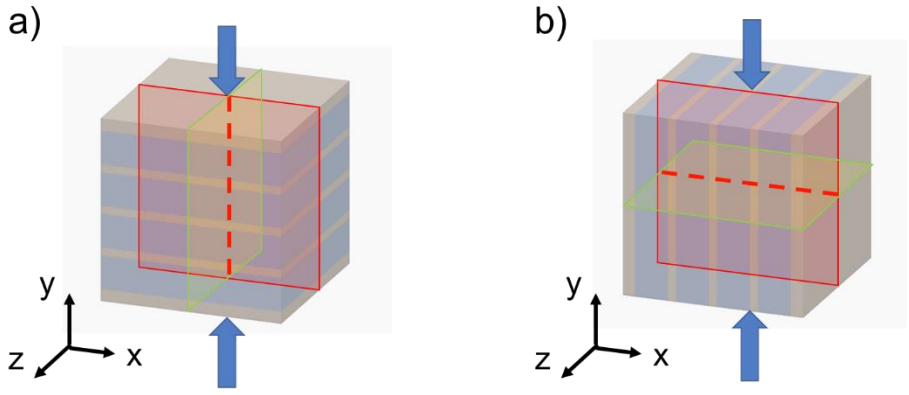

Figure 4.J1: Define the axes for 3D FEA simulation: (a) compression perpendicular to the layers, (b) compression perpendicular to the layers. The red and green planes are the mid-plane cross sections for plotting stress distribution maps; the red dash line is the central axis, along which to plot the stress distribution curves.

Figure 4.J2 plots the stress distribution in the X-Y mid-plane cross section of a MIL composite with soft transition layers (300 MPa yield strength, 3 GPa working hardening rate) under 1.4 GPa compression perpendicular to the layers. The distribution of σ_{XX}, σ_{YY} and σ_{XY} are very close to the results shown in Figure 4.5(b), 4.5(a) and 4.5(c), which were simulated in 2D. The shear stresses σ_{XZ} and σ_{YZ} are almost zero, supporting the conclusion that the shear stresses are insignificant for FeAl-based MIL composites. The distribution of σ_{ZZ} is slightly different from σ_{XX} in the edge region, but the difference does not indicate the broken symmetry between X and Z directions. The difference arises from the orientations of the cross section. As plotted in Figure 4.J3, the stress distribution in Z-Y mid-plane cross section, σ_{YY} in 2(b) is very similar to σ_{ZZ} in 3(c), σ_{ZZ} in 2(c) is very similar to σ_{YY} in 3(b), and σ_{XY} in 2(d) is very similar to σ_{YZ} in 3(f).

Furthermore, Figure 4.J4 plots the stress distribution in the X-Y mid-plane cross section of a MIL composite with hard transition layers (900 MPa yield strength, 8 GPa working hardening rate) under 1.4 GPa compression perpendicular to the layers. The distribution of σ_{XX}, σ_{YY} and σ_{XY} are very close to the results shown in Figure 4.5(e), 4.5(d) and 4.5(f).

As shown in Figure 4.J2(g) and 4.J4(g), the stress distribution across the thickness along the central axis, σ_{XX} is almost identical to σ_{ZZ}, as the fluctuation only occurs after the decimal point. Meanwhile the mesoscale HDI stress (σ_{XX} and σ_{ZZ}) obtained from the 3D FEA simulation, which is 400 MPa in the soft specimen and 810 MPa in the hard specimen, is slightly lower than the 2D simulation (480 MPa in the soft specimen and 910 MPa in the hard specimen). The 15% decrease on average relates to the introduction of the third dimension in the simulation. On the other hand, the magnitude and the tendency stay the same, and would not affect the conclusions about the mesoscale HDI stress.

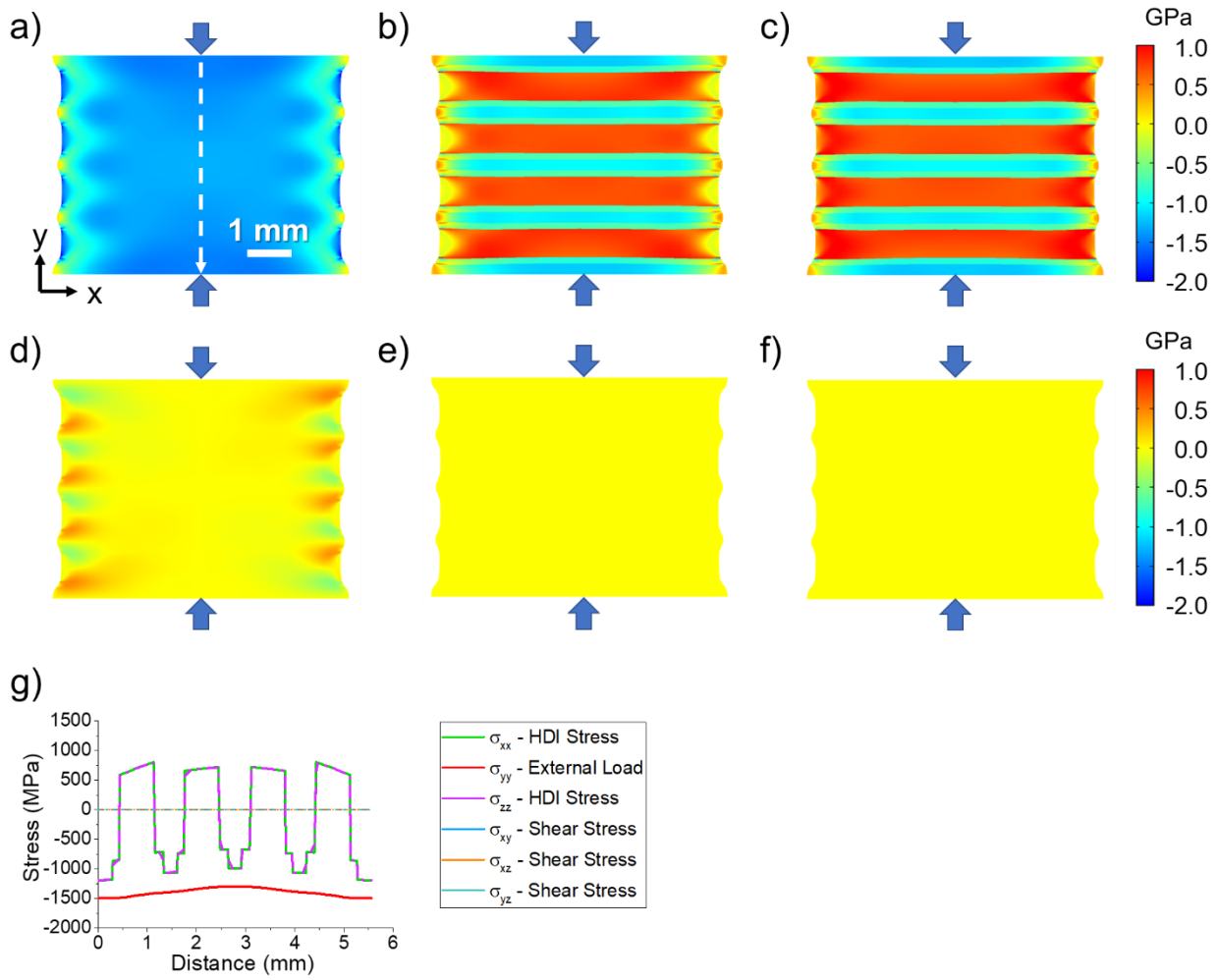

Figure 4.J2: (a) External stress distribution (σ_{YY}), (b) HDI stress distribution (σ_{XX}), (c) HDI stress distribution (σ_{ZZ}), (d) shear stress distribution (σ_{XY}), (e) shear stress distribution (σ_{XZ}), (f) shear stress distribution (σ_{YZ}), and (g) stresses across the thickness of a MIL composite that possesses soft transition layers and is compressed to 1.4 GPa in the perpendicular direction.

Figure 4.J5 plots the stress distribution in the X-Y mid-plane cross section of a MIL composite with soft transition layers (300 MPa yield strength, 3 GPa working hardening rate) under 1.4 GPa compression parallel to the layers. The distribution of σ_{YY} is very close to the results shown in Figure 4.8(a), which was simulated in 2D. The shear stresses σ_{XY}, σ_{XZ} and σ_{YZ} are almost zero, supporting the conclusion that the shear stresses are negligible for FeAl-based MIL composites. The mesoscale HDI stress σ_{XX} is blew 1 MPa; the other mesoscale HDI stress σ_{ZZ} is 5 MPa as compressive on metal layers, and 8 MPa as tensile on FeAl layers. The non-zero

σ_{XX} and σ_{ZZ} arises from the deformation stage between the yield of metal layers and the yield of FeAl layers. At this regime, the Poisson's ratio of the metal layers would be 0.5 as plastic deformation, and the Poisson's ratio of the FeAl layers would be 0.33 for elastic deformation. The difference in Poisson's ratio would induce different Poisson's expansion in the Z direction among the layers, and consequently induce mesoscale HDI stress. As the external load further increases, after the yield of the FeAl phase, the Poisson's ratio of all the layers would be the same again as 0.5, because all the layers deform plastically. The amount of deformation between the yield of metal layers and the yield of FeAl layers is relatively small compared to the total deformation, so the HDI stress induced by this mechanism is two orders of magnitude smaller than the HDI stress in perpendicular loading conditions. The stress at a few MPa level is not expected to cause any significant effect.

Figure 4.J6 plots the stress distribution in Z-X mid-plane cross section, further proving that the stresses distribute uniformly when the MIL composites were loaded parallel to the layers. Among the entire stress tensor, only the external stress (σ_{YY}) is significantly non-zero, whereas other stresses are negligible. Meanwhile, Figure 4.J7 plots the stress distribution in the X-Y mid-plane cross section of a MIL composite with hard transition layers (900 MPa yield strength, 8 GPa working hardening rate) under 1.4 GPa compression parallel to the layers. The stress distribution maps and curves are very close to the 2D simulation in Figure 4.8. The HDI stress σ_{XX} is blew 1 MPa; the other HDI stress σ_{ZZ} is 6 MPa as compressive on metal layers, and 5 MPa as tensile on FeAl layers.

In summary, although 3D FEA simulation would be more accurate and realistic to estimate the stresses in MIL composites, the results are similar to the 2D simulation, which is more efficient to conduct. As the difference is quite small, all the conclusions stay the same.

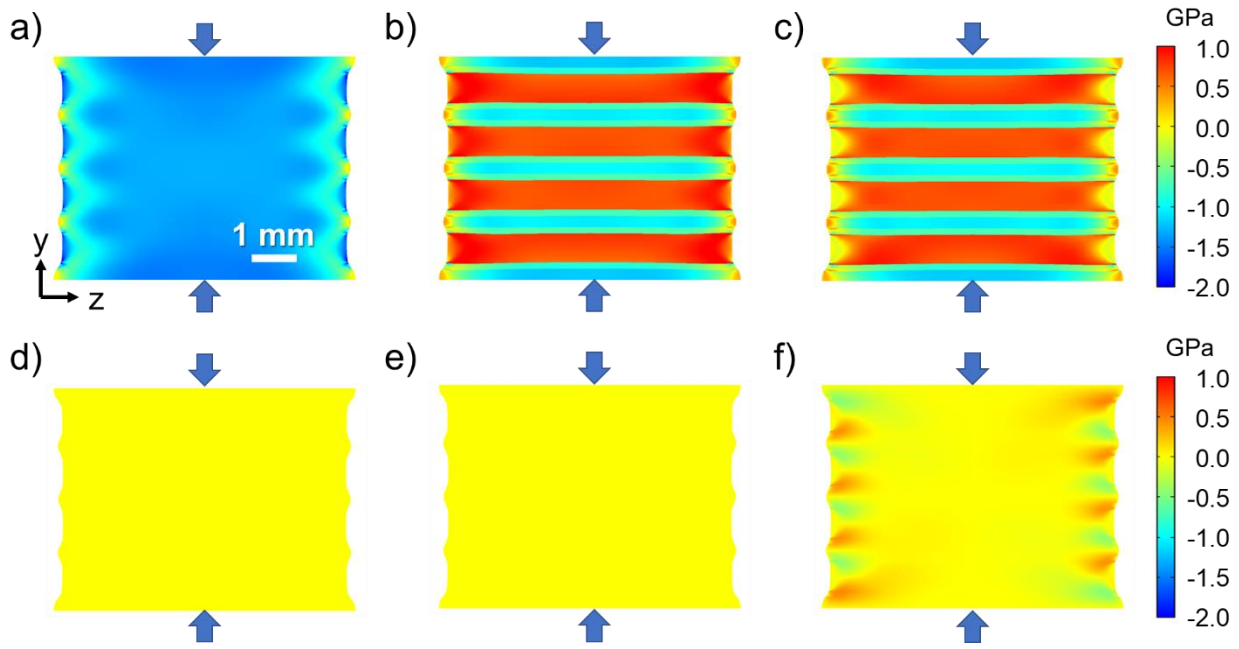

Figure 4.J3: (a) External stress distribution (σ_{YY}), (b) HDI stress distribution (σ_{XX}), (c) HDI stress distribution (σ_{ZZ}), (d) shear stress distribution (σ_{XY}), (e) shear stress distribution (σ_{XZ}), and (f) shear stress distribution (σ_{YZ}) of a MIL composite that possesses soft transition layers and is compressed to 1.4 GPa in the perpendicular direction.

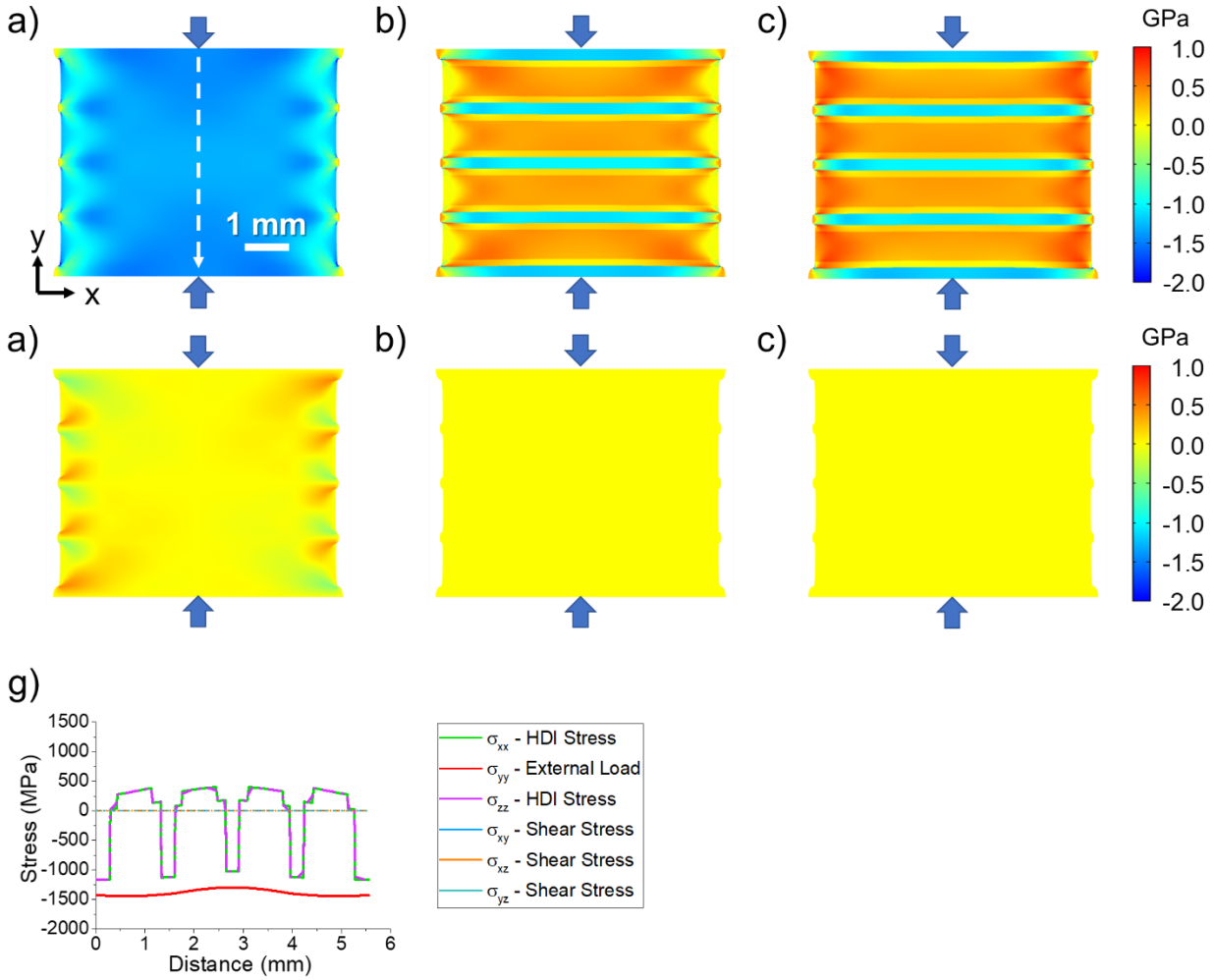

Figure 4.J4: (a) External stress distribution (σ_{YY}), (b) HDI stress distribution (σ_{XX}), (c) HDI stress distribution (σ_{ZZ}), (d) shear stress distribution (σ_{XY}), (e) shear stress distribution (σ_{XZ}), (f) shear stress distribution (σ_{YZ}), and (g) stresses across the thickness of a MIL composite that possesses hard transition layers and is compressed to 1.4 GPa in the perpendicular direction.

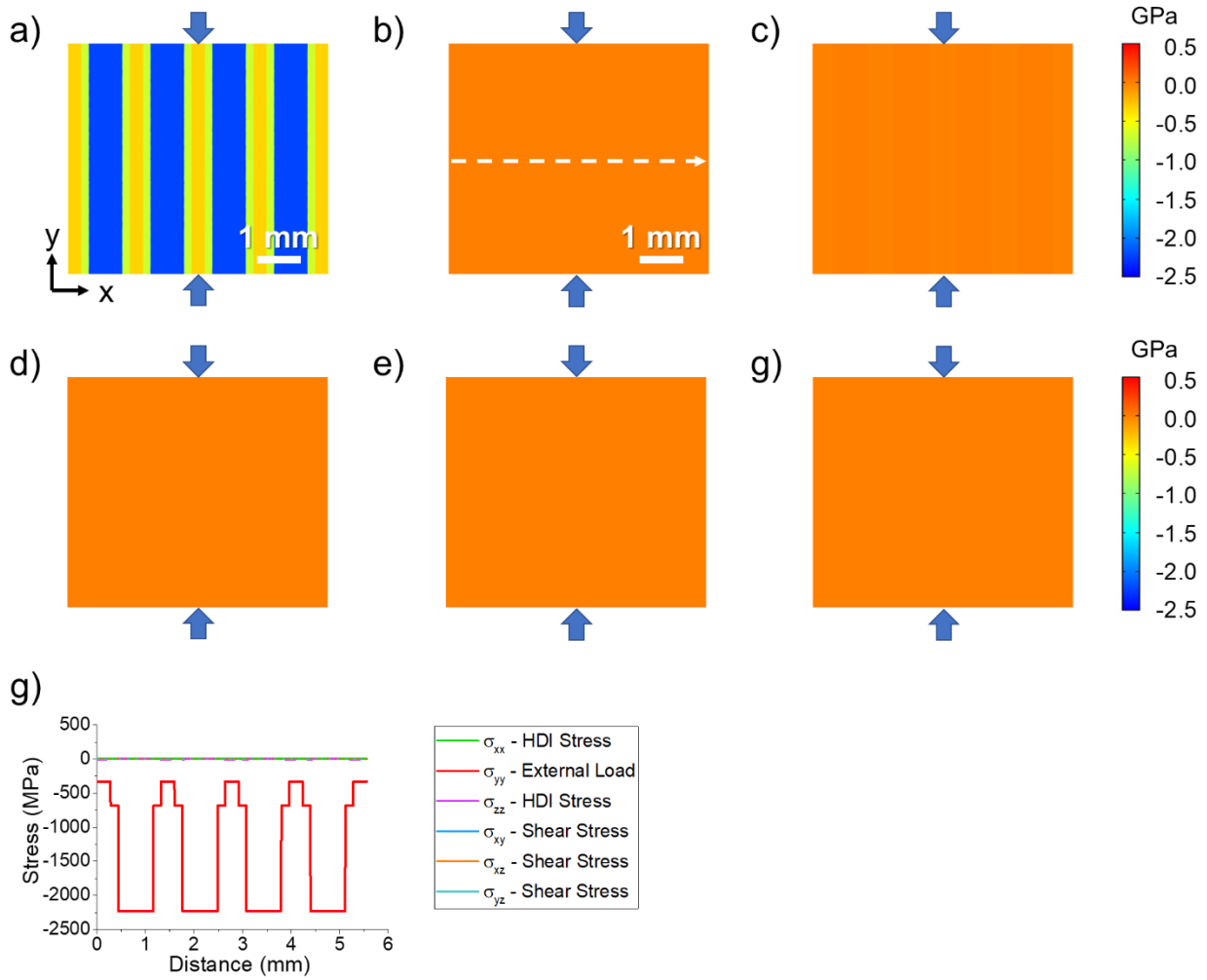

Figure 4.J5: (a) External stress distribution (σ_{YY}), (b) HDI stress distribution (σ_{XX}), (c) HDI stress distribution (σ_{ZZ}), (d) shear stress distribution (σ_{XY}), (e) shear stress distribution (σ_{XZ}), (f) shear stress distribution (σ_{YZ}), and (g) stresses across the thickness of a MIL composite that possesses soft transition layers and is compressed to 1.4 GPa in the parallel direction.

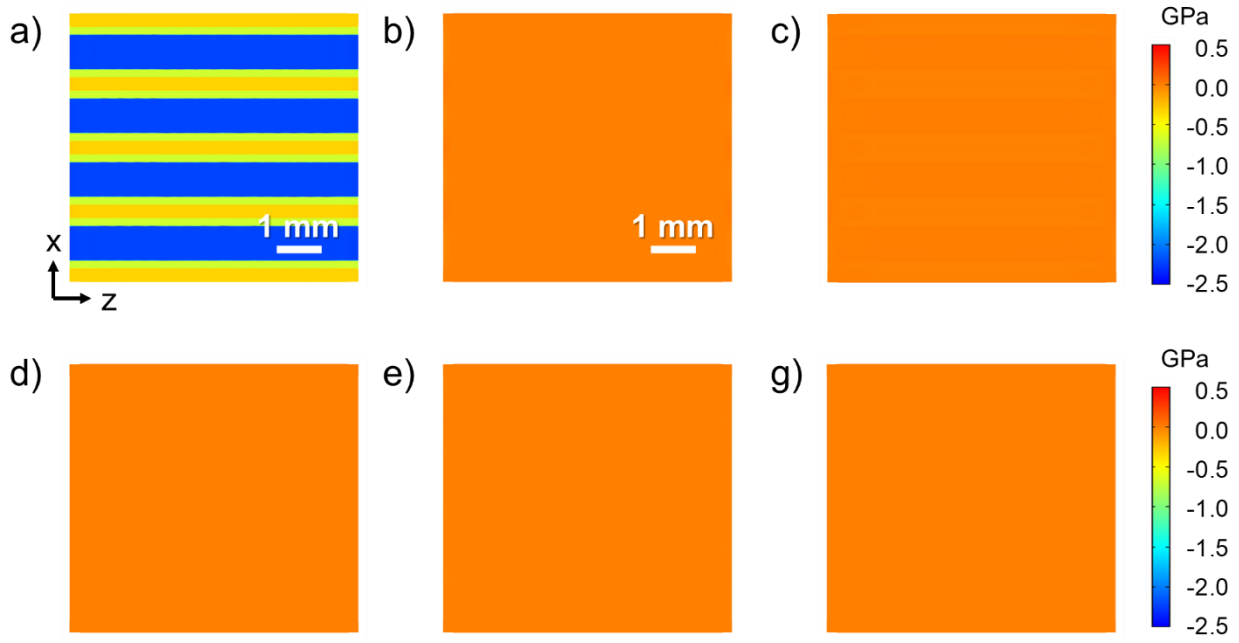

Figure 4.J6: (a) External stress distribution (σ_{YY}), (b) HDI stress distribution (σ_{XX}), (c) HDI stress distribution (σ_{ZZ}), (d) shear stress distribution (σ_{XY}), (e) shear stress distribution (σ_{XZ}), and (f) shear stress distribution (σ_{YZ}) of a MIL composite that possesses soft transition layers and is compressed to 1.4 GPa in the parallel direction.

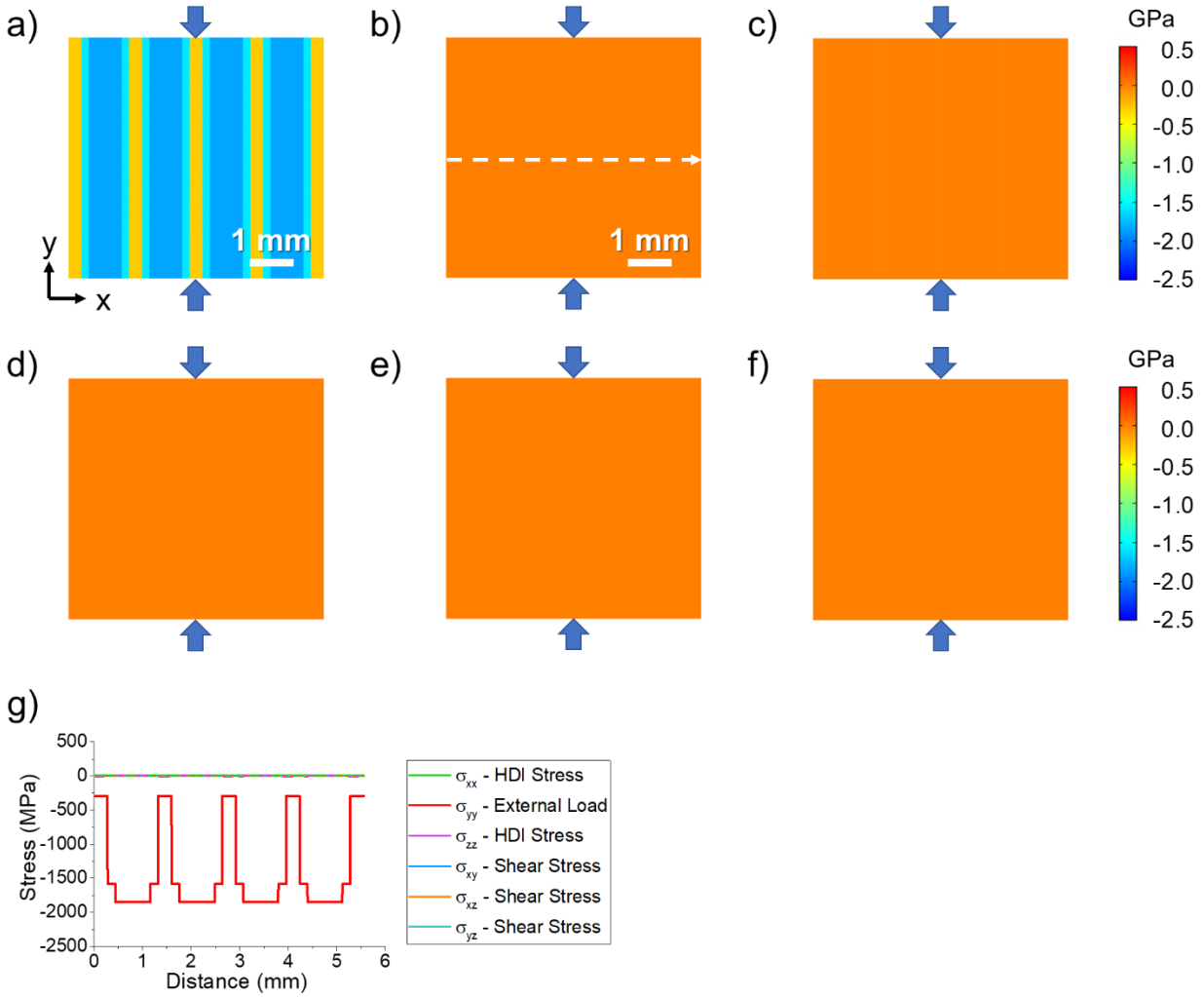

Figure 4.J7: (a) External stress distribution (σ_{YY}), (b) HDI stress distribution (σ_{XX}), (c) HDI stress distribution (σ_{ZZ}), (d) shear stress distribution (σ_{XY}), (e) shear stress distribution (σ_{XZ}), (f) shear stress distribution (σ_{YZ}), and (g) stresses across the thickness of a MIL composite that possesses hard transition layers and is compressed to 1.4 GPa in the parallel direction.

Appendix 4.K Composition Analysis for Metal Foils

Table 4.K1 lists the detailed composition analysis of the metal foils for producing MIL composites and single phase FeAl samples. The information is provided by the vendors, and the results are in wt%.

Table 4.K1: Composition analysis for metal foils.

	Fe	Al	Cr	Ni	Mn	Mo	Si	C	P	S	Cu	Zn
304SS	72.64	/	18	8	0.8	/	0.5	0.06	<0.06	<0.06	/	/
430SS	81.15	/	17.5	/	0.5	0.3	0.4	0.08	0.04	0.03	/	/
Pure Fe	99.5	/	/	/	0.3	/	0.1	<0.08	<0.04	<0.05	/	/
Pure Al	<0.4	99.5	/	/	<0.05	/	<0.3	/	/	/	<0.05	<0.1

Acknowledgment

Chapter 4, in full, is the reprint of the published article in Acta Materialia, Elsevier: Wang, Haoren; Kou, Rui; Yi, Haozhe; Figueroa, Samuel; Vecchio, Kenneth S. Mesoscale Hetero-Deformation Induced (HDI) Stress in FeAl-Based Metallic-Intermetallic Laminate (MIL) Composites. Acta Materialia (2021).

I would like to thank Rui Kou, Haozhe Yi, Samuel Figueroa, and my principal investigator Professor Kenneth Vecchio, for their contribution in this work.

Chapter 5 Design, Fabrication and Optimization of FeAl-$FeAl_2$ Eutectoid MIL Composites

Chapter 5, in full, is the reprint of the published article in Materialia, Elsevier: Wang, Haoren; Kou, Rui; Vecchio, Kenneth S. Design, Fabrication and Optimization of FeAl-$FeAl_2$ Eutectoid Metallic-Intermetallic Laminate (MIL) Composites. Materialia (2020).

Abstract

FeAl/$FeAl_2$ eutectoid metallic-intermetallic laminate (MIL) composites were synthesized using a "multiple-thin-foil" configuration and a "two-stage reaction" strategy. Microstructure analysis via scanning electron microscope (SEM), energy-dispersive X-ray spectrometer (EDS) and electron backscatter diffraction (EBSD) confirms the formation of a two-intermetallic eutectoid structure, which decomposes from the high-temperature Fe_5Al_8 phase. The metal layers of eutectoid-MIL composites are fabricated with either pure iron or two different stainless steels without altering the intermetallic regions. The volume fraction of eutectoid layers is adjusted for optimizing the performance. The off-eutectoid phase is switched between FeAl and $FeAl_2$ to investigate the effect on strength and ductility. The microstructure of the interfacial regions is fine-tuned, further demonstrating the ability to independently control the constituents of MIL composites. Additionally, a hybrid MIL composite of FeAl and the eutectoid structure are synthesized as a 'proof-of-concept'. Finite element analysis (FEA) simulation is utilized to study the internal stress in the MIL composites from a macroscopic point of view. Incremental compression tests were conducted to track the fracture evolution from a microscopic point of view.

5.1 Introduction

Metallic-intermetallic laminate (MIL) composites are metal matrix materials, as layers of brittle intermetallics are incorporated with layers of ductile metals for enhanced mechanical performance. Generally, aluminide-intermetallics possess ordered, low-symmetry crystalline structures, which induce high specific modulus and high specific strength, but limit the toughness and plasticity. The toughness of intermetallics can be enhanced by reinforcing with particles, fibers or layers of ductile metals [1], so that the materials become more effective for unique structural applications.

MIL composites are commonly synthesized via hot pressing alternating stacked dissimilar metal foils to form intermetallic layers by interdiffusion and chemical reactions. By the selection of initial metal foils, the properties of MIL composites can be tuned to fulfill specific performance requirements. The ability to tailor the properties, as well as the utilization of low-cost metal foils, makes MIL composites ideal for structural applications like aerospace vehicles, which require lightweight materials with high specific properties. Furthermore, MIL composites can be synthesized with complex geometry for specific platforms by adjusting the shape of initial metal foils [2]. As an example, the pathway for sensors can be incorporated into MIL composites by machining cavities on initial metal foils, so that the deformation and damage can be in-situ monitored [2].

Layered metallic-intermetallic structures were first synthesized in 1989 using the combustion wave approach [3], although the ability to control microstructure or properties was inherently limited by the self-sustaining reaction kinetics. In 2001, Harach and Vecchio [4] introduced a new concept for fabricating MIL composites, whereby the materials were reactive sintered under moderate temperature and pressure conditions to control the formation of the

intermetallics. Subsequent investigations mostly focused on the Ti-Al MIL system [5–13], due to the very high specific stiffness of these MIL composites. However, Al_3Ti is the only intermetallic phase formed in the Ti-Al system due to limited diffusivity, whereas its very limited plasticity restricts the ability to significantly tailor the performance of the composites. Consequently, the studies of MIL composites were extended to the Ni-Al system [14–16] and Fe-Al system [17–19], aiming for ductile intermetallics, such as the FeAl phase [21–23].

In our previous work, the fabrication process was modified by introducing an innovative foil stack configuration, so that MIL composites with intermetallic regions of single-phase FeAl can be synthesized [77]. Furthermore, we have demonstrated that the metal layers of pure iron in FeAl-MIL can be replaced by stainless steel alloys, without altering the composition or microstructure of intermetallic regions. Among all MIL composites to date [5,15,32,33,24–31], FeAl-MIL exhibits the highest levels in both compressive strength and ductility. The deformation and fracture evolution of FeAl-MIL was recently analyzed using geometrically necessary dislocation (GND) density measurements, to correlate the mechanical response with variation in loading conditions [85].

In the present study, another new type of MIL composite in the Fe-Al system is created by forming the eutectoid structure of FeAl and $FeAl_2$ as the intermetallic regions. The $FeAl_2$ phase, which possesses a triclinic structure, is hard, but extremely brittle. Meanwhile, the lamellar nature of the eutectoid structure itself can be regarded as a natural form of composite, wherein the fine-scale lamellar $FeAl_2$ phase is toughened by the fine-scale, relatively ductile FeAl phase [40–42].

For these eutectoid-MIL composites, the metal layers and volume fraction of the eutectoid structure are varied for optimizing the performance. Heat treatment is utilized to fine-tune the microstructure, demonstrating another approach to adjust the properties rather than only the initial

foil combination. Furthermore, a new hybrid MIL composite, which possesses both single phase FeAl layers and FeAl-$FeAl_2$ eutectoid layers, are synthesized as a 'proof-of-concept' of tailoring structure to performance. Incremental compression testing and finite element analysis (FEA) simulations were conducted to evaluate the mechanical properties and investigate the fracture evolution mechanisms.

5.2 Experimental

5.2.1 Material Processing

Commercially pure aluminum (Goodfellow Cambridge Limited, 99.5%), pure iron (Goodfellow Cambridge Limited and Advent Research Ltd, 99.5%), 430SS (Trinity Brand Industries, 18wt% Cr) and 304SS (Trinity Brand Industries, 18 wt% Cr and 8 wt% Ni) foils were used to fabricate the FeAl-$FeAl_2$ eutectoid MIL composites. The foils were scrubbed using steel wool pads to remove surface containments, and rinsed in acetone for ultrasonic cleaning. Subsequently, the foils were cut into 20-mm-diameter disks, and alternatively stacked in the "multiple-thin-foil" configuration demonstrated in Figure 5.1(a). The relatively thick Fe and/or stainless steel foils (300 μm) would be mostly retained as remnant metal layers in the MIL composites, whereas the alternatingly stacked Al-Fe-Al-Fe thin foils (the combination of 100-μm-thick Al and 50-μm-thick Fe) are designed to transform into the FeAl-$FeAl_2$ eutectoid structure. In addition, there is an extra layer of Fe (100 or 75 μm) to isolate the stainless steel foil from Al foil, to avoid the formation of brittle aluminide with the alloying elements in the stainless steels. The purpose of the "multiple-thin-foil" configuration is to control the chemical composition of the intermetallic regions through short-range diffusion. Details about the "multiple-thin-foil"

configuration have been discussed in our previous study [77]. Furthermore, the metal/intermetallic ratio can be adjusted by changing the number of layers of the "multiple-thin-foil" ensembles.

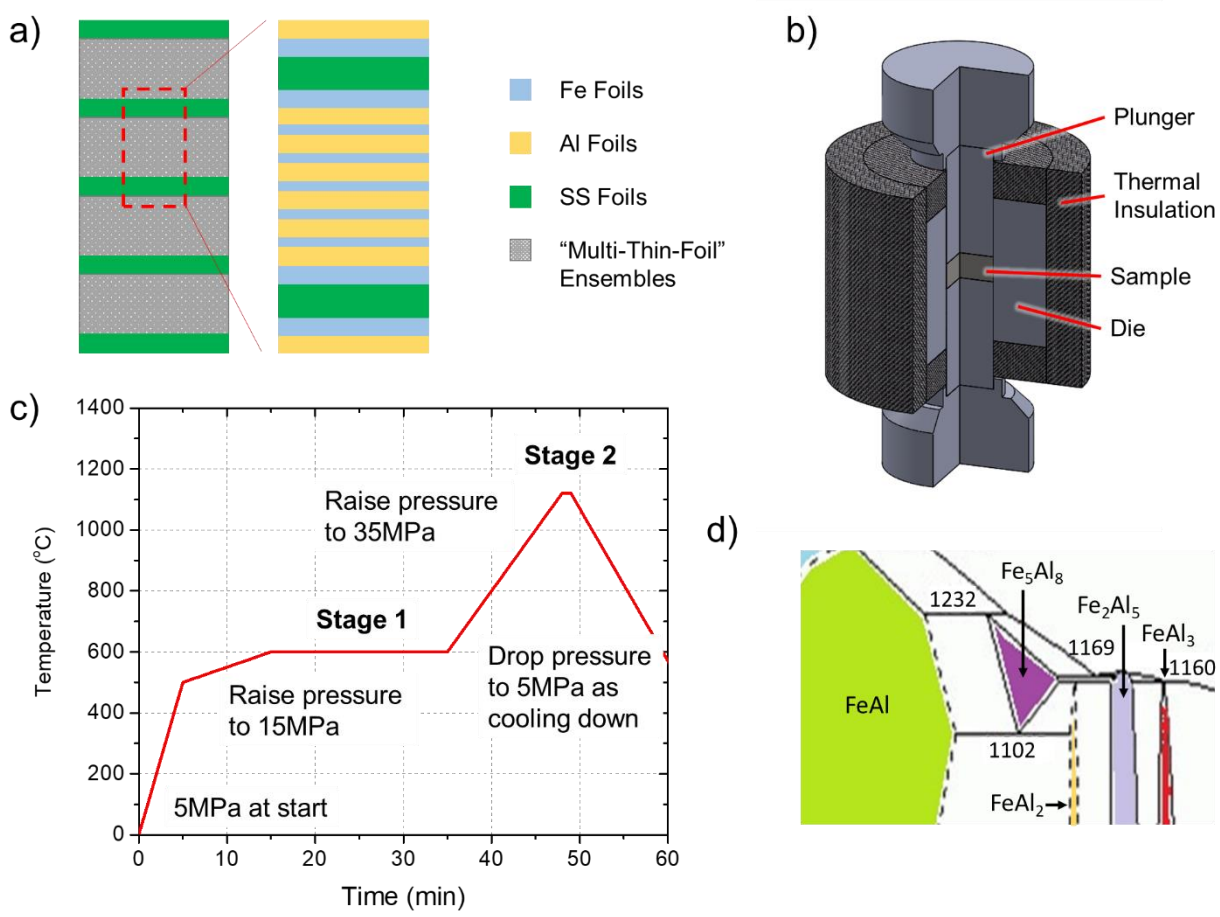

Figure 5.1: (a) The metal foils stack configuration for synthesizing the eutectoid MIL composites. (b) Schematic diagram of SPS setup [77,78,85]. (c) Sintering parameters. (d) Zoomed in Fe-Al phase diagram [67].

The stacked foils were wrapped with molybdenum foil and graphite foil to prevent contamination, and placed into the sintering assembly illustrated in Figure 5.1(b) [77,78]. The assembly was loaded into a Thermal Technology Model GTAT 10-3 Spark Plasma Sintering (SPS, a.k.a. field-assisted sintering) machine for reactive sintering. A representative sintering profile is plotted in Figure 5.1(c). Al layers will completely transform into aluminide in stage one, so that the sintering temperature can be raised above the melting point of aluminum. As demonstrated by

the Fe-Al binary phase diagram [67] in Figure 5.1(d), the high-temperature Fe_5Al_8 phase forms in stage two, which then decomposes into the FeAl phase and $FeAl_2$ phase during cooling.

5.2.2 Characterization

The sintered samples were mounted with the layers perpendicular to the cross-sections, then ground and polished following standard metallographic preparation procedures. The microstructure, chemical composition and grain orientation were characterized using a Thermo-Fisher (formerly FEI) Apreo scanning electron microscope (SEM) equipped with an Oxford Instrument's Symmetry Electron Backscatter Diffraction (EBSD) system and an Oxford Instrument's Energy-Dispersive X-ray Spectrometer (EDS).

After sintering, the MIL composite tablets were cut into 6 mm cubes, then ground and polished following standard ASTM E-9 for compression testing. Strain gauges were mounted to the specimens, and quasi-static compression tests were conducted using a standard screw-driven load frame. Due to the limited measurement range of the strain gauge, large deformation is determined using the displacement of the load frame crosshead, and corrected by the specimen height change after the test. The strain rate used was 10^{-3}/s, and the sample ends were lubricated with grease to minimize friction. The failure point was defined as the moment when the reading of load undergoes a significant drop (>10%). Furthermore, the compression tests were conducted with the load applied either perpendicular or parallel to the layers of MIL composites, referred to hereafter as the 'perpendicular direction' and 'parallel direction', respectively.

5.3 Results

The MIL composites discussed herein contain, for the first time, by design, a two-phase $FeAl/FeAl_2$ eutectoid structure as the intermetallic layer. Figure 5.2(a) presents a low

magnification SEM image of the 304SS-eutectoid MIL composite, to demonstrate the typical structure of the FeAl/$FeAl_2$ eutectoid MIL composites. The relatively brighter layers are the remnant 304SS, which retains the austenite (face-centered cubic) structure during the sintering. Adjacent to the 304SS layers are the chemical gradient regions of α-Fe and FeAl solid solutions, termed as the "transition layer" between the eutectoid structure and 304SS layers. A similar structure also formed in single-phase FeAl-based MIL composites [77], as both types of MIL composites adopt the same design concept. The relatively dark regions are the FeAl/$FeAl_2$ eutectoid structure, which contains more aluminum, and hence lower density. Inherent from the symmetry of the initial foil configuration, the region spanning from the middle of one metal layer to the next can be regarded as a repeating unit representative of the entire sample.

As shown in Figure 5.2(b), the microstructure was investigated via EBSD phase mapping. Compared to the initial foils, the 304SS layers reduce in thickness a small amount, as the alloying elements dissolve into the transition layers. Meanwhile, the transition layers are thicker than the initial Fe foils, primarily due to the diffusion of aluminum from eutectoid regions. The phase mapping also reveals that the eutectoid region is hypoeutectoid, FeAl rich. Unless specified, the term "eutectoid" is used to refer to the intermetallic region of hypoeutectoid (FeAl) + (FeAl/$FeAl_2$). Foils of the exact thickness combination for the composition of the eutectoid point is challenging to obtain, and aluminum will diffuse into the transition layers, and the extent depends on the sintering conditions. Figure 5.2(c) shows an SEM image focusing on the eutectoid region, and the EBSD phase map with the corresponding Euler map are plotted in Figure 5.2(d) and 5.2(e), respectively. Indicated by the Euler map, where the colors are based on the phase orientations, all of the $FeAl_2$ phase is oriented in the same direction within a eutectoid "region", as does the FeAl phase. Inherited from the parent Fe_5Al_8 phase, the FeAl and $FeAl_2$ in the eutectoid regions are

expected to follow certain grain orientation relationships [106–108]. Furthermore, the magnified SEM image and EBSD phase map for the eutectoid region are shown in Figure 5.2(f) and 5.2(g), respectively. The FeAl/$FeAl_2$ eutectoid phase exhibits a lamellar structure, similar to the pearlite structure in carbon steels.

5.4 Discussion

5.4.1 Optimization of FeAl/$FeAl_2$ Eutectoid MIL Composites

The properties of eutectoid MIL composites can be tailored by tuning its constituents to fulfill specific application requirements. However, since MIL composites are synthesized via interdiffusion, adjusting one microstructure feature would inevitably affect other microstructure features. In contrast, the methods for independently adjusting either metal or intermetallic layers are demonstrated herein, creating microstructures that are truly non-equilibrium on the local scale. Furthermore, the mechanical performance of various eutectoid MIL composites are compared to investigate the corresponding effects.

5.4.1.1 Effect of Metal Layers

In these MIL composites, the metal layers quite clearly affect the performance of the overall material. In addition, the alloying elements in the metal layers can diffuse into the transition layers, further influencing their mechanical properties [77,85]. Meanwhile, the magnitude of the influence also depends on the inherent properties of the intermetallic layer. Shown in Figure 5.3(α–c) are SEM images of the Fe-eutectoid, 430SS-eutectoid and 304SS-eutectoid MIL composites, respectively. All three samples utilize the same initial foil configuration, and consequently possess a similar structure, which is described in Table 5.1. The

dark regions in the middle of the images are the hypoeutectoid phase, the bright regions on the left and right edges are the remnant metal layers, and the interfaces are indicated by the dashed line. EDS line scans across the layers are presented in Figure 5.3(d-f). According to the Fe-Al binary phase diagram [67], Al can dissolve into α-Fe (body-centered cubic) up to 50 at%, while a second-order phase transformation (disorder to order) occurs at 25 at%. Rather than randomly occupying all the lattice sites, Al atoms prefer to occupy the body-centered position, defined as the ordered FeAl phase. Consequently, there will form a chemical gradient region as a solid solution between FeAl and α-Fe, which is thereby termed as the "transition layer" in the present work.

As indicated by the blue arrows in Figure 5.3(e) and 5.3(f), the diffusion of Cr and Ni into the Al-rich regions was stopped by the transition layers. Brittle intermetallics form when directly reacting stainless steel with Al [109], whereas the transition layers can dissolve all the undesired intermetallics to enhance the ductility of the composites [77]. Therefore, we are able to select the metal layers for the MIL composites without altering the composition or microstructure of the intermetallics. On the other hand, as demonstrated by the previous work of FeAl-MIL [77] and the present work of eutectoid-MIL, we are able to select intermetallic layers for MIL composites without altering the metal layers.

As indicated by the black arrows in Figure 5.3(e) and 5.3(f), there are peaks in the Fe composition curves. A layer of Fe was inserted between stainless steel foil and Al foil, which eventually becomes the transition layer after sintering. As a result, the Fe concentration in the transition layer could be higher than in the stainless steel layer. Meanwhile, compared to our previous study of FeAl based MIL composites [77], which also formed transition layers, the peaks on the Fe curve are significantly higher in these eutectoid MIL composites. For example, the peak in 304SS-FeAl is at 75 at% Fe [77], while the peak in 304SS-eutectoid is nearly 100% Fe. Since

both materials utilized the 100 μm Fe foils to form the transition layers, the difference results from the sintering condition changes between the two studies.

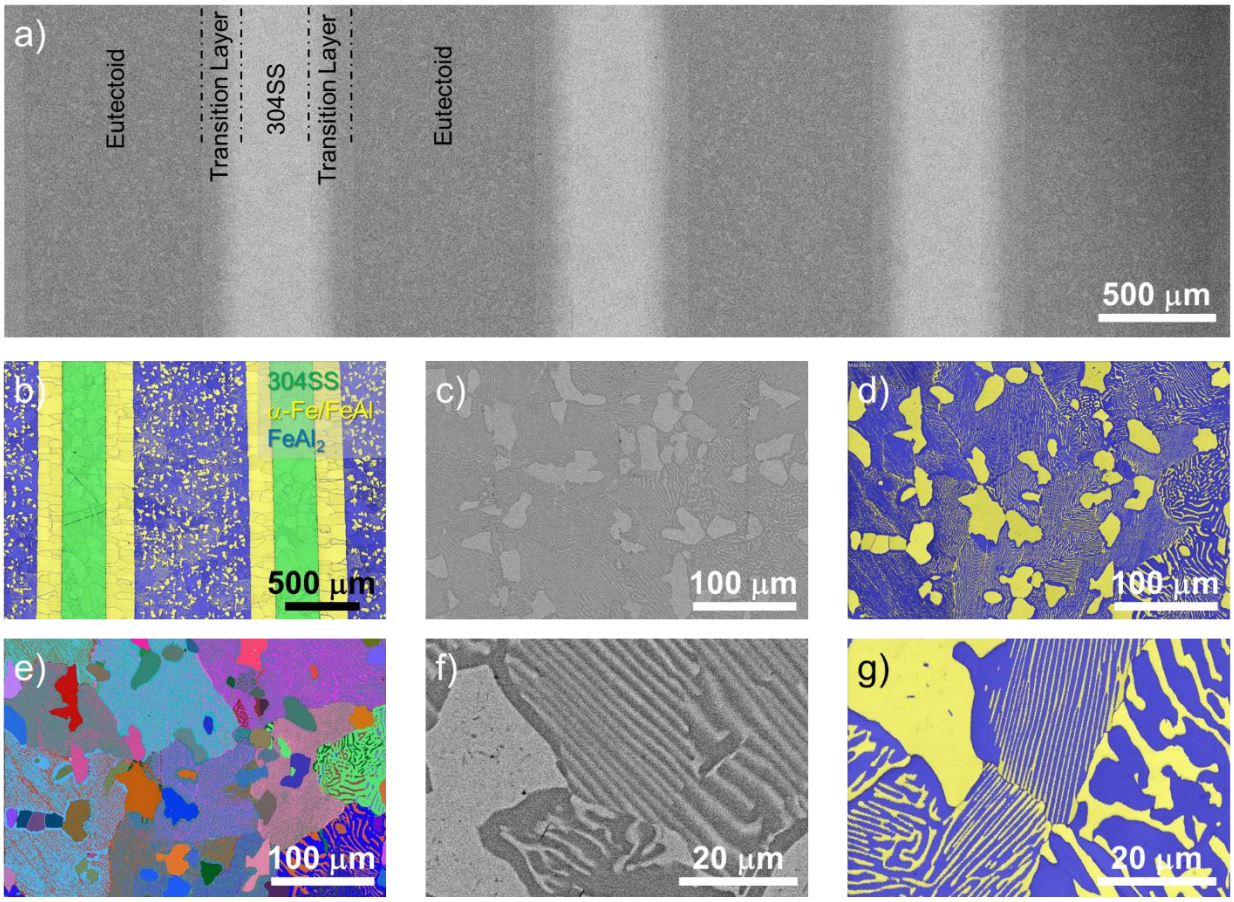

Figure 5.2: (a) SEM image to overview the structure of eutectoid MIL composite. (b) EBSD phase map investigates a "repeat unit" of 304SS-eutectoid. (c) SEM image of the eutectoid region. (d) EBSD phase map of the eutectoid region, and (e) the corresponding Euler map of (d). (f) and (g) are magnified SEM images and EBSD phase map of the eutectoid region, respectively.

Table 5.1 also compares the mechanical performance of the Fe-eutectoid, 430SS-eutectoid and 304SS-eutectoid. The details covering the compression test results are presented in Appendix 5.A. The specimens exhibit ductility and work hardening in the loading perpendicular to the layers, but fail in a brittle manner when loaded parallel to the layers.

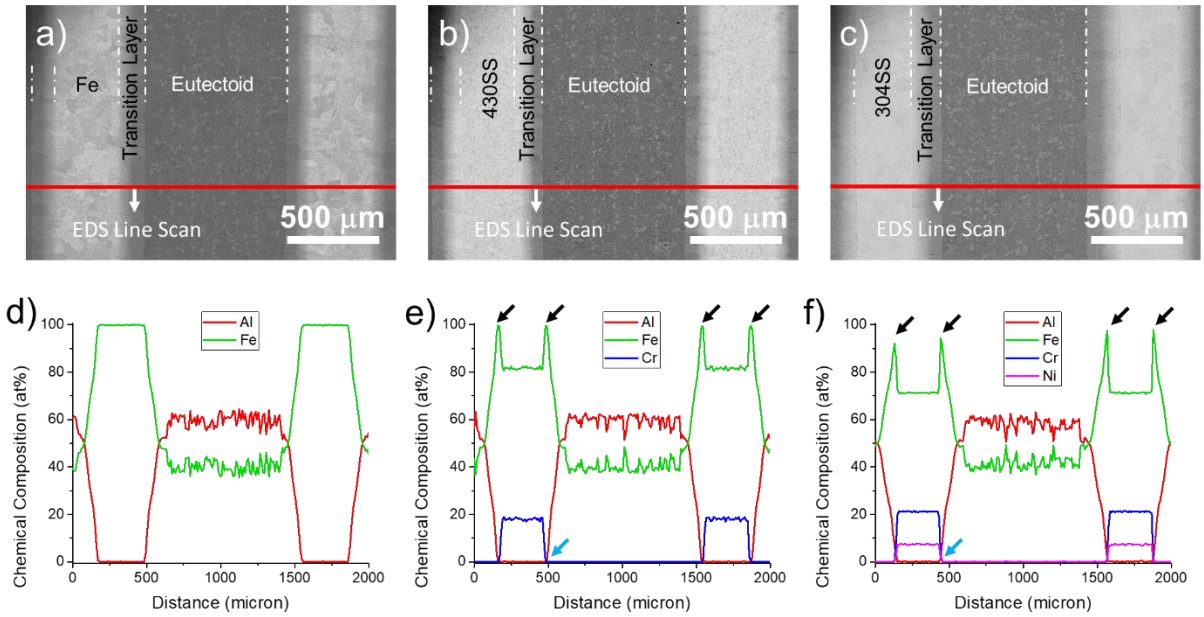

Figure 5.3: SEM images of (a) Fe-eutectoid, (b) 430SS-eutectoid and (c) 304SS-eutectoid MIL composites. (d), (e) and (f) are EDS line scans along the red lines indicated in (a), (b) and (c), respectively.

When compressed in the perpendicular direction, the metal layers yield first, followed by the yielding of transition layers. Subsequently, the formation of cracks in eutectoid layers reduces the slope of the strain-stress curve. The difference in stress-strain response between metals and intermetallics would generate internal stress [85], accelerating the crack growth. 430SS and 304SS are known to possess similar mechanical properties, which are significantly stronger than pure iron. So 430SS-eutectoid MIL and 304SS-eutectoid MIL possess higher strength than the Fe-eutectoid MIL in the perpendicular loading direction. Meanwhile, transition layers are enhanced by the solution strengthening. According to our previous study [85], due to the stronger transition layers, the 304SS-FeAl MIL is nearly 1 GPa stronger than the 430SS-FeAl MIL in the perpendicular loading direction. Such improvement, however, is absent for 304SS-eutectoid MIL. The $FeAl/FeAl_2$ eutectoid structure is significantly stronger, but more brittle than the single phase FeAl, so the eutectoid-based MIL composites are less sensitive to the metal layer materials compared to

the FeAl-based MIL composites. By considering the comparison between 430SS-eutectoid MIL and 304SS-eutectoid MIL, the material selection can be made with lower alloying elements and lower cost metal layers without compromising in the performance.

Table 5.1: Constitution and compression strength of $FeAl/FeAl_2$ eutectoid MIL composites.

Metal Layer	Volume Fraction			Ultimate Strength	
	Metal*	Transition	Eutectoid**	Perpendicular	Parallel
Fe	25%	20%	55%	0.68 GPa	1.52 GPa
430SS	22%	22%	56%	1.13 GPa	1.69 GPa
304SS	22%	24%	54%	1.05 GPa	1.65 GPa

* Excluding α-Fe solid solution in transition layers.

** Including the hypoeutectoid FeAl phase.

In contrast, when compressed parallel to the layers, the internal stress would be considerably smaller [85], and the strength of the composites primarily follows a 'rule of mixtures'. As such, all three eutectoid-MIL composites possess similar compression strengths in the parallel loading direction.

5.4.1.2 Effect of Metal to Intermetallic Ratio

Studies in the Ti-Al system suggest that the volume fraction of metal and intermetallic layers would affect both strength and toughness of the MIL composites [5,12]. Therefore, Figure 5.4(α–c) compare the microstructure of the 304SS-eutectoid MIL composites with different metal to intermetallic ratios. All the samples utilized the same 304SS foils and the same combination of Fe/Al foils for the eutectoid region, while the volume fraction of intermetallics were adjusted by changing the number of foils in the "multi-thin-foil" ensembles listed in Table 5.2. All the samples have received the same thermal processing, which is illustrated in Figure 5.1(c). Consequently,

the samples are expected to possess similar eutectoid regions in terms of composition and microstructure, whereas the thickness of the eutectoid layer varies, changing the metal to intermetallic ratio in the composites.

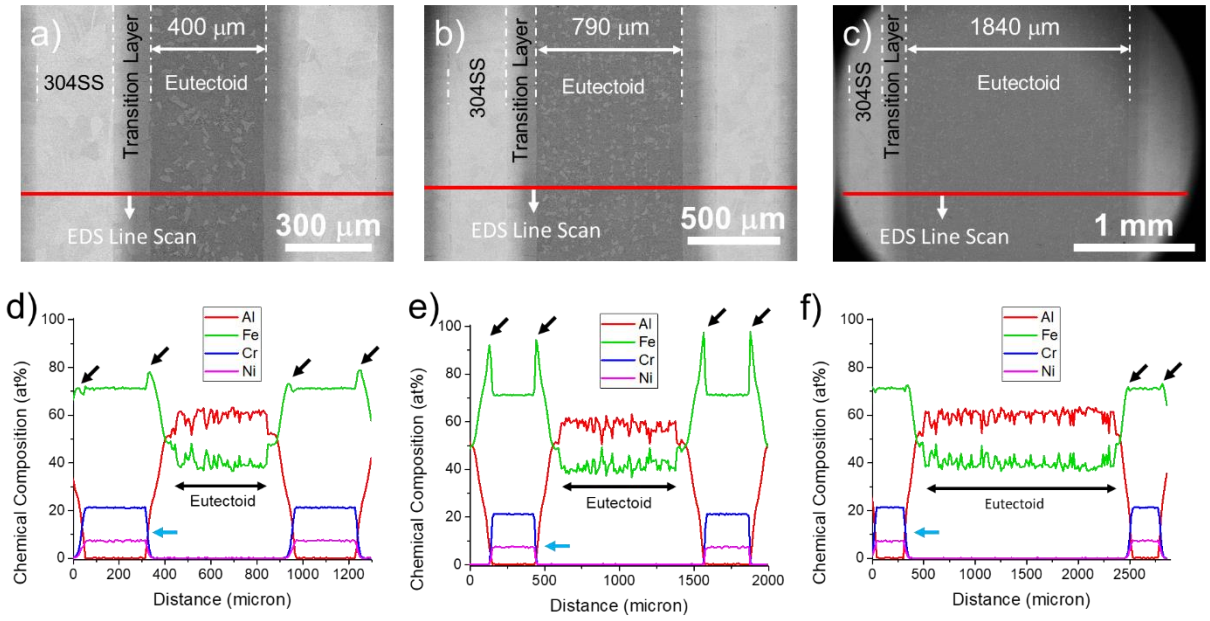

Figure 5.4: SEM images of 304SS-eutectoid with different metal to intermetallic ratio: (a) 43 vol% eutectoid, (b) 54 vol% eutectoid, and (c) 75 vol% eutectoid. (d), (e) and (f) are EDS line scans along the red lines indicated in (a), (b) and (c), respectively. 4(b) and 4(e) are duplicates of 3(c) and 3(f) for a straightforward comparison.

As indicated by the blue arrows in Figure 5.4(d) and 5.4(f), the penetration of Cr and Ni into the transition layer overlap with Al at higher concentrations compared to Figure 5.4(e). In addition, as indicated by the black arrows, the height of the Fe composition peaks have dropped at the same time. The transition layers can dramatically improve the strength for FeAl-based MIL composites [85], and the transition layers are enhanced via the solution strengthening of Al, Ni and Cr [23,74,77]. However, we are not able to obtain the same transition layers in eutectoid-MIL as achieved in the FeAl-MIL, due to the different sintering conditions. Consequently, the thickness of the Fe foil to form the transition layer is reduced from 100 μm to 75 μm, so that the average

concentration of alloying elements in transition layers is higher for strengthening the material. Furthermore, the Fe profile is slightly asymmetric with regards to the metal layers, as the Fe peak is higher on one side than the other. The difference likely results from the electromigration phenomena [78], as the electron flow in the SPS accelerates the diffusion in one direction, but hinders the other.

Table 5.2 investigates the effect of metal to intermetallic ratio by comparing the mechanical performance of the 304SS-eutectoid MIL composites with different eutectoid volume fraction. The compressive strength in the parallel loading direction generally follows a rule of mixtures, as increasing the eutectoid volume fraction increases the strength. The specimen is under uniaxial strain condition when loaded in the parallel direction. Consequently, at the same strain level, the local stress on the intermetallic layers would be higher than the metals [85]. In other words, intermetallic layers would carry more load. Therefore, decreasing the metal to intermetallic ratio would decrease the local stress on intermetallic layers, increasing the global strength of the composites. By contrast, all the materials exhibit similar compressive strength in the perpendicular loading direction. This indicates that the fracture evolution and failure of these eutectoid-MIL composites when loaded perpendicular to their layers is largely insensitive to the metal to intermetallic ratio. Among the volume fraction range investigated in the present work, a greater intermetallic phase fraction would improve the overall compressive strength for these eutectoid MIL composites. Specifically, the MIL composite with 75% eutectoid structure reaches the highest MIL composite compressive strength when loaded parallel to the layer, whereas the previous highest compressive strength for a MIL composite was from a single phase FeAl intermetallic layer MIL composite possessing a significantly lower yield point. On the other hand, the corresponding influence on fracture toughness will be part of a separate future study.

Table 5.2: Comparison of $FeAl/FeAl_2$ eutectoid MIL composites with different volume fraction of the eutectoid phase.

Number of Fe-Al Foils for Eutectoid	Volume Fraction**			Ultimate Strength	
	304SS	Transition	Eutectoid	Perpendicular	Parallel
3+4*	30%	27%	43%	1.16 GPa	1.50 GPa
7+8	22%	24%	54%	1.05 GPa	1.65 GPa
15+16	11%	14%	75%	1.10 GPa	2.01 GPa

* For each eutectoid layer, 3 layers of 50 μm Fe foils and 4 layers of 100 μm Al foils, alternating stacked.

** Same definition as Table 5.1.

5.4.1.3 Effect of Off-eutectoid Phase and Interfacial Precipitation

As discussed in Section 5.3, the intermetallic region in eutectoid MIL composites possesses a structure of hypoeutectoid (FeAl) + ($FeAl/FeAl_2$). Theoretically, if the hypoeutectoid FeAl phase is changed to the hypereutectoid $FeAl_2$ phase, the mechanical properties of the intermetallic region are expected to be different, and consequently affect the entire composite. Shown in Figure 5.5(a) is an SEM image of a 304SS-hypereutectoid MIL composite. An extra layer of 7 μm Al foil was added to each 100 μm Al foil, so that the combination in "multi-thin-foil" ensembles becomes 107-μm-Al and 50-μm-Fe. Due to the increase in Al content, the hypoeutectoid becomes hypereutectoid, as EBSD mapping in Figure 5.5(c) confirms that the off-eutectoid phase is now $FeAl_2$. By comparing the EDS line scan in Figure 5.5(b) and 5.4(f), the metal and transition layers are very similar in the 304SS-hypereutectoid and 304SS-hypoeutectoid MIL composites, which is another demonstration of the ability to independently adjust the intermetallics in MIL composites via the "multi-thin-foil" configuration. Furthermore, since the metal and transition layers are very

similar in the 304SS-hypereutectoid and 304SS-hypoeutectoid MIL composites, it is possible to investigate the influence of the off-eutectoid phase.

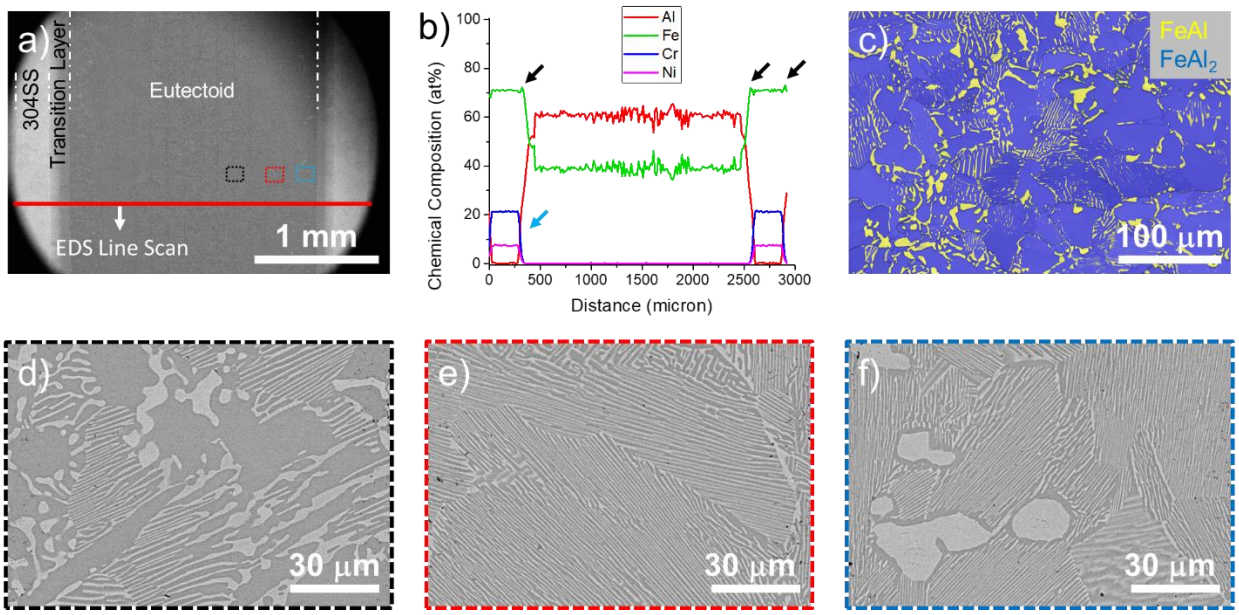

Figure 5.5: (a) SEM image of 304SS-hypereutectoid MIL composite. (b) EDS line scan along the red line indicated in (a). (c) EBSD phase map of the hypereutectoid region. (d), (e) and (f) are magnified SEM images of the areas indicated in black, red and blue rectangles in (a), respectively.

Figure 5.5(d), 5.5(e) and 5.5(f) compare the microstructure in the eutectoid region from the center to edge. Moving closer to the interface between the eutectoid and transition layers, the overall Al concentration decreases, due to the diffusion of Al into the transition layer. Consequently, the hypereutectoid structure first transforms into the eutectoid structure, then hypoeutectoid in the region adjacent to the interface. Although all the regions have experienced identical thermal history, the hypereutectoid MIL composites exhibit slightly coarser microstructure compared to eutectoid and hypereutectoid MIL composites. The structural difference between hypoeutectoid and hypereutectoid is further compared in Appendix 5.B.

Figure 5.6(a) examines the transition layer of a 304SS-hypoeutectoid MIL composite. As indicated by the white circle, there are precipitates within the FeAl grains near the interface between the eutectoid and transition layers. Additionally, as indicated by the yellow circle, precipitation also exists along the FeAl grain boundaries. According to EDS line scans, the region where precipitates exist only contains Fe and Al. Furthermore, the EBSD mapping in Figure 5.6(b) confirms that the precipitates are the $FeAl_2$ phase. Due to the fine-scale of precipitation and limited step size of the EBSD scan, only large precipitates can be identified. Based on the Fe-Al binary phase diagram shown in Figure 5.1(d), the FeAl phase has higher Al solubility at the sintering temperature (1120^{o}C), but the solubility drops upon cooling. Consequently, the supersaturated Al solute will precipitate out as the $FeAl_2$ phase.

In order to investigate the effect of interfacial precipitation, the sintering temperature was raised to 1200^{o}C in stage 2 to reduce the Al concentration at the interface, and the corresponding holding time was reduced from 1 minute to 0 to compensate for the change of diffusivity. Shown in Figure 5.6(c) is the microstructure of the transition layer near the interface with a higher sintering temperature. The amount of precipitation has dramatically decreased, but the precipitates still exist. As indicated by the black arrow, there is a vertical line in the transition layer, which is identified as the "centerline" based on our previous studies [4,77]. During the stage one sintering, as the evolving reaction front moves towards the Al foil side, contaminants on the metal foils' surface are also pushed towards the Al. When aluminum is completely transformed into Fe_2Al_5, oxides and impurities from both sides would accumulate at the former Al foil center. The centerline is less obvious in Figure 5.6(a), because the feature is overwhelmed by the $FeAl_2$ precipitation.

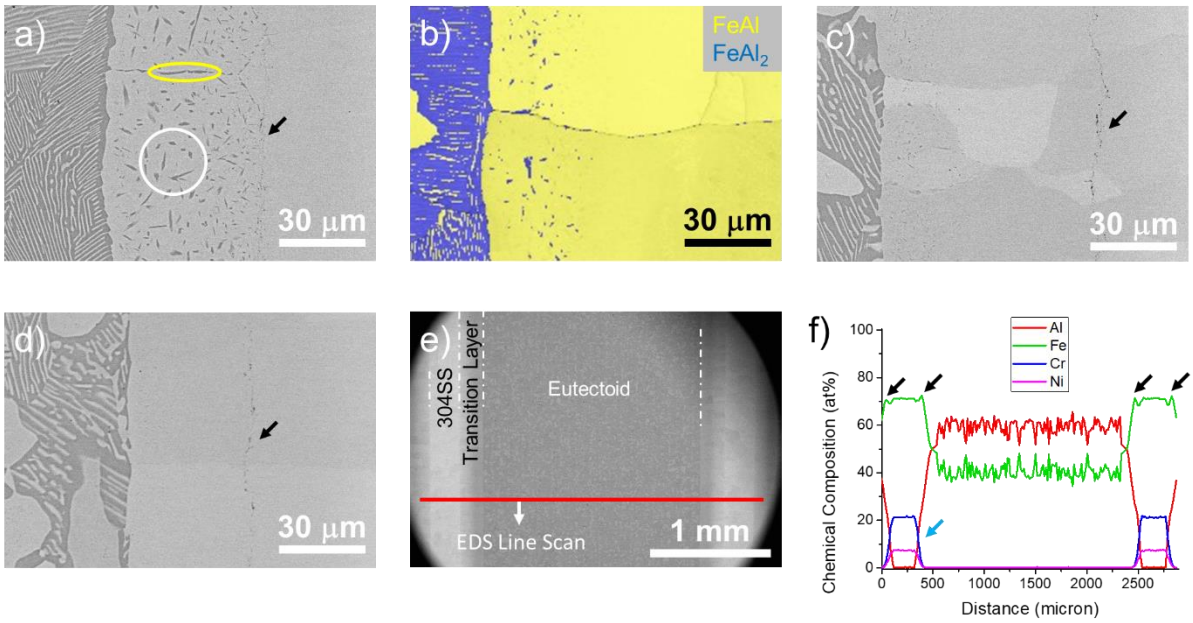

Figure 5.6: (a) SEM image and (b) EBSD phase map of the interfacial region between eutectoid and transition layers in 304SS-eutectoid sintered at 1120°C for 1 minute. SEM images of the interfacial region in 304SS-eutectoid (c) sintered at 1200°C for 0 minutes, and (d) sintered at 1200°C for 0 minutes then annealed at 885°C for 2 hr. (e) SEM image to overview 304SS-eutectoid MIL composite without interfacial precipitation. (f) EDS line scan along the red line indicated in (e).

To eliminate the precipitation in the transition layers, the sample was annealed at 885°C for 2 hrs., instead of directly cooling from 1200°C to room temperature. As revealed in Figure 5.6(d), the transition layer is free of $FeAl_2$ precipitates. Driven by a chemical gradient, Al in eutectoid and transition layers trend to diffuse toward the Fe-metal layers. As a result, $FeAl_2$ precipitates, which possess higher Al concentration, are consumed by the diffusion process during annealing. Figure 5.6(e) shows an overview of a micrograph 304SS-hypoeutectoid MIL composite without interfacial precipitation. As plotted in Figure 5.6(f), the eutectoid layer and metal layers are very similar to Figure 5.4(d), which also demonstrates the ability to independently tune the constituents of these MIL composites via the "multi-thin-foil" configuration. The transition layers become slightly thicker due to the extra diffusion during annealing, whereas the concentration of

Fe and the penetration of alloy elements are almost unchanged, allowing the direct comparison to investigate the influence of the interfacial precipitation.

Table 5.3 compares the mechanical performance by changing the off-eutectoid phase or eliminating interfacial precipitation. However, neither of the changes affects the strength of the material, as the differences are relatively small. In the eutectoid region, the mismatch in properties between the FeAl phase and the $FeAl_2$ phase is expected to induce stress concentrations under loading, and eventually becomes the source of fracture. Compared to the bulk off-eutectoid phase, there are orders of magnitude more FeAl/$FeAl_2$ interfaces within the eutectoid structure. Therefore, the influence of the off-eutectoid phase would be overwhelmed by the eutectoid structure itself, suggesting it is unnecessary to pursue the exact eutectoid compositions for these 'eutectoid' MIL composites. Theoretically, precipitation in the transition layers would also induce stress concentration under loading, facilitating crack initiation and crack propagation, and consequently degrade the mechanical performance of the entire composites.

Table 5.3: Comparison of FeAl/$FeAl_2$ eutectoid MIL composites with difference off-eutectoid phase or interfacial precipitation.

MIL Composite Structure	Volume Fraction*			Ultimate Strength	
	304SS	Transition	Eutectoid	Perpendicular	Parallel
Hypoeutectoid	11%	14%	75%	1.10 GPa	2.01 GPa
Hypereutectoid	10%	12%	78%	1.04 GPa	1.94 GPa
Hypoeutectoid without Interfacial Precipitation	10%	16%	74%	1.13 GPa	2.03 GPa

* Same definition as Table 5.1.

5.4.2 FeAl-Eutectoid Hybrid MIL Composites

Shown in Figure 5.7(a) is an SEM image of a 304SS-FeAl MIL composite, which was sintered using the parameters for the eutectoid-MIL. The sample utilized 6 layers of 75 μm Fe foils and 7 layers of 100 μm Al foils for each FeAl region. Both microstructure and composition profiles in Figure 5.7(d) are similar to the 304SS-FeAl of our previous work [77], where the sintering parameters are different. By increasing the temperature, the sintering time for the FeAl phase can be dramatically reduced from 1.5 hr to 1 min without any change in microstructure or mechanical performance. In the eutectoid-MIL composites, the FeAl phase either forms in transition layers as the solid solution, or is present in the hypoeutectoid region. In contrast, FeAl-MIL composites possess single-phase intermetallic layers of FeAl. Since FeAl-MIL can be fabricated via the same processing as the eutectoid-MIL composites, it is feasible to obtain a hybrid MIL composite that consists of both FeAl layers and eutectoid intermetallic layers, which provides an extra tool for tailoring the properties of the composites.

Shown in Figure 5.7(b) and 5.7(c) are the 304SS-hybrid MIL composites with different volume fraction of FeAl and eutectoid layers. The microstructure is achieved by adjusting the number and thickness of the Fe foils in the "multi-thin-foil" ensembles. The combination of 100-μm-Al and 75-μm-Fe generates a single-phase FeAl layer, whereas the combination of 100-μm-Al and 50-μm-Fe generates the eutectoid layer. Furthermore, to compensate for the loss of Al from eutectoid layers to the FeAl layers, three extra layers of 7-μm-Al-foil were added to each 100-μm-Al-foil for the eutectoid region.

According to the composition profiles in Figure 5.7(d), 5.7(e) and 5.7(f), although the three materials are sintered at the same condition, the Fe concentration and the penetration of alloying

elements are slightly different. Due to the setup for SPS, where the sample is heated up by the Joule heating effect, and the temperature is controlled by a thermocouple not directly contacting the sample [78], small temperature fluctuation from sample to sample is unavoidable. On the other hand, as revealed in Sections 5.4.1.1 and 5.4.1.3, the difference in transition layer composition at this level would induce a very limited influence. Figure 5.7(g) and 5.7(h) compare the transition layers of 304SS-FeAl and 304SS-hybrid MIL composites, as both exhibit very similar microstructure. As shown in Figure 5.7(h) and 5.7(i), precipitates form in the FeAl layer adjacent to the eutectoid layer, which has been explained in Section 5.4.1.3.

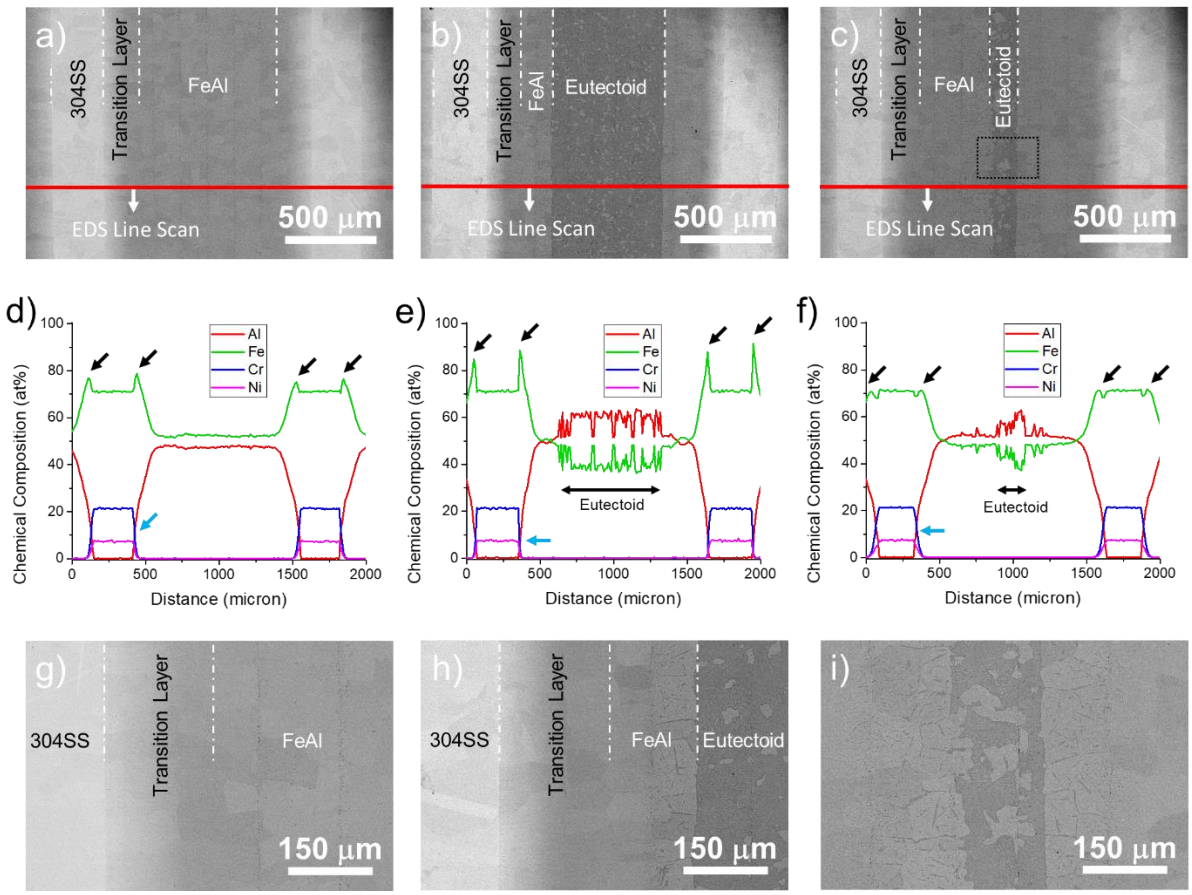

Figure 5.7: SEM images of (a) 304SS-FeAl, (b) 304SS-hybrid (39 vol% eutectoid), and (c) 304SS-hybrid (10 vol% eutectoid). (d), (e) and (f) are EDS line scans along the red lines indicated in (a), (b) and (c), respectively. (g), (h) and (i) are magnified SEM images for (a), (b) and (c), respectively.

Table 5.4 compares the strength of 304SS-hybrid MIL composites by changing the volume fraction of FeAl and eutectoid layers. Additionally, 304SS-eutectoid and 304SS-FeAl with similar metal to intermetallic ratios are also listed as the two extreme cases for hybrid-MIL. Compared to our previous work on 304SS-FeAl MIL composites [85], the 304SS-FeAl processed here, which was sintered using the parameters for the eutectoid-MIL composites, exhibits similar mechanical performance. As the eutectoid phase is added to the system, the yield strength in the parallel loading direction improves more than 50%, but sacrifices the ultimate strength by 20%. On one hand, the $FeAl_2$ phase is inherently harder than the FeAl phase, so the apparent yield strength for the composite is improved. On the other hand, although the eutectoid structure can reduce the impact of the brittle $FeAl_2$ phase, it is still not able to enhance the ductility to the level of the single phase FeAl. Therefore, the hybrid MIL composites possess lower ultimate strength due to the lack of any work hardening effect in the intermetallic layers.

5.4.3 Internal Stress for Eutectoid MIL Composites

As demonstrated in Section 5.4.1 and Appendix 5.A, FeAl/$FeAl_2$ Eutectoid MIL composites exhibit very different stress-strain behaviors between perpendicular and parallel loading directions. However, in either situation, the specimen is under uniaxial compression. Appendix 5.C suggests that the texture is relatively weak in the eutectoid-MIL composites, so the difference is not due to grain orientation, and as such the local stress-strain state should be investigated. Our previous work has qualitatively analyzed the internal stress in MIL composites [85]: the metal and intermetallic layers exhibit dissimilar stress-strain responses. At the same stress level, i.e., the deformation level of individual intermetallic layers is significantly lower than the individual metal layers. On the other hand, when loaded perpendicular to layers, all the layers are under the same level of stress, and the strain of metals and intermetallics at their interface

should be the same. The difference in stress-strain response thereby induces internal stress, constraining the deformation of the metal layers, but inducing tension in the intermetallic layers.

Table 5.4: Comparison of FeAl-FeAl/$FeAl_2$ hybrid MIL composites with different volume fraction of FeAl and eutectoid layers.

Number of Foils for Intermetallic	Volume Fraction*				Ultimate Strength	
	304SS	Transition	FeAl**	Eutectoid	Perpendicular	Parallel
8x100μm Al 7x50μm Fe	22%	24%	0	54%	1.05 GPa	1.65 GPa
8x100μm Al (3x50μm + 4x75μm) Fe	18%	23%	20%	39%	1.16 GPa	1.58 GPa
8x100μm Al (1x50μm + 6x75μm) Fe	16%	26%	48%	10%	1.38 GPa	1.64 GPa
7x100μm Al 6x50μm Fe	19%	28%	53%	0	2.03 GPa	2.01 GPa

* Same definition as Table 5.1.

** Only counts the single-phase FeAl layers, excluding FeAl solid solution in transition layers, or FeAl phase in the eutectoid region.

Figure 5.8 quantitatively investigates the stress-strain state of these MIL composites via FEA simulation; the details about the FEA model are provided in Appendix 5.D. Figure 5.8(a) plots the stress in the loading direction, which is the external stress applied to the specimen. The specimen is compressed across the top, and the sample is theoretically under uniaxial stress. Rather than being concentrated near the interface, the internal stress distributes relatively uniformly among each layer. In addition, the edge effects induce stress concentrations, which is critical for metal-ceramic composites [103]. However, since almost no difference was found in edge regions on the failed specimens, and the stress concentration primarily occurs on the ductile metal layers, the edge effect is expected to have a very limited influence on these MIL composites.

The internal stress distribution, which is in the direction normal to the loading, is plotted in Figure 5.8(b), and the external and internal stresses along the center of the specimen are compared in Figure 5.8(c). When the applied stress is 800 MPa in compression, the internal stress on the eutectoid layers can be as high as 450 MPa in tension, inducing axial splitting of the intermetallic layers.

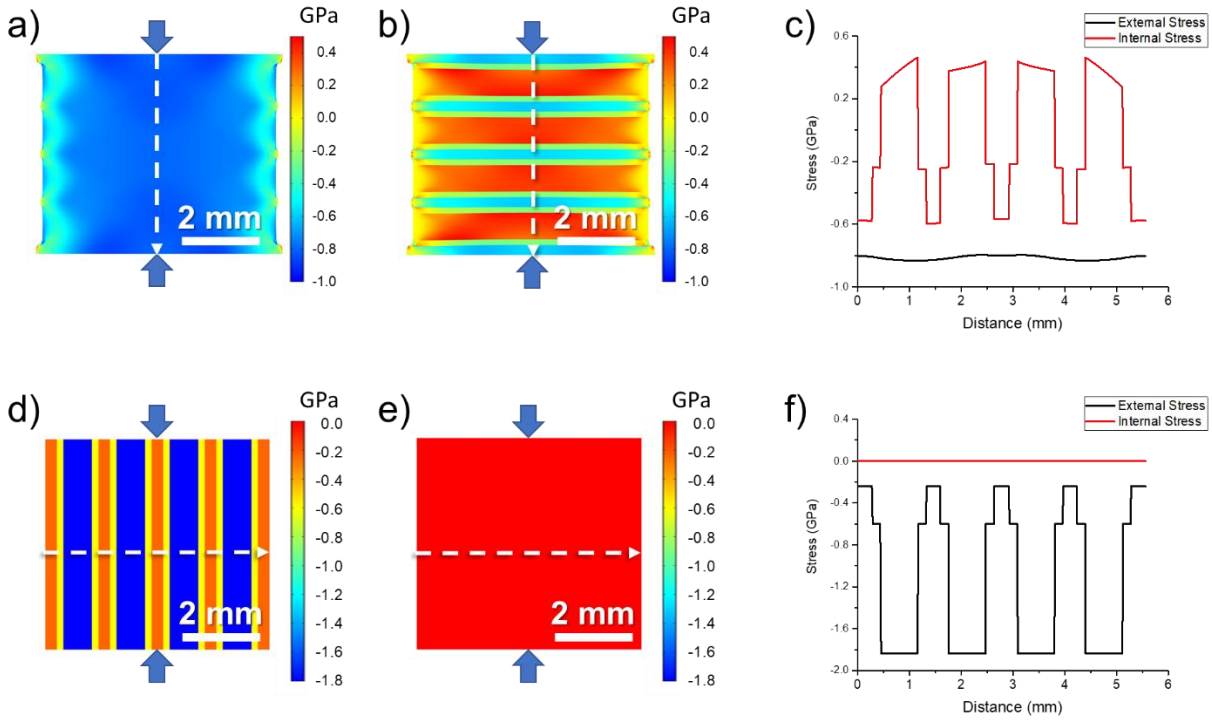

Figure 5.8: FEA simulation for (a) external stress and (b) internal stress when eutectoid MIL composite is loaded in perpendicular direction with 800 MPa load. (c) Stress profiles along the white dash lines indicated in (a) and (b). FEA simulation for (d) external stress and (e) internal stress when eutectoid MIL composite is loaded in parallel direction with 1150 MPa load. (f) Stress profiles along the white dash lines indicated in (d) and (e).

The external and internal stresses, when loaded parallel to the layers, are shown in Figure 5.8(d) and 5.8(e), respectively. As discussed in Section 5.4.1.2, the local stress on the metal, transition, and eutectoid layers are different, depending on the stiffness of each layer. For example, when the applied stress is 1.15 GPa, the local stress on the eutectoid layers is 1.8 GPa, while, as revealed in Figure 5.8(f), the internal stress is negligible.

The maximum normal stress criterion is insufficient for predicting the fracture of these eutectoid-MIL composites, otherwise, the strength should be higher in the perpendicular direction. The Tresca criterion predicts the fracture by the maximum shear stress [110], as the maximum shear stress τ_{max} can be calculated as:

$$\tau_{max} = (\sigma_{max} - \sigma_{min})/2 \tag{5.1}$$

where σ_{max} and σ_{min} are the maximum and minimum normal stresses, which are the external and internal stresses for the intermetallics in MIL composites, since there is no external shear load. The Mohr-Coulomb criterion predicts fracture using both normal and shear stresses [110]:

$$\tau + \mu \cdot \sigma \geq \tau_0 \tag{5.2}$$

where μ and τ_0 are constants for the material, and the classical von Mises criterion establishes the equation based on distortion energy theory [110]:

$$(\sigma_1 - \sigma_2)^2 + (\sigma_2 - \sigma_3)^2 + (\sigma_3 - \sigma_1)^2 \geq 6Y^2 \tag{5.3}$$

where σ_1, σ_2 and σ_3 are normal stresses, and Y is constant for the material.

From a macroscopic point of view, when loaded parallel to the layers, the intermetallic layers are only under compression in one direction, and free for deformation in the other two orthogonal directions. In contrast, when loaded perpendicular to the layers, the intermetallics are under compression in one direction, and tension in the other two orthogonal directions, due to internal stress. As predicted by Eqns. (5.1), (5.2) and (5.3), the addition of internal stress lowers the strength in the perpendicular loading orientation. On the other hand, if the eutectoid-MIL composite was compressed in a laterally confined condition, where the in-plane deformation can be restricted, it would likely exhibit significantly higher strength in the perpendicular direction.

5.4.4 Fracture Evolution in $FeAl/FeAl_2$ Eutectoid MIL Composites

Section 5.4.3 investigates the stress-strain behavior of the eutectoid MIL composites from a macroscopic point of view, suggesting that the internal stress could induce axial splitting of the intermetallics, which is a microscopic phenomenon. Therefore, to investigate the fracture evolution in MIL composites, an incremental loading approach is utilized to track the initiation of cracks. The details about the incremental compression test have been explained in our previous work [85]. Among all the eutectoid-MIL composites studied here, those with the lowest and highest eutectoid volume fraction, as well as a hybrid-MIL, were selected to compare the failure mechanisms. The microstructure of the corresponding undeformed samples has been shown in Figure 5.4(a), 5.4(c) and 5.7(c) as a reference. The specimens were loaded to 800 MPa in the perpendicular direction, or 1150 MPa in the parallel direction, the same loading conditions as the simulation in Section 5.4.3.

Shown in Figure 5.9(a) is the 304SS-eutectoid MIL with the lowest eutectoid volume fraction in the present study (43%), which was compressed in the perpendicular loading direction with 800 MPa pressure. Most cracks are vertical, driven by the internal stress that splits the eutectoid phase apart. Within the white circle are some cracks that changed their growth direction from vertical to horizontal at the crack tip. The anisotropy of eutectoid, especially the $FeAl_2$ phase, may induce local stress redistribution as cracks penetrate through $FeAl/FeAl_2$ interfaces. Figure 5.9(b) presents the sample at failure (1.16 GPa in perpendicular loading), as cracks become wider and unload the ruptured eutectoid regions. Meanwhile, the crack penetration is stopped by the transition layers, because the stress concentration at crack tip is relieved by the deformation of the relatively ductile regions [85].

Shown in Figure 5.9(c) is the 304SS-eutectoid MIL with the highest eutectoid volume fraction in the present study (75%), which was compressed in the perpendicular loading direction with 800 MPa pressure. The crack morphology is very similar to Figure 5.9(a), as the change in eutectoid volume fraction does not alter the nature of the internal stress. Figure 5.9(d) presents the sample at failure (1.05 GPa in perpendicular loading). Within the white circle, delamination occurs at the interface between eutectoid and transition layers. Primary cracks in the vertical direction will generate a local stress field, inducing secondary cracks in the horizontal direction. When the secondary cracks occur at the interface, it leads to delamination. On the one hand, delamination would relieve internal stress, slowing crack propagation. On the other hand, delamination can only occur when significant cracking exists and it is unable to prevent failure.

Figure 5.9(e) and 5.9(f) present the 304SS-hybrid MIL composites loaded in the perpendicular direction with 800 MPa and 1.38 GPa (failure point) load, respectively. The addition of the FeAl layers to the composites does not change the fracture evolution, since FeAl-MIL itself also cracks in a similar manner [85].

Figure 5.9(g), 5.9(h) and 5.9(i) present the microstructure of three materials compressed in parallel direction with 1.15 GPa pressure. Only a few cracks form in the samples, either along the centerline, or at the interface between the eutectoid and transition layers. Unless steered by the laminar structure of the eutectoid regions, cracks mostly propagate vertically, delaminating the layers. Although the FEA simulation in Section 5.4.3 indicates no driving force for delamination, from a microscopic point of view, the anisotropy could induce a local stress field, initiating crack at the weakest point, such as centerlines. When the specimen fails in the parallel direction, it splits into multiple pieces, so we are unable to investigate the microstructure at failure.

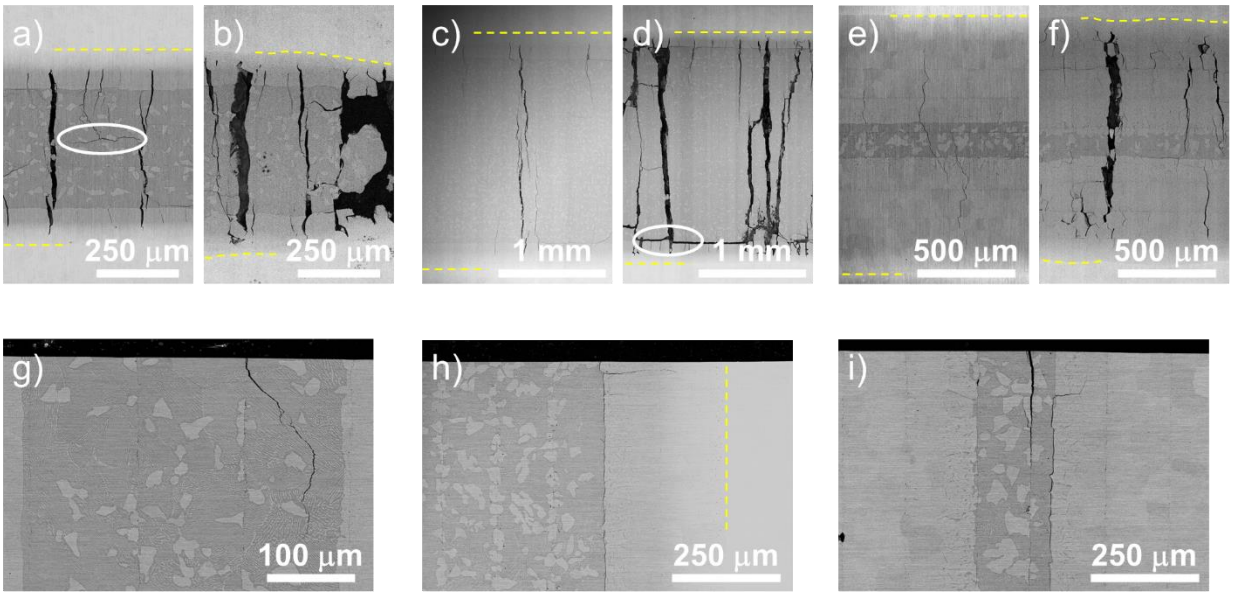

Figure 5.9: SEM images after compression test conducted perpendicular to the layers: (a) 304SS-eutectoid (43 vol% eutectoid) with 800 MPa loading, (b) 304SS-eutectoid (43 vol%) failed at 1.16 GPa, (c) 304SS-eutectoid (75 vol% eutectoid) with 800 MPa loading, (d) 304SS-eutectoid (75 vol%) failed at 1.10 GPa, (e) 304SS-hybrid (10 vol% eutectoid) with 800 MPa loading, and (f) 304SS-hybrid (10 vol% eutectoid) failed at 1.38 GPa. SEM images after compression test conducted parallel to the layers at 1.15 GPa: (g) 304SS-eutectoid (43 vol%), (h) 304SS-eutectoid (75 vol%), and (i) 304SS-hybrid (10 vol% eutectoid). The yellow dash lines indicate the boundary between meal and transition layers.

5.5 Conclusion

The present work discussed the microstructure and properties of Fe-Al MIL composites, containing the $FeAl/FeAl_2$ eutectoid structure by design, as the intermetallic layers synthesized for the first time. Material design, fabrication, characterization and simulation are utilized to understand their properties. The main conclusions are:

1. Synthesis of MIL composites, where the intermetallic regions are the eutectoid structure of FeAl and $FeAl_2$, is feasible.

2. A method for independently adjusting metal layers, metal to intermetallic ratio, off-eutectoid phase and interfacial microstructure is established, so that the specific application

requirements can be fulfilled by adjusting the microstructure of the eutectoid MIL composites. The corresponding influences on mechanical performance are studied via compression testing.

3. Eutectoid MIL composites are less sensitive to the metal layer material compared to FeAl MIL composites. Higher intermetallic volume fraction generates higher strength when loaded parallel to layers, whereas the difference in the perpendicular loading direction is limited. Overwhelmed by the eutectoid structure, the influence of the off-eutectoid phase and interfacial precipitation is negligible.

4. The hybrid MIL composites of FeAl and eutectoid layers have been synthesized to demonstrate the concept. The selection between the eutectoid structure and the FeAl phase provides the ability to optimize between yield strength with ductility and ultimate strength. A greater fraction of eutectoid structure can improve the yield strength, but sacrifices ductility, lowering the ultimate strength due to the lack of any work hardening effect in the intermetallic layers.

5. Fracture evolution in eutectoid-MIL composites is investigated from both a macroscopic point of view using FEA simulation, and microscopic point of view using an incremental compression testing approach. The internal stress, which plays an important role in MIL composites, is quantitatively estimated from FEA simulation, and its influence on fracture evolution is assessed. The internal stress, as a tensile force on the eutectoid layers, induces and facilitates crack initiation and crack propagation.

Appendix 5.A Results for Compression Tests

Figure 5.A1 presents the photos of specimens after the compression test in perpendicular direction. All the specimens failed in a similar manner, as all the major cracks are vertical to the metal layers, but do not penetrate through the metal layers. Specimens fail in a much more violent manner when compress in parallel direction, as the eutectoid layers break into pieces, and metal layers bend in buckling. The strain stress curve for the compression test in perpendicular and parallel directions are shown in Figure 5.A2 and Figure 5.A3, respectively.

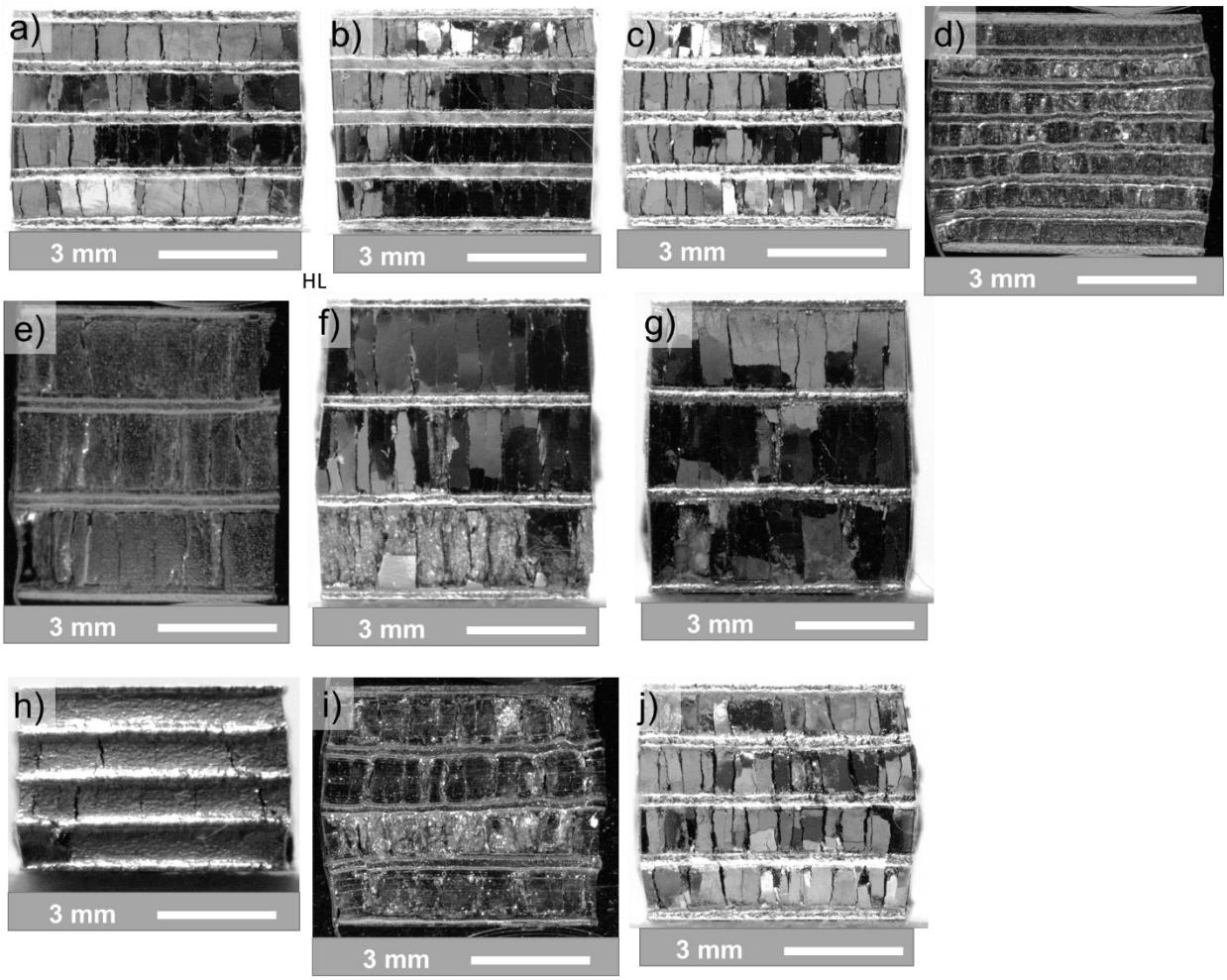

Figure 5.A1: Photos of specimens after compression test in perpendicular direction: (a) Fe-Eutectoid, (b) 430SS-Eutectoid, (c) 304SS-Eutectoid (54 vol%), (d) 304SS-Eutectoid (43 vol%), (e) 304SS-Eutectoid (75 vol%), (f) 304SS-Hypereutectoid, (g) 304SS-Eutectoid without interfacial precipitation, (h) 304SS-FeAl, (i) 304SS-Hybrid (10 vol% eutectoid), and (j) 304SS-Hybrid (39 vol% eutectoid). (d), (e) and (i) are captured from the polished cross section, while others are captured from the surface.

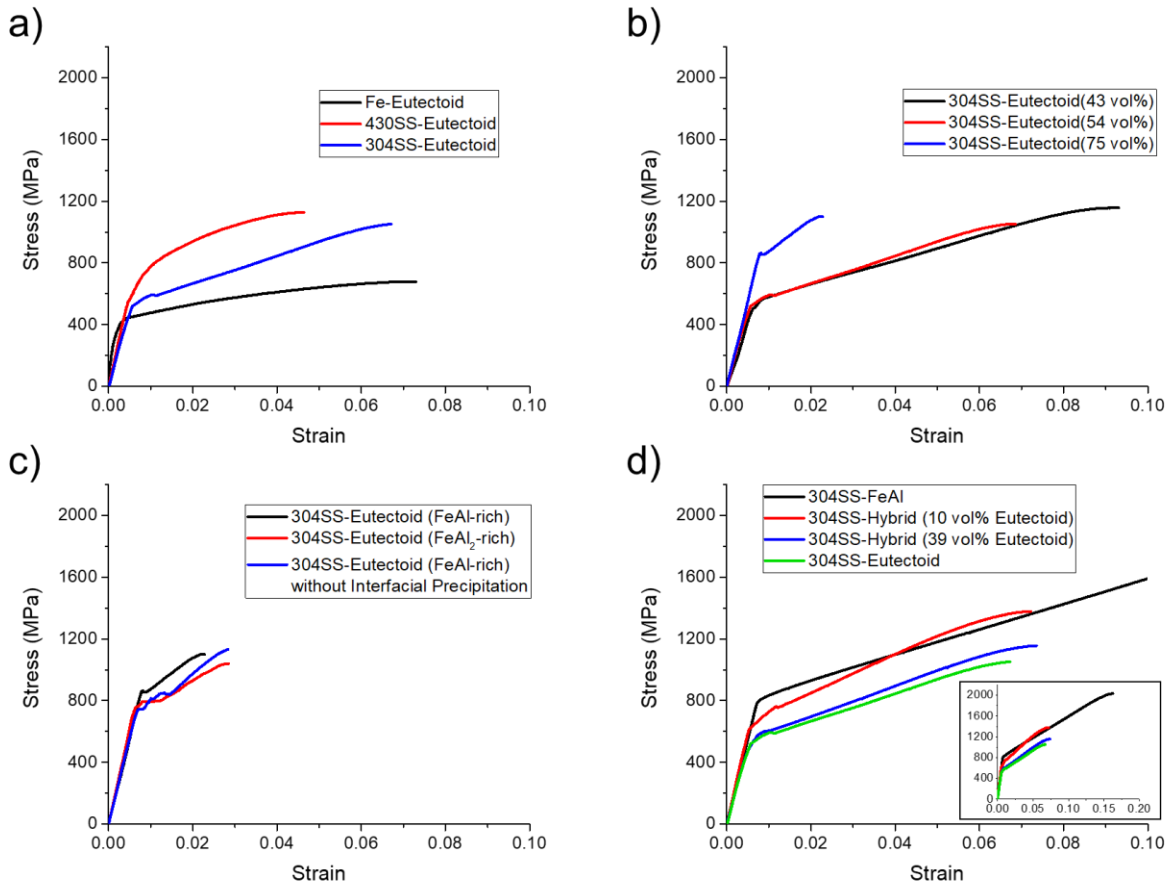

Figure 5.A2: Strain-Stress curves of MIL composites compressed in perpendicular direction: (a) Effect of metal layers, (b) effect of metal to intermetallic ratio, (c) effect of off-eutectoid phase and interfacial precipitation, and (d) FeAl-Eutectoid hybrid MIL composites.

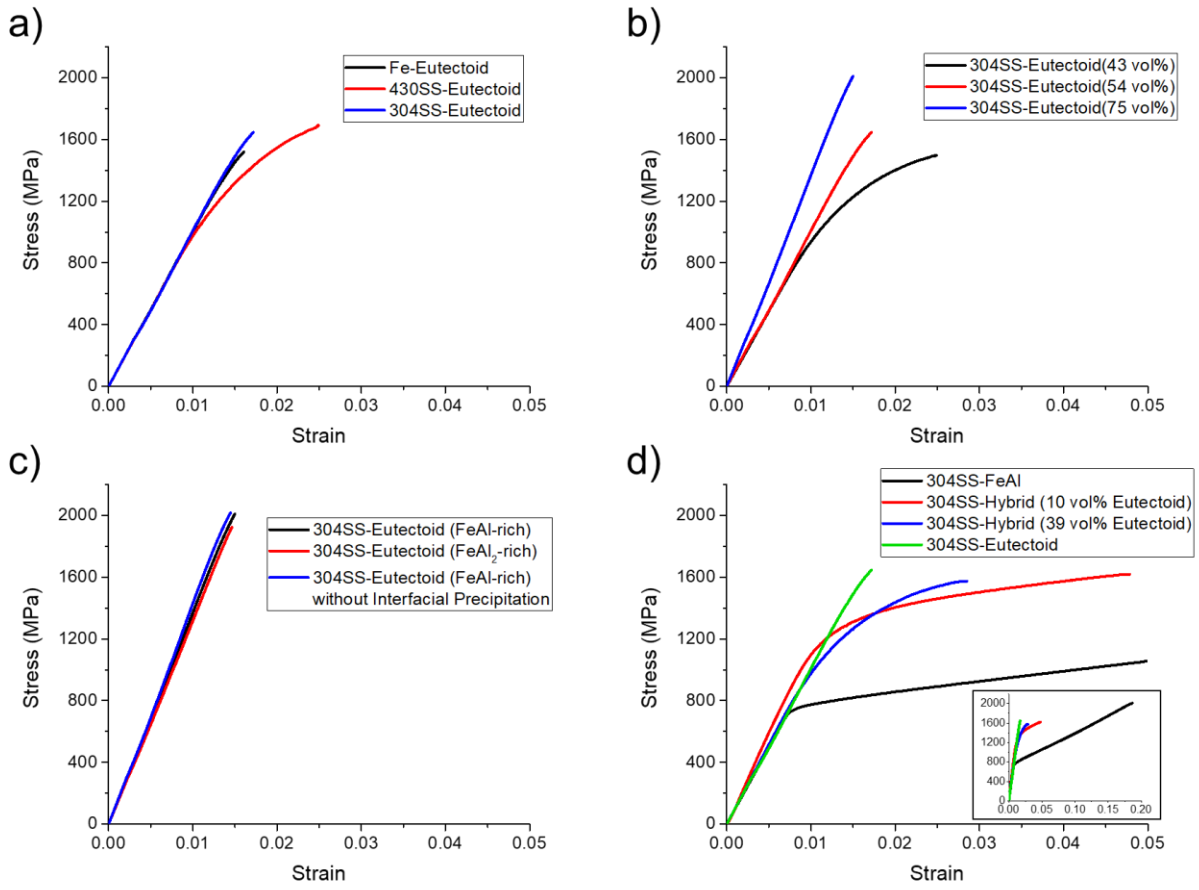

Figure 5.A3: Strain-Stress curves of MIL composites compressed in parallel direction: (a) Effect of metal layers, (b) effect of metal to intermetallic ratio, (c) effect of off-eutectoid phase and interfacial precipitation, and (d) FeAl-Eutectoid hybrid MIL composites.

Appendix 5.B Hypoeutectoid and Hypereutectoid MIL Composites

The microstructure of hypoeutectoid (FeAl rich) and hypereutectoid ($FeAl_2$ rich) is compared in Figure 5.B1. Both samples possess similar metal to intermetallic ratio, whereas the microstructure is adjusted via slight addition of aluminum.

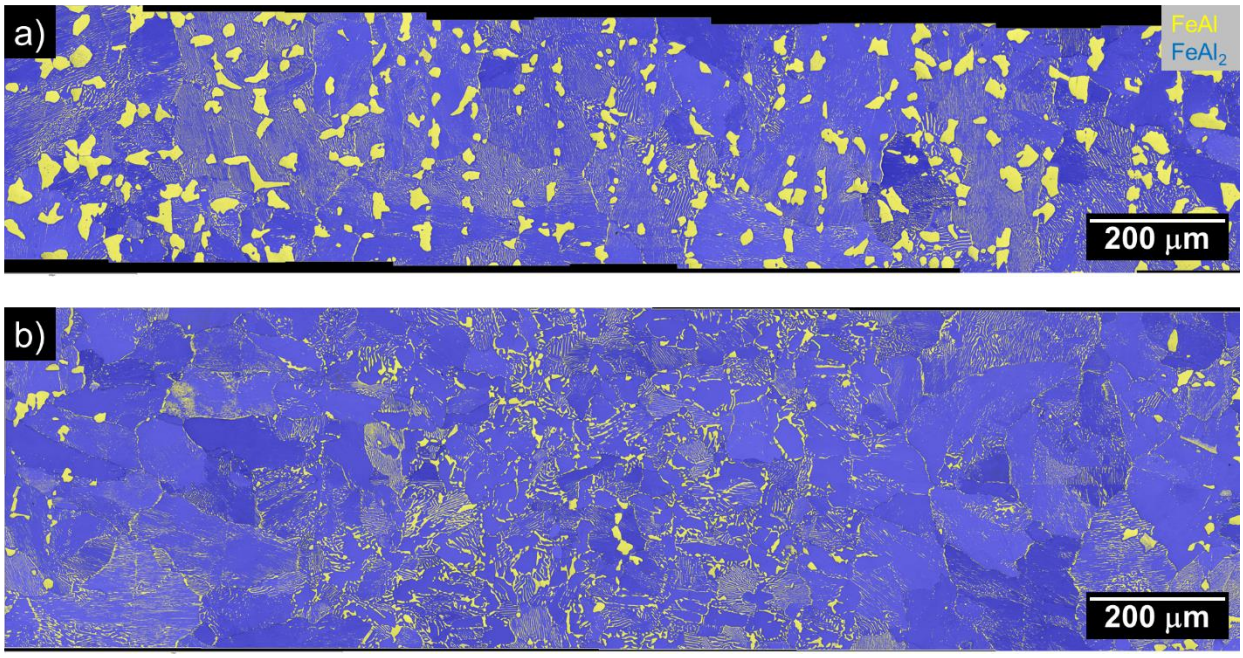

Figure 5.B1: EBSD phase map of eutectoid layer in (a) 304SS-hypoeutectoid and (b) 304SS-hypereutectoid.

Appendix 5.C Texture of Phases in MIL Composites

Since eutectoid "grains" are relatively huge (several hundred microns), we must scan over a very large area to cover enough grains to determine the textures. Shown in Figure 5.C1(a) is the band contrast map of the area scanned for EBSD. The inverse pole figures of FCC phase (304SS austenite), BCC phase (α–Fe and FeAl) and $FeAl_2$ phase are plotted in Figure 5.C1(b), (c) and (d), respectively. The conventional EBSD can not distinguish FeAl phase from α–Fe phase. Based on the times random number, the textures of all the phases in eutectoid-MIL are relatively weak.

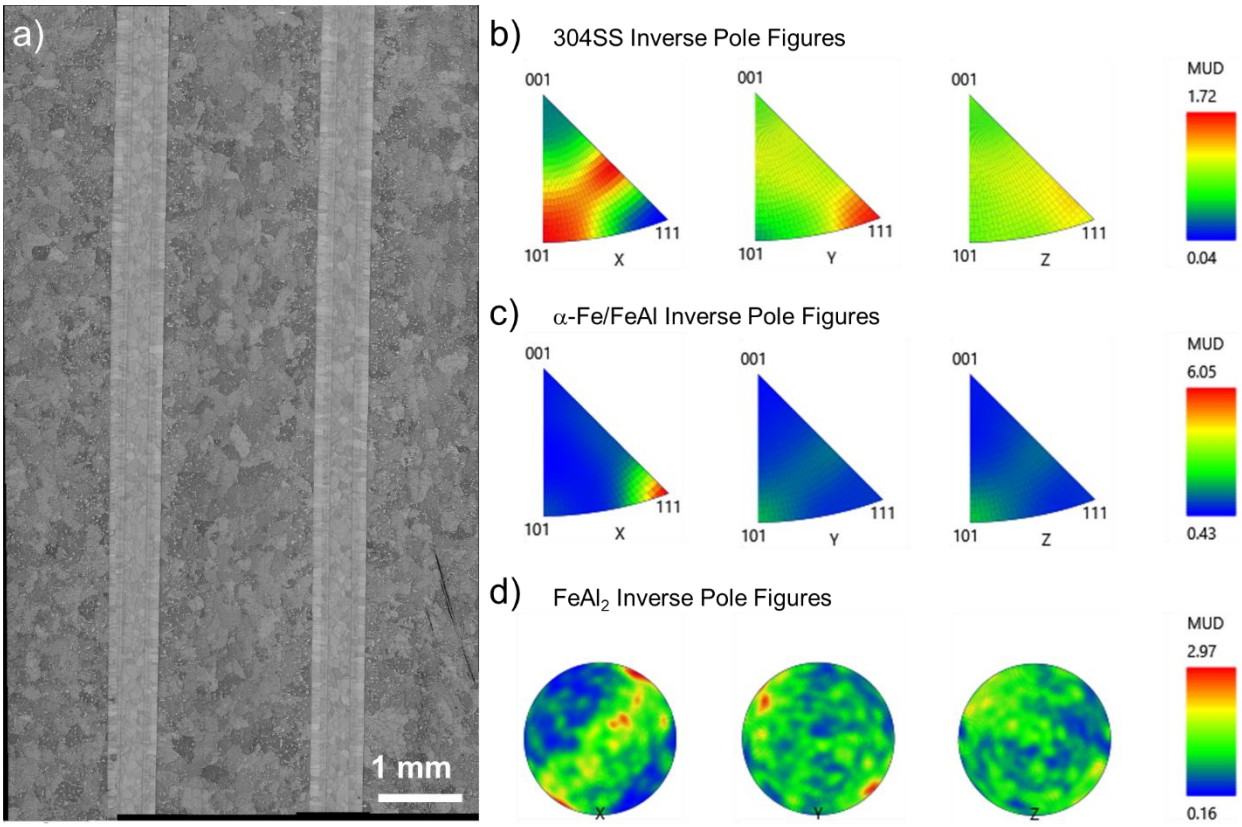

Figure 5.C1: (a) EBSD band contrast map of the area scanned for texture. Inverse pole figures for (b) 304SS austenite phase, (c) α–Fe/FeAl phase, and (d) FeAl2 phase, respectively.

Appendix 5.D FEA Simulation for Stress Distribution in MIL Composites

Shown in Figure 5.D1(a) is the mesh for the FEA simulation. The simulation is executed using software COMSOL with the default mechanical model. To simulate the compression test in perpendicular direction, the displacement in the y-axis of the bottom edge is fixed, then we arbitrarily set the displacement in the y-axis of the top edge to reach the desired external stress level. Similarly, to simulate the compression test in parallel direction, the displacement in the x-axis of the right edge is fixed, then we arbitrarily set the displacement in the x-axis of the left edge to reach the desired external stress level.

Strain-stress responses of individual layers are plotted in Figure 5.D1(b). Linear elasticity and liner plasticity are assumed for both metal and transition layers, while the yield strength and work hardening rate are estimated from our previous work about FeAl-MIL [85]. Based on the compression test in parallel direction, the eutectoid layers are assumed to be fully elastic. The mechanical properties are listed in Table 5.D1

Table 5.D1: Mechanical properties of materials for simulation.

	Metal Layers	Transition Layers	Eutectoid Layers
Young's Modulus	200 GPa	200 GPa	200 GPa
Yield Strength	200 MPa	700 MPa	/
Work Hardening Rate	1 GPa	5 GPa	/

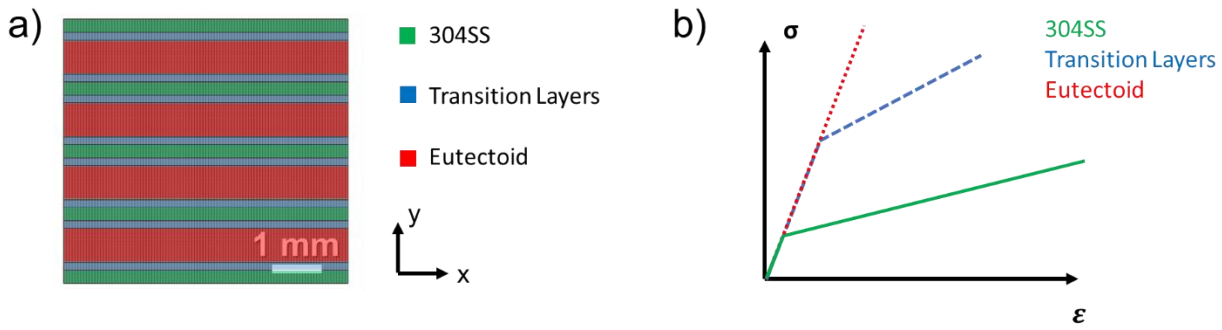

Figure 5.D1: (a) Configuration for FEA simulation. (b) The estimated strain-stress responses of individual layers.

Acknowledgment

Chapter 5, in full, is the reprint of the published article in Materialia, Elsevier: Wang, Haoren; Kou, Rui; Vecchio, Kenneth S. Design, Fabrication and Optimization of FeAl-$FeAl_2$ Eutectoid Metallic-Intermetallic Laminate (MIL) Composites. Materialia (2020).

I would like to thank Rui Kou, and my principal investigator Professor Kenneth Vecchio, for their contribution in this work.

Chapter 6 Electromigration Effect in Fe-Al Diffusion Couples with Field-Assisted Sintering

Chapter 6, in full, is the reprint of the published article in Acta Materialia, 2020, Elsevier. Wang, Haoren; Kou, Rui; Harrington, Tyler; Vecchio, Kenneth S. Electromigration Effect in Fe-Al Diffusion Couples with Field-Assisted Sintering. Acta Materialia (2020).

Abstract

The electromigration effect in spark plasma sintering (SPS) (a.k.a. field assisted sintering) is quantitively analyzed in the Fe-Al diffusion couple system. In SPS, the samples are heated by a high applied voltage and electric current, which can lead to an electromigration effect. Finite element analysis is utilized to determine the voltage applied to the Fe-Al diffusion couple, which is found to be order of magnitudes smaller than the overall system voltage, indicating the electron wind force would be the dominant mechanism for electromigration in SPS. Additionally, the simulation suggests the temperature and current density distribution is uniform across the metallic diffusion couple, which makes quantitative measurement feasible. A mathematic algorithm that allows diffusivity and electromigration coefficients to be solved, is developed for the Fe-Al, where multiple intermetallic phases coexist. At temperatures below aluminum melting, Fe_2Al_5 is the single intermetallic phase formed in Fe-Al system, for which electromigration is negligible. At temperatures above aluminum melting, $FeAl_2$, FeAl and α-Fe solid solution phases coexist. Among them, the electromigration effect is noticeable in FeAl phase and is significant in the $FeAl_2$ phase. The corresponding electromigration enhancement constants are calculated.

6.1 Introduction

The electromigration phenomenon was first discovered by Gerardin in 1861 [43], which refers to the motion of atoms in metals under an applied voltage. Under the concept of electromigration, two opposite effects were proposed: the direct electrostatic force acting on the positive-charged metal ions, and the scattering of the current (electron flow) off the metal atoms [44]. The balance between the direct electrostatic force and the electron force is captured in a quantity called the effective charge Z^*, written as Equation (1):

$$\boldsymbol{F} = \boldsymbol{F}_{direct} + \boldsymbol{F}_{wind} = (Z_{direct} + Z_{wind})eE = Z^* eE \tag{6.1}$$

Evaluation of Equation (1) via quantum mechanics demonstrates that the electron flow force would typically dominate the system [45], moving atoms towards the anode direction. The motion of atoms would accumulate voids in metals, causing failure in integrated circuits [46]. As a result, investigations on electromigration became intensive in the 1990s, while the early-stage studies primarily focused on pure metal like aluminum and copper [47–49]. The electromigration effect upon the interface of dissimilar metals was first reported in the Ni-Al binary system [50], as the microscopic motion of atoms induced by electromigration would alter the macroscopic diffusivity, and consequently the thickness of the intermetallic layers. Since then, the electromigration phenomenon has been found in other metallic diffusion couples, such as Al-Au [51], Ni-Ti [52] and Ag-Zn [53]. Furthermore, quantitative analysis of electromigration in diffusion couples, which were used to calculate the diffusivity and the electromigration coefficient, and provides the prediction of intermetallic layer thickness, was first demonstrated in the Sn-Ag system, which forms a single intermetallic phase of Ag_3Sn [54]. However, the quantitative analysis of the system where multiple intermetallic phases coexist, which is common for transition metals, is still lacking.

The pioneering works of sparking plasma sintering (SPS) were first developed in 1906 [55], and became an industrial processing technology since the 1990s [56]. SPS equipment generally involves vacuum, load, cooling, control and electrical power supply systems, along with a sample-die-plunger assembly [57]. The samples (typically powders) would be sintered with pressure and the applied voltage, which heats up the materials. The early-stage studies about SPS proposed two mechanisms that raise the temperature: Joule heating effect, and spark discharge that was believed to occur at the tiny gap between the powder particles[57], hence the name. Doubt about the existence of the spark discharge remains, and the SPS technology consequently derived other names, such as pulsed electric current sintering (PECS) [58,59], plasma activated sintering (PAS)[60], electric current activated/assisted sintering (ECAS) [61], and field assisted/activated sintering (FAST) [62]. In this work, we will continue to use the most common term, SPS, although neither spark nor plasma is expected to exist in the situation we are studying.

As the SPS has been widely used in both academia and industry, the investigations about the electromigration phenomena in SPS were thereby conducted [63–66] to evaluate the SPS technology. Unlike the conventional electromigration studies, where the electric field and temperature can be independently controlled, the electric field and temperature are strongly coupled in SPS. Any attempt to increase the electric field would inevitably raise the temperature. Meanwhile, SPS requires considerably higher voltage and current across the sample compared to other sintering approaches, because the heat energy is entirely generated from the applied electric field. However, SPS related electromigration studies are typically qualitative, while the quantitative analysis for the diffusivity and electromigration coefficient is lacking. Furthermore, the in-situ sample conditions, which are complicated in the SPS, but essential for a systematic study, are seldom considered due to the challenges in measurements.

In the present study, the electromigration effect via SPS in the Fe-Al diffusion couple system, where Fe_2Al_5 phase dominates at low temperature, and $FeAl_2$, FeAl and α–Fe solid solution coexist at high temperature, is investigated. As illustrated in Figure 6.1, the Fe-Al diffusion couple sintered via SPS exhibits a significant difference in the intermetallic layer thickness between forward and reverse directions, while the comparison group sintered via hot press yields similar thickness in both directions. The voltage directly applied to the diffusion couple, along with the temperature and current density distribution, are evaluated via finite element analysis simulation. A mathematic algorithm is developed for not only the Fe-Al diffusion couple system, but also other metallic diffusion couples where multiple intermetallic phases can coexist, allowing diffusivity and electromigration coefficient to be solved.

6.2 Experimental

6.2.1 Material Processing

Foils of commercial pure 1100 aluminum and pure iron (99.5%) were taken as the diffusion couple to study the electromigration effect in SPS. The foils were first scrubbed using steel wool pads for removing surface oxides, then ultrasonically cleaned in acetone for dissolving contaminants. Subsequently, five layers of 500 μm Fe and four layers of 175 μm Al foils were cut into 20 mm diameter disks, then alternatingly stacked in the configuration shown schematically in Figure 6.2(a).

The metal foil diffusion couple was placed in a Thermal Technology Spark Plasma Sintering (SPS) machine, Model GTAT 10-3, for reactive sintering. As demonstrated in Figure 6.2(b), the sintering assembly consists of a graphite die, cylindrical graphite plungers and thermal

insulation blanket that is made of graphite filter (CeraMaterials graphite rayon felt). Additionally, the inside of the die was wrapped by two layers of graphite films (0.12-mm-thick) coated with boron nitride for electric insulation, so that all the electric current would pass through the stacked metal foils. A piece of molybdenum foil (99.95%, 0.025-mm-thick) was inserted between the Fe foil and the graphite plunger to protect the sample from carbon contamination. The plunger-die assembly was axially loaded into the vacuum chamber of the sintering machine. The assembly was heated up by the Joule heating effect alone, with the sintering system set to direct current (DC) mode. As the comparison group, the identical assembly (except no thermal insulation blanket) was loaded in a Thermal Technology Hot Press Model HP20-4080-W system, where the sample would be heated up by the thermal radiation from the tungsten filament. In the hot press, no voltage or electric current is applied across the sample, and hence no field or current effect can occur.

A typically sintering curve for studying electromigration effect in $FeAl_2$, FeAl and α–Fe solid solution is plotted in Figure 6.2(d). In stage 1, the temperature is ramped to 570^{o}C to transform Al into the Fe_2Al_5 phase with the adjacent Fe foils. Once all the Al has been converted to intermetallic, the temperature can be ramped to 700^{o}C for the second stage of the diffusion-induced growth of $FeAl_2$, FeAl and α–Fe solid solution. In the case of studying the electromigration effect in the Fe_2Al_5 phase, only stage 1 was undertaken, while the sintering temperature was varied among 350^{o}C, 400^{o}C, 450^{o}C, 500^{o}C and 570^{o}C.

6.2.2 Characterization

Cross-sections of the sintered diffusion couples sectioned perpendicular to the metal layers were mounted and polished following standard metallographic preparation procedures. Thermo-Fisher (formerly FEI) Apreo scanning electron microscope (SEM), equipped with an Oxford

Instrument's Energy-Dispersive X-ray Spectrometer (EDS) and an Oxford Instrument's Symmetry electron backscattered diffraction (EBSD) system, was utilized for microstructure characterization. The thickness of Fe_2Al_5 and $FeAl_2$ layers were measured from EDS mapping, while the thickness of FeAl and α–Fe solid solution layers were measured from EDS line scans. To ensure statistically representative results, EDS mapping scanned over at least 6-mm in length of phase boundary for each sample, and EDS line scan investigated at least 30 sites from each sample.

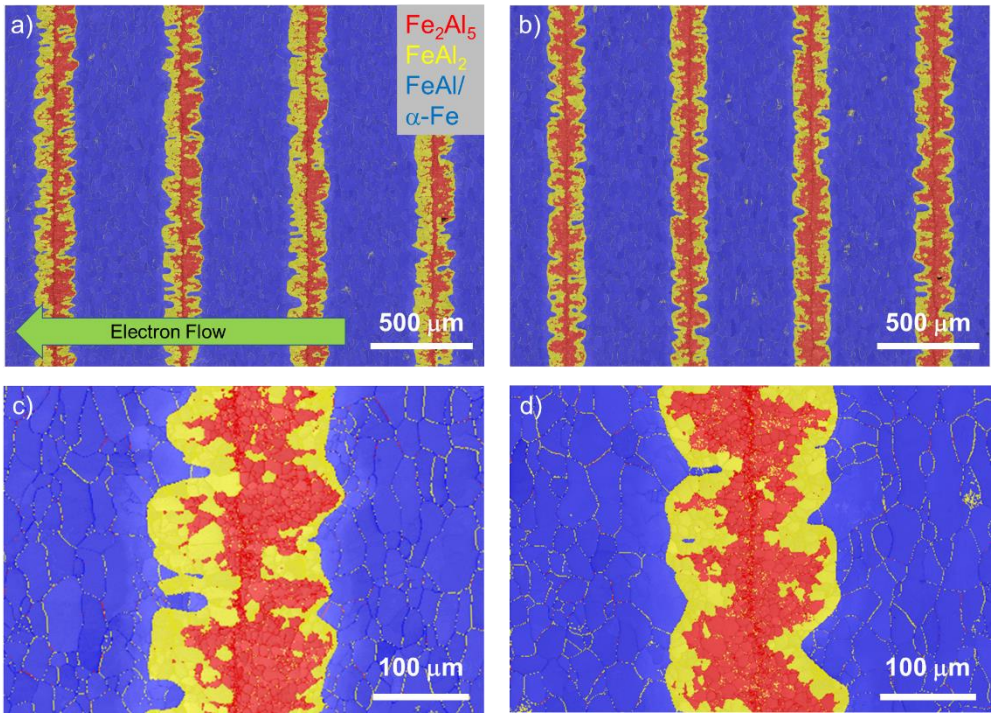

Figure 6.1: (a) and (b) EBSD phase map coupled with band contrast for Fe-Al diffusion couple sintered at 850°C for 0.5 hr. via SPS and hot press, respectively. (c) and (d) Magnified map of (a) and (b), respectively. The sintering load direction and electrical field would be in the horizontal direction perpendicular to the layers; the electron wind (opposite to the current/field direction) flows from right to left. On the left side, the primary diffusion of aluminum is the same as the electron flow, noted as "forward direction", while the diffusion on the right side is opposite, noted as "reverse direction".

6.2.3 Simulation

An electro-thermal model was developed based on Finite Element Analysis (FEA) and utilized to investigate the temperature gradient and current distribution in the SPS setup at steady

state. Since the SPS machine can only measure the total voltage applied to the entire plunger-die assembly, the strength of the electric field applied to the sample is also evaluated by the FEA simulation. The simulation approach primarily follows the work of Manière *et al* [111].

Figure 6.2(c) demonstrates the model built for simulation via the COMSOL Multiphysics package, and the electrical and thermal properties for the materials implemented are listed in Appendix 6.A. The outmost surfaces were regarded as the radiative surface. The top and bottom, which contact the chilling system, were assumed to be the heat sink at a constant temperature. Experimentally, thermocouples were inserted in the top and bottom positions, and provide stable output readings at steady state. At steady state, thermal radiation and heat exchange with the chiller are balanced with Joule heating induced by the applied voltage. Because the loose contact between the thermal insulation (graphite filter) and other parts, its thermal contact resistance is set to $0.01\ Km^2/W$ [111]. Since all the other materials/parts are highly compacted, we assume there is no electrical and thermal interfacial impedance between them [111]. Additionally, a thermocouple is inserted into the plunger, 5 mm away from the sample. The thermocouple reading, as well as the total current recorded by the SPS machine are the validation for the FEA simulation; the applied voltage and the heat sink temperature are the inputs.

6.3 Results and Discussion

6.3.1 Simulation: Temperature and Current Distribution

The physical model for the FEA simulation is based on the equations that describe the conservation of current and heat transfer by conduction [112]. Since the current is a conservative quantity: $\nabla \cdot \vec{j} = 0$, where the current density $\vec{j}$ can be expressed in terms of the electric field $\vec{E}$ and

electric conductivity λ as $\vec{j} = \lambda\vec{E}$. Furthermore, the electric field $\vec{E}$ can be expressed in terms of the electric potential U as $\vec{E} = -\nabla U$, yielding the first governing equation:

$$\nabla \cdot \vec{j} = \nabla \cdot \left(\lambda\vec{E}\right) = \nabla \cdot [\lambda(-\nabla U)] = -\nabla \cdot (\lambda \nabla U) = 0 \tag{6.2}$$

The conservation of energy can be described as:

$$\rho_{eff} C_p \frac{\partial T}{\partial t} + \nabla \cdot \vec{q} = h \tag{6.3}$$

where ρ_{eff} is the density, C_p is the heat capacity, T is the temperature, t is the time, $\vec{q}$ is the heat flux, and h is the Joule heating. Meanwhile, the heat flux can be expressed in terms of the thermal conductivity k_t as $\vec{q} = -k_t \nabla T$, and Joule heating can be written as $h = \vec{j} \cdot \vec{E}$. We thereby get the second governing equation:

$$\rho_{eff} C_p \frac{\partial T}{\partial t} - \nabla(k_t \nabla T) = \vec{j} \cdot \vec{E} = \lambda |\nabla U|^2 \tag{6.4}$$

The boundary conditions are the constant temperature at the top and bottom, as well as the radiative heat flux q_r described by Eq. (6.5) [111]:

$$q_r = \sigma_s \cdot \epsilon \cdot (T_r^4 - T_a^4) \tag{6.5}$$

where σ_s is the Stefan-Boltzmann's constant, T_r is the radiative surface temperature, and T_a is the chamber wall at room temperature.

The SPS machine, controlled by its feedback loop, adjusts the output voltage to achieve the desired setpoint temperature and remain in quasi-static equilibrium during sintering. In contrast, the simulated system, which uses an applied constant voltage, would evolve with time until the desired accuracy is achieved, as shown in Appendix 6.D.

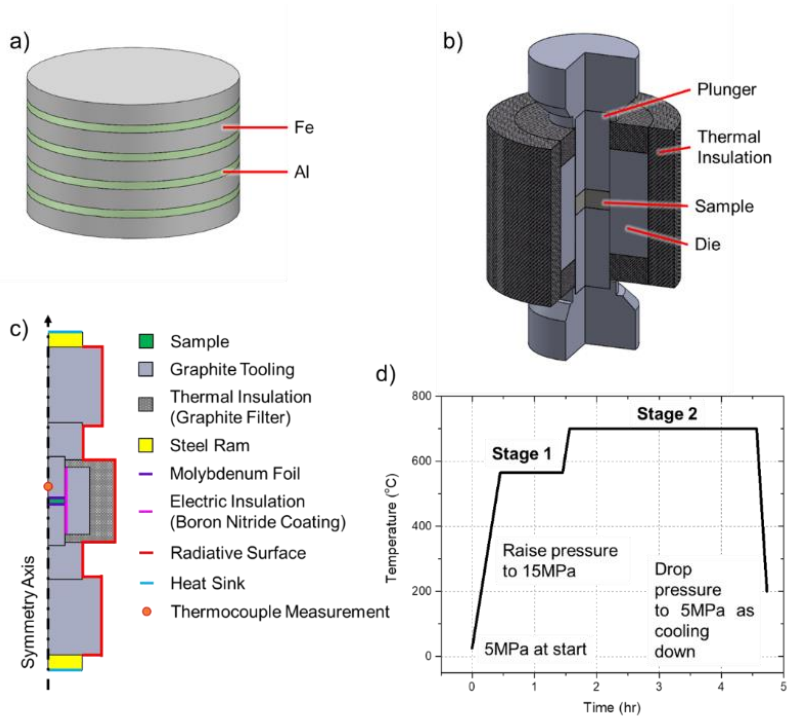

Figure 6.2: (a) Metal foils stacks for the electromigration study. (b) An illustration of SPS setup. (c) Schematic diagram illustrates the configuration for the FEA simulation. (d) Sintering parameters.

The accuracy of the simulation is very sensitive to the properties of the materials utilized in the model [113], therefore the high temperature properties, such as thermal and electrical conductivities, are derived from the literature and reasonable estimates of these data, as listed in Table 6.A1, to match the tooling and sample materials utilized in our experiment. The measured and simulated quantities, such as the temperature and the total current, are compared in Table 6.1,

Temperature and current distributions in the samples of the Fe-Al diffusion couples are plotted in Figure 6.3. The temperature gradient within the samples at 570°C (sintering stage for transforming Al into Fe_2Al_5) and 700°C (sintering stage for growing $FeAl_2$, FeAl and α–Fe solid solution) are both less than 10°C, partially due to the good thermal conductivity of the metal layers. The variation of current density at both stages are within 0.3%. Consequently, it is reasonable to assume that the samples experience a uniform distribution in terms of temperature and electric

field across the sample diameter, and the measurements of intermetallic layers at different sites reflect the diffusion under identical thermal and electrical conditions.

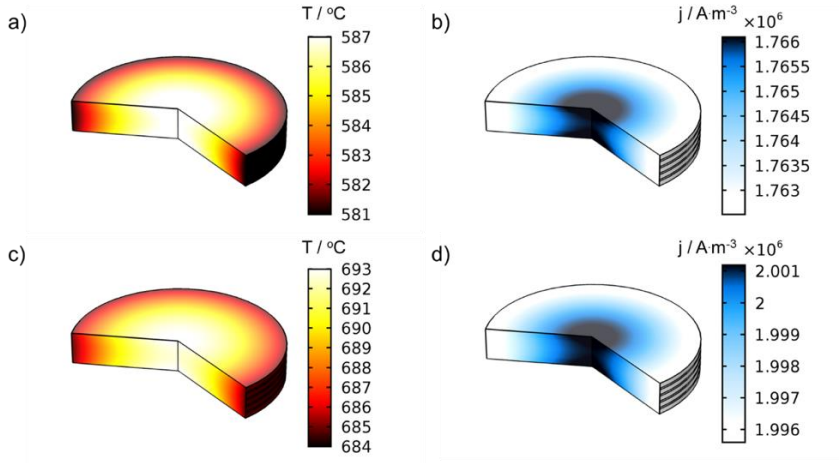

Figure 6.3: (a) and (b) Temperature and current distribution within the Fe-Al diffusion couple sintered in SPS at 570°C, respectively. (c) and (d) Temperature and current distribution within the Fe-Al diffusion couple sintered in SPS at 700°C, respectively.

6.3.2 Electromigration: Theory and Derivation

Another critical piece of information extracted from the simulation is the electric potential applied to the sample. The electric field throughout the sample, which is necessary to determine the electromigration effect, is difficult to measure experimentally: 1) a special voltmeter is required for the measurement at high temperature, and 2) probes need to directly contact the sample, requiring a cavity in the graphite tooling and the thermal insulation, which could alter the uniformity of temperature and current distribution. In contrast, it is fairly convenient to calculate the voltage from the simulation results, as $U = 0.0012$ V at 570°C, and $U = 0.0014$ V at 700°C. The voltage applied to the sample is three order of magnitude lower than the total voltage applied to the entire system, because the electrical conductivity of Al and Fe is an order of magnitude higher than that of the graphite, and the thickness of the sample is an order of magnitude shorter than the tooling. Electric potential at such low levels cannot alter the energy barrier for the

diffusion process, so the electron flow is expected to be the dominant force for the electromigration effect upon metallic couples in SPS.

Table 6.1: Measured and simulated quantities for the sintering device.

Temperature (Setpoint)	570°C		700°C	
	Measured	Simulated	Measured	Simulated
Total Voltage	2.017V		2.185V	
Temperature (Heat Sink)	175.5°C		201.4°C	
Temperature (Sample)	570°C	586.6°C	700°C	691.9°C
Total Current	512.4A	507.9A	582.3A	575.3A

The most fundamental equation that describes the mass flux across the interface of a diffusion couple induced by chemical potential gradient and electric field is given by Eq. (6.7) [43]:

$$J_i = -\frac{D_i \cdot c_i}{RT}\left(RT\frac{d\ln c_i}{dx} + Fz_a^* E\right) \tag{6.7}$$

where J_i is the flux of atom i, D_i is the diffusion coefficient of atom i, c_i is the atomic concentration, R is the ideal gas constant, T is the temperature, x is the distance, F is the Faraday's constant, z_a^* is the apparent effective charge, and E is the electric field. The first part of the equation is the contribution of diffusion induced by the chemical potential gradient, while the second part is the contribution of electromigration. If the second part equals zero, which represents the situation of negligible electromigration, Eq. (6.7) would reduce to Fick's first law:

$$J_i = -\frac{D_i \cdot c_i}{RT}\frac{d\mu_i}{dx} = -\frac{D_i \cdot c_i}{RT}\frac{d(\mu_{i,0}+RT\ln c_i)}{dx} = -\frac{D_i \cdot c_i}{RT}\left(RT\frac{d\ln c_i}{dx}\right) \tag{6.8}$$

as the chemical potential $\mu_i = \mu_{i,0} + RT\ln c_i$.

6.3.2.1 System with Single Intermetallic Phase

Now considering a hypothetical binary system of metal A and B, where α is the phase of the pure element A, β is the phase of pure B, and γ is the intermetallic phase of A–B. If the diffusivity of A is much faster than B, we can regard atoms of A as the only moving species in the system [109]. Therefore, moving the α/γ interface is equivalent to the growth of γ phase, and depends on the flux of A across the α/γ interface [54]:

$$J_A = \widetilde{c_A} \frac{dX}{dt} \tag{6.9}$$

where $\widetilde{c_A}$ is the average atomic concentration of A in γ phase, and X is the thickness of the γ phase. Another critical approximation is that the concentration gradient in γ phase is linear [54]:

$$\frac{d \ln c_A}{dx} = \frac{\Delta \ln c_A}{\mathrm{X}} \tag{6.10}$$

$\Delta \ln c_A$ is a constant for the isothermal reaction, which only depends on the mole fraction of A in γ phase at the α/γ and γ/β boundaries. Applying Eqns. (6.9) and (6.10) to Eq. (6.7) generates the differential equation that describes the relationship between time and thickness of the γ phase:

$$\widetilde{c_A} \frac{d\Delta x}{dt} = -\frac{D_A \cdot \widetilde{c_A}}{RT}\left(RT \frac{\Delta \ln c_A}{\mathrm{X}} + F z_A^* E\right) \tag{6.11}$$

$$-D_A \Delta \ln c_A - \frac{D_A}{RT} F z_A^* E \cdot \mathrm{X} = \mathrm{X} \frac{d\Delta x}{dt} \tag{6.12}$$

Then let $$M_A = -D_A \Delta \ln c_A \tag{6.13}$$

and $$\mathrm{U}_A = -\frac{D_A}{RT} F z_A^* E \tag{6.14}$$

M_A only relates to the concentration gradient induced diffusivity, and is always positive based on the definition, because $d(\ln c_i) < 0$. U_A is the electromigration coefficient, and would

be positive when the electron flow force is stronger than the electrostatic force, which makes $z_A^* < 0$. Furthermore, both M_A and U_A are constant for the isothermal reaction. Then Eq. (6.12) and be simplified as:

$$M_A + U_A \cdot \mathrm{X} = \mathrm{X}\frac{d\mathrm{X}}{dt} \tag{6.15}$$

If the diffusion couple of A–B begins with negligible γ phase, which gives the initial condition $X = 0|_{t=0}$, Eq. (6.15) can be analytically solved by regarding t as a function of X:

$$t = \frac{X}{U_A} - \frac{M_A}{U_A^2}\ln\left(1 + \frac{U_A}{M_A}X\right) \tag{6.16}$$

The thickness of the intermetallic layer X can be experimentally determined via sintering the diffusion couple at an isothermal condition with the corresponding diffusion time t. Therefore, the constants M_A and U_A can be calculated from Eq. (6.16), then the diffusion coefficient D_A and the apparent effective charge z_A^* are determined.

When electromigration is negligible as $U_A = 0$, one can take a Taylor expansion for the ln( ) function (if one directly takes $U_A = 0$ to Eq. (6.16), it would be a singularity):

$$t = \frac{X}{U_A} - \frac{M_A}{U_A^2}\left[\left(\frac{U_A}{M_A}X\right) - \frac{1}{2}\left(\frac{U_A}{M_A}X\right)^2 + \sum_{n=3}^{\infty}\frac{(-1)^{n-1}}{n}\left(\frac{U_A}{M_A}X\right)^n\right]$$

$$= \frac{X}{U_A} - \frac{X}{U_A} + \frac{1}{2M_A}X^2 + \sum_{n=3}^{\infty} M_A U_A^{n-2}\frac{(-1)^{n-1}}{n}\left(\frac{x}{M_A}\right)^n = \frac{1}{2M_A}x^2 \tag{6.17}$$

Eq. (6.17) can be rewritten as $\mathrm{X} = \sqrt{2M_A t}$, which becomes the classical parabolic equation for diffusion controlled growth [70].

6.3.2.2 System with Multiple Intermetallic Phases

Now considering a hypothetical binary system of metal A and B, where α is the phase of the pure element A, β is the phase of pure B, and $\gamma_1 \ldots \gamma_n$ are n independent intermetallic phases of A–B with ascending concentration of element A. As discussed in Section 3.2.1, we assume the atoms of A are the only moving species in the system. Consequently, the growth of γ_n phase depends on the flux of A across the α/γ_n interface and γ_n/γ_{n-1} interface:

$$J_{\alpha/\gamma_n} - J_{\gamma_n/\gamma_{n-1}} = \widetilde{c_n}\frac{dX_n}{dt} \tag{6.18}$$

where $\widetilde{c_n}$ is the average atomic concentration of A in γ_n phase, and X_n is the thickness of γ_n phase. Similarly, for γ_k phase ($1 < k < n$):

$$J_{\gamma_{k+1}/\gamma_k} - J_{\gamma_k/\gamma_{k-1}} = \widetilde{c_k}\frac{dX_k}{dt} \tag{6.19}$$

and for γ_1 phase:

$$J_{\gamma_2/\gamma_1} = \widetilde{c_1}\frac{dX_1}{dt} \tag{6.20}$$

Let
$$M_k = -D_k \Delta \ln c_k \tag{6.21}$$

and
$$U_k = -\frac{D_k}{RT} F z_k^* E \tag{6.22}$$

for $1 \le k \le n$. Then M_k and U_k are constants under isothermal conditions, and only determined by the corresponding properties of γ_k phase. Applying Eqns. (6.21) and (6.22) into Eqns. (6.19) and (6.20) would thereby generate the differential equation that describes the relationship between time and thickness of the γ_k phase

$$\frac{dX_1}{dt} = \frac{M_1}{X_1} + U_1 \tag{6.23}$$

$$\frac{dX_k}{dt} + \sum_{j=1}^{k-1} \frac{\widetilde{c_j}}{\widetilde{c_k}} \frac{dX_j}{dt} = \frac{M_k}{X_k} + U_k \tag{6.24}$$

Eq. (6.23) takes the same form as Eq. (6.15), and therefore has the same solution. Its general solution, Eq. (6.16), however, is mathematically impossible to get the analytical inverse function as $X_1 = f^{-1}(t)$. As a result, Eq. (6.24) does not have an analytical solution, because of the term $\frac{dX_1}{dt}$.

The only exception is the situation where $U_k = 0$ for any k. In this case, diffusion in the A–B couple is fully induced by the chemical potential gradient without electromigration. Consequently, the solution should take the form [$X_k = A_k\sqrt{t}$], which is the analytical solution for Eq. (6.24) and can be proven by the following derivation:

$$\frac{A_k}{2}\frac{1}{\sqrt{t}} + \sum_{j=1}^{k-1} \frac{\widetilde{c_j}}{\widetilde{c_k}} \frac{A_j}{2}\frac{1}{\sqrt{t}} = \frac{M_4}{A_k}\frac{1}{\sqrt{t}} \tag{6.25}$$

Multiplying $\sqrt{t}$ to both side of the Eq. (6.25) and reorganizing it would generate the general formula for the coefficient A_k:

$$A_k^2 + \left(\sum_{j=1}^{k-1} \frac{\widetilde{c_j}}{\widetilde{c_k}} A_j\right) \cdot A_k - M_k = 0 \tag{6.26}$$

Eq. (6.26), as a quadratic equation, always has a positive root, because its discriminant is positive:

$$\Delta = \left(\sum_{j=1}^{k-1} \frac{\widetilde{c_j}}{\widetilde{c_k}} A_j\right)^2 + 4M_k > 0 \tag{6.27}$$

For the normal situation of Eq. (6.24), assume that the numerical functions $X_1(t), \ldots, X_{k-1}(t)$, which describe the relationship between the sintering time and the

corresponding intermetallic layer thickness, have already been established. Then $X_k(t)$ can be determined in the following manner:

Construct a function $G_k(t_0)$ as:

$$G_k(t_0) = \sum_{j=1}^{k-1} \frac{\widetilde{c_j}}{\widetilde{c_k}} \frac{dX_j(t_o)}{dt}, \tag{6.28}$$

and utilize the finite difference method to Eq. (6.24) as $\frac{dX_k(t_0)}{dt} = \frac{X_k(t_0+\Delta t)-X_k(t_0)}{\Delta t}$.

$$G_k(t_0) + \frac{X_k(t_0+\Delta t)-X_k(t_0)}{\Delta t} = \frac{M_k}{X_k(t_0)} + U_k. \tag{6.29}$$

This algorithm requires two diffusion couple samples of sandwich configuration B-A–B to be sintered for time t_0 and $t_0 + \Delta t$ under direct current (DC) conditions. X_k measured from the forward direction will be taken into Eq. (6.29), while X_k measured from the reverse direction will be taken into the equation with $-U_k$ as:

$$G_k(t_0) + \frac{X_k(t_0+\Delta t)-X_k(t_0)}{\Delta t} = \frac{M_k}{X_k(t_0)} - U_k \tag{6.30}$$

The unknown variable M_k and U_k are thereby solved from the set of simultaneous equations as Eq. (6.29) and (6.30).

Since $X_1(t)$ already has an analytical solution, $G_2(t_0)$ is then feasible to calculate for obtaining $X_2(t)$. With the iterations, all the $X_k(t)$ with corresponding M_k and U_k are consequently determined.

Mathematically, shortening the time increment Δt would improve the accuracy as the finite difference $\frac{X_k(t_0+\Delta t)-X_k(t_0)}{\Delta t}$ approaching the derivative $\frac{dX_k(t_0)}{dt}$. In practice, however, similar sintering time would generate almost the same intermetallic layer thickness, where the fluctuation

in data would be greater than the difference induced by the extra reaction time. As a result, the numerical function $X_k(t)$ becomes inaccurate, especially in the case when the fluctuations in the thickness are large, such as the intermetallics formed in the Fe-Al system.

Another algorithm requires three diffusion couple samples of sandwich configuration B-A–B to be sintered for time t_0, $t_0 + \Delta t$ and $t_0 - \Delta t$ under DC conditions. Since the numerical function $X_k(t)$ is smooth and continuous, we can obtain the approximation of the derivative $\frac{dX_k(t_0)}{dt}$ based on the mean value theorem:

$$\frac{dX_k(t_0)}{dt} = \frac{X_k(t_0+\Delta t)-X_k(t_0-\Delta t)}{2\Delta t} \tag{6.31}$$

Then
$$G_k(t_0) + \frac{X_k(t_0+\Delta t)-X_k(t_0-\Delta t)}{2\Delta t} = \frac{M_k}{X_k(t_0)} + U_k \tag{6.32}$$

Similar to the previous algorithm, the measurement from forward and reverse directions and the iterations would solve all the constants about the diffusivity and the electromigration coefficient for all the intermetallic phases. Since the mean value theorem has no limitation as to the magnitude of Δt, Δt can be equal to t_0, so that only two samples are required and Eq. (6.32) becomes

$$G_k(t_0) + \frac{X_k(2t_0)}{2t_0} = \frac{M_k}{X_k(t_0)} + U_k \tag{6.33}$$

Furthermore, the accuracy of the calculation can be improved with extra samples.

Let
$$Y = \begin{cases} G_k(t_0) + \frac{X_k(t_0+\Delta t)-X_k(t_0-\Delta t)}{2\Delta t} & \text{for the forward direction} \\ -G_k(t_0) - \frac{X_k(t_0+\Delta t)-X_k(t_0-\Delta t)}{2\Delta t} & \text{for the reverse direction} \end{cases} \tag{6.34}$$

and
$$Z = \begin{cases} \frac{1}{X_k(t_0)} & \text{for the forward direction} \\ -\frac{1}{X_k(t_0)} & \text{for the reverse direction} \end{cases} \tag{6.35}$$

So M_k and U_k become the slope and intercept for the linear equation $Y = M_k \cdot Z + U_k$, while linear regression of various data points can solve them. Subsequently, the numerical function $X_k(t)$ is inversely obtained via the finite difference method in term of $t(X_k)$. We can arbitrarily assign the increment in X_k as ΔX_k, so that the corresponding Δt is calculated from Eq. (6.30):

$$\Delta t = \frac{\Delta X_k}{\frac{1}{X_k} M_k + U_k - G_k}, \tag{6.36}$$

and then integrate Δt to get t. Note that it is impossible to directly integrate for X_k, otherwise, the zero point would become a singularity.

After establishing the numerical function $X_k(t)$, the inherent error introduced by the mean value theorem can be eliminated via the least squares method and bisection method. In Eq. (6.31), we assume that the derivative at the middle point $X_k(t_0)$ is equal to the straight line defined by its two ends, which is not necessarily true. As a consequence, M_k and U_k, as well as the predicted $X_k(t)$ curve, would depart from their actual values. Such error can be evaluated as the sum:

$$S = \sum_i \left[X_{k,t_i} - X_k(t_i) \right]^2 \tag{6.37}$$

where X_{k,t_i} is the measured thickness at the time t_i, and $X_k(t_i)$ is the prediction based on M_k and U_k. Similar to the bisection method for root-finding, we can manually assign a starting range, such as $[50\%; 150\%]$, with respect to the calculated M_k and U_k, and then take iterations to minimize the summation function S.

6.3.3 Temperature Dependence for Electromigration

Indicated by Eq. (6.7), if the electric field and the apparent effective charge are independent of temperature, the ratio of the flux induced by the chemical gradient to the flux induced by electromigration, denoted as r, is proportional to temperature:

$$\mathrm{r} = \frac{-\frac{D_i \cdot c_i}{RT} \cdot RT \frac{d \ln c_i}{dx}}{-\frac{D_i \cdot c_i}{RT} \cdot F z_a^* E} = \frac{RT \frac{d \ln c_i}{dx}}{F z_a^* E} \propto T \tag{6.38}$$

In the case of the SPS, in the quasi-static state, Joule heating ($\propto I^2$) balances with the heat flux to the chilling water and thermal radiation. Since the heat zone is wrapped by the thermal insulation, the temperature at the radiative surface is expected to be considerably lower than the sample. As a consequence, the thermal radiation is negligible compared to the heat flux to the chiller, so that the heat flux to the chiller would be approximately equal to the Joule heating.

If the heat flux to the chiller is roughly proportional to the temperature difference between the sample T and the chilling water T_w, and the electric field on the sample E is roughly proportional to the total current I, then the ratio r would increase with temperature, indicating a less noticeable electromigration effect at higher temperatures.

$$I^2 \sim (T - T_w) \tag{6.39}$$

$$E \propto I \sim \sqrt{T - T_w} \tag{6.40}$$

so
$$r \propto \frac{T}{E} \sim \frac{T}{\sqrt{T - T_w}} = \sqrt{\frac{T^2}{T - T_w}} \tag{6.41}$$

and
$$\frac{dr}{dt} = \frac{1}{2} \frac{1}{\sqrt{\frac{T^2}{T - T_w}}} \frac{1}{(T - T_w)^2} [T(T - 2T_w)], > 0 \ for \ T > 2T_w \tag{6.42}$$

In reality, although the heat flux increases with T, and E increases with I, their exact relationship is complicated. As demonstrated in Appendix 6.B, data collected in this work produces the empirical equation as:

$$I \propto (T - T_w)^{0.72} \tag{6.43}$$

which still suggests the electromigration effect would be more significant at lower temperatures. The temperature dependence of the electromigration phenomenon suggests that the samples should be sintered at low temperature for determining the corresponding constants. Otherwise, the electromigration effect would be overwhelmed by the concentration gradient induced diffusion at high temperature.

Additionally, if thermal radiation becomes dominant compared to the heat flux to the chiller, such as the case where the sample is exposed for thermal radiation, and the temperature is high, the conclusion would get reversed as the electromigration effect would be more noticeable at high temperature:

$$I^2 \sim T^4 \tag{6.44}$$

$$E \propto I \sim T^2 \tag{6.45}$$

so

$$r \propto \frac{T}{E} \sim \frac{T}{T^2} = T^{-1} \tag{6.46}$$

6.3.4 Electromigration in Fe-Al Binary System

As shown in Figure 6.4, in the equilibrium Fe-Al binary system, there are in total 9 phases: pure Al, $FeAl_3$, Fe_2Al_5, $FeAl_2$, Fe_5Al_8, FeAl, Fe_3Al, γ-Fe and α-Fe[67]. Among them, pure aluminum possesses almost zero Fe solubility, while Fe_5Al_8 and γ-Fe only stabilize at high temperature, which makes it invalid or impossible to study their diffusivity. Furthermore, although

thermodynamic supports the existence of $FeAl_3$ and Fe_3Al at room temperature, the extremely slow growth kinetics make them neglectable compared to Fe_2Al_5, $FeAl_2$, FeAl, and α–Fe, which are studied in this work.

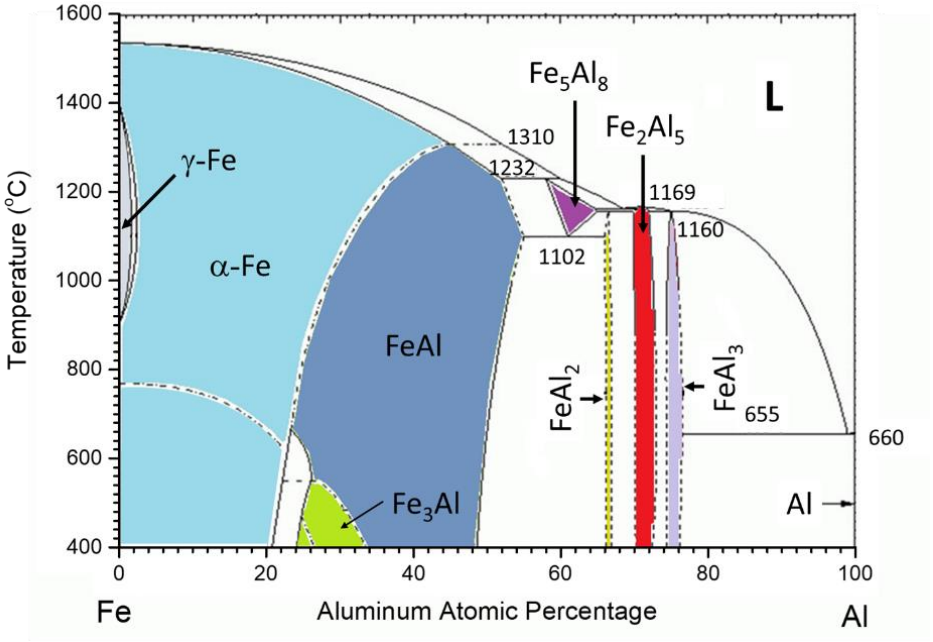

Figure 6.4: Fe-Al equilibrium phase diagram[67].

6.3.4.1 Electromigration in Fe_2Al_5 Phase

Fe_2Al_5 is the first-formed and dominant intermetallic phase at the temperature below the melting of aluminum (660°C) [69]. At the reaction front, a very thin layer of $FeAl_3$ may form at Fe_2Al_5/Al interface, but always remains negligible [17]. Other phases, including $FeAl_2$, FeAl and α–Fe solid solution, would also remain negligible below 660°C due to extremely slow growth kinetics [69]. Therefore, electromigration in Fe_2Al_5 can be classified as the condition of single intermetallic phase forming, which was discussed in Section 3.2.1.

Figure 6.5(a) to 6.5(f) compares the Fe-Al diffusion couple sintered at 350°C ,400°C, 450°C, 500°C and 570°C, respectively. The sintering time is adjusted with respect to the sintering

temperature, so that the Fe_2Al_5 layer would exhibit similar thickness for each sample. At 350°C, the Fe/Al interface retains a sharp and clear structure, indicating that insufficient thermal energy at this temperature restricts the thermodynamically favorable diffusion process. At 400°C, discrete Fe_2Al_5 nodules form at the Fe/Al interface, but do not grow larger. Due to the existence of oxides on the metal foil surface, the nucleation of Fe_2Al_5 must break the oxide barrier, which generates discrete intermetallic nodules located along the initial Fe/Al interface [17]. As the sintering temperature is further raised, the intermetallic nodules grow and then become a continuous layer, whose thickness follows the parabolic equation for diffusion-controlled growth [32]. Theoretically, as a diffusion-controlled process, the growth of Fe_2Al_5 should create a flat interface, because the thicker layer grows slower, eliminating fluctuation in thickness. However, the Fe_2Al_5 layer exhibits an irregular Fe_2Al_5/Fe interface somewhat like fingers. The Fe_2Al_5 'fingers' become more irregular at higher temperatures, while decreasing in number. Consequently, it appears that the growth of Fe_2Al_5 phase competes with the nucleation process, and the nucleation process is less temperature-sensitive than the diffusion process. At higher temperatures, the first nucleated Fe_2Al_5 nodules grow faster compared to at lower temperatures, consuming more surrounding aluminum, which hinders the nucleation of new Fe_2Al_5 nodules. As fewer Fe_2Al_5 'fingers' are present, the fluctuation in size becomes greater. Figure 6.5(g) compares the thickness of Fe_2Al_5 layers grown in the forward and reverse directions (forward being defined as in the electron flow direction), which is found to be statistically equal. Since 450°C is the lowest sintering temperature where the growth of Fe_2Al_5 is feasible, and the discussion in Section 3.3 demonstrated that electromigration is more significant at low temperature, it is reasonable to conclude that the electromigration effect in the Fe_2Al_5 phase is always negligible using the present SPS setup. Meanwhile, the negligible electromigration effect in Fe_2Al_5 creates an experimental opportunity. After all the aluminum is

converted into the Fe_2Al_5 phase, as shown in Figure 6.5(f), the sintering temperature can be increased to study the electromigration in other Fe-Al intermetallic phases. Furthermore, a sample of the Fe-Al diffusion couple was sintered via SPS first to convert Al into Fe_2Al_5, then sintered at a higher temperature via the hot press to investigate the influence of the Fe_2Al_5 on the growth of the higher temperature phases. As discussed in Appendix 6.E, the Fe_2Al_5 wound not pre-condition the growth asymmetry of the $FeAl_2$ phase.

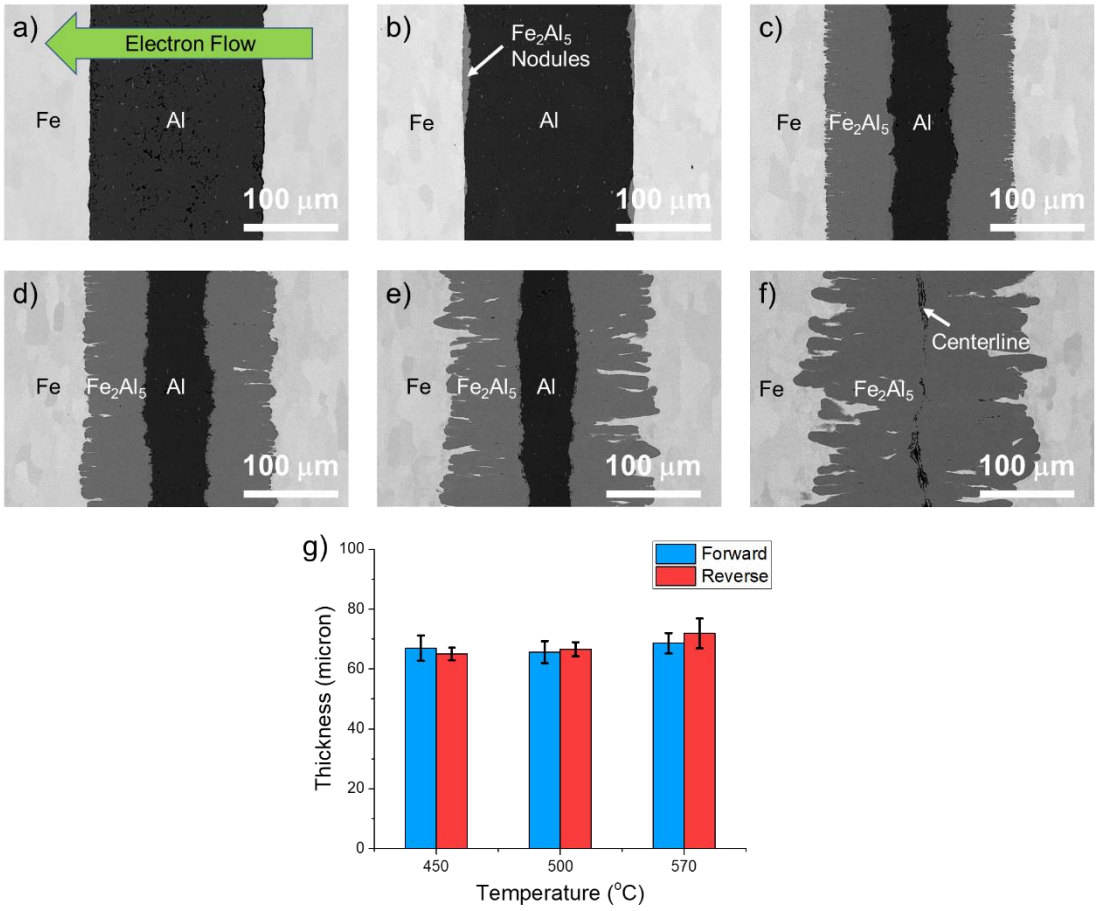

Figure 6.5: SEM images for Fe-Al diffusion couples sintered via SPS at (a) 350°C for 24 hr.; (b) 400°C for 22 hr.; (c) 450°C for 10 hr.; (d) 500°C for 1.5 hr.; (e) 570°C for 15 min; (f) 570°C for 1 hr. The 'centerline' results from the accumulation of impurities[4]. The electron flows from right to left. (h) Comparison of Fe_2Al_5 layer thickness in forward and reverse directions.

6.3.4.2 Electromigration in FeAl and α-Fe Phase

The growth of the $FeAl_2$, FeAl and α–Fe solid solution phases is activated as the sintering temperature increases. As the result of similar growth rates, $FeAl_2$, FeAl and α–Fe solid solution will coexist in the Fe-Al diffusion couple over a wide temperature range, from 700°C, to at least 1000°C [77], which is classified as the conditions for multiple intermetallic phases discussed in Section 3.2.2.

Figure 6.6(a), 6.6(b) and 6.6(c) present examples of the Fe-Al diffusion couple sintered at 700°C for 3 hr. The darkest regions are the Fe_2Al_5 phase, adjacent to which is a layer of the $FeAl_2$ phase. The relatively bright FeAl and α–Fe solid solution region forms as Al diffuses from $FeAl_2$ to pure Fe, which are the brightest regions. Although the growth of $FeAl_2$, FeAl and α–Fe solid solution are diffusion controlled, the phase boundaries are relatively irregular, which is considered to be inherited from the finger-like parent Fe_2Al_5 phase. Furthermore, a study in binary metal systems has already shown some degree of grain orientation dependence for diffusivity [114], and the diffusivity could vary more than one order of magnitude. $FeAl_2$ possesses the lowest symmetrical crystal structure (triclinic, space group 1), and Appendix 6.C of inverse pole figures reveals significant texture in the Fe_2Al_5 and $FeAl_2$ phases formed. Therefore, the grain orientation dependence for diffusion may contribute to the irregular $FeAl_2$/Fe_2Al_5 interface, although the lack of the corresponding diffusivity data limits the ability to prove this hypothesis.

As revealed in Figure 6.6(d) and 6.6(e), the EDS maps suggest that FeAl and α–Fe solid solution layer is relatively uniform. The boundary between the pure Fe and the solid solution layer, indicated by the white dash line, generally follows the shape of the $FeAl_2$/FeAl interface.

Meanwhile, a previous study found that the $FeAl_2$/FeAl interface would eventually be flattened by diffusion-controlled growth [77].

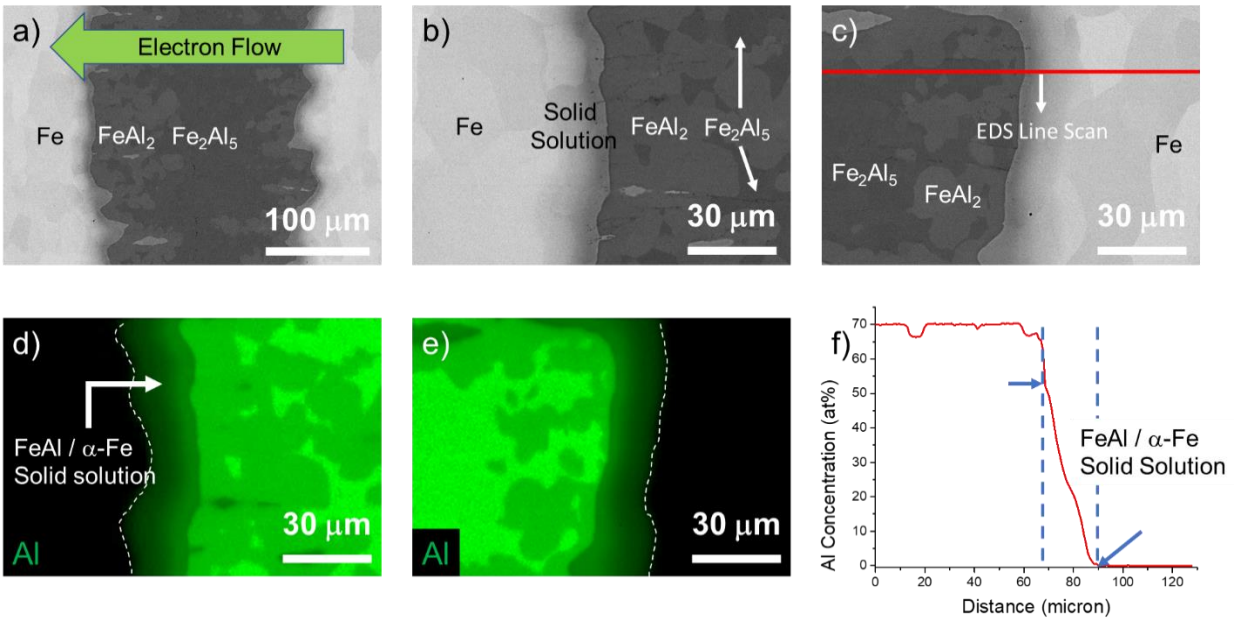

Figure 6.6: (a) SEM images for Fe-Al diffusion couples sintered via SPS at 570°C for 1 hr., then 700°C for 3 hr. (b) and (c) magnified images at phase boundary region in forward and reverse directions, respectively. (d) and (e) EDS map for the areas in (b) and (c). (f) EDS line scan along the red line notated in (c).

According to Figure 6.4, at high temperatures, the phase transformation of disordered α–Fe solid solution to ordered FeAl [B2] belongs to the second-order phase transformation, occurring at ~25 at% Al without a step change in composition. Furthermore, a compositional step would be introduced to the α–Fe/FeAl interface when the temperature drops below 650°C. The EDS line scan shown in Figure 6.6(f) produces a smooth and continuous composition curve across the FeAl and α–Fe layers, indicating that the microstructure evolution formed at 700°C remains when cooled to room temperature. Consequently, in this study, FeAl and α–Fe are treated as the same phase, and divided into three sub-layers to investigate the diffusion and electromigration behavior. Sub-layer 1 refers to the α–Fe solid solution of 0~20 at% Al, whose thickness is described by Eq.

(6.23). Similarly, sub-layer 2 refers to the solid solution of 20~30 at% Al, which represents the ambiguous FeAl/α–Fe boundary that varies with temperature, and sub-layer 3 refers to the FeAl solid solution of 30~50 at% Al.

Subsequently, Eq. (6.24) becomes:

$$\frac{0.1}{0.25}\frac{dX_1}{dt} + \frac{dX_2}{dt} = \frac{M_2}{X_2} + U_2 \tag{6.47}$$

and

$$\frac{0.1}{0.4}\frac{dX_1}{dt} + \frac{0.25}{0.4}\frac{dX_2}{dt} + \frac{dX_3}{dt} = \frac{M_3}{X_3} + U_3 \tag{6.48}$$

Figure 6.7(a) compares the thickness of the three sub-layers of the FeAl/α–Fe phase regions in the forward and reverse directions. T-test, as a statistical criterion for determining whether two sets of data are significantly different, is employed to the measured results. Statistically, electromigration is negligible in sub-layers 1 and 2, and weak but present in sub-layer 3. Additionally, a previous study of Fe-Al microstructure evolution at 1000°C, which was also performed via SPS, did not find any difference in thickness between the forward and reverse directions for FeAl and α–Fe phases [77]. Following the second algorithm described in Section 3.2.2, while samples of 1 hr. and 2 hr. are taken for calculation, the diffusivity-related coefficient M_k is solved for each sub-layer: $M_1 = 0.002083\,\mu m^2/s$, $M_2 = 0.001637\,\mu m^2/s$ and $M_3 = 0.004718\,\mu m^2/s$, while the electromigration coefficient for sub-layer 3 (FeAl solid solution) is $U_3 = 9.84 \times 10^{-5}\,\mu m \cdot C/s$. Subsequently, the numerical functions $X_k(t)$, for the prediction of layer thickness, are plotted in Figure 6.7(b) to 6.7(d).

6.3.4.3 Electromigration in $FeAl_2$ Phase

Figure 6.8(a) presents another example as an EBSD map of the Fe-Al diffusion couple sintered at 700°C for 3 hr. The thickness of the $FeAl_2$ layers in the forward and reverse direction

is obviously different, indicating a strong electromigration effect. The quantitative analysis involves Eq. (6.24):

$$\frac{0.1}{0.6655}\frac{dX_1}{dt}+\frac{0.25}{0.6655}\frac{dX_2}{dt}+\frac{0.4}{0.6655}\frac{dX_3}{dt}+\frac{dX_4}{dt}=\frac{M_4}{X_4}+U_4 \tag{6.49}$$

The composition range for the $FeAl_2$ phase is 65.8~67.3 at% Al [115], which gives $\tilde{c_4}=0.6655$. Fe-Al diffusion couples sintered at 700°C for 1 hr. and 2 hr. are taken for calculation, which yields $M_4=0.097441\ \mu m^2/s$ and $U_4=0.001678\,\mu m\cdot\frac{C}{s}$. Furthermore, as shown in Figure 6.8(b), 0.5 hr. and 3 hr. samples are measured as the validation to evaluate the accuracy of the numerical functions $X_4(t)$.

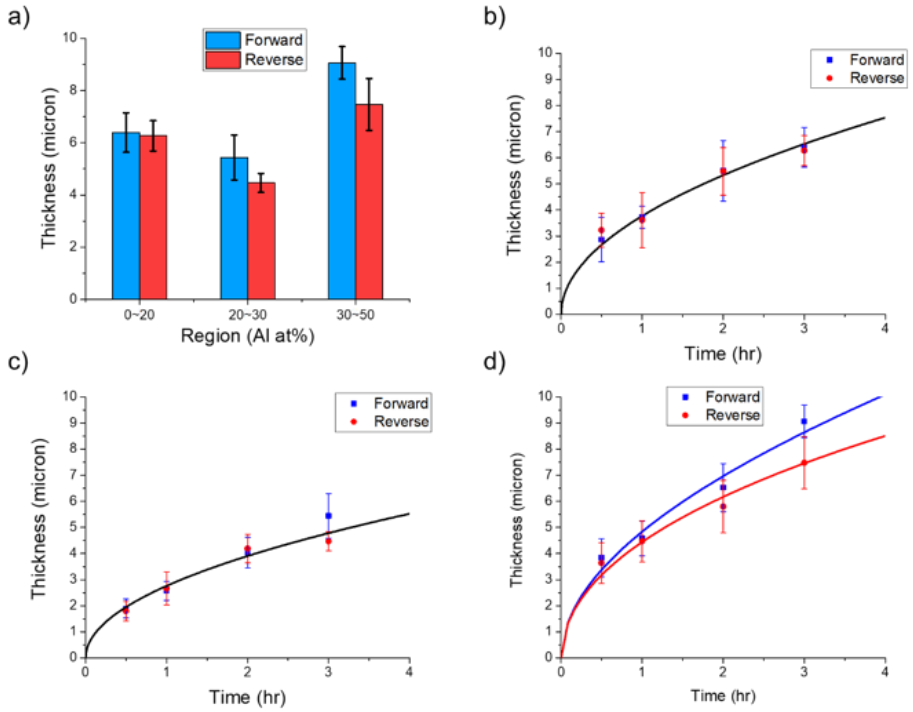

Figure 6.7: (a) Comparison of α–Fe and FeAl solid solution layer thickness in forward and reverse directions of Fe-Al diffusion couples sintered via SPS at 570°C for 1 hr., then 700°C for 3 hr. (b), (c) and (d) Measurements and predictions for the solid solution layer thickness of the Fe-Al diffusion couples sintered via SPS at 700°C. (b) is for α–Fe solid solution of 0~20 at% Al, (c) is for the solid solution of 20~30 at% Al, and (d) is for FeAl solid solution of 30~50 at% Al. Predictions in (b) and (c) only calculate concentration gradient induced diffusion, while (d) also takes electromigration effect into consideration.

Subsequently, based on Eq. (6.13) and (6.14), the diffusion coefficient D_i and the apparent effective charge Z_a^* are listed in Table 6.2. The diffusion coefficient for α–Fe/FeAl and $FeAl_2$ is at the same order of magnitude as the prediction from the literatures ($10^{-3}\mu m^2/s$ for α–Fe/FeAl, and $10^{0}\mu m^2/s$ for $FeAl_2$), which were measured at higher temperature [109,116–118] and can be converted to 700°C with the activation energy [119]. Furthermore, if the electromigration was absent, the diffusion coefficient can be calculated from Eq. (6.17), the classical parabolic equation for the diffusion-controlled growth. Then we would get the similar values for the diffusion coefficient, because without the electromigration, the thickness of the intermetallic layer would be between that of the forward and reverse directions.

Table 6.2: Diffusion coefficient and apparent effective charge for intermetallics in Fe-Al system.

	M $(\mu m^2/s)$	D $(\mu m^2/s)$	U $(\mu m \cdot C/s)$	Z_a^*
α–Fe (0~20 at% Al)	0.002083	0.001229	/	/
α–Fe/FeAl (20~30 at% Al)	0.001637	0.004037	/	/
FeAl (30~50 at% Al)	0.004718	0.009236	9.84×10^{-5}	-2040
$FeAl_2$ is (65.8~67.3 at% Al)	0.097441	4.323	0.001678	-74

Due to the lack of published values in the Fe-Al system, the direct validation about the accuracy for the apparent effective charge calculated in the present work is impossible at the current stage. As the indirect comparison, the apparent effective charge for Ag_3Sn, which exhibits strong electromigration phenomenon, is -90 [54], the same order of magnitude as $FeAl_2$. Additionally, the apparent effective charge for Cu is -1400 [48], the same order of magnitude as FeAl. Meanwhile, a counterintuitive result is that although FeAl phase possesses significantly larger apparent effective charge than $FeAl_2$, its electromigration phenomenon is considerably

weaker. It is because the diffusivity in FeAl phase is three orders of magnitudes lower than FeAl2. Consequently, as implied by Eq. (6.7), the extra mass flux induced by electromigration is significantly less, creating less difference in the growth rate. Plus, since the diffusivity is tiny, the thickness of FeAl layer is thin. As the result, the concentration gradient, the first term of Eq. (6.7), is large. Therefore, the mass flux induced by the concentration gradient would be relatively higher than that of electromigration, making the asymmetric growth rate less noticeable.

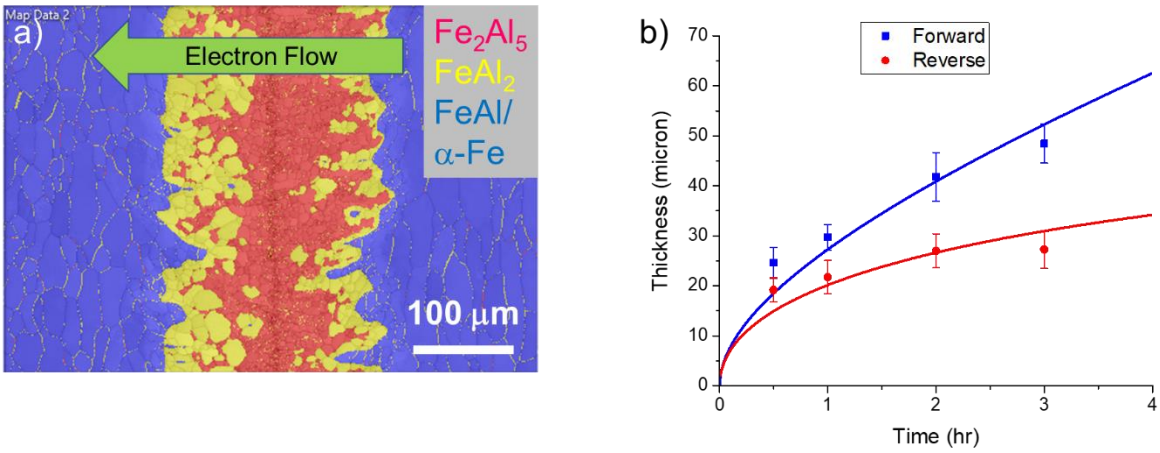

Figure 6.8: (a) EBSD phase map coupled with band contrast for the Fe-Al diffusion couple sintered via SPS at 570°C for 1 hr., then 700°C for 3 hr. The electrons flow from right to left. This figure illustrates the more rapid conversion of the Fe_2Al_5 phase (red) to the $FeAl_2$ phase (yellow) via the electromigration effect. (b) Measurements and predictions for $FeAl_2$ layer thickness of the Fe-Al diffusion couples sintered at 700°C for both forward and reverse directions.

All the quantitative analysis in this work assumes that the interface is flat, which is appropriate for the common situation of diffusion-controlled growth. Under this flat-interface assumption, diffusion in the system is uniform and one-dimensional, along the axis of the macroscale concentration gradient and the applied electric field. However, Fe_2Al_5 phase and $FeAl_2$ phases in the Fe-Al system possess irregular interfaces. As a consequence, off-axis diffusion occurs, where the Fe_2Al_5 or $FeAl_2$ phases grow into the α–Fe region, increasing the apparent

diffusivity. In order to demonstrate the influence of the irregular interface, a correction term $A(\zeta)$ can be introduced to Eq. (6.7) as:

$$J_i = -\frac{D_i \cdot c_i}{RT}\left(A(\zeta)RT\frac{d\ln c_i}{dx} + Fz_a^* E\right) \tag{6.50}$$

where ζ represents the geometry of the interface. $A(\zeta)$ would take a positive value that is greater than 1 at the beginning, and gradually reduces to 1 as diffusion-controlled growth will flatten the interface. Therefore, the numerical function $X_k(t)$, which ignores the influence of the irregular interface, would underestimate the thickness for a short time, and overestimate the thickness at longer times.

6.4 Conclusion

The present work quantitively analyzes the electromigration effect in the Fe-Al system with spark plasma sintering/field assisted sintering. Simulation, mathematical derivation and experiments are combined to systematically study the electromigration effect, while all the major Fe-Al phases, including Fe_2Al_5, $FeAl_2$, FeAl and α–Fe, have been investigated. The main conclusions are:

1. FEA simulation demonstrates that temperature and current are uniform across the diameter of the Fe-Al diffusion couple in the SPS machine.

2. The current effect, rather than the field effect, is the dominant electromigration mechanism for metals sintered via SPS.

3. A mathematical model for the electromigration effect in a system with multiple intermetallics is developed, and a numerical algorithm is derived to solve for the corresponding diffusion and enhancement coefficients.

4. Electromigration is negligible for the Fe_2Al_5 and α–Fe phases, weak but noticeable for FeAl, and significant for $FeAl_2$. Diffusivities and electromigration coefficients are calculated for all these phases.

Appendix 6.A The Material Properties for FEA Simulation

The thermal and electrical properties of Fe, Al and Mo are directly taken from the database of the Comsol software. The material properties of graphite, boron nitride and the thermal insulation (graphite filter), if Comsol does not have it in the database, are either taken from the literature or the vendors, and listed in Table 6.A1.

Table 6.A.1: Material Properties for the Simulation.

Properties	Graphite	BN	Graphite Filter
Thermal Conductivity (W/mK)	0.8*(123-6.99e-2*T+1.55e-5*T^2) [120]	76	0.44
Electrical Conductivity (S/m)	1.32*(45.414*T+ 46870) [121]	10e-3	556
Heat Capacity $(J/kg*K)$	34.27+2.72*T-9.6e-4*T^2 [120]	267.4312 + 5.131074*T - 0.005026586*T^2+2. 358517E-6*T^3- 4.273412E-10*T^4	720
Density (kg/m^3)	1950	2000	85
Properties	Fe	Al	Mo
Thermal Conductivity (W/mK)	44.5	39.646+1.684*T - 0.0054134*T^2+ 8.4313E-6*T^3 6.537E-9*T^4+ 2.002E-12*T^5	138
Electrical Conductivity (S/m)	4.032e6	1/(-1.037048E-8+ 1.451201E-10*T- 8.192563E-14*T^2+ 6.619834E-17*T^3)	1.87e7
Heat Capacity $(J/kg*K)$	475	595.6585+ 1.513029*T- 0.002070065*T^2+ 1.303608E-6*T^3	250
Density (kg/m^3)	7850	2736.893- 0.006011681*T- 7.012444E-4*T^2+ 1.3582E-6*T^3- 1.367828E-9*T^4+ 5.177991E-13*T^5	10200

Appendix 6.B Sintering Temperature and Total Current

Table 6.B1 lists the total current for different sintering temperatures of Fe-Al diffusion couples described in section 2.1. The temperature for the chilling water is assumed to be the room temperature (25^{o}C).

Table 6.B.1: Sample temperature and total current for Fe-Al diffusion couples sintered via SPS.

Temperature	Total Current
350^{o}C	310 A
400^{o}C	370 A
450^{o}C	430 A
500^{o}C	462 A
570^{o}C	512 A
700^{o}C	582 A
850^{o}C	644 A

Appendix 6.C Texture in Fe-Al Diffusion Couple

Based on the times random number from the inverse pole figure in Figure 6.C1, the Fe_2Al_5 phase possesses a very strong texture, and the $FeAl_2$ phase possesses a strong texture. FeAl and α–Fe phases, whose crystal structure are very similar and cannot be distinguished by the conventional EBSD, possesses medium texture. The texture of FeAl/α–Fe could be inherited from the pure iron foils that were initially rolled to the desired thickness.

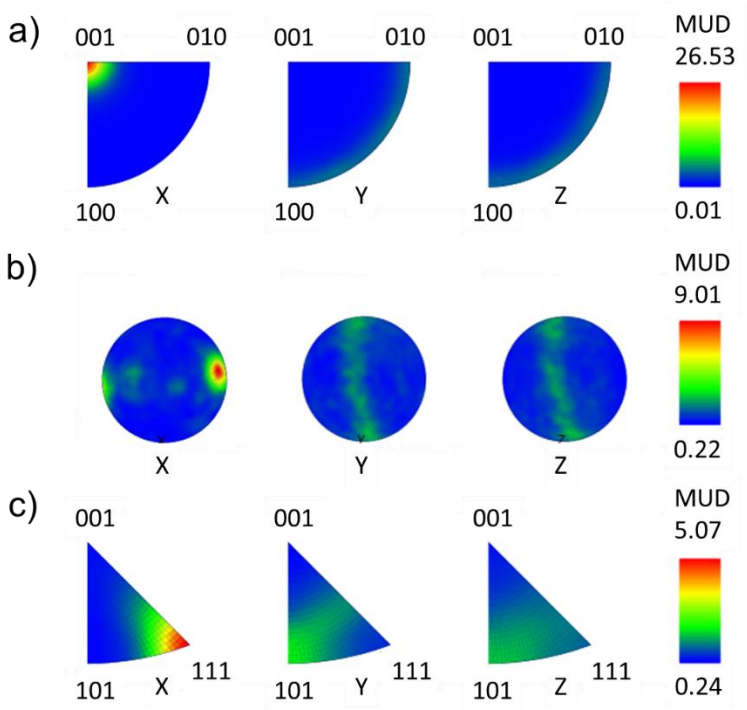

Figure 6.C1: Inverse pole figures of the area in Figure 6.1(a) for (a) the Fe_2Al_5 phase, (b) the $FeAl_2$ phase, and (c) the FeAl/α–Fe phase.

Appendix 6.D Temperature and Sample Voltage Evolution During the Simulation.

Shown in Figure 6.D1 is the temperature evolution simulated by applying the constant voltage to the system. As the temperature ramping, the sample voltage would evolve as well, but would not vary a lot. The temperature gradient within the sample, is represented by the temperature difference between the center and edge of the sample, as indicated in Figure 6.3. The temperature difference within the sample also evolves but would not vary a lot.

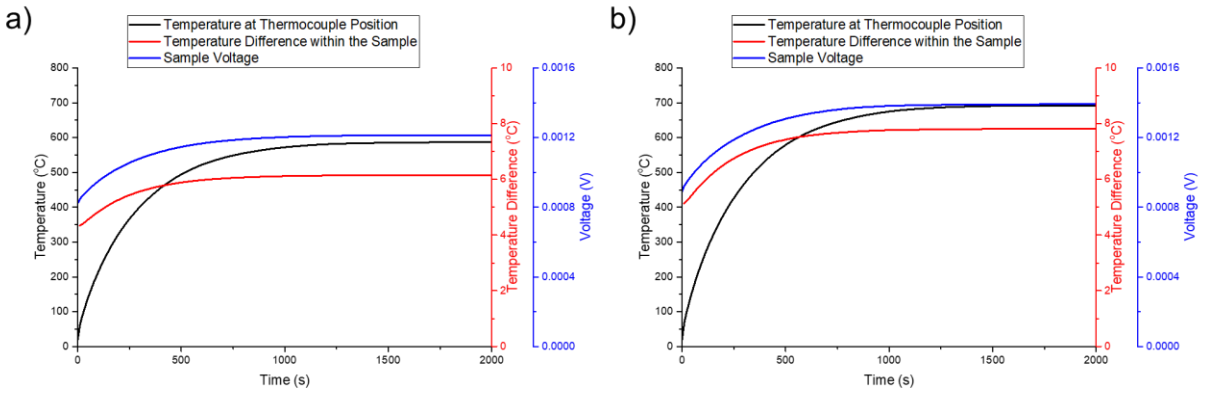

Figure 6.D.1: Temperature and sample voltage evolution by simulation at (a) 570°C, and (b) 700°C.

Appendix 6.E Influence of Fe_2Al_5 Sintering Conditions on the Growth of $FeAl_2$ Phase

Figure 6.E1 is the Fe-Al diffusion couple sintered via SPS first to convert Al into Fe_2Al_5, then sintered at a higher temperature via the hot press. As shown in Figure 6.E1(a), the morphology is similar to Figure 6.1(d), which was sintered at the sample temperature and time entirely via the hot press. Meanwhile, as shown in Figure 6.E1(b), the growth of the $FeAl_2$ layer is symmetrical, and the T-test confirms that the thickness in forward and reverse directions is statistically equal. Therefore, the Fe_2Al_5 wound not pre-condition the growth asymmetry of the $FeAl_2$ phase.

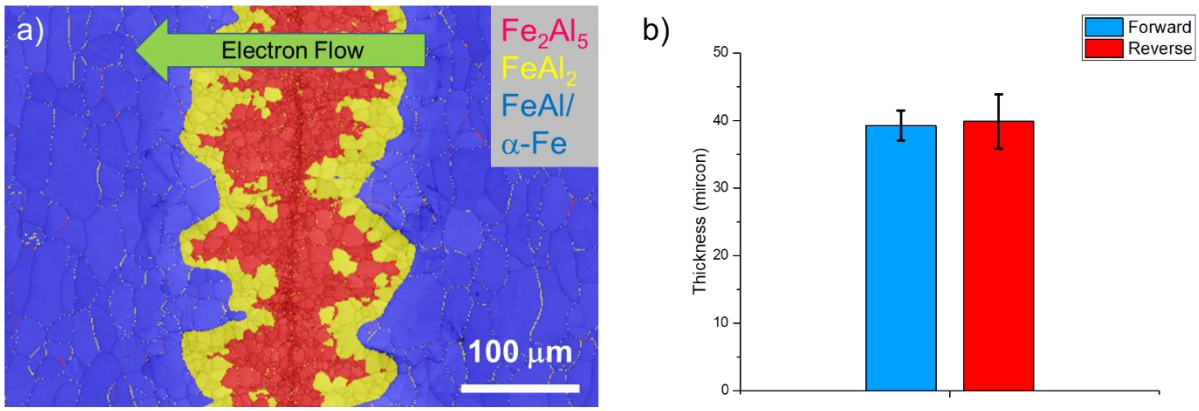

Figure 6.E.1: (a) EBSD phase map coupled with band contrast for the Fe-Al diffusion couple sintered via SPS at 570oC for 1 hr, then cooled down and sintered via hot press at 850oC for 0.5 hr. (b) Comparison of FeAl2 layer thickness in forward and reverse directions.

Acknowledgment

Chapter 6, in full, is the reprint of the published article in Acta Materialia, 2020, Elsevier. Wang, Haoren; Kou, Rui; Harrington, Tyler; Vecchio, Kenneth S. Electromigration Effect in Fe-Al Diffusion Couples with Field-Assisted Sintering. Acta Materialia (2020).

I would like to thank Rui Kou, Tyler Harrington, and my principal investigator Professor Kenneth Vecchio, for their contribution in this work.

REFERENCES

[1] H.E. Dève, M.J. Maloney, On the toughening of intermetallics with ductile fibers: Role of interfaces, Acta Metall. Mater. 39 (1991) 2275–2284.

[2] K.S. Vecchio, Synthetic multifunctional metallic-intermetallic laminate composites, JOM. 57 (2005) 25–31.

[3] U. Anselmi-Tamburini, Z.A. Munir, The propagation of a solid-state combustion wave in Ni-Al foils, J. Appl. Phys. 66 (1989) 5039–5045.

[4] D.J. Harach, K.S. Vecchio, Microstructure evolution in metal-intermetallic laminate (MIL) composites synthesized by reactive foil sintering in air, Metall. Mater. Trans. A Phys. Metall. Mater. Sci. 32 (2001) 1493–1505.

[5] A. Rohatgi, D.J. Harach, K.S. Vecchio, K.P. Harvey, Resistance-curve and fracture behavior of Ti-Al3Ti metallic-intermetallic laminate (MIL) composites, Acta Mater. 51 (2003) 2933–2957.

[6] R.R. Adharapurapu, K.S. Vecchio, A. Rohatgi, F. Jiang, Fracture of Ti-Al3Ti metal-intermetallic laminate composites: Effects of lamination on resistance-curve behavior, Metall. Mater. Trans. A Phys. Metall. Mater. Sci. 36 (2005) 3217–3236.

[7] T. Li, F. Grignon, D.J. Benson, K.S. Vecchio, E.A. Olevsky, F. Jiang, A. Rohatgi, R.B. Schwarz, M.A. Meyers, Modeling the elastic properties and damage evolution in Ti-Al3Ti metal-intermetallic laminate (MIL) composites, Mater. Sci. Eng. A. 374 (2004) 10–26.

[8] T. Li, F. Jiang, E.A. Olevsky, K.S. Vecchio, M.A. Meyers, Damage evolution in Ti6Al4V-Al3Ti metal-intermetallic laminate composites, Mater. Sci. Eng. A. 443 (2007) 1–15.

[9] Y. Cao, S. Zhu, C. Guo, K.S. Vecchio, F. Jiang, Numerical Investigation of the Ballistic Performance of Metal-Intermetallic Laminate Composites, Appl. Compos. Mater. 22 (2015) 437–456.

[10] F. Jiang, R.M. Kulin, K.S. Vecchio, Use of Brazilian disk test to determine properties of metallic-intermetallic laminate composites, JOM. 62 (2010) 35–40.

[11] R.R. Adharapurapu, K.S. Vecchio, F. Jiang, A. Rohatgi, Effects of ductile laminate thickness, volume fraction, and orientation on fatigue-crack propagation in Ti-Al 3 Ti metal-intermetallic laminate composites, Metall. Mater. Trans. A. 36 (2005) 1595–1608.

[12] R.D. Price, F. Jiang, R.M. Kulin, K.S. Vecchio, Effects of ductile phase volume fraction on the mechanical properties of Ti-Al3Ti metal-intermetallic laminate (MIL) composites, Mater. Sci. Eng. A. 528 (2011) 3134–3146.

[13] K.S. Vecchio, F. Jiang, Fracture toughness of Ceramic-Fiber-Reinforced Metallic-

Intermetallic-Laminate (CFR-MIL) composites, Mater. Sci. Eng. A. 649 (2016) 407–416.

[14] V.C. Srivastava, T. Singh, S.G. Chowdhury, V. Jindal, Microstructural characteristics of accumulative roll-bonded Ni-Al-based metal-intermetallic laminate composite, J. Mater. Eng. Perform. 21 (2012) 1912–1918.

[15] M. Konieczny, Microstructural characterisation and mechanical response of laminated Ni-intermetallic composites synthesised using Ni sheets and Al foils, Mater. Charact. 70 (2012) 117–124.

[16] Y. Wang, H. Wang, X. Liu, K.S. Vecchio, Microstructure evolution in Ni and Ni-superalloy based metallic-intermetallic laminate (MIL) composites, Intermetallics. 87 (2017) 70–80.

[17] Y. Wang, K.S. Vecchio, Microstructure evolution in Fe-based-aluminide metallic-intermetallic laminate (MIL) composites, Mater. Sci. Eng. A. 649 (2016) 325–337.

[18] Y. Wang, S. Zhou, K.S. Vecchio, Annealing effects on the microstructure and properties of an Fe-based Metallic-Intermetallic Laminate (MIL) composite, Mater. Sci. Eng. A. 665 (2016) 47–58.

[19] Y. Wang, K.S. Vecchio, Microstructure evolution in a martensitic 430 stainless steel-Al metallic-intermetallic laminate (MIL) composite, Mater. Sci. Eng. A. 643 (2015) 72–85.

[20] S. Kobayashi, T. Yakou, Control of intermetallic compound layers at interface between steel and aluminum by diffusion-treatment, Mater. Sci. Eng. A. 338 (2002) 44–53.

[21] E.M. Schulson, T.P. Weihs, D. V. Viens, I. Baker, The effect of grain size on the yield strength of Ni3Al, Acta Metall. 33 (1985) 1587–1591.

[22] I. Baker, P.R. Munroe, Mechanical properties of FeAl, Int. Mater. Rev. 42 (1997) 181–205.

[23] M. Zamanzade, A. Barnoush, C. Motz, A Review on the Properties of Iron Aluminide Intermetallics, Crystals. 6 (2016) 10.

[24] E. Wang, Y. Tian, Z. Wang, F. Jiao, C. Guo, F. Jiang, A study of shape memory alloy NiTi fiber/plate reinforced (SMAFR/SMAPR) Ti-Al laminated composites, J. Alloys Compd. 696 (2017) 1059–1066.

[25] E. Wang, C. Guo, P. Zhou, C. Lin, X. Han, F. Jiang, Fabrication, mechanical properties and damping capacity of shape memory alloy NiTi fiber-reinforced metal-intermetallic-laminate (SMAFR-MIL) composite, Mater. Des. 95 (2016) 446–454.

[26] C. Lin, F. Jiang, Y. Han, E. Wang, D. Yuan, C. Guo, Microstructure evolution and fracture behavior of innovative Ti-(SiCf/Al3Ti) laminated composites, J. Alloys Compd. 743 (2018) 52–62.

[27] C. Guo, H. Huang, F. Jiang, C. Lin, E. Wang, Y. Han, D. Yuan, Z. Wang, Microstructure and mechanical properties of continuous ceramic SiC and shape memory alloy NiTi hybrid fibers reinforced Ti-Al metal-intermetallic laminated composite, J. Alloys Compd. 729 (2017) 1145–1155.

[28] Y. Han, C. Lin, X. Han, Y. Chang, C. Guo, F. Jiang, Fabrication, interfacial characterization and mechanical properties of continuous Al2O3ceramic fiber reinforced Ti/Al3Ti metal-intermetallic laminated (CCFR-MIL) composite, Mater. Sci. Eng. A. 688 (2017) 338–345.

[29] Z. Lu, N. Wei, P. Li, C. Guo, F. Jiang, Microstructure and mechanical properties of intermetallic Al3Ti alloy with residual aluminum, Mater. Des. 110 (2016) 466–474.

[30] S. Qin, X. Cui, Z. Tian, L. Geng, B. Liu, J. Zhang, J. Chen, Synthesis and mechanical properties of innovative (TiB/Ti)-Ti3Al micro-laminated composites, J. Alloys Compd. 700 (2017) 122–129.

[31] H. Duan, Y. Han, W. Lu, L. Wang, J. Mao, D. Zhang, Configuration design and fabrication of laminated titanium matrix composites, Mater. Des. 99 (2016) 219–224.

[32] X. Li, Y. Sun, Z. Wang, F. Jiang, Fabrication, microstructure characterization and mechanical property of the Ti6Al4V-(NiTif/Mg3AlZn) laminate composite, J. Alloys Compd. 774 (2019) 656–667.

[33] Y. Zhang, X. Cheng, H. Cai, H. Zhang, Effects of annealing time on the microstructures and tensile properties of formed laminated composites in Ti-Ni system, J. Alloys Compd. 699 (2017) 695–705.

[34] C. Zhu, T. Harrington, V. Livescu, G.T. Gray, K.S. Vecchio, Determination of geometrically necessary dislocations in large shear strain localization in aluminum, Acta Mater. 118 (2016) 383–394.

[35] M.F. Ashby, The deformation of plastically non-homogeneous materials, Philos. Mag. 21 (1970) 399–424.

[36] Y. Zhu, K. Ameyama, P.M. Anderson, I.J. Beyerlein, H. Gao, H.S. Kim, E. Lavernia, S. Mathaudhu, H. Mughrabi, R.O. Ritchie, N. Tsuji, X. Zhang, X. Wu, Heterostructured materials: superior properties from hetero-zone interaction, Mater. Res. Lett. 9 (2021) 1–31.

[37] Y. Zhu, X. Wu, Perspective on hetero-deformation induced (HDI) hardening and back stress, Mater. Res. Lett. 7 (2019) 393–398.

[38] C.X. Huang, Y.F. Wang, X.L. Ma, S. Yin, H.W. Höppel, M. Göken, X.L. Wu, H.J. Gao, Y.T. Zhu, Interface affected zone for optimal strength and ductility in heterogeneous laminate, Mater. Today. 21 (2018) 713–719.

[39] M.X. Yang, R.G. Li, P. Jiang, F.P. Yuan, Y.D. Wang, Y.T. Zhu, X.L. Wu, Residual stress

provides significant strengthening and ductility in gradient structured materials, Mater. Res. Lett. 7 (2019) 433–438.

[40] A. Schmitt, K.S. Kumar, A. Kauffmann, X. Li, F. Stein, M. Heilmaier, Creep of binary Fe-Al alloys with ultrafine lamellar microstructures, Intermetallics. 90 (2017) 180–187.

[41] X. Li, M. Palm, A. Scherf, D. Janda, M. Heilmaier, F. Stein, Microstructure and Phase Transformation Temperatures of Two-Phase FeAl (B2) + FeAl 2 Alloys, MRS Online Proc. Libr. Arch. 1760 (2014) 2–7.

[42] A. Schmitt, K.S. Kumar, A. Kauffmann, M. Heilmaier, Microstructural evolution during creep of lamellar eutectoid and off-eutectoid FeAl/FeAl 2 alloys, Intermetallics. 107 (2019) 116–125.

[43] C. Chen, S. Chen, Electromigration effect upon the Sn / Ag and Sn / Ni interfacial reactions at various temperatures, Acta Mater. 50 (2002) 2461–2469.

[44] A. Lodder, Electromigration theory unified, Europhys. Lett. 72 (2005) 774–780.

[45] L.J. Sham, Microscopic theory of the driving force in electromigration, Phys. Rev. B. 12 (1975) 3142.

[46] J.W. Morris, S.H. Kang, The Metallurgical Control of Electromigration Failure in Narrow Conducting Lines, J. Miner. 48 (1996) 43–46.

[47] J.J. Lloyd, J.R.; Clement, Electromigration in copper conductors, Thin Solid Films. 262 (1995) 135–141.

[48] C.-K. Hu, Electromigration failure mechanisms in bamboo-grained Al(Cu) interconnections, Thin Solid Films. 260 (1995) 124–134.

[49] C. Hu, B. Luther, Electromigration in two-level interconnects of Cu and Al alloys, Mater. Chem. Phys. 41 (1995) 1–7.

[50] W. Liu, S. Chen, C. Chen, The Al / Ni Interfacial Reactions Under the Influence of Electric Current, J. Electron. Mater. 27 (1998) 6–9.

[51] N. Bertolino, J. Garay, Z.A. Munir, Electromigration effects in Al-Au multilayers, Scr. Mater. 44 (2001) 737–742.

[52] J.E. Garay, Z.A. Munir, Enhanced growth of intermetallic phases in the Ni – Ti system by current effects, Acta Mater. 51 (2003) 4487–4495.

[53] J.R. Friedman, J.E. Garay, Z.A. Munir, Modified interfacial reactions in Ag – Zn multilayers under the influence of high DC currents, Intermetallics. 12 (2004) 589–597.

[54] C.-M. Chen, S.-W. Chen, Electric current effects on Sn/Ag interfacial reactions, J. Electron. Mater. 28 (1999) 902–906.

[55] B. AG, GB Patent, No. 27,002; and GB Patent, No. 9020., 1906.

[56] M. Tokita, Development of Large-Size Ceramic/Metal Bulk FGM Fabricated by Spark Plasma Sintering, Mater. Sci. Forum. 308–311 (1999) 83–88.

[57] G. Xie, Spark Plasma Sintering: A Useful Technique to Develop Large-Sized Bulk Metallic Glasses, J. Powder Metall. Min. 02 (2013) 2–4.

[58] M. Yoshimura, Synthesis of nanograined ZrO 2 -based composites by chemical processing and pulse electric current sintering, Mater. Lett. 38 (1999) 18–21.

[59] K. Vanmeensel, A. Laptev, O. Van Der Biest, J. Vleugels, The influence of percolation during pulsed electric current sintering of ZrO 2 – TiN powder compacts with varying TiN content, Acta Mater. 55 (2007) 1801–1811.

[60] R.S. Mishra, J.A. Schneider, J.F. Shackelford, Plasma Activated Sintering of Nanocrystalline gamma-Al203, Nanostructured Mater. 5 (1995) 525–544.

[61] S. Grasso, Y. Sakka, G. Maizza, a review of patents 1906 – 2008 Electric current activated / assisted sintering (ECAS): a review of patents, Sci. Technol. Adv. Mater. 10 (2009) 053001.

[62] K. Vanmeensel, A. Laptev, J. Hennicke, J. Vleugels, O. Van Der Biest, Modelling of the temperature distribution during field assisted sintering, Acta Mater. 53 (2005) 4379–4388.

[63] U. Anselmi-tamburini, J.E. Garay, Z.A. Munir, Fundamental investigations on the spark plasma sintering / synthesis process III . Current effect on reactivity, Mater. Sci. Eng. A. 407 (2005) 24–30.

[64] W. Chen, J.E. Garay, J.R. Groza, Z.A. Munir, Fundamental investigations on the spark plasma sintering / synthesis process I . Effect of dc pulsing on reactivity, Mater. Sci. Eng. A. 394 (2005) 132–138.

[65] Y. Kodera, Æ.M. Ohyanagi, Æ.Z.A. Munir, Effect of pulsed DC current on atomic diffusion of Nb – C diffusion couple, J. Mater. Sci. 43 (2008) 6400–6405.

[66] Z. Trzaska, J. Monchoux, Electromigration experiments by spark plasma sintering in the silver – zinc system, J. Alloys Compd. 635 (2015) 142–149.

[67] O. Kubaschewski, Iron—Binary phase diagrams, Springer Science & Business Media, 2013.

[68] N. Wang, Y. Ji, Y. Wang, Y. Wen, L.Q. Chen, Two modes of grain boundary pinning by coherent precipitates, Acta Mater. 135 (2017) 226–232.

[69] H. Springer, A. Kostka, E.J. Payton, D. Raabe, A. Kaysser-Pyzalla, G. Eggeler, On the formation and growth of intermetallic phases during interdiffusion between low-carbon steel and aluminum alloys, Acta Mater. 59 (2011) 1586–1600.

[70] M. Kajihara, Analysis of kinetics of reactive diffusion in a hypothetical binary system, Acta Mater. 52 (2004) 1193–1200.

[71] J.H. Schneibel, E.D. Specht, W.A. Simpson, Solid solution strengthening in ternary B2 iron aluminides containing 3d transition elements, Intermetallics. 4 (1996) 581–583.

[72] R.L. Fleischer, Substitutional solutes in AlRu-I. Effects of solute on moduli, lattice parameters and vacancy production, Acta Metall. Mater. 41 (1993) 863–869.

[73] R.L. Fleischer, Substitutional solutes in AlRu-II. Hardening and correlations with defect structure, Acta Metall. Mater. 41 (1993) 1197–1205.

[74] A. Barnoush, M. Zamanzade, Effect of substitutional solid solution on dislocation nucleation in Fe3Al intermetallic alloys, Philos. Mag. 92 (2012) 3257–3268.

[75] M. Zamanzade, J.R. Velayarce, O.T. Abad, C. Motz, A. Barnoush, Mechanical behavior of iron aluminides: A comparison of nanoindentation, compression and bending of micropillars, Mater. Sci. Eng. A. 652 (2016) 370–376.

[76] K. Momma, F. Izumi, An integrated three-dimensional visualization system VESTA using wxWidgets, Comm. Crystallogr. Comput. IUCr Newslett. 7 (2006) 106–119.

[77] H. Wang, T. Harrington, C. Zhu, K.S. Vecchio, Design , fabrication and characterization of FeAl-based metallic- intermetallic laminate (MIL) composites, Acta Mater. 175 (2019) 445–456.

[78] H. Wang, R. Kou, T. Harrington, K.S. Vecchio, Electromigration Effect in Fe-Al Diffusion Couples with Field-Assisted Sintering, Acta Mater. 186 (2020) 631–643.

[79] C. Zhu, T. Harrington, G.T. Gray, K.S. Vecchio, Dislocation-type evolution in quasi-statically compressed polycrystalline nickel, Acta Mater. 155 (2018) 104–116.

[80] C. Zhu, V. Livescu, T. Harrington, O. Dippo, G.T. Gray, K.S. Vecchio, Investigation of the shear response and geometrically necessary dislocation densities in shear localization in high-purity titanium, Int. J. Plast. 92 (2017) 148–163.

[81] A.J. Wilkinson, D. Randman, Determination of elastic strain fields and geometrically necessary dislocation distributions near nanoindents using electron back scatter diffraction, Philos. Mag. 90 (2010) 1159–1177.

[82] D.R. Lesuer, C.K. Syn, O.D. Sherby, J. Wadsworth, J.J. Lewandowski, W.H. Hunt, Mechanical behaviour of laminated metal composites, Int. Mater. Rev. 41 (1996) 169–197.

[83] G.S.W. Gerard, A Study of Poisson's Ratio in the Yield Region, Natl. Advis. Aeronaut. (1952).

[84] R.R. Keller, A. Roshko, R.H. Geiss, K.A. Bertness, T.P. Quinn, EBSD measurement of strains in GaAs due to oxidation of buried AlGaAs layers, Microelectron. Eng. 75 (2004) 96–102.

[85] H. Wang, C. Zhu, K.S. Vecchio, Deformation and Fracture Evolution of FeAl-based Metallic-Intermetallic Laminate (MIL) Composites., Acta Mater. 194 (2020) 496–515.

[86] L. Li, I.J. Beyerlein, W. Han, Interface-facilitated stable plasticity in ultra-fine layered FeAl/FeAl2 micro-pillar at high temperature, J. Mater. Sci. Technol. 73 (2021) 61–65.

[87] L.L. Li, Y. Su, I.J. Beyerlein, W.Z. Han, Achieving room-temperature brittle-to-ductile transition in ultrafine layered Fe-Al alloys, Sci. Adv. 6 (2020) 1–10.

[88] J.W. Zhang, I.J. Beyerlein, W.Z. Han, Hierarchical 3D Nanolayered Duplex-Phase Zr with High Strength, Strain Hardening, and Ductility, Phys. Rev. Lett. 122 (2019) 255501.

[89] H. Wang, R. Kou, K.S. Vecchio, Design, fabrication and optimization of FeAl–FeAl2 eutectoid metallic-intermetallic laminate (MIL) composites, Materialia. 13 (2020) 100859.

[90] F. Jiang, K.S. Vecchio, Fracture of Nitinol under quasistatic and dynamic loading, Metall. Mater. Trans. A Phys. Metall. Mater. Sci. 38 A (2007) 2907–2915.

[91] R.K. Desu, H. Nitin Krishnamurthy, A. Balu, A.K. Gupta, S.K. Singh, Mechanical properties of Austenitic Stainless Steel 304L and 316L at elevated temperatures, J. Mater. Res. Technol. 5 (2016) 13–20.

[92] M.A. Morris-Muñoz, A. Dodge, D.G. Morris, Structure, strength and toughness of nanocrystalline FeAl, Nanostructured Mater. 11 (1999) 873–885.

[93] T. Godecke, W. Koster, Physical Measurements on Iron-aluminium Alloys Between 10 and 50 at-percent .7. The Thermal-expansion Behavior on Annealing of 26.5 to 50 at-percent Al-alloys Quenched from Decreasing Furnace Temperatures, Zeitschrift Fur Met. 75 (1984) 161–169.

[94] M.R. Harmouche, A. Wolfenden, Temperature and composition dependence of young's modulus for ordered B2 polycrystalline CoAl and FeAl, Mater. Sci. Eng. 84 (1986) 35–42.

[95] J.D. Baker, I.; Xiao, H.; Klein, O.; NelsonJ, C.; Whittenberger, The effect of temperature and Fe: Al ratio on the flow and fracture of FeAl, Acta Metall. Mater. 43 (1995) 1723–1730.

[96] A. Fakhimi, B. Hemami, Axial splitting of rocks under uniaxial compression, Int. J. Rock Mech. Min. Sci. 79 (2015) 124–134.

[97] W.R. Wawersik, C. Fairhurst, A study of brittle rock fracture in laboratory compression experiments, Int. J. Rock Mech. Min. Sci. 7 (1970) 561–575.

[98] G.R. Holzhausen, A.M. Johnson, Analyses of longitudinal splitting of uniaxially compressed rock cylinders, Int. J. Rock Mech. Min. Sci. 16 (1979) 163–177.

[99] T.N. Dey, C.Y. Wang, Some mechanisms of microcrack growth and interaction in compressive rock failure, Int. J. Rock Mech. Min. Sci. 18 (1981) 199–209.

[100] H. Horii, S. Nemat-Nasser, Compression-induced microcrack growth in brittle solids: Axial splitting and shear failure, J. Geophys. Res. 90 (1985) 3105.

[101] Z.P. Bažant, Y. Xiang, Size Effect in Compression Fracture: Splitting Crack Band Propagation, J. Eng. Mech. 123 (1997) 162–172.

[102] F. Freddi, G. Royer-Carfagni, Variational fracture mechanics to model compressive splitting of masonry-like materials, Ann. Solid Struct. Mech. 2 (2011) 57–67.

[103] A.. Dalgleish, B.J., Lu, M.C. and Evans, The strength of ceramics bonded with metals, Acta Metall. 36 (1988) 2029–2035.

[104] D.J. Gaydosh, M. V. Nathal, Influence of testing environment on the room temperature ductility of FeAl alloys., Scr. Metall. 24 (1990) 1281–1284.

[105] X. Ma, C. Huang, J. Moering, M. Ruppert, H.W. Höppel, M. Göken, J. Narayan, Y. Zhu, Mechanical properties of copper/bronze laminates: Role of interfaces, Acta Mater. 116 (2016) 43–52.

[106] A. Scherf, A. Kauffmann, S. Kauffmann-Weiss, T. Scherer, X. Li, F. Stein, M. Heilmaier, Orientation relationship of eutectoid FeAl and FeAl2, J. Appl. Crystallogr. 49 (2016) 442–449.

[107] G.F.BastinF.J.J.van LooJ.W.G.A.VrolijkL.R.Wolff, Crystallography of aligned Fe-Al eutectoid, J. Cryst. Growth. 43 (1978) 745–751.

[108] A. Hirata, Y. Mori, M. Ishimaru, Y. Koyama, Role of the triclinic Al2Fe structure in the formation of the Al5Fe2-approximant, Philos. Mag. Lett. 88 (2008) 491–500.

[109] Y. Wang, S. Zhou, K.S. Vecchio, Annealing effects on the microstructure and properties of an Fe-based Metallic-Intermetallic Laminate (MIL) composite, Mater. Sci. Eng. A. 665 (2016) 47–58.

[110] Z.F. Zhang, J. Eckert, Unified tensile fracture criterion, Phys. Rev. Lett. 94 (2005) 1–4.

[111] C. Manière, C., Pavia, A., Durand, L., Chevallier, G., Afanga, K., Estournès, Finite-element modeling of the electro-thermal contacts in the spark plasma sintering process, J. Eur.

Ceram. Soc. 36 (2016) 741–748.

[112] E.A. Olevsky, C. Garcia-Cardona, W.L. Bradbury, C.D. Haines, D.G. Martin, D. Kapoor, Fundamental aspects of spark plasma sintering: II. Finite element analysis of scalability, in: J. Am. Ceram. Soc., 2012: pp. 2414–2422.

[113] Y. Achenani, M. Saâdaoui, A. Cheddadi, G. Bonnefont, G. Fantozzi, Finite element modeling of spark plasma sintering : Application to the reduction of temperature inhomogeneities , case of alumina, Mater. Des. 116 (2017) 504–514.

[114] T. Surholt, D.A. Molodov, C.H.R. Herzig, Oritentation Dependence of Ge Diffusion along Symmetrical [111] Tilt Grain Boundary in Al, Acta Mater. 46 (1998) 5345–5355.

[115] X. Li, A. Scherf, M. Heilmaier, F. Stein, The Al-Rich Part of the Fe-Al Phase Diagram, J. Phase Equilibria Diffus. 37 (2016) 162–173.

[116] K. Murakami, N. Nishida, K. Osamura, Y. Tomota, Aluminization of high purity iron by powder liquid coating, Acta Mater. 52 (2004) 1271–1281.

[117] J.S. Kirkaldy, Diffusion in Multicomponent Metallic Systems, Can. J. Phys. 35 (1957) 435–440.

[118] T. Helander, J. Ågren, Diffusion in the B2-B.C.C. phase of the Al-Fe-Ni system - application of a phenomenological model, Acta Mater. 47 (1999) 3291–3300.

[119] S.G. Denner, R.D. Jones, Kinetic interactions between aluminiumliquid and iron/steelsolid for conditions applicable to hot-dip aluminizing, Met. Technol. 4 (1977) 167–174.

[120] C. Manière, A. Pavia, L. Durand, G. Chevallier, K. Afanga, C. Estournès, Finite-element modeling of the electro-thermal contacts in the spark plasma sintering process, J. Eur. Ceram. Soc. 36 (2016) 741–748.

[121] D. Li, Z. Shen, Sintering by intense thermal radiation (SITR): A study of temperature distribution by simulation and experiments, J. Eur. Ceram. Soc. 35 (2015) 3303–3309.